Sven Passinger

Two-Photon Polymerization and application to Surface Plasmon Polaritons

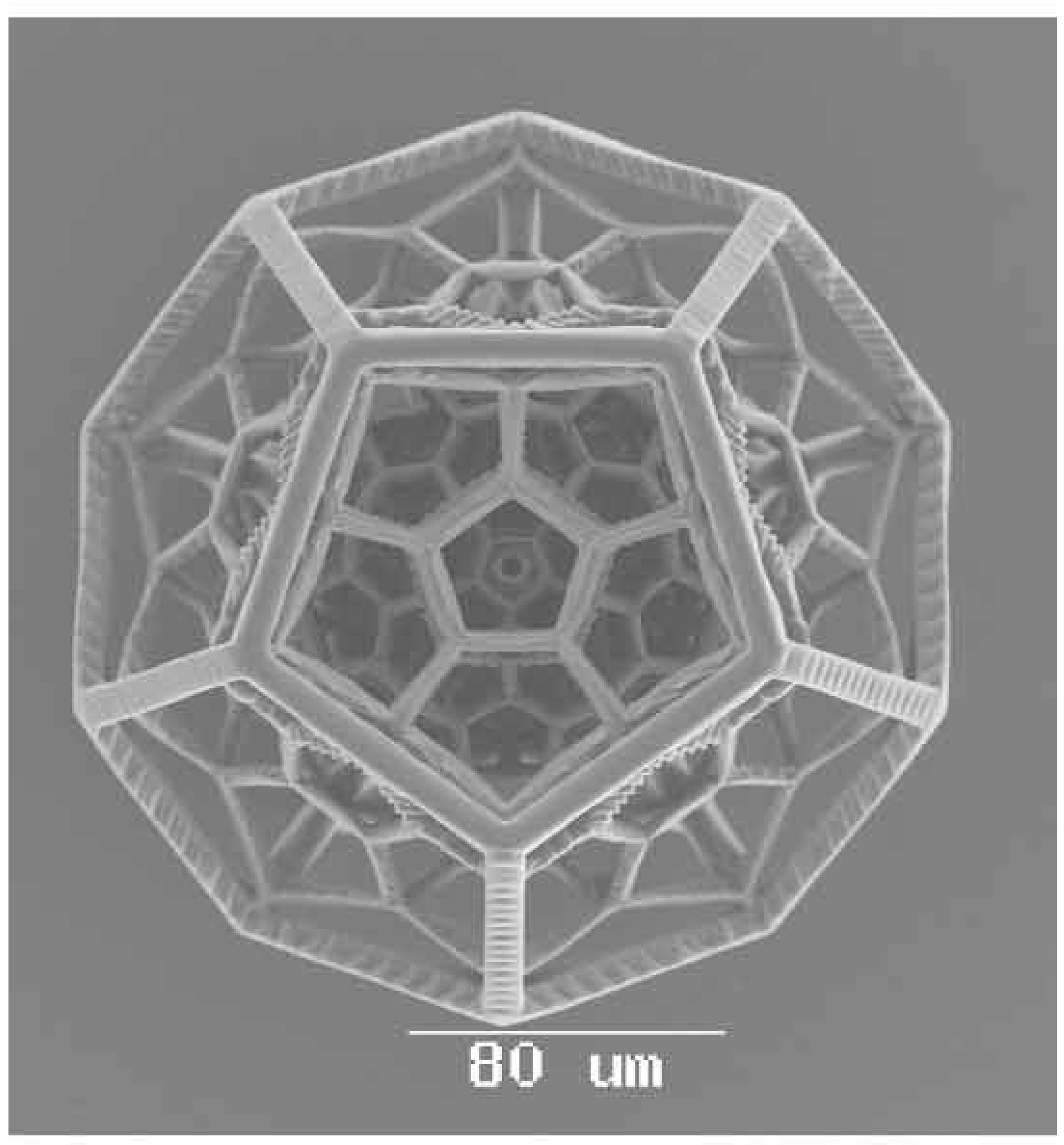

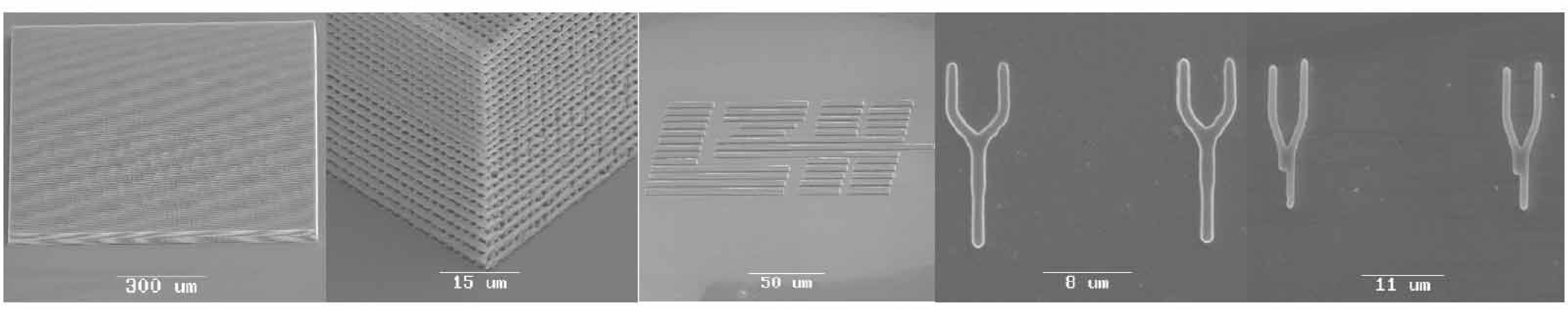

Cuvillier Verlag Göttingen

Two-Photon Polymerization and application to Surface Plasmon Polaritons

Von der Fakultät für Mathematik und Physik
der Gottfried Wilhelm Leibniz Universität Hannover
zur Erlangung des Grades eines

Doktors der Naturwissenschaften

- Dr. rer. nat. -

genehmigte Dissertation
von

Dipl.-Phys. Sven Passinger

geboren am 19.03.1979 in Hildesheim

2008

Bibliografische Information der Deutschen Nationalbibliothek
Die Deutsche Nationalbibliothek verzeichnet diese Publikation in der Deutschen Nationalbibliografie; detaillierte bibliografische Daten sind im Internet über http://dnb.ddb.de abrufbar.
1. Aufl. - Göttingen : Cuvillier, 2008
Zugl.: Hannover, Univ., Diss., 2008

978-3-86727-662-7

Referent:	Prof. Dr. Boris N. Chichkov
Korreferent:	Prof. Dr. Uwe Morgner
Tag der Promotion:	16. Juli 2008

Nonnenstieg 8, 37075 Göttingen
Telefon: 0551-54724-0
Telefax: 0551-54724-21
www.cuvillier.de

1. Auflage, 2008
Gedruckt auf säurefreiem Papier

978-3-86727-662-7

Kurzzusammenfassung

Plasmonic ist ein großer Bereich der Nanophotonic. Neben einer großen Anzahl bereits entwickelter industrieller Anwendungen, z.B. verbesserte Biosensoren und Dioden, bieten Oberflächen-Plasmonen Polaritonen (SPPs) ein immer noch wachsendes Forschungsfeld.

In der konventionellen Optik ist das Arbeiten in Größenordnungen unterhalb der Wellenlänge nicht einfach. Strukturen mit Auflösungen unterhalb der halben Wellenlänge führen nicht zu den von konventioneller Optik vorhergesagten Resultaten. Moderne Mikrochips und optische Datenspeicher werden am Limit der konventionellen Optik hergestellt, und SPPs können, wie von Ebbesen in 1998 gezeigt, den Weg zu Auflösungen weit unterhalb des Beugungslimits öffnen. Die Tatsache, dass die relevanten Längen für SPPs sieben Größenordnungen umfassen, von der Eindringtiefe in Metal mit einigen Nanometern, bis zur Propagationslänge von weitreichenden Plasmonen (long range plasmons) mit einigen Zentimetern, macht sie sehr interessant für wissenschaftliche Untersuchungen.

Die Aufgabe dieser Arbeit ist die Untersuchung von dielektrischen Wellenleitern für SPPs (dielectric loaded surface plasmon polariton waveguides (DLSPPWs)). DLSPPWs werden für die Telekommunikationswellenlänge von $1550\,nm$ theoretisch mittels Computersimulation analysiert. Die Wellenleiter werden experimentell für $632\,nm$ und $800\,nm$ Wellenlänge unter der Verwendung eines Leck-Strahlungs Mikroskops (leakage radiation microscope) untersucht. Die experimentell erhaltenen Werte werden mit den Simulationen für die entsprechende Wellenlänge verglichen. Weiterhin werden SPP Strukturen, wie z.B. gekrümmte und sich verzweigende Wellenleiter, untersucht. Ein neues 'cut'-Splitter Design für einen sich verzweigenden Wellenleiter wird entwickelt und mit bereits existierenden Splitter Entwürfen verglichen. Es wird eine erhöhte Effizienz und bessere Tolleranz gegenüber Fabrikationsfehlern des 'cut'-Splitters im Vergleich zu herkömmlichen Splitter Entwürfen mittels Simulation und Experiment demonstriert.

Für die Herstellung von DLSPPWs wird die 2-Photonen-Polymerisation (2PP) auf Grund ihrer sehr guten Flexibilität und geringen Kosten im Vergleich zu anderen Strukturierungstechnologien ausgewählt. Seit der ersten Veröffentlichung über die 2PP im Jahre 1997 von S. Kawata ist das Interesse und die Forschungsarbeit an dieser Technologie beständig gewachsen. Der Fortschritt wurde hauptsächlich durch wissenschaftliches Interesse an der Nutzung der 2PP als 'rapid-prototyping' Technologie vorangetrieben. Um die 2PP in die industrielle Anwendung zu überführen wurde während dieser Arbeit ein neuartiges Strukturierungssystem entwickelt und aufgebaut. Die Schreibgeschwindigkeit für die 2PP wurde im Vergleich zu anderen Veröffentlichungen um das 100 fache verbessert. Drei dimensionale Strukturen wurden mit einer Auflösung unterhalb von $300\,nm$ und mit Schreibgeschwindigkeiten von $30\,mm/s$ reproduzierbar hergestellt.

Schlagworte: Oberflächen Plasmonen Polaritonen, Nanophotonik, Ultra kurze Laserpulse, Zwei-Photonen-Polymerisation

Abstract

Plasmonics is a large part of the field of nanophotonics. Besides a wide range of industrial applications already developed, e.g. enhanced biosensors and diodes, surface plasmon polaritons (SPPs) are still an expanding field of research.

In conventional optics, working on the sub-wavelength scale is not trivial, and structures smaller than half the wavelength will not lead to results expected by traditional optics. State-of-the-art microchips and optical data storage devices are fabricated at the limit of conventional optics. SPPs could open up the way to sub-wavelength optics far beyond the diffraction limit as demonstrated by Ebbesen in 1998. The length scales for SPPs span over seven orders of magnitude, from several nanometers, the penetration depth into metal, to several centimeters, the propagation length of long range plasmons, making them very interesting objects for investigation.

The subject of this thesis is the investigation on dielectric loaded surface plasmon polariton waveguides (DLSPPWs). DLSPPWs are theoretically analysed by computational simulations at telecommunication wavelength at $1550\,nm$. The waveguides are experimentally examined using leakage radiation microscopy for $632\,nm$ and $800\,nm$ wavelength. The experimental results are compared with simulation results of corresponding wavelengths. Furthermore, SPP structures like bends and Y-splitters are investigated. A novel cut-splitter design for an SPP Y-splitter is introduced and compared to existing designs. For the cut-splitter an improved efficiency and a better tolerance against fabrication imperfections due to limited resolution than for conventional Y-splitter designs is demonstrated through experimental investigations and simulations.

For the fabrication of DLSPPWs, 2-Photon Polymerization (2PP) is, because of its high flexibility and low costs compared to other nanostructuring technologies, and easy adaptability. Since the first publication about 2-Photon-Polymerization by S. Kawata in 1997, the interest and research in this technology has been continuously increasing. Progress in this technique has been mainly initiated by scientific interest for use as a rapid prototyping technology. To transfer the 2PP technology to industrial applications, a novel structuring system is developed and set up during this work. The 2PP writing speed is increased by a factor of about 100, compared to results in other publications. Three-dimensional structures with resolutions smaller than $300\,nm$ are reproducible fabricated with writing speeds of about $30\,mm/s$.

Key words: surface plasmon polariton, nanophotonic, ultra short laser pulses, two-photon polymerization

Contents

Definitions

A	'domain'
a	'acceleration'
a_g	'grating constant'
a_I	'interference period'
α	'distance from edge'
α_F	'angle of funnel'
$\overrightarrow{B}$	'magnetic field'
β^2	'eigenvalue'
c	'speed of light in vacuum $\sim 2.998 \times 10^8 m/s$'
C_{w40}	'crosstalk after $40\mu m$ in a double waveguide'
χ	'first order nonlinearity'
χ^2	'second order nonlinearity'
χ^3	'third order nonlinearity'
d	'diameter'
D_0	'electric displacement field'
d_a	'lattice distance'
d_B	'distance between the entrance and exit of a bend (shift / deviation) perpendicular to the waveguide direction'
Δx	'grid size in x-direction'
Δy	'grid size in y-direction'
Δz	'grid size in z-direction'
δ_{max}	'loss tangent'
DOF	'depth of focus'
d_W	'distance between center of two waveguides'
d_Y	'distance between the exit arms of a splitter'
$\overrightarrow{E}$	'electric field'
e	'elementary charge'
ϵ	'permittivity'
η	'efficiency of initiation process'
η_R	'reflection factor'
E_{Ti}	'values of the field along each edge'
E_{Zi}	'values of the field at each node'
f_i	'focal length of lens i with i an integer'
$f(r_0)$	'spatial excitation of ϕ_L'
$g(t)$	'temporal excitation of ϕ_L'

$\overrightarrow{H}$	'magnetizing field'
$\hbar$	'Dirac constant $\sim 1.054571 \times 10^{-34}\,Js$'
I	'intensity'
i	'integer number'
I_0	'start intensity'
I_1	'intensity one'
I_2	'intensity two'
I_{in}	'input intensity'
I_{out}	'output intensity'
k_i	'wavevector i, with i an integer'
k_x	'wavevector component along x direction'
k_y	'wavevector component along y direction'
k_z	'wavevector component along z direction'
l	'length of a line'
L	'propagation length'
L_{PML}	'thickness of PML'
L_0	'propagation length of surface plasmon polaritons'
λ	'wavelength'
λ_L	'wavelength of laser'
λ_P	'wavelength of plasma oscillation'
L_B	'bend length'
L_c	'coupling length'
L_{defect}	'length of a defect'
L_f	'length of a function'
L_{mms}	'length of a multi-mode-section'
L_{Path}	'path length'
m_0	'electron mass'
μ	'permeability'
n	'number of applied pulses'
n_b	'basis dimension'
n_e	'electron density'
N_0	'photon flux'
NA	'numerical aperture'
n_{Au}	'refractive index of gold'
n_{die}	'refractive index of dielectric'
n_{eff}	'effective refractive index'
n_{met}	'refractive index of metal'
n_{Poly}	'refractive index of polymer'
n_{SPP}	'effective index of SPPs'
ν	'repetition rate of laser'
ω_L	'laser frequency'
ω_P	'plasma frequency'
ω_{SPP}	'frequency of surface plasmon polaritons'

P	'average laser power'
$\overrightarrow{P}$	'polarization'
ϕ_L	'starting filed'
P_i	'position of focussing i μm above or below the metal surface'
π	'$\sim$ 3.14159265'
r	'radius'
r_0	'radius of focal spot'
ρ_0	'density of radicals'
ρ_{th}	'threshold of radicals'
s	'distance'
$\overline{s}$	'identity tensor'
Si	'sensor i with i an integer'
σ_2	'effective two-photon cross section'
σ_2^a	'ordinary two-photon cross section'
t	'time'
T	'transmission'
τ_L	'puls length of laser'
T_{bend}	'bend transmission'
T_{curve}	'transmission of a curved waveguide'
T_{diff}	'diffraction transmission'
θ	'half angle of cone of light'
θ_0	'angle of incidence'
T_L	'time to write a line'
T_{ohmic}	'Ohmic transmission'
T_{split}	'splitter transmission'
T_{total}	'total transmission'
v	'speed'
w	'width of waveguide'
w_B	'width of base'
x	'coordinate'
y	'coordinate'
z	'coordinate'
z_R	'Rayleigh length'

List of abbreviations

1PA	'one-photon-absorption'
1PP	'one-photon-polymerization'
2PA	'two-photon-absorption'
2PCS	'two-photon absorption cross section'
2PP	'two-photon-polymerization'
AOM	'acousto-optical-modulator'
ATR	'attenuated total reflection'
CAD	'computer assisted design'
cw	'continuous wave'
DLSPPW	'dielectric-loaded surface plasmon polariton waveguide'
E-beam	'electron-beam'
EDX	'energy dispersive X-ray analysis'
fcc	'face centered cubic'
FDTD	'finite-difference time-domain'
FEM	'finite element method'
fs	'femtosecond'
LR	'leakage radiation'
MSL	'micro-stereolithography'
MZI	'Mach-Zehnder-interferometer'
OPO	'optical parametric oscillator'
PEC	'perfect electrical conductor'
PhC	'photonic crystal'
PML	'perfectly matched layer'
RP	'rapid prototyping'
SEM	'scanning electron microscope'
SH	'second harmonic'
SNOM	'scanning-near-field-optical-microscope'
SPP	'surface plasmon polariton'
STL	'stereolithography'
UV	'ultra violet'
voxel	'volume pixel'

1. Introduction

Investigations of electromagnetic surface waves already date back to the beginning of the 20th century. In 1907, Zenneck [Zen07] and in 1909, Sommerfeld [Som09] demonstrated theoretically that radio-frequency electromagnetic surface waves occur at the boundary of two media if one medium is either a 'lossy' dielectric or a metal, and the other is a loss-free dielectric medium. More than 50 years later, in 1960, Powell and Swan [PS57] found the first experimental evidence that SPPs contribute to the energy loss of fast electrons in thin-film transmission following the theoretical prediction by Ritchie [Rit57] in 1957. Ritchie investigated the impact of the film boundaries on the production of collective excitations, and found that the boundary effect causes the appearance of a new lowered loss, due to the excitation of surface collective oscillations. In 1958, Ferrell extended this work and showed theoretically the coupling of electromagnetic radiation to surface plasmon polaritons (SPPs), presenting the first published SPP dispersion relation [Fer58]. The SPP excitation by light was demonstrated by Otto [Ott68] using an attenuated-total-reflection (ATR) setup, and by Kretschmann and Raether [KR68] independently in 1968. Since this time, a significant advance in theoretical and experimental investigations of SPPs has taken place. This progress has played a key role in many research fields, such as condensed matter and surface physics, for the interpretation of many experiments, and the understanding of various fundamental properties of solids. Some examples of this are the understanding of the nature of Van der Waals forces [IW75] [ZK76] [Ser05], the classical image potential acting between a point classical charge and a metal surface [Fei71] [Rit72] [RM72] [MSL72], the energy transfer in gas-surface interactions [GM80], surface energies [SL72] [WI77] [LP77], the damping of surface vibrational modes [CS80] [PR85], the energy loss of charged particles moving outside a metal surface [EP75] [EPMJ81] and the de-excitation of adsorbed molecules [Ueb92]. SPPs are also used in many studies ranging from electrochemistry [Kno98], wetting [SHP97] and biosensing [Mal93] [Bra98] [CC03] to scanning tunnelling microscopy [RBJ91], the ejection of ions from surfaces [SC93], nanoparticle growth [RJZ01] [RJM03], surface plasmon microscopy [RK88] [GFE95] and surface plasmon resonance technology [GE80] [BLL83] [SSCI93] [Sch97] [JHG99] [RR99] [RGT00].

The interest in SPPs has been renewed by investigations of the electromagnetic properties of nanostructured materials [Pen99] [EPN03], and especially concerning the feasibility of sub-wavelength optics. An example for this is the enhanced transmission of light through a periodic array of sub-wavelength holes in metallic films [TEW98] [HLE02]. The advantage of SPPs compared to classical optics is the tight bonding of light to a metal-dielectric interface with a penetration depth of about

$10\,nm$ into the metal, and more than $100\,nm$ into the dielectric, depending on the wavelength. SPPs concentrate light in a region that is smaller than their wavelength, opening up the possibility of using them for the fabrication of nanoscale photonic circuits at optical frequencies [Ozb06] [WBE03], and giving the possibility of merging optical and electronic circuits on the same length scale. Using this the problems related to the size mismatch between the micrometer optical circuits and the nanometer electronic chips can be overcome. SPPs, as they are investigated in this work, can provide a basis for the construction of nano-circuits able to work for optical signals and electric currents. These optoelectronic circuits could consist of various components such as couplers, waveguides, switches, and modulators.

The main topic of this thesis is the fabrication and analysis of dielectric loaded surface plasmon polariton waveguides (DLSPPWs). The investigation on these structures and their application are realized theoretically by computational simulations, and also experimentally by leakage radiation microscopy. For the fabrication of the DLSPPWs, 2-Photon-Polymerization (2PP) is applied, and the fabrication process is optimized, from which the second task for this work arises. 2PP processing is investigated, and the fabrication speed is increased drastically to bring 2PP from a purely scientific rapid prototyping tool to a reliable, high speed rapid prototyping nanotechnology. To achieve this, a novel, 3-dimensional structuring system has been set up, allowing writing speeds up to $30\,mm/s$, more than 100 times faster than 2PP writing speeds reported so far.

The thesis is structured as follows:

- At the beginning of chapter 2, the state-of-the-art for different nanostructuring technologies is compared and 2-Photon-Polymerization is introduced in detail. A novel system for real, 3-dimensional structuring using 2PP developed during this work is described. Different laser systems are tested and compared in respect to their applicability to 2PP, and the two-photon absorption cross sections achievable with the laser systems in commercial ORMOCER material are determined. High speed 2PP structuring is demonstrated, with writing speeds of $30\,mm/s$, about 100 times higher than reported before. At the end, different examples of 2PP fabricated structures are given in the fields of micromechanics, micro-fluidics, micro-optics, and bio-medicine.

- In chapter 3, the theoretical framework to describe surface plasmon polaritons (SPPs) is introduced, and guiding in dielectric loaded surface plasmon polariton waveguides (DLSPPWs) is investigated using numerical simulations which use the Finite-Difference-Time-Domain method (FDTD) and Finite-Element-Method (FEM). After giving a brief overview of possible materials for DLSPPWs, two programs for the simulation of SPPs and their propagation are described. First basic investigations on DLSPPWs are performed and the properties of SPPs inside these waveguides are analysed.

- In chapter 4, the simulations of DLSPPWs are continued with more complex SPP structures. An SPP Y-splitter suggested by [KZ07] is analysed in detail. For the first time, inaccuracies induced by fabrication limitations of DLSPPW structures are taken into account, and a real-Y-splitter model is simulated. From this starting point, different possibilities for an improved Y-splitter design are suggested and simulated. At the end, a novel Y-splitter design, the so called cut-splitter, is introduced. The efficiency and tolerance to the fabrication defects of the cut-splitter is compared to the Y-splitter design, and a high efficiency and better defect tolerance is demonstrated.

- In chapter 5, the experimental investigations on DLSPPWs fabricated by 2PP are presented. Starting from the modes propagating in waveguides of different size and for different wavelengths, the measured efficiency of simple SPP components such as curved waveguides, bends and splitters are compared with results obtained from simulations. Also, the efficiency of the novel cut-splitter design, suggested in this work, is compared with theoretical predictions. Furthermore, Mach-Zehnder-interferometers are fabricated, analysed and simulated as first wavelength dependent component. As an outlook, some 3-dimensional structures for SPPs are suggested, as these can only be fabricated using 2PP.

2. Two-Photon Polymerization and experimental realization

In this chapter, different techniques for micro- and nanostructuring are reviewed and compared. The state of the art for Two-Photon Polymerization (2PP) is summarized, and a brief introduction to the theory of 2PP is given. After that, the 2PP system developed and commercialized during this work is introduced. The progress in 2PP with this system is pointed out, and different laser systems are tested in respect to their usability in 2PP. The two-photon absorption cross sections (2PCSs) for different wavelengths are compared, and the writing speed for 2PP is increased by a factor of about 500 with respect to previously published results. At the end of this chapter, various application examples of 2PP fabricated structures are presented briefly.

2.1. Overview of nanostructuring techniques

Micro- and nanotechnology are fast growing fields in research and industry. Many different technologies have been developed to structure materials with micrometer and nanometer resolution. The main goal of these developments is an improvement in resolution, and at the same time an increase in the fabrication speed and reduction of the fabrication costs. Also, the trend from pure 2-dimensional structures to 2.5-dimensional and 3-dimensional structures can be observed. The techniques mainly used for the generation of micro- and nano-structures can be divided into parallel and serial processing methods. The most important techniques for micro- and nanostructuring are shortly presented in this chapter.

Optical lithography is the most commonly used technique for nanostructuring, belonging to the parallel processing technologies [Mor88] [Ell89] [LFTB83]. It is mostly used on the scale of wafer size illumination, especially for the fabrication of computer chips. Since the late 1960s, when integrated circuits had line widths of $5\,\mu m$, to 1997, when minimum line widths reached $0.35\,\mu m$ in 64Mb DRAM circuits, optical lithography has been used for manufacturing. In 2006 a resolution of $32\,nm$ has been demonstrated by using a high index lens [Han06] as the next step of enhancement. This dominance of optical lithography in production is the result of a worldwide effort to improve optical exposure tools and resists. Although lithography system costs, which are typically more than one third the costs of processing a wafer to completion, increase as minimum feature size on a semiconductor chip decreases, optical lithography remains attractive because of its high wafer throughput. The drawback of this technology is the lack of flexibility. The illumination in optical lithography takes place through a mask which must first be manufactured. These masks are commonly produced using electron-beam technology, as discussed later [TRGB93]. Optical lithography is a 2-dimensional technique which is extended to 2.5-dimensions using layer by layer fabrication techniques. This layer by layer structuring slows down the fabrication process, but the throughput remains high, due to the large areas which can be processed. Optical lithography is performed with different wavelengths, ranging from 355 nm down to 193 nm and 157 nm in the deep-UV. The feature size recently demonstrated with 193 nm illumination was less than 40 nm [MTK07] [JdKH07]. Optical lithography has the drawback of a low flexibility and 2-dimensionality. Nevertheless, it is the best technique for the fabrication of computer chips today. In research the high costs and the leak of flexibility are very important drawbacks resulting in only little use.

Another technology representing a parallel processing approach is nanoimprint lithography. For this, a master stamp is used to imprint structures into a polymer [MBK02] [Cho06]. Three different approaches are used for polymerization. The first possibility is to heat the polymer above its glass transition temperature during imprinting, making it flexible. The polymer cools down after the stamp is pressed into the polymer and solidifies, taking over the structures from the stamp. Another possibility for imprinting techniques is stamping into a liquid photosensitive polymer and illuminating it with UV-light through a transparent stamp. For these two techniques, the stamp is separated from the surface after the polymer hardened. In the next processing step the polymer is etched down to remove the residual layer resulting from the stamping process, and achieving polymer structures on a clean substrate. The third possibility for imprinting is the electro-chemical approach. For this, a stamp made from a fast ion (superionic) conductor such as silver sulfide is used. The stamp is brought into contact with a metal. In this configuration, electrochemical etching can be carried out by applying voltage, structuring the metal with the inverse pattern of the stamp.

With imprinting technologies a minimal resolution of about 20 nm is achievable and used for mass fabrication [SC96] [XL07]. The drawback is the stamp, which has to be fabricated using other nano-writing techniques, like e-beam direct writing.

The other group of technologies are the serial techniques mainly represented by electron and ion-beam, and direct UV writing. Also 2PP belongs to this group.

The primary advantage of electron beam lithography is the resolution in the nanometer regime. Beam widths can be in the order of nanometers [Man98] [HHT95] [dJK95]. This form of lithography has found wide usage in mask-making for optical and nanoimprint lithography, low-volume production of semiconductor components, and research and development. E-beam lithography is not suitable for high-volume manufacturing because of its limited throughput. It is a serial process because the beam must be scanned across the surface. This makes pattern generation very slow compared with a parallel technique like optical lithography, in which the entire surface is patterned at once. Typical writing speeds of e-beam system nowadays are in the range of $\mu m/s$, making it impossible to compete with optical lithography for mass production.

Ion-beam lithography works in the same way as E-beam lithography, but uses accelerated ions instead of electrons. It has more or less the same advantages of high resolution and flexibility, and the drawbacks of high costs and slow production

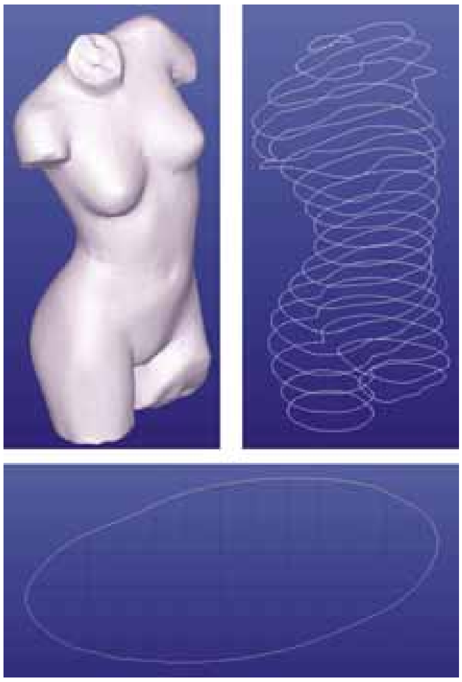

Figure 2.1.: The principle of slicing. Starting from a 3-dimensional file (left top) it is sliced into layers (right top) and each layer is filled with a hatching to give the structure more stability (bottom).

speed as E-beam lithography, but it is a much younger technique and not so wide spread.

An example of the direct write UV technique is the micro-stereolithography (MSL). Stereolithography (STL) is the best known laser based rapid prototyping (RP) technology, and was first reported in 1981, independently by [Hul84], [JAdW84], [Kod81]. It is a 2.5 dimensional production process based on polymerization of a photosensitive monomer by a laser beam scanning the surface of the photocurable resin. MSL is the extension of stereolithography to a better resolution of a few micrometers. Stereolithography starts from a 3-dimensional CAD (computer assisted design) model (a STL-file) which is sliced into a series of horizontal planes representing the 2-dimensional cross sections of the object (see figure 2.1) at different z-coordinates. The 2-dimensional models are translated into a machine control code and send to the writing system. In each slice the contour obtained from the STL-file can be filled with different styles of hatching (mostly lines). By filling the contour, the structure becomes more stable or can be provided with a sub-structure. The structure is built from a UV-curable resin in a layer-by-layer technique. The advantage of this technique is a quite fast and highly flexible production of 2.5-dimensional structures. Also, the relatively low costs compared to E-beam and ion-beam lithography are an advantage, while the drawback is the resolution of only about $5\mu m$.

For micro-stereo-lithography, it should be mentioned that the writing speed is not the only limiting factor to production speed. Because the polymerized material is moved relative to the liquid polymer, there must be a waiting time between the structuring of two layers, reducing the effective fabrication time and leading to a very strong dependence of fabrication time on the structural design.

Technology	Typical dimensions	Reso-lution	Speed	Costs per part	Flexibility
optical lithography	4″ wafer	$30\,nm$	fast	low	very poor
nano imprint lithography	4″ wafer	$20\,nm$	fast	low	very poor
electron- / ion-beam lithography	$< 1\,mm^2$	$3\,nm$	very slow (typical $< 100\,\mu m/s$)	very high	good
micro-stereo lithography	$< 10 \times 10\,mm^2$	$5\,\mu m$	medium (typical 1 to $200\,mm/s$)	high	good
2PP	$50 \times 50\,\mu m$	$30\,nm$	very slow (typical $< 100\,\mu m/s$)	high	very good
2PP (with improvements achieved in this work)	$15 \times 10\,cm^2$	$100\,nm$	medium 30 to $50\,mm/s$)	medium - high	very good

Table 2.1.: Comparison of different micro- and nanofabrication technologies: the typical dimensions of substrates worked on, the resolution limit, the typical fabrication speed for one part or for direct writing technologies the typical writing speed, the typical costs per fabricated part (for the fabrication of a large number of identical parts), and the flexibility to fabricate different structures.

2-Photon-Polymerization (2PP) is the youngest of all these techniques. It was first demonstrated in 1997 [SMK97]. Since then, a few research labs in different parts of the world have established this technology, but up to now no industrial application of 2PP has been implemented. 2PP is based on the same principal, the light induced polymerization, as MSL or 1PP. The difference in multi-photon processing is the laser system used (the principal and setup of 2PP technique are described in more detail in chapter 2.2). The advantage of 2PP is the achievable resolution, which is below $100\,nm$, and thus far below the diffraction limit of the wavelength used. The unique point of 2PP compared to all the other techniques discussed here is the real 3-dimensionality. In 2PP, one is not restricted to a layer-by-layer technique, but can really build a 3-dimensional free form part.

The techniques discussed here are summarized together with their advantages and disadvantages in table 2.1. For 2PP, the parameters are given when this work started. In the last row, the results achieved in this work are included in the specifications of 2PP.

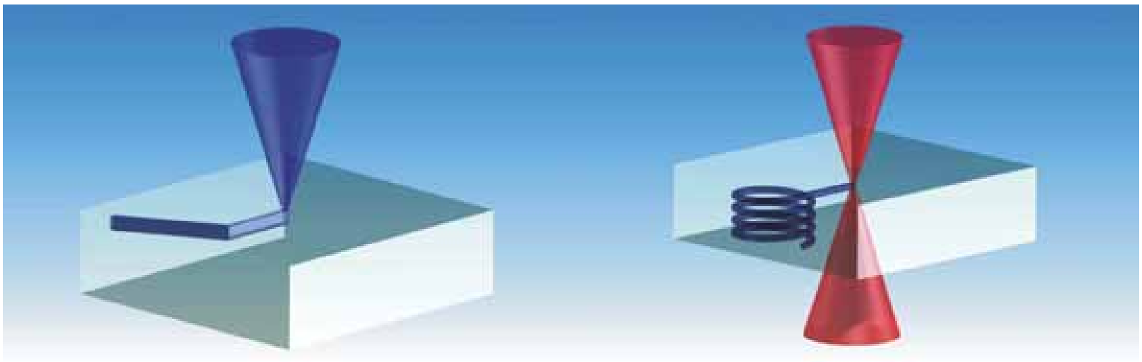

Figure 2.2.: The principle of 1PP (left) with the absorption of the laser at the top of the UV sensitive material and 2PP (right) with the focussing and absorption inside the material.

2.2. State-of-the-art and basics of Two-Photon Polymerization

Two-Photon Polymerization (2PP) is based on Two-Photon Absorption (2PA), a radiation-matter interaction relying on the excitation of an atom or molecule. In 2PA, the atom or molecule is transferred from a lower state to an excited state of the same parity in a single step [IPAR03], which in contrast to a single photon process can not be described as a dipole transition. The 2PA theory was first developed by [GM31] in 1931, and experimentally realized in 1961 by [KG61]. The long period of 30 years until 2PA was observed for the first time is reasonable considering the fact that a high intensity is needed for 2PA, which can only be achieved using a laser, which was first developed in 1960.

2PA has a wide range of applications, especially in laser spectroscopy. One of the most common applications is the two-photon confocal microscopy [BH02], in which a dye molecule is excited by 2PA and the fluorescence is observed. The advantage of 2PA, compared to a one photon process, is the possibility for the local excitation of molecules anywhere inside a 3-dimensional volume.

Besides 3-dimensionality, 2PA techniques have the further advantage of a high resolution of about $100\,nm$ laterally and $500\,nm$ axially using high numerical aperture objectives [Rez02].

As the excitation of a dye molecule is possible by using one-photon absorption (1PA) or 2PA, this principle can be applied to the polymerization of a photosensitive molecule, leading to One-Photon Polymerization (1PP) and Two-Photon Polymerization (2PP). As shown in figure 2.2, a UV-sensitive resin is used for polymerization. UV-light is used for 1PP and absorbed within the first few micrometers, depending on the concentration of photoinitiators and absorber molecules [VKVV01]. Due to this fact, 1PP is a 2-dimensional process which achieves a 2.5-dimensional structuring by packaging layer by layer.

In contrast to 1PP, the 2PP process is initiated by wavelengths larger than $450\,nm$, and very intense light fields. The polymer and initiators used for this are mostly transparent for the applied wavelength and show a high absorption cross-section at

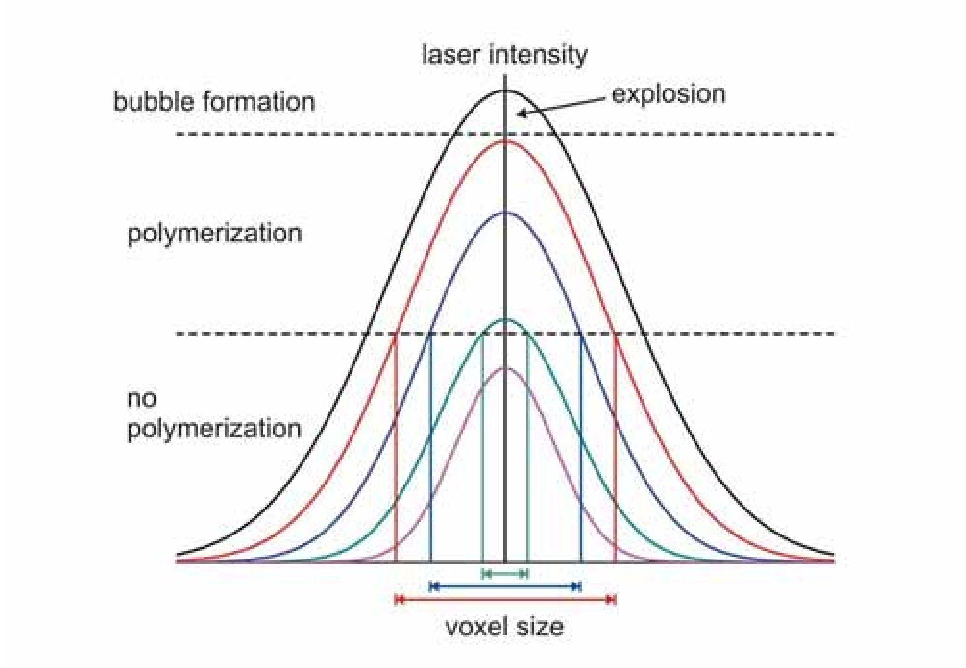

Figure 2.3.: Dependence of the polymerized volume on the laser intensity in 2PP, with the polymerization threshold and the threshold for polymer destruction.

half of the wavelength used. This makes it possible to focus the laser inside the polymer and induce a non-linear polymerization process. 2PP initiation depends on the intensity of the light used because it is a non-linear effect. Due to this, polymerization only takes place at the focal volume, which makes 3-dimensional writing possible. Furthermore, the non-linearity of the effect provides the possibility to reduce the size of the polymerized volume below the diffraction limit, as illustrated in figure 2.3.

2PP has two threshold values, one for starting the polymerization, and one for the destruction of the polymer. In theory, by applying the correct intensity it is possible to achieve infinitesimal small polymerized volumes (volume pixel (voxel)) limited only by the polymer properties. In reality the stability of the laser system and the setup limit the resolution. At present, about $100\,nm$ laterally is achieved. 2PP has two main advantages compared to 1PP. Obviously, the 3-dimensionality of 2PP, compared to a 2-dimensional process like 1PP, or in general lithographic processes, which allow only a quasi 3-dimensional structuring by stacking layer-by-layer, is the first great advantage. The second is the achievable resolution below the diffraction limit, which is not possible using a linear process. With 2PP structures with a resolution below $500\,nm$ are fabricated easily, while achieving even a resolution in the range of single micrometer is very difficult for 1PP. Furthermore, the presence of oxygen on a polymerizing layer leads to quenching of the radicalized molecules on the surface of the resin, and thus to a suppression of the polymerization. For this reason, high resolution 1PP must take place in an inert gas atmosphere. For 2PP, this quenching does not take place because polymerization is performed inside a volume, and has no contact to the surrounding oxygen. The drawback of 2PP compared to 1PP was, up to now, the writing speed of less than $100\,\mu m/s$, while 1PP achieves writings speeds around $1 - 200\,mm/s$. The writing speed of 1PP strongly depends on the geometry of the part and the necessary resolution. Because the polymerized material is moved relative to the liquid polymer, a delay time between the structuring of two layers is necessary, reducing the effective fabrication time. Nevertheless, with $100\,\mu m/s$ 2PP was still a slow technology. This drawback of the lower 2PP speed will be dealt with in chapter 2.4.

The derivation of the formulas describing 2PP will not be part of this work. A detailed description of the formulas for 2PP can be found in [Ser04].

In conventional linear optics, the resolution d (perpendicular to the laser beam) and the depth of field (DOF) (along the direction of the laser beam), and with this the resolution laterally and axially are given by formula 2.1 and 2.2, respectively

$$d = k_1 \frac{\lambda}{NA}, \tag{2.1}$$

$$DOF = k_2 \frac{\lambda}{NA^2}. \tag{2.2}$$

In these formulas, λ is the wavelength, NA is the numerical aperture of the focussing optic and k_1 and k_2 are constants defined by properties of the material and the illumination system. With conventional linear optics, values between 0.5 and 1 are achievable. Novel, off-axis illumination and alternating phase-shifted-mask-enhanced lithography are techniques that can be used to overcome this fundamental resolution limit, essentially by eliminating the zero diffracted order, and thereby imaging with properties similar to a two-beam interference system. With this, the values can be extended to the resolution limit of 0.25, which is the best value achieved up to now [LLD01]. From this it is clear, that with conventional optical techniques using $355\,nm$ and numerical apertures between 0.5 and 0.75 as done today, even the theoretical limit is $236\,nm$ (lateral) and $315\,nm$ (axial), what is worse than the resolution demonstrated by 2PP.

Due to the fact that 2PP is a nonlinear process, the formulas for the resolution change to a more complex form, which can be seen in 2.3 and 2.4 for the lateral and axial resolution, respectively

$$d(N_0, t) \;=\; r_0 \sqrt{ln(\sigma_2 N_0^2 n \tau_L / C)}, \tag{2.3}$$

$$l(N_0, t) \;=\; 2 z_R \sqrt{\sqrt{\sigma_2 N_0^2 n \tau_l / C} - 1}. \tag{2.4}$$

In these formulas, r_0 is the radius of the focal spot, z_R is the Rayleigh Length, $n = \nu t$ is the number of applied pulses, ν is the repetition rate of the laser system, t is the exposure time, τ_L is the length of the laser pulses, N_0 is the photon flux, $\sigma_2 = \sigma_2^a \eta$ is the effective two-photon absorption cross section for the generation of radicals $[cm^4s]$, σ_2^a is the ordinary two-photon cross section, $\eta < 1$ is the efficiency of the initiation process and C is given by $C = ln(\rho_0/(\rho_0 - \rho_{th}))$, with ρ_0 the density of radicals and ρ_{th} the threshold of radicals. To compare experimental results with the theoretical prediction, N_0 has to be replaced by

$$N_0 = \frac{2}{\pi r_0^2 \tau_l} \frac{PT}{\nu \hbar \omega_L}, \tag{2.5}$$

with P the average laser power, T the fraction of light transmitted through the focussing objective and ω_L the laser frequency. With this equation, 2.3 and 2.4 become formula 2.6 and 2.5, respectively

$$d(N_0, t) = r_0 \sqrt{ln \left(\frac{4\sigma_0^2}{\pi^2 r_0^4 \tau_L} \frac{P^2 T^2 n}{\nu^2 \hbar^2 \omega_L^2 C} \right)}, \tag{2.6}$$

$$l(N_0, t) = 2 z_R \sqrt{\sqrt{\frac{4\sigma_0^2}{\pi^2 r_0^4 \tau_L} \frac{P^2 T^2 n}{\nu^2 \hbar^2 \omega_L^2 C}} - 1}. \tag{2.7}$$

These formulas describe the resolution depending on the applied laser intensity in 2PP, and thus can be used for the interpretation of experimental results as they are discussed in chapter 2.4.

2.3. System for Two-Photon Polymerization

Before this work, only small scale, self-built laboratory systems for 2PP have been available. The drawback of these systems are the very slow structuring speed of about $100\,\mu m/s$. Also, all these setups have been laboratory systems assembled by the research institution itself, and not appropriate for use in an industrial environment. These systems are also far from commercialization. To overcome this drawbacks and to bring 2PP into industrial applications a commercial setup for 2-Photon Polymerization was designed and constructed during this work. All 2PP systems (laboratory and also the new developed commercial setup) are based on the same principal design which is shown in figure 2.4.

A 2PP setup consists of a femtosecond-laser source (typically a femtosecond oscillator), a fast shutter system (typically an acousto-optical modulator (AOM), from which the first diffraction order is used), a power adjustment which is usually realized by a $\lambda/2$ waveplate in combination with a polarization depending beamsplitter, an optional XY-galvoscanner for fast beam displacement, a focussing optic (in most cases a $100\times$ immersion oil microscope objective with a high numerical aperture), a XYZ-stage for the sample movement and placement, and a camera, viewing along the laser beam path for online process observation. This kind of laboratory setup and the working principal of the components are well described in [Ser04]. This kind of self-built laboratory setup is commonly used in laboratories doing research on

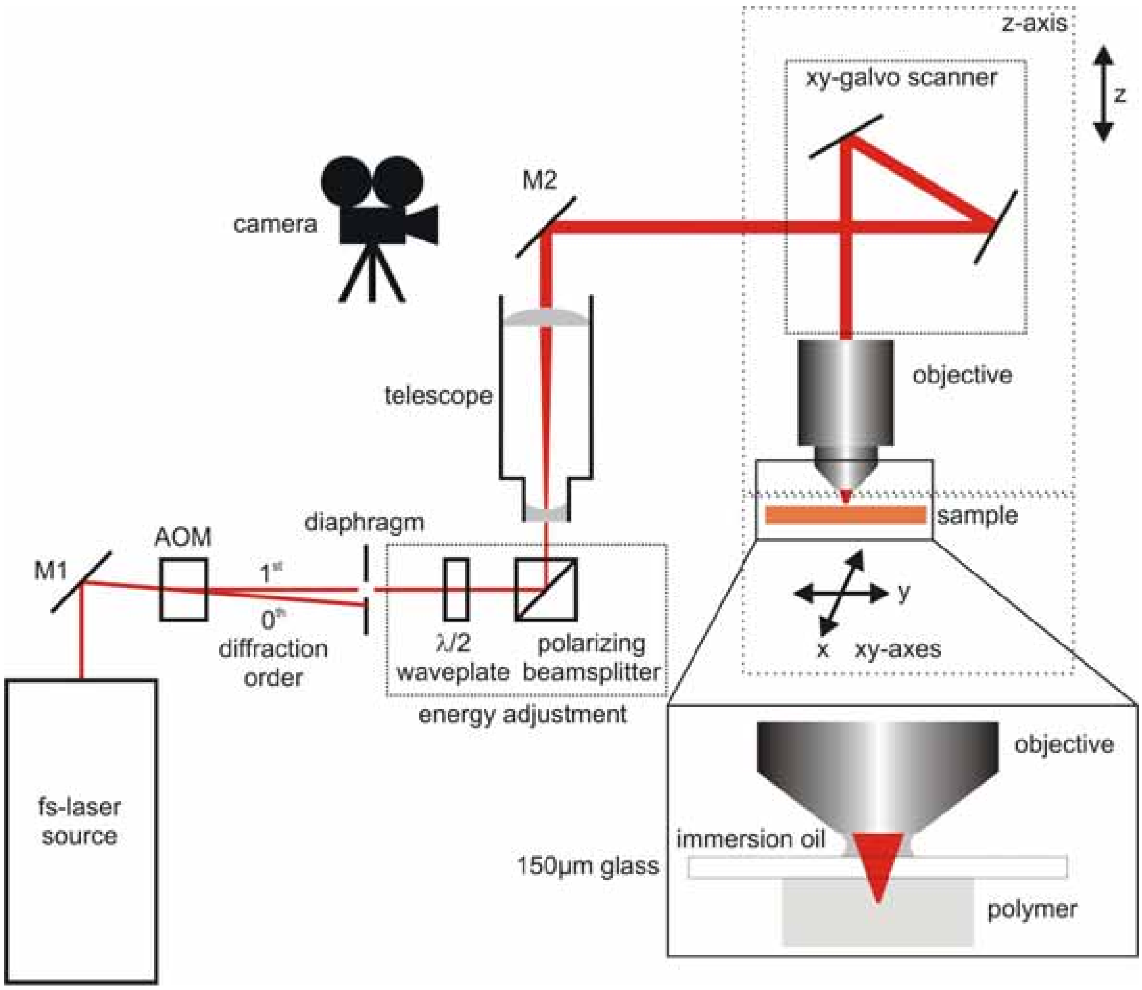

Figure 2.4.: Principal setup for a 2PP system with the fs-laser source, the AOM working as shutter system, the energy adjustment, a beam expander, the camera for online observation, the XY-galvoscanner, the focussing objective, and the sample on the positioning system.

2PP. These systems existing in some laboratories all over the world are suitable for scientific research on 2PP, but not for applications requiring large scale structuring, and thus for industrial applications or industrial related research.

With 2PP laboratory systems, there are in general two structuring possibilities. One is by moving the laser beam with a XY-galvoscanner. This has the advantage of high dynamical movement and very precise structuring. But for high resolution structuring, a high magnification immersion oil objective (e.g. a 100× magnification objective with a numerical aperture of 1.4 from *Carl Zeiss AG*) is necessary, which typically has a viewing field of smaller than $30 \times 30\,\mu m^2$. So the working field for structuring using a galvoscanner is limited to this size. Furthermore, the sample placement and the z-positioning still has to be done using a translation stage.

The other possibility for high resolution structuring is the use of a piezo-positioning system placed on top of a XY-translation stage. These systems provide nanometer-precise positioning of the sample, but are available only with a maximum travel range of $800 \times 800 \times 200\,\mu m^3$. The dynamics of the piezo systems are worse than a galvoscanner, but provide a larger travel range.

Nevertheless, both systems only provide structuring possibilities in very small areas, and need an additional XYZ-positioning system for larger travel distances and sample positioning. These kinds of systems are limited to structure sizes smaller than a millimeter, and for structures with a resolution smaller than $1\,\mu m$ a typical writing speed of $100\,\mu m/s$ or less is achieved, which is very slow. Beside these drawbacks, the self-built laboratory systems are typically set up on an optical table, and take a lot of space and require time-consuming programming. To overcome these drawbacks, the worldwide first commercial system for 2PP, the 'Micro-3-Dimensional Structuring System' (M3D), has been designed and constructed. This system is described in more detail in this chapter.

The 'Micro-3-Dimensional Structuring System' (M3D) was developed as a construction kit system: a stand-alone system called M3D, and a laboratory version called M3DL which is placed on an optical table. Structures and results presented in this work have been obtained with the M3D. The 3-dimensional construction drawing of the M3D setup is shown in figure 2.5, with the beampath illustrated in red.

The basic equipment of the M3D consists of a hard stone base and an XYZ-positioning stage. The hard stone base is necessary for the stability and stiffness of the system, and for the precise mounting of the XYZ-stage, which needs a mounting surface roughness of better than $5\,\mu m$. The XYZ-positioning system is a combination of three ABL1000 Air Bearing Stages from *Aerotech GmbH*, with travel ranges of $150\,mm$ (X-direction), $100\,mm$ (Y-direction) and $100\,mm$(Z-direction). The X- and Y-axes are combined to an XY-system mounted on the horizontal space of the hard stone front, while the Z-axis is mounted on the vertical front. The high precision alignment of these two hard stone surfaces guarantees a very precise alignment of the XY-axes with the Z-axis. Further specifications of the axes are shown in table 2.2.

The precision of these axes is high enough to work without a high precision beam or sample displacement, like a galvoscanner or a piezosystem. Furthermore, the travel range of the complete system is with $15 \times 10 \times 10\,cm^3$ very large and nearly

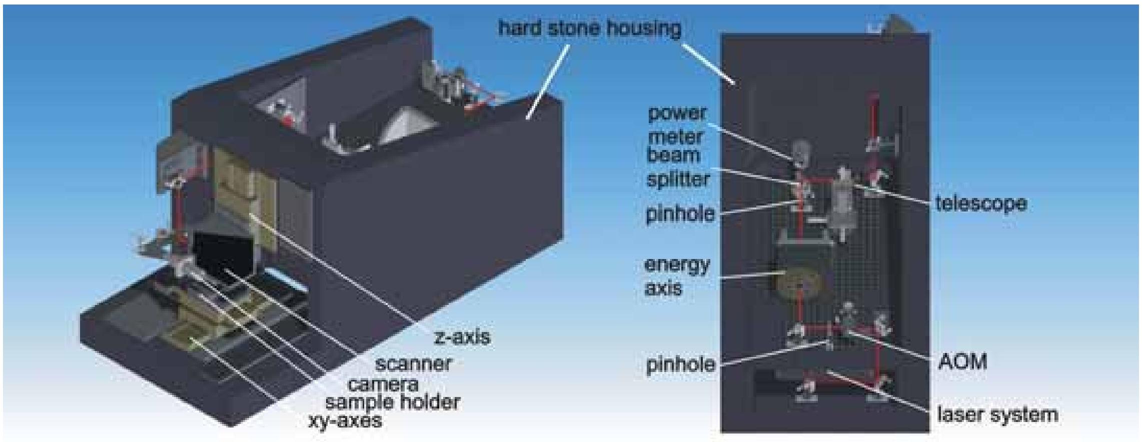

Figure 2.5.: 3-dimensional construction drawing of the M3D system with names of components and the beampath (in red) shown from the front (left) and from the backside (right).

Parameter	**Value**
Drive system	Linear Brushless Servomotor
Feedback	Noncontact Linear Encoder
Resolution	$1\,nm$
Max. travel speed	$50\,mm/s$
Max. linear acceleration	$10\,m/s^2$ (with no load)
Maximum load horizontal	$15.0\,kg$
Maximum load for XY-table	$10.0\,kg$
Accuracy	$< \pm 500\,nm$
Repeatability	$\pm 50\,nm$
Straightness and flatness differential	$0.25\,\mu m\,/25\,mm$
Straightness and flatness max. deviation	$< \pm 400\,nm$
Pitch and Yaw	$< \pm 1.5\,arc\,sec$

Table 2.2.: Specifications of the ABL1000 Air Bearing Stages

large enough for a complete 4 inch wafer. One very important thing many positioning systems have problems with is precision during movement, when vibrations can take place. The chosen ABL1000 axes show very good precision even during movement, and guarantee the values specified not only for positioning, but also during movement. With these axes and the hard stone, the problems of high precision and large travel range are solved. For this reason, there is no need of a further galvoscanner or piezosystem. Nevertheless, an additional galvoscanner can be implemented to increase the dynamics of the writing system. For this a 'HurryScan14' from *Scanlab* is used, which can be mounted on the Z-stage. For power adjustment, a $\lambda/2$ waveplate was mounted inside an ADRT-150 rotary stage from *Aerotech GmbH*, which provides a precision of ± 5 arc sec and 600 rounds per minute speed. With the $\lambda/2$ waveplate in combination with a polarization depending beamsplitter, the power can be tuned from zero to 100% during a 45^o movement of the $\lambda/2$ waveplate. This allows with ADRT-150 axis tuning the power from a minimum to a maximum in less than 0.1 seconds, with a power failure of less than 0.01% of the maximum power. By default, an acousto-optical modulator (AOM) is used as a shutter for turning the laser in the experimental setup on or off. For this, the first diffraction order of the AOM is adjusted into the focussing optics, while the zero diffraction order is blocked by a diaphragm. The positioning systems (XYZ-axes and rotation axis), the galvoscanner and the AOM are all controlled directly by a computer, which allows complete automatic structuring. Besides this active control elements there are two measuring or observation components included in the M3D. The FieldMaxII powermeter from *Coherent* is used for online power measurement. For this the measurement head is placed in the beam passing through the polarizing beamsplitter cubed measuring the power not used for structuring. With the knowledge of the maximum laser power available the one used for structuring can be calculated in realtime. The second component is a camera WAT902 from *Watec* for the online process observation. The camera is mounted on the Z-stage and views along the laser beam path through the focussing objective allowing the observation of the polymerization process. One important component for the performance of the M3D is the laser system. Any laser can be implemented into this system, but for 2PP normally a femtosecond oscillator is used.

The exact designs of the M3D is shown in figure 2.6. The laser delivers the femtosecond laser beam, which is adjusted through the AOM over mirror 1, 2 and 3. The AOM is mounted on a special holder making a very precise angle adjustment possible and allowing to adjust the power deflected into the first diffraction order. Mirror 4 is used to reflect the beam through the $\lambda/2$ waveplate onto the polarization dependent beamsplitter. The diaphragms 1 and 2 are placed directly behind the AOM and before the beamsplitter to fix the beampath, and to block the zeroth order from the AOM. The portion of the laser not used in the setup is transmitted through the beamsplitter directly onto the powermeter head. This powermeter is monitored by the computer, and can continuously measure the beam power used in the experiment. This is done by measuring the power fraction transmitted through the focussing objective during the adjustment of the system, and which can be applied to the sample, depending on the power measured by the powermeter. In this way, also the power in the setup can be calibrated depending on the position of the

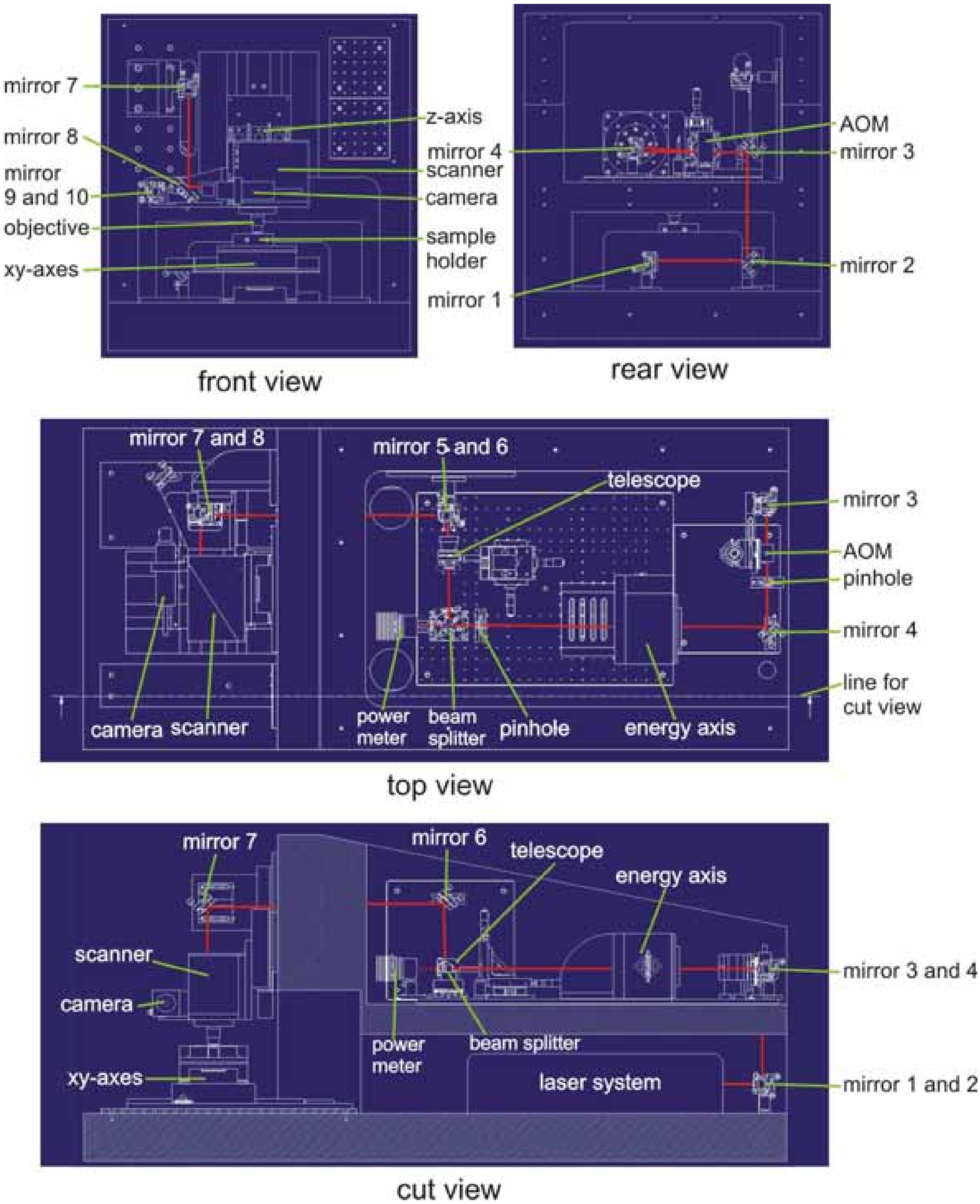

Figure 2.6.: Design and beampath of the M3D seen in front view (top left), rear view (top right), top view (middle) and in cut along the line shown in the top view (bottom).

Parameter	Value
Structuring area	$10 \times 15\,cm^2$ in XY-plane
Max. structure height	depending on the used focussing objective from $200\,\mu m$ to several mm
Structural resolution (guaranteed)	$500\,nm$
(achievable for experienced operator)	$<\ 100\,nm$
Max. structuring speed	up to $50\,mm/s$ depending on laser and polymer used

Table 2.3.: Specifications of the M3D and M3DL.

$\lambda/2$ waveplate, and the power applied to the sample can be measured permanently during the experiments. The second portion of the laser power is reflected 90^o by the beamsplitter, and passes through a telescope, which is, depending on the diameter of the laser beam, a $3\times$ or $5\times$ magnifying telescope. The beam is expanded to a diameter, so that the diameter of the Gaussian beam profile is much larger than the entrance aperture of the objective used and the intensity profile passing through the entrance aperture is a nearly flat top profile. This reduces the laser intensity passing through the objective drastically but it is necessary to use the maximum numerical aperture of the objective to achieve the highest possible resolution (see formula 2.1 and 2.2). Behind the telescope, the laser beam is directed over mirror 5 and 6 upwards and to the front of the stone and over mirror 7 and 8 through the galvoscanner into the focussing objective mounted directly under the scanner. The scanner and focussing objective are moved by the Z-axis while the sample is moved in the horizontal plane by the XY-axes. The camera for process observation is mounted on the scanner, and views via two metallic mirrors (mirror 9 and 10) through mirror 8 along the beam path. The sample can be illuminated in two possible ways. One red light source is mounted below the sample in the sample holder to achieve a transmitted light illumination. The second light source is assembled behind mirror 7, and illuminates the sample through mirror 7 along the beam path. This light serves as incident illumination, and is especially suitable for reflecting samples. With this setup, high resolution writing with a large travel range is possible. The specifications of the complete system are shown in table 2.3.

This system was developed during this work beginning from the design and enhanced to a commercially available system.

The complete system, starting from sample positioning and structuring over the laser shutter control to the illumination light, is controlled by a computer. The software 'Micro-3-Dimensional Structuring System Control' (M3DC) was developed during this work, and consists of a main control window and subprograms for specific structuring functions. The main control window is shown in figure 2.7.

The window consists of three main parts. The first part on the top left provides the camera control functions and the display for the live camera picture and saved pictures and videos of the structuring. The second part on the top right allows direct control of the laser shutter, the power adjustment and the lights. The lower part

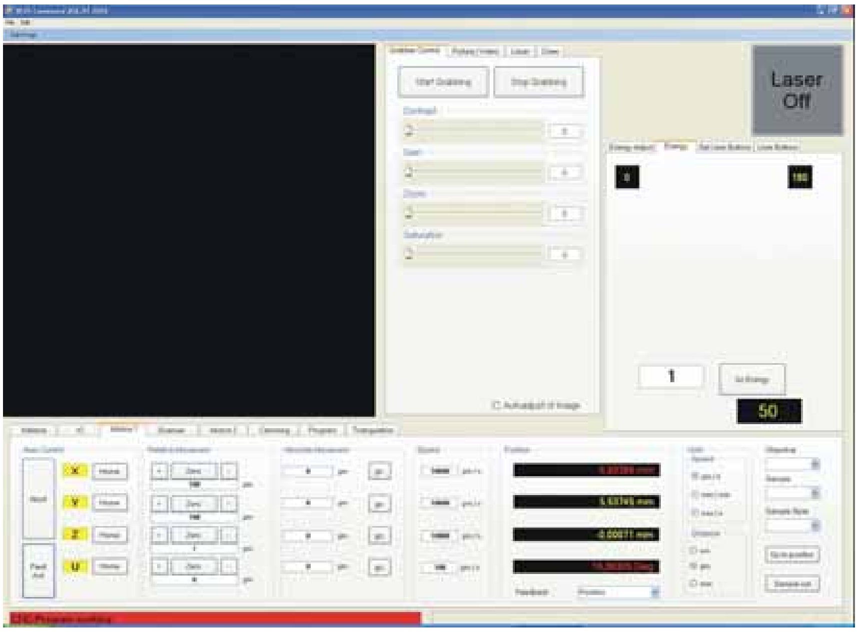

Figure 2.7.: The main control window for the M3D, with the camera control (upper left), the laser and energy control (upper right), and the axes system control (bottom).

of the main window is the direct axes and scanner control. Also, the triangulation control, allowing a software based compensation of sample tilting, and the feedback of axes and faults are placed in this sector. Triangulation is necessary, because the XY-axes can not be tilted mechanically, and for this reason tilting of the sample cannot be mechanically adjusted. This adjustment is done by the triangulation, where three positions on the sample are fixed, and a compensation plane is calculated, which is used as reference. During the movement of the XY-axes system, the Z-axis is automatically moved to stay in the reference plane or in general in a plane parallel to this reference.

Other important parts of the software used in this work are the directly programmed structures which can be easily described mathematically. These are mainly photonic crystals, plasmonic components, and voxels. They are described in detail in chapter 2.5, 2.4 and 5 where they investigated.

The last important part of this software used in this work is the 3-dimensional structuring from stereolithography files (STL-files). The principle of this structuring is explained very well in [Ser04], and should be only explained here very briefly. The software slices the 3-dimensional STL-model into layers. Within the layers, substructuring called hatching can be applied in different styles (e.g. a photonic crystal or a circular substructure). The sliced and hatched layers are transferred into machine commands, and submitted to the M3D. This makes it possible to realize arbitrary, complex, 3-dimensional structures directly from 3-D datafiles, as provided by any 3-dimensional construction program.

A more detailed description of the adjustment and use of the M3D and M3DL and the software, which would go too far for this work, can be found in [Las07], while more detailed information about 2PP theory can be found in [Ser04].

2.4. Comparison of different laser systems for 2PP

One task in this work were principal investigations on 2PP, and the question concerning how the writing speed can be increased, and 2PP in general can become more efficient. To increase the writing speed, it is favorable to use a polymer with a high two-photon absorption cross section (2PCS). This reduces the polymerization threshold, and the power necessary for 2PP. This provides the advantage of using a less powerful and less expensive laser system. Also, a larger 2PCS results in a larger processing window. This can be understood by viewing on the lower and upper threshold for 2PP. The processing window for 2PP is given by the polymerization threshold as lower limit, and by the threshold of polymer destruction as upper limit, as shown in figure 2.3. The lower limit is shifted to less laser intensity by a higher 2PCS, enlarging the processing window to lower laser powers. The upper limit, or the polymer destruction limit, is reached by applying too much laser power, heating up the polymer. This upper threshold is not as strongly influenced by the 2PCS as the lower limit, because it consists of the nonlinear absorption and a small additional linear absorption. The 2PCS influences only the nonlinear absorption part, and for this reason the upper threshold is not as strongly influenced as the lower threshold. Thus, the processing window is enlarged resulting in better processibility.

Two approaches to increase the 2PCS are possible. First, the polymer used for 2PP could be tailored to shift its absorption maximum to an appropriate wavelength - half of the laser wavelength used. Thus, a more efficient absorption of the laser power in the polymer can be achieved. This results in an increased 2PCS, and a higher writing speed. Nevertheless, this chemical approach is not targeted in this work because there are already many polymers available for UV-polymerization. The properties of these polymers are optimized for different applications, ranging from optical, e.g. waveguiding, over mechanical, e.g. microgears, to biological applications, e.g. implants. For all these applications, different optical, mechanical and chemical properties are necessary. Thus, the development of a special polymer optimized for 2PP would be very time consuming for one application. It would be more favorable to use existing polymers, which have already been tailored for specific applications. UV-polymerization is normally applied with laser wavelengths around and below $355\,nm$. Because of this, most commercially available polymers have a very high absorption for these wavelengths. The absorption for wavelengths longer than $355\,nm$ normally decreases very fast, and reaches nearly no absorption around $400\,nm$.

The other possibility to increase the 2PCS is to shift the laser wavelength fitting to the absorption of the polymers. This could be very easily realized by using an Optical Parametric Oscillator (OPO). This allows a shift of the wavelength of a femtosecond laser in a wide range. The drawback of this is loss of intensity and a maintenance-intensive setup. In this work, the optimization of 2PP is targeted in respect to industrial realization. For this reason, no OPO is used. There are several femtosecond laser systems available at different wavelengths. At the moment, very robust and maintenance-free laser systems at two wavelengths are available. First, there is the standard wavelength range around $800\,nm$ addressed by Ti:Sa-lasers [SMK97] [YVMW03]. Such laser systems are well known in research, and are

System	Manu-facturer	Wave-length [nm]	Pulse-length [fs]	Repetition-rate [MHz]	Average power [mW]
Tsunami	*Spectra Physics*	780	120	80	300
Femtotrain	*HighQ Laser*	800	100	73	200
t-pulse 200	*Amplitude Systems*	1030 515	200 150	10 10	2000 1000
IQO Yb:glass	*University of Hanover*	1030 515	250 200	1 1	200 50

Table 2.4.: Specifications of the laser systems used in this work

available with different pulse lengths, repetition rates and output powers. These systems are very close to being a reliable industrial tool. The problem with this wavelength is that most UV-polymers have a very small absorption cross section at 400 nm. Also, the 2PCS is expected to be very small.

The second wavelength range femtosecond lasers became available during the last few years is around 1030 nm to 1060 nm by Nd:Glass or Ytterbium lasers [JAdAK98] [AKK04] [AKK05]. These systems have already reached an output similar or even higher than comparable Ti:Sa systems. Furthermore, these systems are more stable than Ti:Sa laser systems, in respect to their long term power and pointing vector stability. The drawback of the systems operating around 1030 nm is that they have to be frequency doubled to around 515 nm. The reason for the frequency doubling of these lasers is given by the absorption wavelengths of the polymers. UV-photopolymers are normally polymerized with wavelengths below 400 nm. For this reason, for 2PP, only wavelengths in the range from about 400 nm to 800 nm are possible and lasers operating at about 1030 nm have to be frequency doubled to be suitable for 2PP.

There is also a completely different class of femtosecond lasers being developed during the last years, the femtosecond fiber lasers. Most of them operate at 1030 nm to 1060 nm, or 1550 nm and have average output powers of about 350 mW at repetition rates from 80 MHz to 110 MHz. These lasers have to be frequency doubled to be suitable for 2PP. After frequency doubling, an average output power of 90 mW is possible. This is enough power for 2PP, but up to now the stability of these systems is much worse, and the price is higher compared to solid-state femtosecond lasers. For these reasons, fibre lasers were not tested in this work.

In this work, different laser systems from different manufacturers are tested for 2PP. The specifications of these systems are shown in table 2.4. For laser systems working at 1030 nm wavelength, also the parameters for the frequency doubled wavelength are given, which are suitable for 2PP.

To compare the different laser systems, fields of single volume pixel (voxel) were fabricated. This is done by focussing the femtosecond laser pulses very tightly into the photosensitive resin without moving the sample or laser beam. Voxels are 3-dimensional structures, and both the diameter and the length of the voxels are of interest. Because of the 3-dimensionality, the truncation of the voxels has to be taken into account. The principle of this is shown in figure 2.8.

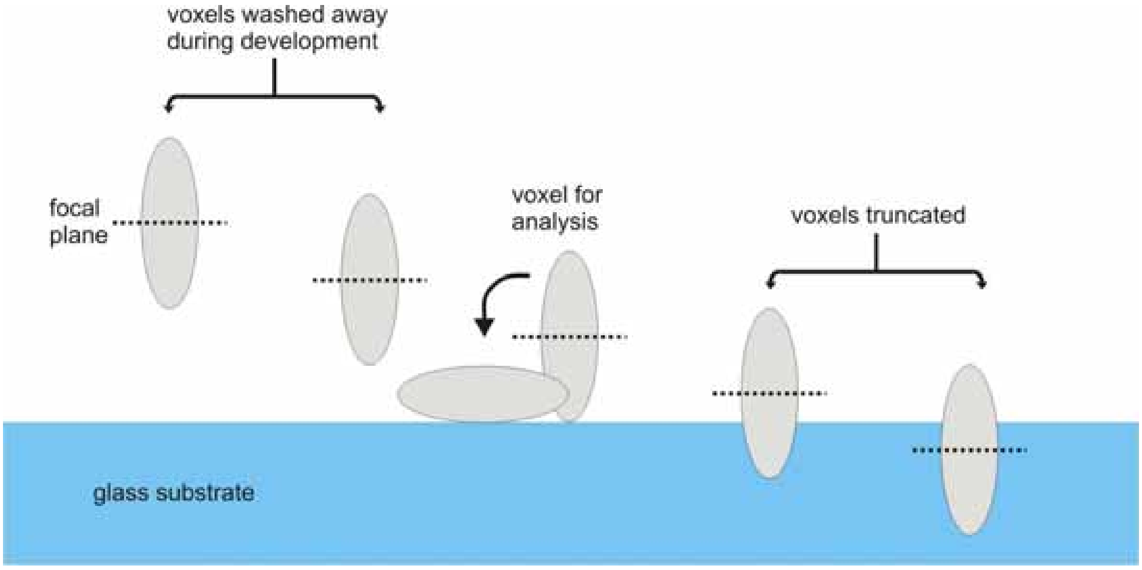

Figure 2.8.: Single voxels and their appearance depending on the distance to the substrate. Voxels too far above the substrate (left) are washed away during development, voxels in the substrate are truncated (right) and voxels at the correct height for the analysis (middle).

On the one hand, if the voxel is too far from the substrate surface, it is washed away during the development (figure 2.8 left part). On the other hand, a voxel truncated by the surface will adhere to it, but the length of the voxel cannot be measured (figure 2.8 right part). In between these two possibilities, there are several z-positions where the voxel is not truncated, but falls and adheres to the surface during development (figure 2.8 middle part). On these voxels, the diameter and the length can be measured. Each voxel is shot with different parameters and the parameters varied in one voxel field are the z-position and the illumination time. For each laser system, some voxel fields with different laser intensities have been fabricated. Such a field is shown in figure 2.9. The polymer used for all these investigations is ORMOCER, with 1.8%wt starter Irgacure 369 from *micro resist technology GmbH*.

In this figure, the length and diameter of the voxel is also illustrated. From the values obtained by these measurements, the dependency of the voxel size for the different laser systems from the irradiation parameters is achieved. The measured voxel lengths and diameters are plotted over the irradiation time. Exemplarily the measured voxel dimensions achieved with the IQO Yb:glass laser are shown in figure 2.10 together with the fitting by equation 2.6 for the voxel diameter and equation 2.7 for the length. The fitting parameters are the focus radius r_0, the Rayleigh-length z_R and the effective 2PCS σ_2/C, while the transmission through the objective was measured for each laser during the experiment.

For the Tsunami laser, the transmission is $T = 0.25$, and the fitting parameters result in $r_0 = 291\,nm$, $z_R = 690\,nm$, and $\sigma_2/C = 3.16 \times 10^{-54}\,cm^4 s$.

For the Femtotrain laser, the transmission is $T = 0.25$, and the fitting parameters result in $r_0 = 472\,nm$, $z_R = 753\,nm$, and $\sigma_2/C = 8.32 \times 10^{-53}\,cm^4 s$.

For the t-pulse 200 laser, the transmission is $T = 0.15$, and the fitting parameters

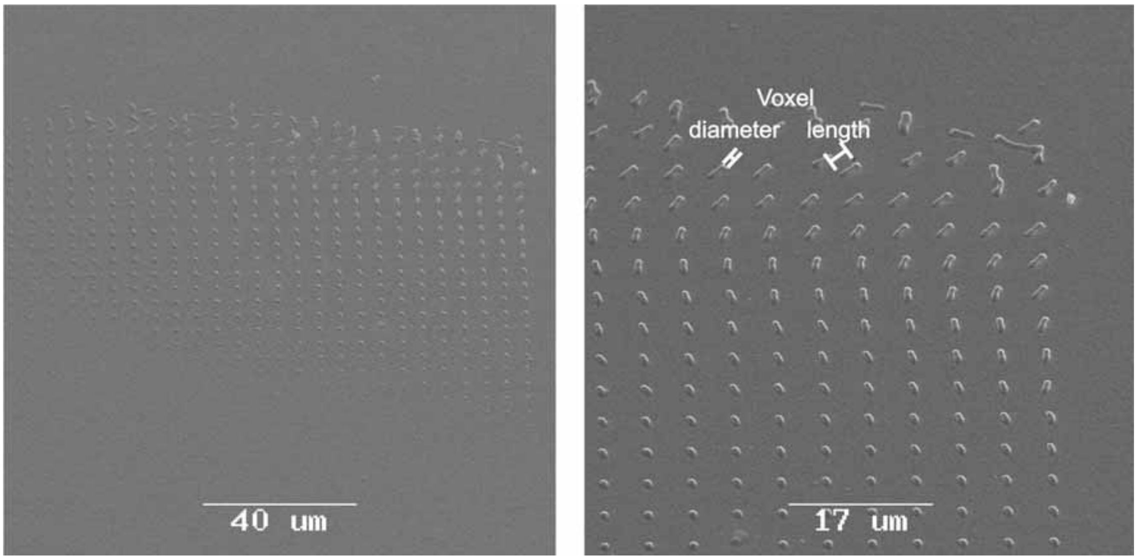

Figure 2.9.: On the left, a voxel field with voxels shot with different illumination times (from left to right) and at different z-position (from top to down) is shown. On the right, a closeup of several voxels with voxel diameter and length is illustrated.

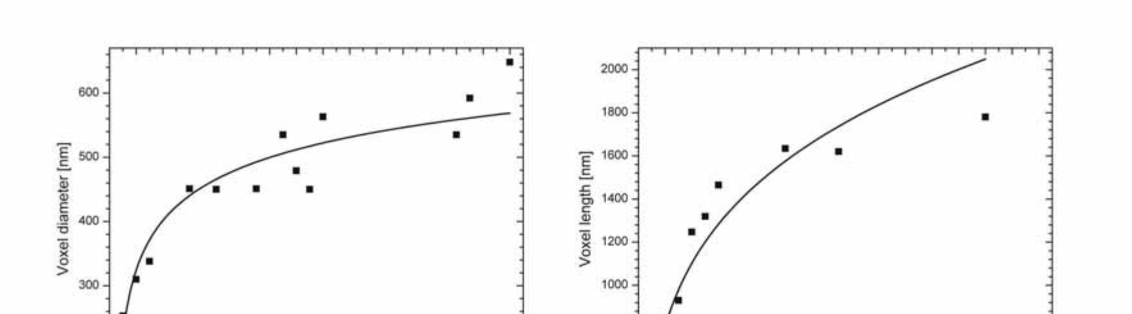

Figure 2.10.: Voxel dimensions (diameter on the left and length on the right) fabricated by the IQO Yb:glass laser depending on the illumination time with theoretical fit curve for a measured laser power of $20\,mW$.

System	r_0 $[nm]$	z_R $[nm]$	σ_2/C $[cm^4 s]$	$r_{objective}$ $[nm]$	$z_{objective}$ $[nm]$
[Ser04]	320	725	2.76×10^{-54}	340	1194
Tsunami	291	690	3.16×10^{-54}	340	1194
Femtotrain	472	753	8.32×10^{-53}	349	1224
t-Pulse 200	1049	1690	4.00×10^{-52}	224	788
Yb:glass	284	420	2.33×10^{-52}	224	788

Table 2.5.: Results obtained from the voxel measurements for the four different laser systems

result in $r_0 = 1049\,nm$, $z_R = 1690\,nm$, and $\sigma_2/C = 4.00 \times 10^{-52}\,cm^4 s$.

For the IQO Yb:glass laser, the transmission is $T = 0.07$, and the fitting parameters result in $r_0 = 284\,nm$, $z_R = 420\,nm$, and $\sigma_2/C = 2.33 \times 10^{-52}\,cm^4 s$.

The results obtained from fitting the voxel sizes from all lasers are summarized once more in table 2.5. Besides the results obtained during this work, also the results reported from [Ser04] are included in this table. The laser used in [Ser04] was an *MTS Mini Ti:Sapphire Laser Kit* (*Kapteyn-Murnane Laboratories L.L.C.*) pumped by an Ar:Ion laser (*Beam Lock* by *Spectra Physics*). The system had a wavelength of $780\,nm$, a repetition rate of $90\,MHz$ and a puls length of $60\,fs$.

Also, the resolution limit for a linear optical process is given for the different wavelengths. The lateral resolution of the objective used, a $100\times$ magnification immersion oil objective with $NA = 1.4$ from *Carl Zeiss AG* is given by $r_{objective} = 0.61\lambda/NA$, and the axial resolution by $z_{objective} = 2\lambda n_{oil}/NA^2$. The refractive index of the immersion oil is $n_{oil} = 1.5$.

It can be seen from the different 2PCSs that the 2PCS is depending on the applied laser wavelength. This was expected, and is also well known from 1PP processes. The initiator used in the ORMOCER during these investigations is Irgacure 369. The one-photon absorption spectrum of this initiator is shown in figure 2.11.

This one photon absorption must not correspond to the 2PCS, but should give an idea of expectable differences in the 2PCS of two different wavelengths. In this figure, the wavelength for a two-photon absorption of a $515\,nm$ wavelength laser and for $760\,nm$ is shown. For wavelengths above $380\,nm$, no absorption efficiencies are available. For this reason, the absorption for $380\,nm$ corresponding, to a two-photon absorption of $760\,nm$ wavelength, is taken as reference for the TiSa-laser systems working at $780\,nm$ or $800\,nm$. For the first three laser systems in table 2.5, the wavelength is about $800\,nm$, resulting in $400\,nm$ for the second harmonic, while for the t-pulse 200 and the Yb:glass lasers, the wavelength is $515\,nm$ resulting in $257\,nm$ for 2PP. For $257\,nm$, one photon absorption is higher than for $400\,nm$. This is reflected in the 2PCS, which is higher for the $515\,nm$ laser systems, compared to $800\,nm$ wavelength. This higher 2PCS is an advantage of the $515\,nm$ laser systems. Nevertheless, the most efficient 2PCS could be expected for a laser wavelength of about $640\,nm$, corresponding to the absorption peak at $320\,nm$ in the one photon absorption spectra. The problem is that no fs-laser system with a wavelength of $640\,nm$ is available. The only possibility to achieve a fs laser beam at this wavelength would be the frequency shift of existing fs laser systems, e.g. with an OPO (optical

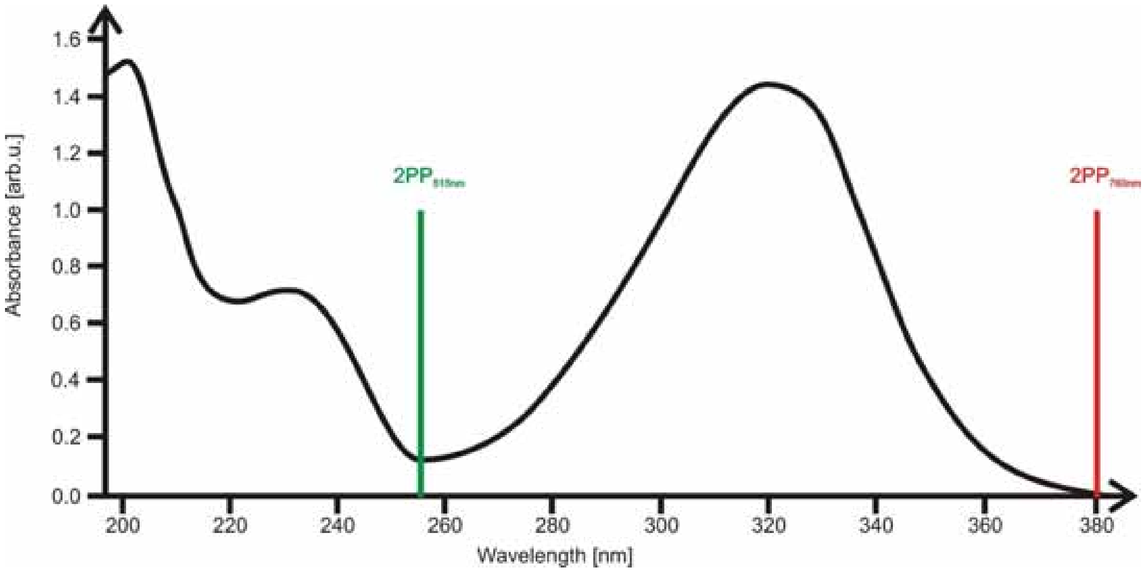

Figure 2.11.: The absorption curve of the used initiator Irgacure 369. The wavelength corresponding to the 2PP of 515nm and 760nm is illustrated as green and red line respectively.

parametric oscillator). This is not investigated in this work, because a stable and hands-free system should be developed.

Besides this, the laser systems with 515 nm wavelength can be focused more tightly than 800 nmwavelength systems, because first of all the diffraction limit is smaller for these systems, and second the optical components, especially the microscope objective used, are made for the visible wavelength region, giving a better focussing for 515 nm than for 800 nm. The high vales of r_0 and z_R for the t-Pulse 200 can be explained by a non ideal alignment of the laser beam and are expected to be in the same order of magnitude than for the Yb:glass laser for a better alignment.

The higher 2PCS for 515 nm also enables one to polymerize using less power, or less illumination time. This results in lower laser intensity and a larger processing window, because this is limited by the destruction of the polymer if the laser intensity is too high.

In general, 2PP with the Irgacure 369 starter works better with the 515 nm wavelength lasers compared to the 800 nm systems.

The laser systems used not only work at different wavelengths, but also have different repetition rates and pulse lengths. Comparing the two 515 nm systems, one can see that the repetition rate change from 10 MHz to 1 MHz does not influence the 2PCS. Also, different pulse lengths do not seem to influence the 2PCS drastically (as seen by comparing the lasers working around 800 nm wavelength).

In summary the highest 2PCS is obtained with the two 515 nm laser systems, making them the best tools for 2PP. The differences in focussing for the t-pulse and the Yb:glass laser are due to adjustment, and both systems should provide a similar focal size. Nevertheless, the choice for the laser system for the following experiments is the Yb:glass laser. This was chosen because of the lower costs of a IQO system compared to the t-pulse 200.

Figure 2.12.: The principal design of a woodpile photonic crystal showing the layer distance Δz, the lattice period d_a, and the layer number.

2.5. High speed 2PP structuring

Up to now, the disadvantage of 2PP was the low structuring speed. Typical writing speeds are much smaller, or in the scale of $100\,\mu m/s$, e.g. in [SMK97]. Up to now no writing velocities above a few hundreds of micrometers have been demonstrated. Also, sizes of structures generated by 2PP are mostly limited to $50 \times 50\,\mu m^2$ or $100 \times 100\,\mu m^2$. This is due to the limited travel range of the piezo positioning systems, which are used in most 2PP systems. Also, XY-galvo scanners with a $100\times$ magnification objective have only a structuring area of $30 \times 30\,\mu m^2$. With the positioning system used in this work, a maximum travel range of $10 \times 15\,cm^2$ is achievable, and the maximum travel speed of the system is $50\,mm/s$. With this, it is theoretically possible to write structures in an area of $10 \times 15\,cm^2$ in relatively small production times.

After investigating the 2PCS of ORMOCER for different laser systems in the last chapter, the investigations are extended to 3-D structuring. For these a mechanically more stable material, Ormosil [BBC06], is used. As starter molecule for polymerization Irgacure 369 is used as in the ORMOCER of the last chapter. With the same starter molecule, the absorption spectra should remain more or less the same. For all the experiments presented in this chapter, the second harmonic (SH) of the Yb:glass laser is used.

Photonic crystals (PhCs) were chosen as structures for high speed writing tests. The fabrication of PhCs by means of 2PP has been investigated a long time, e.g. in [Ser04], and these structures are very well known. The simplest PhC to fabricate is a woodpile structure as shown in figure 2.12.

The woodpile structure consists of 2-dimensional layers of 1-dimensional lines with a stacking sequence repeated every four layers. The distance between two layers is

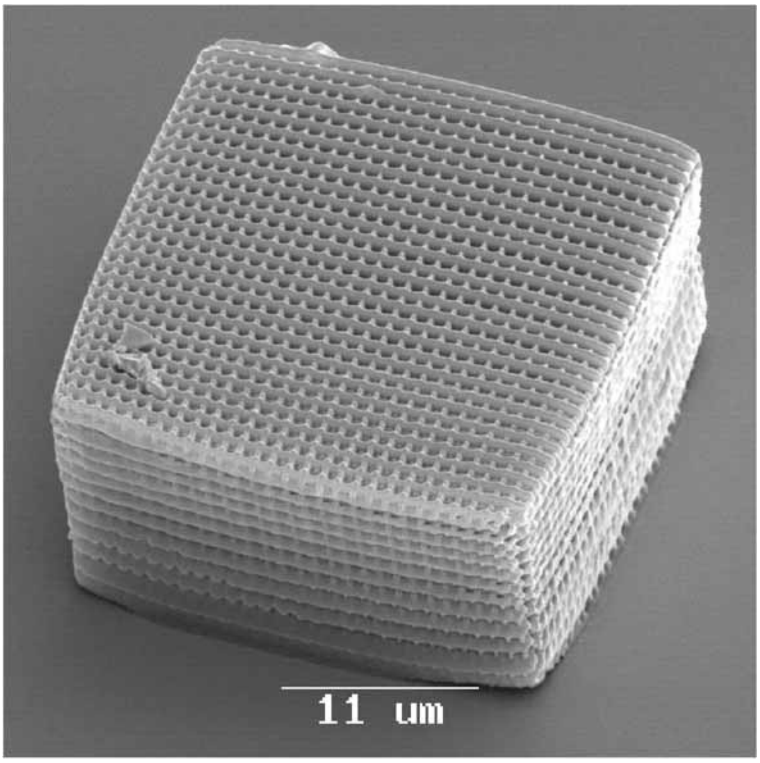

Figure 2.13.: A woodpile photonic crystal fabricated by 2PP with a writing speed of $20 \mu m/s$.

given as Δz. Within each layer, the axes of the rods are parallel to each other with the lattice distance d_a in between. The adjacent layers are rotated by 90^o. Between every second layer, the rods are shifted relative to each other by $d_a/2$. The resulting structure has a face-centered-tetragonal lattice symmetry. For the special case of $4\Delta z/d_a = \sqrt{2}$, the lattice can be derived from a face-centered-cubic (fcc) unit cell with the basis of two rods [SLS98].

A woodpile structure with $d_a = 1\,\mu m$ and $\Delta z = 0.707\,\mu m$ and a size of $30 \times 30\,\mu m^2$ is shown in figure 2.13.

The size of the rods in this structure is about $500\,nm$, and the structure was fabricated with a writing speed of $20\,\mu m/s$. Such structures have been fabricated and investigated e.g. by [Ser04] and [SMK97]. All publications about 2PP report on a writing speed in the range from $1\,\mu m/s$ up to about $100\,\mu m/s$. The structure shown in figure 2.13 was fabricated with $20\,\mu m/s$, corresponding to a production time of about 20 minutes. This clearly shows the problem of writing speed for large scale structures. With a writing speed of $20\,\mu m/s$, a photonic crystal of only 25 layers and a size of $100 \times 100\,\mu m^2$ would need about 3 hours, while a $1 \times 1\,mm^2$ crystal would need 14.5 days making it nearly impossible to fabricate such a large structure.

To investigate the possibility of high speed 2PP structuring and the reduction of fabrication time, a fcc PhC with $d_a = 2\,\mu m$ and $\Delta z = 0.707\,\mu m$ was fabricated with different writing speeds ranging from $20\,\mu m/s$ up to $50\,mm/s$.

For the high writing speeds applied during these investigations, the acceleration of the axes system has to be taken into account. The maximum acceleration of the

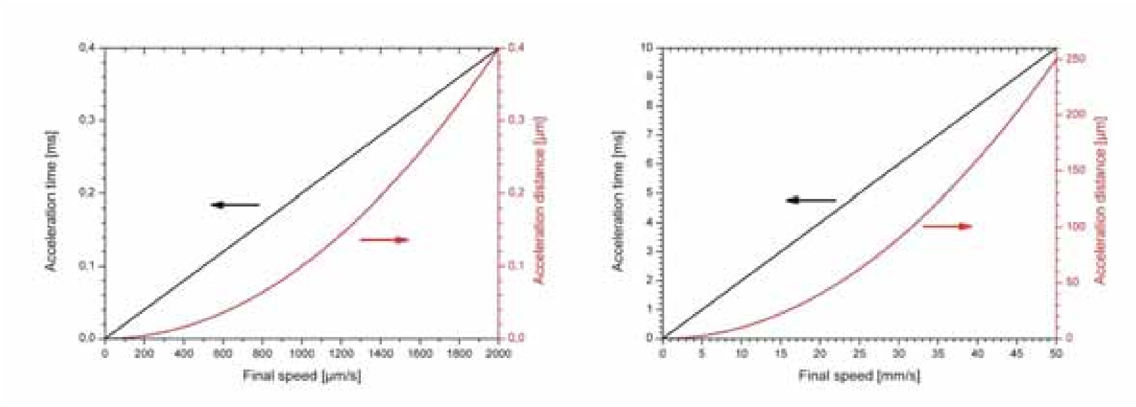

Figure 2.14.: Acceleration time and distance depending on the final speed of the axes system for velocities smaller than $2\,mm/s$ (left) and up to $50\,mm/s$ (right).

axes system is $10\,mm/s^2$ for an axis without load. Because of the load of the XY-axes system, the maximum acceleration is smaller than $10\,mm/s^2$. For the following calculations, it is assumed to be $5\,mm/s^2$. The necessary distance to accelerate the axes system can be calculated from the basic coherences for a uniformly accelerated movement starting at zero velocity of the distance s, the speed v, the acceleration a and the time t. From $s = 0.5a \cdot t^2$ and $v = a \cdot t$, the dependence of the distance from the acceleration and the speed can be calculated as $s = 0.5v^2/a$, and the time needed for this acceleration as $t = v/a$. Figure 2.14 shows the results obtained for the acceleration time and distance, depending on the final speed of the axes system.

This clearly shows, for writing speeds smaller than $1\,mm/s$, that the acceleration, with a distance smaller than $100\,nm$ and a time smaller than $0.2\,ms$, can be neglected. For larger velocities, the acceleration and deceleration has to be taken into account as illustrated in figure 2.15.

At the top of figure 2.15, writing without taking acceleration into account is illustrated. The laser is activated at the same time the axis starts movement. This leads to a higher energy flux to the regions where acceleration takes place. The same happens for deceleration, when first the speed is decreased, and the laser is shut down at the same time the axis stops. At the bottom of figure 2.15, writing with additional acceleration and deceleration is illustrated. The laser is turned on and off at the targeted writing speed. This results in a uniform power deposition over the whole structure. Acceleration is negligible for slow writing speeds below $1\,mm/s$. For such slow speeds, the acceleration distance is smaller than $100\,nm$, and the time needed is only $0.2\,ms$ leading not to a significant higher energy flux. For higher speeds acceleration becomes more important. The distance and time to accelerate the axis to $50\,mm/s$ are $250\,\mu m$ and $0.01\,s$. This does not seem to be very much, but taking into account the typical sizes of nanostructures in the region of a few hundred micrometers, this can play a significant role in the fabrication time. Also the power has to be much higher for high writing speeds. Such high power would destroy the material at low structuring speeds. Because of this it is impossible to achieve a high writing speed without taking the acceleration into account. To investigate the dependence of fabrication time on the writing speed and the size of a written

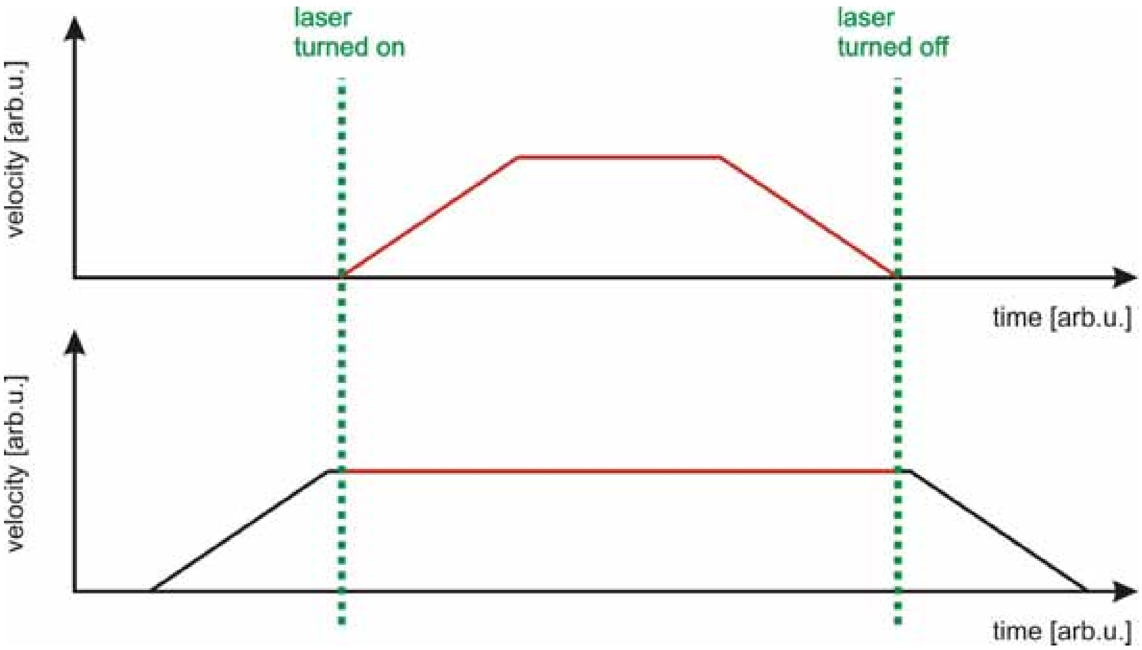

Figure 2.15.: The principal of writing without (top) and with (bottom) an additional acceleration distance.

structure, the following calculation is performed on the example of a simple line. The time needed to write this line (t_L) with the axes system depends on the length of the line (l) and the writing speed (v), and is given by

$$t_L = \frac{l}{v} + 2\frac{v}{a}, \tag{2.8}$$

with $a = 5\,m/s$ the acceleration of the axis. The first term of the formula is the intrinsic writing time, while the second term represents the acceleration and deceleration. In general, a higher writing speed leads to a shorter fabrication time. Unfortunately, this is not completely correct. For short line lengths, acceleration and deceleration can compensate and even invert the advantage of a higher writing speed. This is illustrated in figure 2.16.

On the left of figure 2.16, the calculated fabrication time for line lengths in the range of $0\,cm$ to $10\,cm$ and writing speeds from $0\,mm/s$ to $50\,mm/s$ are shown. The writing time seems to depend linearly on both parameters. This is correct for long line lengths. Nevertheless, for short line lengths in the range of $0\,\mu m$ to $100\,\mu m$, figure 2.16 on the right shows clearly that this is not correct. For these lengths, the fabrication time first decreases for higher writing speeds, but after reaching a minimum increases again. After analysing equation 2.8 this becomes clear. The first term leads to a decreasing fabrication time ($\sim 1/v$) with increasing writing speed, while the second term becomes larger $\sim v$. The fastest fabrication is achieved when both terms are as small as possible. This is achieved when $l = v/a$ is fulfilled. For the used axis system with a maximum velocity of $50\,mm/s$ and an acceleration of $5\,m/s$ this means that for line lengths smaller than $500\,\mu m$ the acceleration has to be taken into account. For longer lengths the minimum of fabrication time is reached for writing speeds larger than the achievable $50mm/s$.

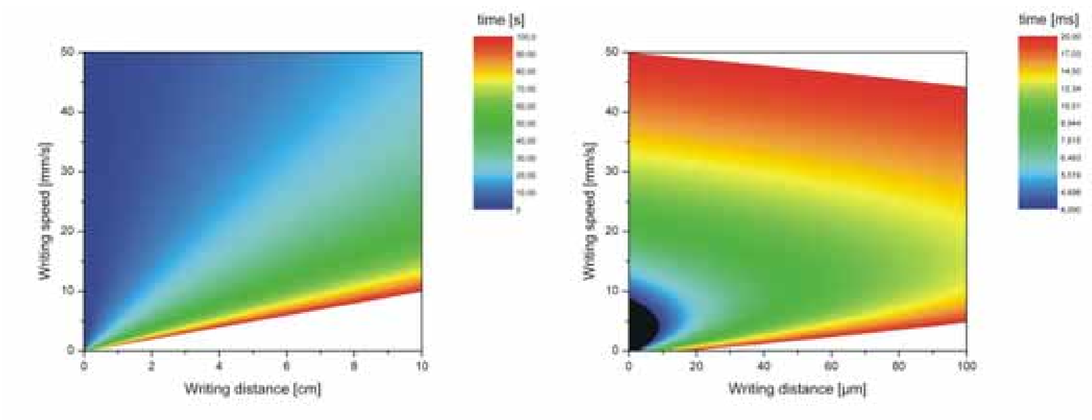

Figure 2.16.: The writing time of a line depending on the length of the line and the writing speed. For the calculated writing times, an accelerated movement is used. On the left, the time needed for large writing distances is shown. On the right, the times for writing distances below 100 μm is magnified, showing the non-linear correlation between applied writing speed and writing time because of the acceleration. White areas of the graph are out of the scale.

Even though the fabrication time does not increase with the writing speed, the whole time for structure lengths smaller than 500 μm, a fcc woodpile PhC with an edge length of 50 μm was chosen for testing the process parameters for different writing velocities. The reason for this is that a $50 \times 50\,\mu m^2$ large structure is a good compromise between the targeted resolution and the structural size, which can be imaged in a scanning electron microscope (SEM). The writing speed was varied from 100 $\mu m/s$ up to 50 mm/s. SEM images of the resulting PhCs are shown in figure 2.17 depending on the writing speed and the laser power applied.

In figure 2.17, the writing speed was varied from 100 $\mu m/s$ to 25 mm/s, while the power was scanned from 1 mW to 21 mW. In this figure, the good PhCs are marked with a white surrounding. In general, the power from 1 mW up to about 9 mW is needed for writing speeds from 0.1 mm/s to 25 mm/s. To investigate the processing window in more detail, more PhCs with different writing speeds (from 100 $\mu m/s$ to 50 mm/s) and power were fabricated.

From the SEM images of these PhCs the processing window is derived. If velocities are too high or laser intensities are too low, the structure collapses, because it is not completely polymerized and mechanical not stable. If velocities are too low or laser intensities too high, explosions can occur, destroying parts of the structure. Between the threshold of no or too weak polymerization and explosion, the processing window can be used for structuring. The processing window for fcc woodpile PhCs with a lattice constant of 2 μm, depending on the writing speed and the applied laser power is shown in figure 2.18.

This is the special processing window for this kind of structure. For other lattice constants or other kind of structures the processing window can shift slightly. The lower threshold can vary, because other structure designs need a different mechanical stability, and with this a different degree of polymerization. The upper limit depends

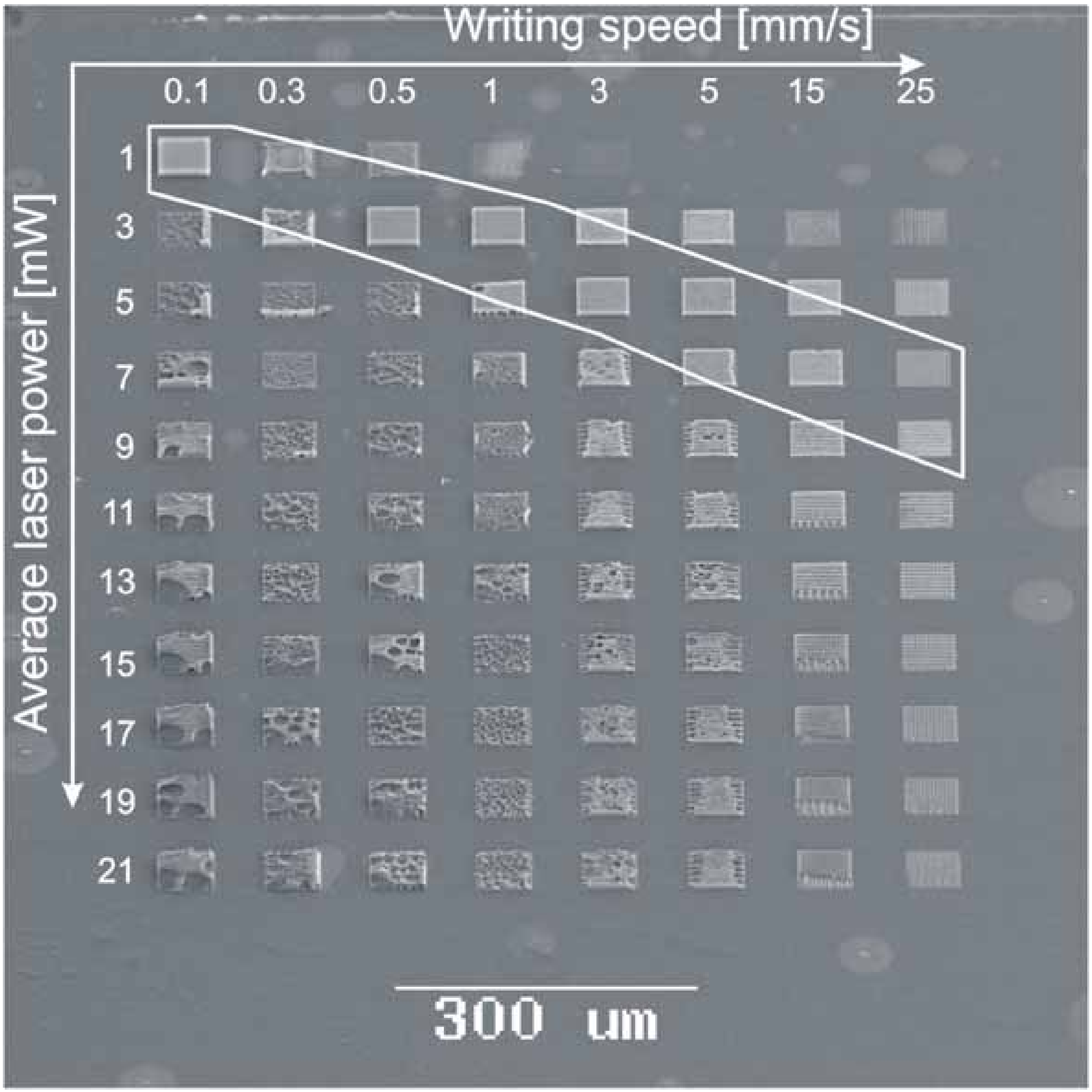

Figure 2.17.: PhCs written with different speeds and laser intensities - an overview of writing speeds from 0.1 mm/s to 25 mm/s. The area given by the white lines shows the processing window of 2PP for writing fcc PhCs with a lattice period of 2 μm. The PhCs above the processing window are not stable, while the ones below the processing window show material destruction.

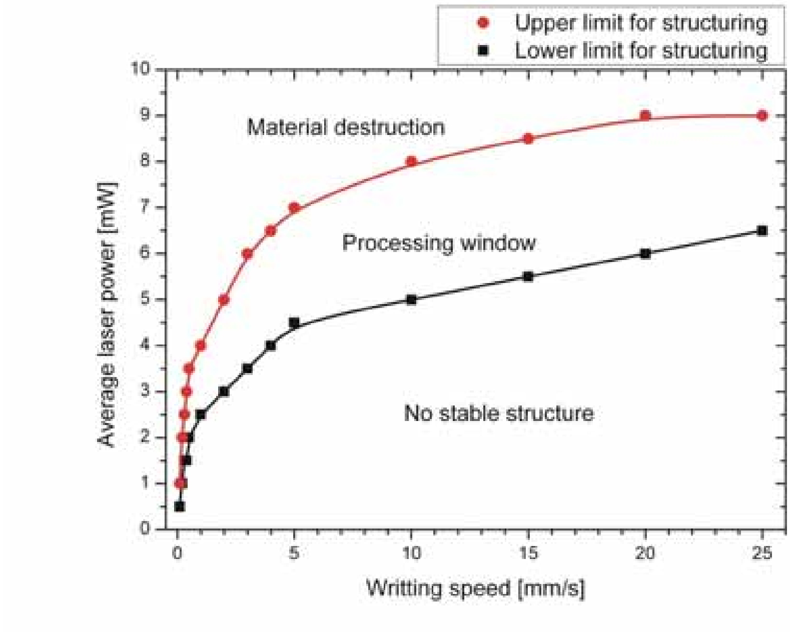

Figure 2.18.: The processing window for woodpile fcc PhCs with a lattice constant of $2\,\mu m$ fabricated in Ormosil by 2PP.

on the polymer, because it is not influenced by mechanical properties, but by the destruction threshold of the polymer itself.

To conclude this part of the work, figure 2.19 shows a 50 layer large scale fcc woodpile Photonic Crystal with an edge length of $1\,mm$, a lattice constant of $2\,\mu m$ and a rod thickness of $500\,nm$.

The overall line length needed to write this crystal is $25\,m$. It was written with a speed of $30\,mm/s$, and shows the good reproducibility of 2PP, even for such high writing speed. The fabrication time for this structure was 2 hours. These are very impressive values compared to fabrication times and speeds reported in previous publications.

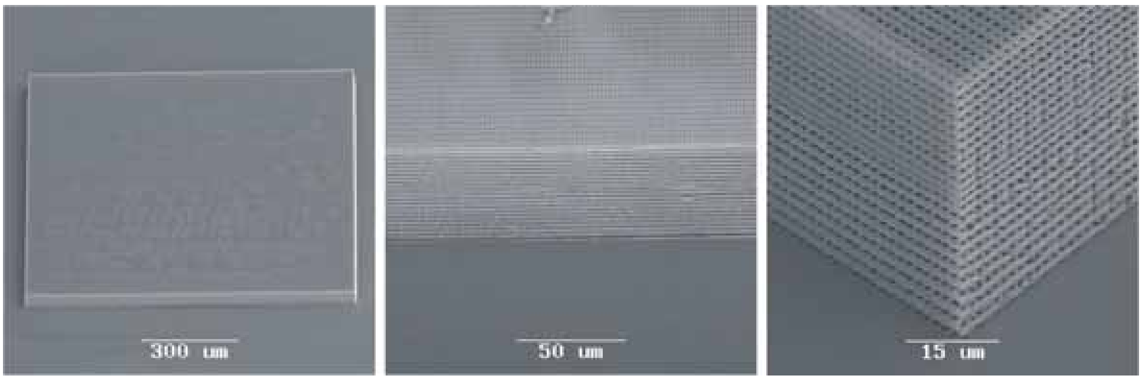

Figure 2.19.: A 50 layer large scale fcc woodpile Photonic Crystal with an edge length of $1\,mm$, a lattice constant of $2\,\mu m$ and a rod thickness of $500\,nm$.

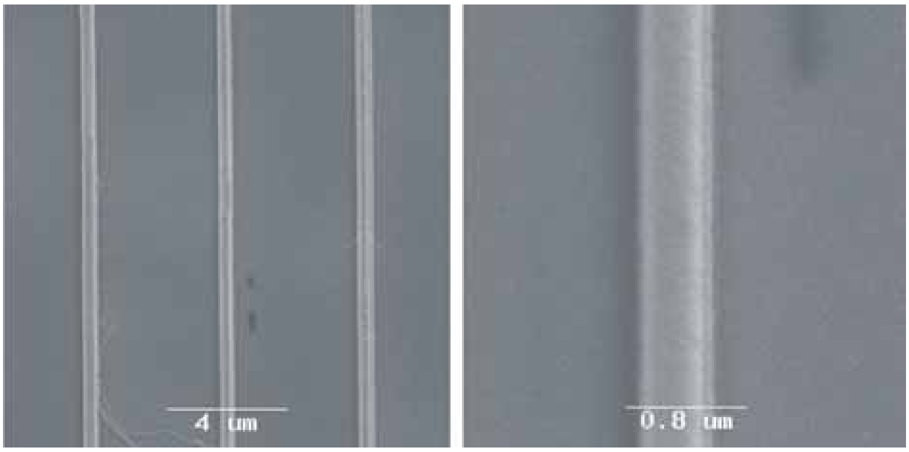

Figure 2.20.: Lines fabricated using 2PP in a spin-coatable TiO_2 resist.

2.6. Example applications for 3-dimensional structuring

After investigating the process parameters in the last section, several application examples for 2PP are demonstrated. 2PP can be used in a wide range of applications in research and industry. The range of possible applications is so wide, that in this work only the structures can be demonstrated shortly, while the demonstration of functionality and optimization of structural parameters are left to other publications.

As already seen in chapter 2.5, woodpile photonic crystals can be easily fabricated. The problem with PhCs is the refractive index of the material. The goal of PhC fabrication is a full photonic bandgap in three dimensions in the visible, or at telecommunication wavelengths [Ser04]. For a complete bandgap, a refractive index difference between the PhC and the surrounding material of about 1.4 is needed. Taking air as surrounding medium into account, the PhC must be fabricated from a material with a refractive index higher than 2.4. Commonly used polymers have a refractive index around 1.6, and special polymers with refractive indices about 1.7 or 1.8 are already used as high refractive index materials. The high refractive index (about 2.4) and high transparency in the visible spectrum makes TiO_2 a very promising photonic material [SPW07]. Conventionally, TiO_2 is patterned by sputtering it onto a pre-patterned organic resist followed by lift-off. When thick films of TiO_2 or complicated (especially 3-dimensional) features are desired, the lift-off process does not work. 2PP opens the opportunity to build even complex structures. To enable such fabrication, a photosensitive sol gel-based spin-coatable TiO_2 resist has been used. The TiO_2 resist is transparent (refractive index = 1.68) to the femtosecond laser radiation of $780\,nm$ wavelength (the wavelength of the Tsunami Oscillator, which was used for this investigations), and therefore, laser pulses can be tightly focussed into the material volume. Scanning electron microscopy (SEM) images of the line structures fabricated with femtosecond laser pulses, as shown in figure 2.20, demonstrate that a feature size down to $400\,nm$ can be achieved, and that the resulting structures have a very homogeneous shape.

More challenging, however, is the photofabrication of 3-D structures. For this

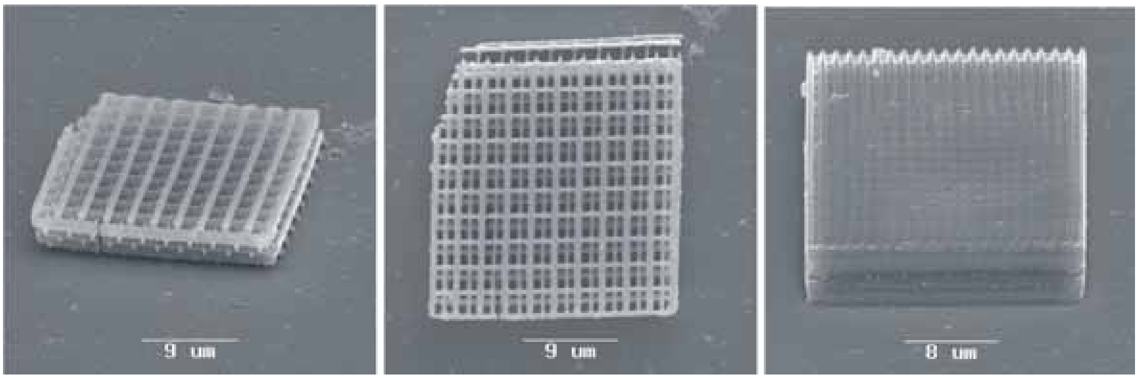

Figure 2.21.: A 7 layer high fcc woodpile Photonic Crystal with an edge length of $20\,\mu m$, a lattice constant of $2\,\mu m$ and a rod thickness of $300\,nm$.

purpose, TiO_2 resist with a layer thickness of about $10\,\mu m$ is spin-coated on a glass substrate and structured in three dimensions, as shown in figure 2.21.

These structures are fabricated by scanning the laser beam of the femtosecond oscillator at a speed of $2000\,\mu m/s$ over the sample. During the writing of each layer, the average laser power applied is increased from $5\,mW$ to $12\,mW$ in 2000 steps. The time needed to adjust to each increment in laser power is $0.2\,s$. The total writing time for each layer is 12 minutes. Between each layer, an illumination interruption of $10\,s$ is performed to allow the volatile components, possibly lower molecular weight inorganic molecules [MSMSK04] formed during the bond breaking, to leave the structure. By introducing a time delay between the fabrication of successive layers, the structure quality is improved, and the possibility of structural distortion are reduced. The structure has a periodicity of $3.5\,\mu m$ with a distance of $1.2\,\mu m$ between single layers (figure 2.21 left and middle). The results show that it is possible to achieve very smooth 3-D structures. By illuminating TiO_2 resist with a slightly higher energy laser pulses, it is possible to produce bulk 3-D TiO_2 structures (figure 2.21 right), which can be used for the realization of optical 3-D micro components. This bulk structure is fabricated in a similar way to the 3-D PhC. However, the periodicity was set to $1\,\mu m$, and the power was varied between $5\,mW$ and $18\,mW$. The distance between the single layers was set to $350\,nm$.

In [NTM94a] it has been observed that metal alkoxides chemically modified with b-diketones and b-ketoesters have optical absorption bands in the UV range, which is characteristic of the pp* transition in chelate bonds. This property was utilized in the photolithography of spin-coatable TiO_2 resists prepared by chemically modifying the metal alkoxide. Exposure to UV radiation results in the breakdown of the ν(C=C) and ν(C=O) bonds in the chelate ring, which in turn reduces their solubility in alcohols and acidic solutions. In fine patterning studies of TiO_2 resists using UV radiation, benzoylacetone was used as the chelating agent, because the chelated compound gave absorption bands that could be excited by the available UV source [NTM94b]. Similar bond-breaking processes were also observed when TiO_2 resists were exposed to an electron beam, or heated to a temperature higher than 200^oC [MSMSB03]. It appears that a similar bond-breaking process also takes place when a TiO_2 resist is exposed to the near-IR femtosecond laser pulses of $780\,nm$ wavelength. The bond-breaking process results in enrichment of the inorganic phase and

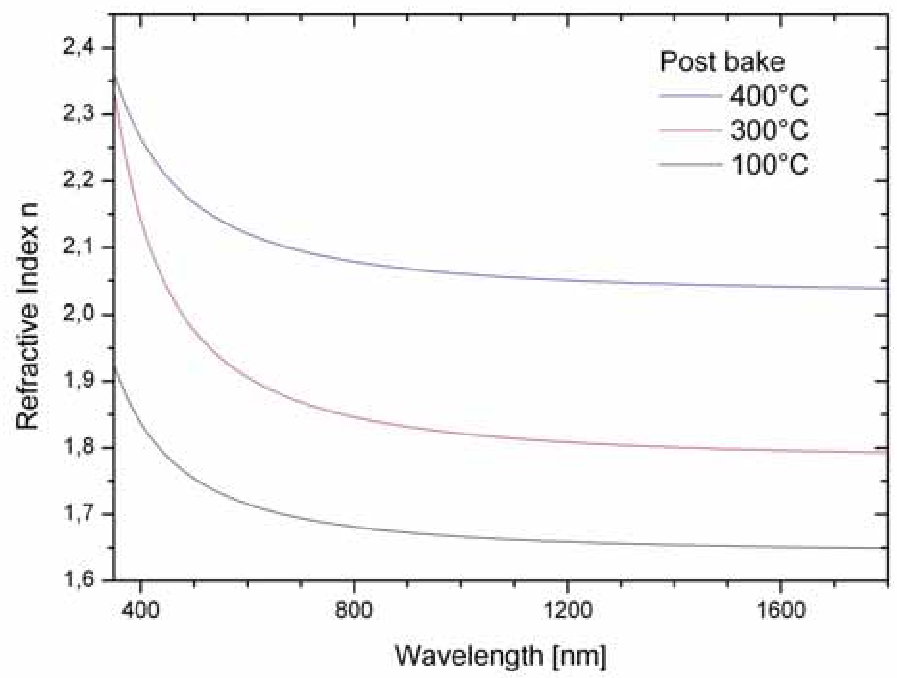

Figure 2.22.: The refractive index of the spin coatable TiO_2, depending on the one hour post bake temperature.

makes the exposed region in the focal volume of the laser pulse insoluble in organic solvents such as acetone. The bond-breaking processes can be induced due to two- or multiphoton excitation using near-IR laser pulses. Furthermore, since the TiO_2 resist is transparent to the laser radiation, it can be patterned using the 2PP process. The spin-coatable TiO_2 resist is heat treated at various temperatures to study the effect on the refractive index in the visible and near-IR regions, and to determine the appearance of the crystalline phase. Smooth layers of TiO_2 resist are spin-coated on a glass substrate and heat treated at various temperatures for one hour. As shown in figure 2.22, the refractive index increases with the post-bake temperature.

The reason for the increasing refractive index with temperature can be understood by studying the X-ray diffraction and the ratio of carbon to titanium of the film, as shown in figure 2.23.

TiO_2 exists in an anatase phase at low temperatures and transforms to a rutile phase at temperatures above 650^oC. The rutile phase has a higher refractive index than the anatase phase. As for the ratio of carbon and titanium in TiO_2 resist, it is dependent upon the heat treatment temperature. Energy dispersive X-ray analysis (EDX) shows that the carbon-to-titanium ratio in the film approaches zero above 400^oC. This is due to the removal of organic components from the TiO_2 resist with increasing temperature, which is reflected in the change of the refractive index. When heated to more than 500^oC, TiO_2 resist reaches a refractive index of over 2.1 in the visible and near-IR region. Thermal treatment of 3-D structures is a challenge because TiO_2 resist shows shrinkage of about 50% when heated treated at

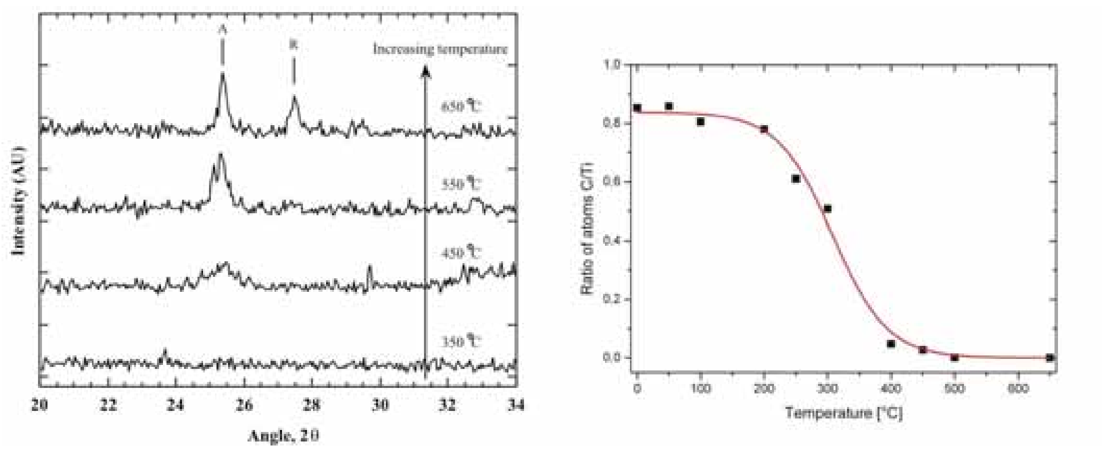

Figure 2.23.: X-ray diffraction study (left) and the ratio of carbon to titanium (right) in the layer depending on the post bake temperature.

400^oC. Figure 2.24 show the SEM images of the 3-D structures before and after heat treatment.

It can be seen that heat treatment not only results in shrinkage, but also distortion and delamination of the 3-D pattern. The latter is most likely due to a vast difference between the level of shrinkage of the substrate and the patterned structure. For successful heat treatment, the substrate should have the same level of shrinkage as that of the patterned structure, or a free-standing structure should be used. Despite the problems associated with distortion and delamination of the 3-D structures, no fragmentation or breakdown to smaller pieces is observed, thus, structural integrity is maintained before and after the heat treatment.

Even though spin coatable TiO_2 is a new material, which was first structured using 2PP during this work, the woodpile PhC is a simple structure, consisting of parallel lines in a square volume. The advantage of 2PP is the flexibility. An example of a 3-dimensional structure is shown in figure 2.25.

The structure given by an STL-file is written directly into the polymer. The inner part of the left structure is completely hatched, and the outer contour is written to achieve a smooth surface. On the right, a Venus statue shown is hatched in a photonic crystal shape, and written without outer contour. This results in a photonic crystal with an outer shape of a Venus, and shows the ability of arbitrary structuring using 2PP. The PhC Venus does not have any use besides demonstrating the ability of 2PP. Nevertheless, shaped photonic crystals working as a lens can be seen in figure 2.26.

On the left in figure 2.26, six different lens PhCs are shown. The upper three are round lenses, while the lower three are conical. The middle and right image show the magnification of one conical PhC. This shows the ability of 2PP in fabricating different shaped structures side by side.

2PP can be used for the fabrication of structures in different fields application. Some possible examples of their usage will be briefly described in the following.

The first application example is the micro-fluidic mixer shown in figure 2.27, while in figure 2.28 microgears for the use in micro-mechanics are demonstrated. Figure 2.29 completes with a first micro-electro-mechanic structure the MOEMS

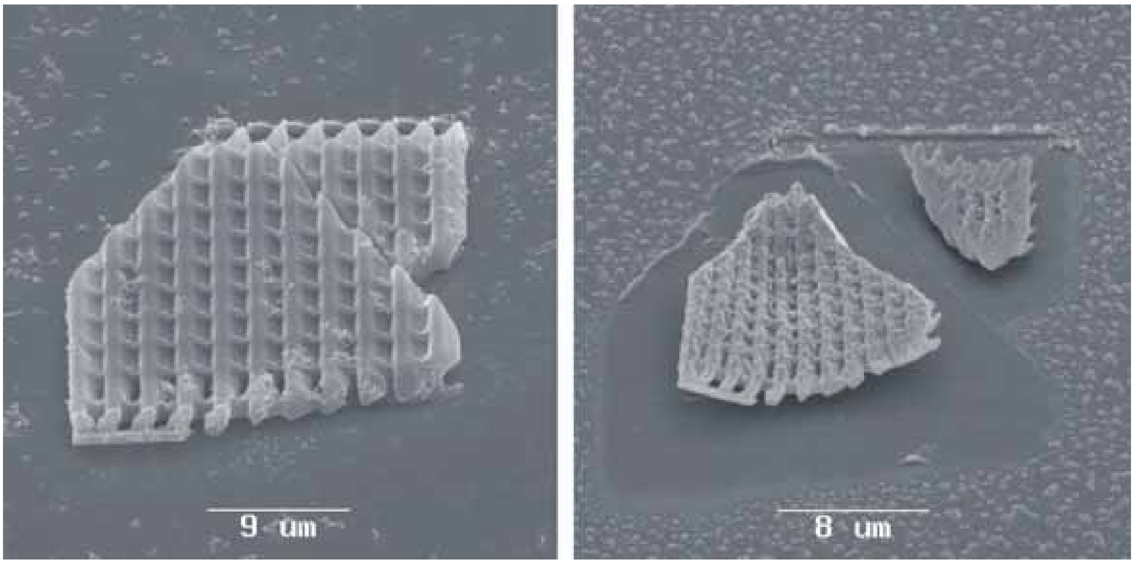

Figure 2.24.: SEM images showing the effect of heat treatment on a TiO_2 structure: a) before the heat treatment and b) after the heat treatment at 400^oC. The particles on the surface and on the structure are from gold, which was sputtered onto the sample to facilitate SEM images before and after the heat treatment.

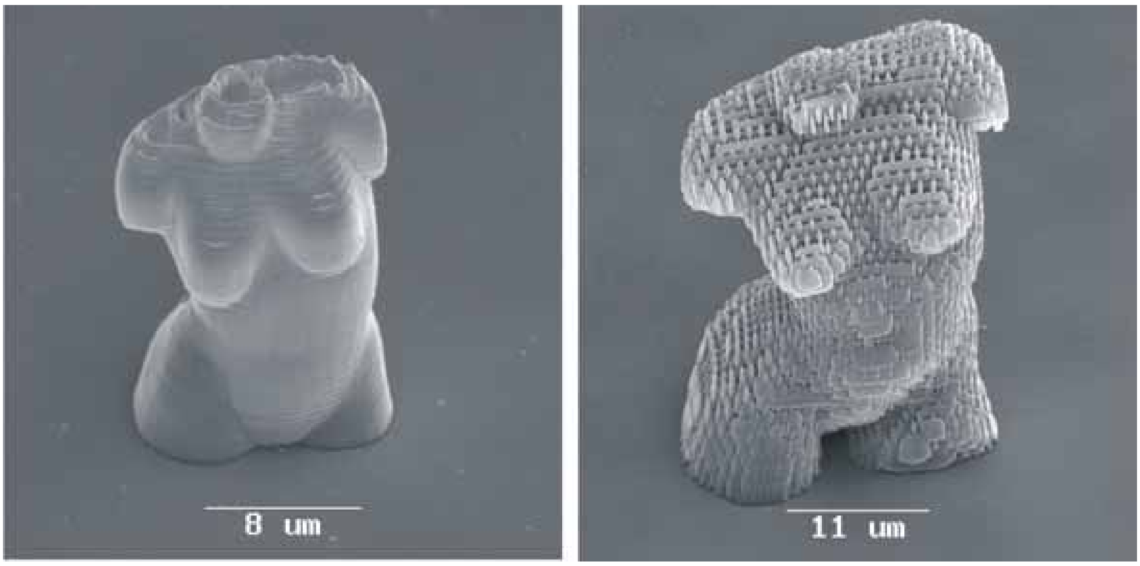

Figure 2.25.: A solid Venus statue fabricated by 2PP (left) and a Venus statue with the sub-shape of a photonic crystal (right) made from Ormosil

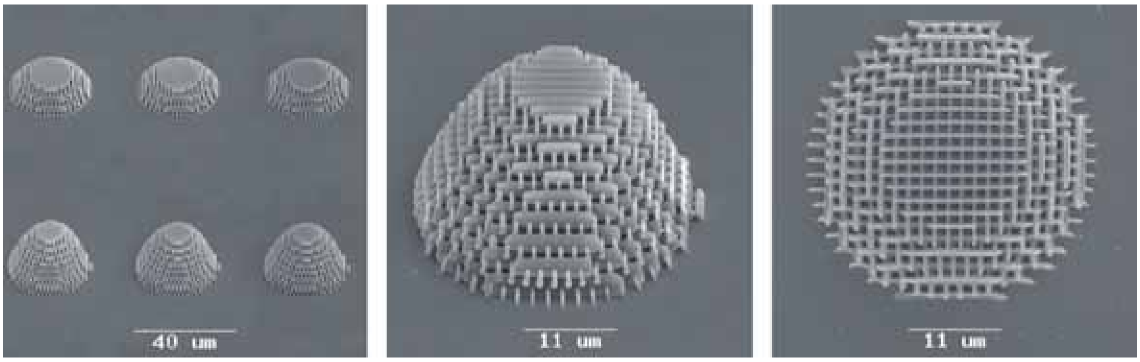

Figure 2.26.: Lens shaped photonic crystals illustrating the possibilities in fabricating micro optical devices. On the left image six different lens PhCs are shown. The upper three are round lenses, while the lower three are conical. The middle and right image show the magnification of one conical PhC. different shapes of lens shaped PhCs show the possibility of fabricating and positioning of arbitrary structures with a very good quality offering a wide range of application in micro-optics.

(micro-opto-electromechanical systems). With the combination of these demonstrators shown in the last three figures the realization of a complete MOEMS can be targeted.

Besides the MOEMS, there is a large field of possible applications in biomedicine. Ranging from medical tools like micro-needles for painless drug injection [RNC05] to customized engineered tissue for artificial organs, 2PP has many possible applications. An example for this is shown in figure 2.30.

The previously shown examples of 2PP fabricated structures all have an obvious application. The structures shown in figure 2.31 have no direct application, but show well the possibilities of 2PP.

2.7. Summary

In this chapter, different techniques of micro- and nanostructuring have been compared. The state-of-the-art for 2-Photon Polymerization has been briefly reviewed, and a commercially available system for 2PP developed during this work has been introduced and described. Different laser systems have been tested and the 2-Photon-absorption-Cross-Section and efficiencies of structuring for these laser systems have been investigated. The structuring speed of 2PP has been increased from 100 $\mu m/s$ to about 50 mm/s with the newly developed structuring system. Example applications of 2PP in micro-optic, micro-fluidic, micro-mechanic, and biomedicine have been demonstrated. Structures in the millimeter range have been fabricated for the first time using 2-Photon Polymerization, opening the possibility of large area structuring.

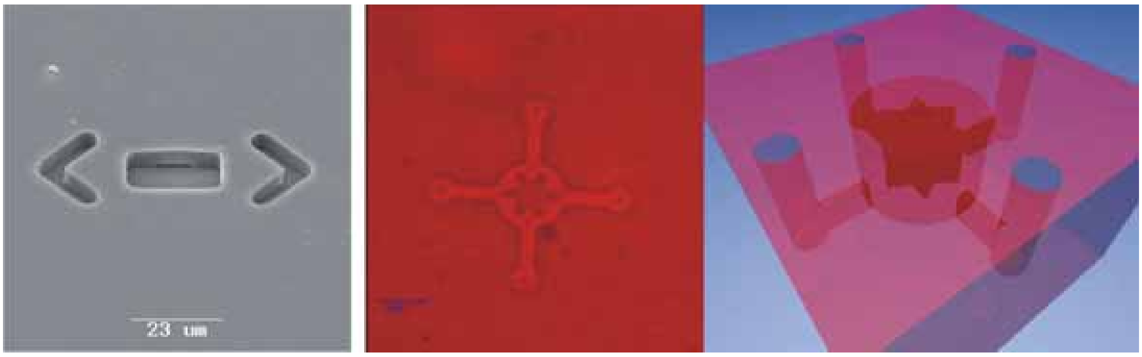

Figure 2.27.: A cut through a laser cavity for a dye laser (left), and a micro-fluidic mixer (right) fabricated using 2PP. The laser cavity with the fluid inlet seen at the top wall and the very good quality of the triangular mirror walls demonstrates the ability of 2PP in combining micro-fluidic and micro-optics. The micro-fluidic-mixer gives a first impression of the new possibilities and freedom to the design of micro-fluidic components enabled by the 3-dimensionality of 2PP. With the four channels connected through the polymer surface, while the middle chamber with the gearwheel has a cover layer of polymer and the gearwheel rotatable hung on an axis, the advantage of 3-dimensional structuring is demonstrated.

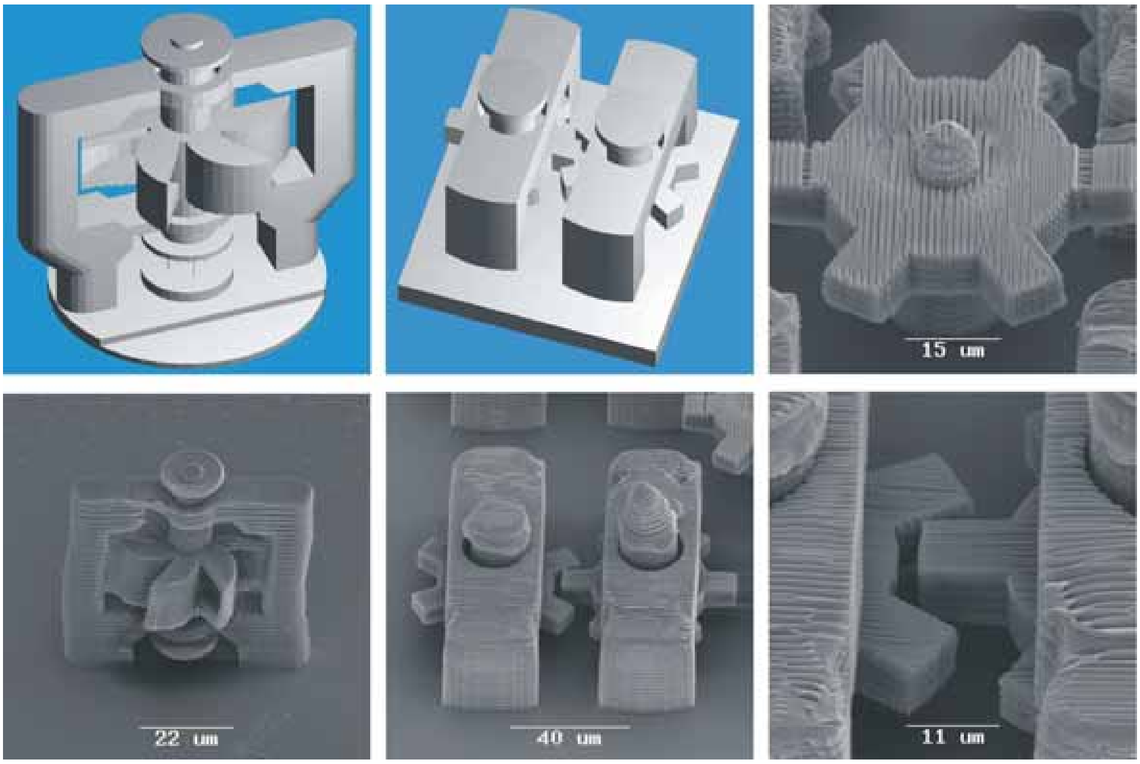

Figure 2.28.: The 3-dimensional design of a paddle wheel (top left), a paddle wheel fabricated by 2PP (left bottom), the 3-dimensional design of gears (middle top), gears fabricated by 2PP (middle bottom), a closeup of the gap between the two wheels (right bottom), and a gear without top carrier (right top). 2PP can fill the lack of a real 3-dimensional structuring technique restricting the micro-mechanical designs. The 3-dimensionality of 2PP extends the possibilities in micro mechanics. 2PP is the only technique, which allows the fabrication of these structures on this length scale.

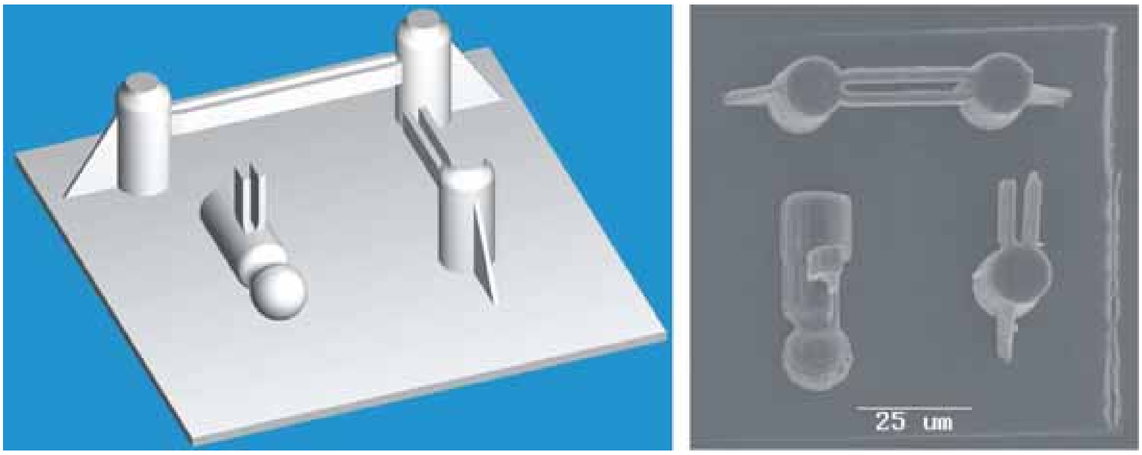

Figure 2.29.: Design of a clapping structure and SEM picture of the fabricated structure for first application tests in micro-electro-mechanics. The arms between the two pillars have a distance of $2\,\mu m$. After fabrication, the whole structure is sputtered with gold, and the arms represent the two plates of a capacitor. The application of high voltage should lead to a repelling force between and a movement of the arms.

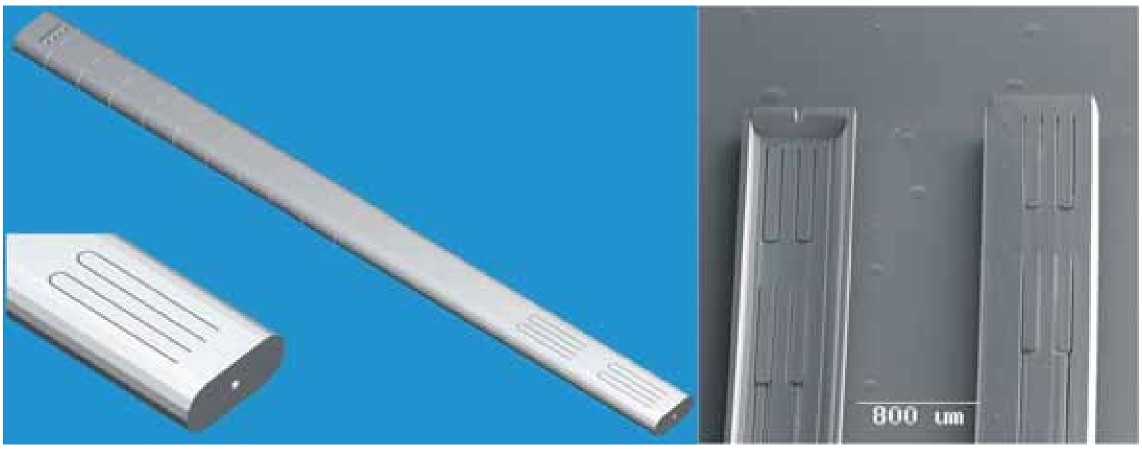

Figure 2.30.: The $10\,mm$ long design for an ophthalmologic stent (left), a close-up of the stent exit with flap-valves (inlet), and a SEM image of the stent flap-valves of a $10\,mm$ long stent fabricated by 2PP (right). The left fabricated stent was interrupted during fabrication to be able to look inside. For the use in ophthalmology, a stent with an outer diameter of less than $500\,\mu m$ is needed. Furthermore, the valves and other design components of the stent are a novelty, which can not be fabricated using the standard stent cutting techniques. For this reason, this kind of novel stent is addressed in the 'Sonderforschungsbereich-Transregio 37' started in the middle of 2007 using 2PP fabrication technique.

Figure 2.31.: A 3-dimensional sphere (left), the logo of the Laser Zentrum Hannover e.V. (middle), and a rabbit (right) fabricated using 2PP. The sphere structure (left) is a very complex structure, which can not be fabricated in this size by other technologies. It nicely shows the unique ability of arbitrary shapes fabricated by 2PP. Besides 3-dimensional structuring 2PP, can also be applied to 2-D structures. The LZH logo represents a small 2-D structure. This is a first step for applications in 2-D, like mask fabrication for lithography technologies. The rabbit on the right demonstrates the ability of massive 3-dimensional structuring even on a micrometer or millimeter scale. Thus, 2PP opens up the possibilities of high speed 2- and 3-dimensional structuring in the range of sub-micrometer to several millimeters and even centimeter structures.

3. Surface Plasmon Polaritons

Surface Plasmon Polaritons (SPPs) represent electro-magnetic surface fields with their intensity maximum at an interface between a metal and a dielectric. They are a topic of great research interest and promise a lot of possible applications in sub wavelength optics, data storage, solar cells, microscopy and biosensing. The surface plasmons photonics, or plasmonics, could be a way of miniaturizing optical devices to a sub wavelength scale. Besides this, working with electrical and optical signals on the same length scale and in the same metallic / dielectric circuits opens up new possibilities for integration. As long-term objective SPPs have been considered as a means of transmitting information on computer chips. Their advantage compared to electrical signals is the support of much higher frequencies, in the range of $100\,THz$, compared to electrical signals becoming very lossy for frequencies in the GHz range. Besides the promise of a bright future SPPs have already found first applications. With SPPs it is possible to improve the resolution of far-field optical microscopes from the diffraction limit to better than $60\,nm$ with a $515\,nm$ illumination [ISD05]. While this enhanced microscope is a research device demonstrated in laboratory environment only, also first industrial applications of SPPs arise. The company *Applied Plasmonics, Inc.* offers SPP enhanced 'Plasmon Enabled Device light emitters' on standard CMOS silicon technology.

In this chapter, SPPs and the basic theory describing SPPs are introduced. The dispersion relation and the consequences arising from this are presented. Material and experimental conditions and requirements for SPPs are introduced. A design for single mode SPP waveguides is dealt with theoretically, and the simulation programs used in this work are described. Finally, the propagation distance of SPPs inside polymer waveguides and the guiding properties of these waveguides are investigated. Also, parameters for all simulations in this work are identified.

3.1. Introduction to Surface Plasmon Polaritons

From solid state physics, volume plasmons are well known quasi particles (polaritons) arising from the quantization of plasma oscillations in bulk materials [JK00]. Surface plasmon polaritons (SPPs) are plasmons strongly confined to surfaces. The theory of SPPs should be discussed here briefly, while an intensive discussion of SPP theory can be found in [Rae88].

Volume plasmons are characterized by the plasma frequency

$$\omega_P = \sqrt{4\pi n_e e^2/m_0}, \tag{3.1}$$

where n_e is the electron density, e is the elementary charge, and m_0 is the electron mass. This formula is derived by treating a bulk as an electron plasma. The theory of

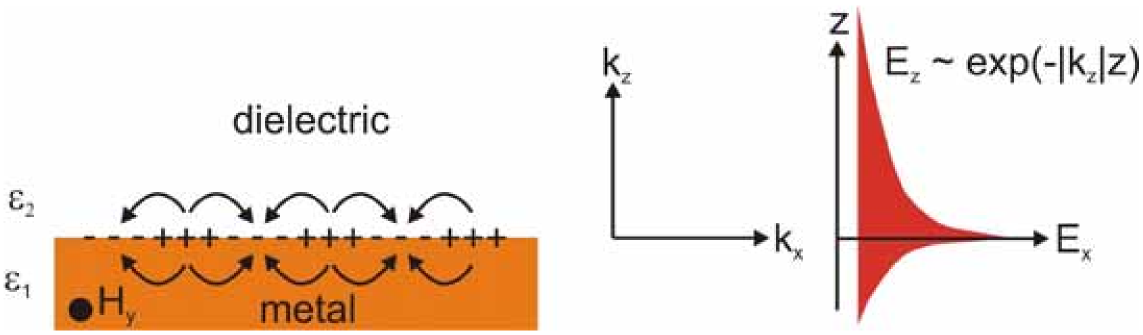

Figure 3.1.: The charges and electromagnetic field SPPs propagating on a surface in the x-direction (left) and the exponential dependence of the filed E_z (right)

SPPs can be developed analogous to the one of volume plasmons with the difference that SPPs propagate along metallic surfaces or thin metal films and are very well confined perpendicular to the surface. The SPPs are directly retrieved starting from Maxwell's equations at a metallic-dielectric interface [Rit57]. A schematic sketch of the charges and the electromagnetic field of SPPs is shown in figure 3.1.

These charge fluctuations are very well localized in the z-direction (within 1 $\AA$ perpendicular to the metallic surface), vanish for $|z| \rightarrow \infty$ and with a maximum at the metal surface ($z = 0$.) The field of SPPs at the metal-dielectric boundary is described by formula 3.2 [Rae88]

$$E = E_0^{\pm} \exp\left(+i(k_x x \pm k_z z - \omega t)\right), \tag{3.2}$$

with + for $z \geq 0$, − for $z < 0$, and imaginary wavevector component k_z resulting in an exponential decreasing field perpendicular to the interface. The wavevector $k_x = 2\pi/\lambda_p$, with λ_p being the wavelength of plasma oscillation, is parallel to the x-direction. From the assumption of a semi-infinite metal (with $\varepsilon_1 = \varepsilon_1' + i\varepsilon_1''$ the permittivity of the material) and the interface to a dielectric (with ε_2) as air or vacuum, formulas 3.3 and 3.4

$$\frac{k_{z1}}{\varepsilon_1} + \frac{k_{z2}}{\varepsilon_2} = 0, \tag{3.3}$$

$$\varepsilon_i \left(\frac{\omega}{c}\right)^2 = k_x^2 + k_{zi}^2,\ i = 1, 2\,, \tag{3.4}$$

arise from Maxwell's equation with c the speed of light and the condition of a continues wavevector k_x through the interface. Formula 3.3 can be written as

$$k_x = \frac{\omega}{c}\sqrt{\frac{\varepsilon_1 \varepsilon_2}{\varepsilon_1 + \varepsilon_2}}. \tag{3.5}$$

Assuming a real ω and ε_2, and $\varepsilon_1'' < |\varepsilon_1'|$ the wavevector $k_x = k_x' + ik_x''$ results in

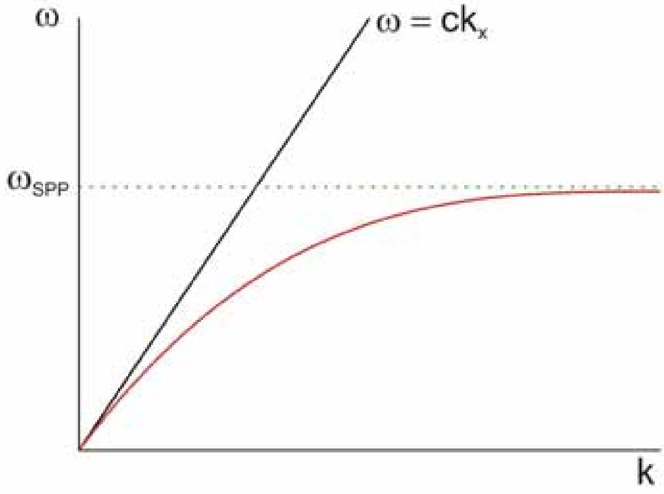

Figure 3.2.: The dispersion relation of SPPs (red line) compared with the light line (black line). The SPP dispersion relation approaches the light line, but has no osculation point with it.

$$k'_x = \frac{\omega}{c}\left(\frac{\varepsilon'_1\varepsilon_2}{\varepsilon'_1+\varepsilon_2}\right)^{1/2}$$
$$k''_x = \frac{\omega}{c}\left(\frac{\varepsilon'_1\varepsilon_2}{\varepsilon'_1+\varepsilon_2}\right)^{3/2}\frac{\varepsilon''_1}{2(\varepsilon'_1)^2}. \tag{3.6}$$

For a real k'_x the condition of $\varepsilon'_1 < 0$ and $|\varepsilon'_1| > \varepsilon_2$ must be fulfilled, which is possible for metal or semiconductors near their eigenfrequency. k''_x gives the absorption of the media.

The dispersion relation 3.6 for SPPs can be seen in figure 3.2. For small k_x, it approaches the lightline $\sqrt{\varepsilon_2}\omega/c$, but the dispersion relation function does not cross the lightline. Because of this SPPs can not transform into light without an additional wavevector, and are called 'nonradiative' SPP. For $k_x \to \infty$ ω approaches

$$\omega_{SPP} = \frac{\omega_p}{\sqrt{1+\varepsilon_2}}, \tag{3.7}$$

the SPP frequency, with $\omega_p = \sqrt{4\pi ne^2/m_0}$, corresponding to a free electron gas.

Nevertheless, SPPs can be excited by electron beam or light. The topic of SPP excitation by electron beam is not addressed in this work, while the excitation by light is not possible on a smooth surface, because the dispersion relation of SPPs does not cross the lightline. This can be overcome by providing an additional wavevector. A grating coupler or an attenuated total reflection (ATR) coupler are possible solutions for this purpose.

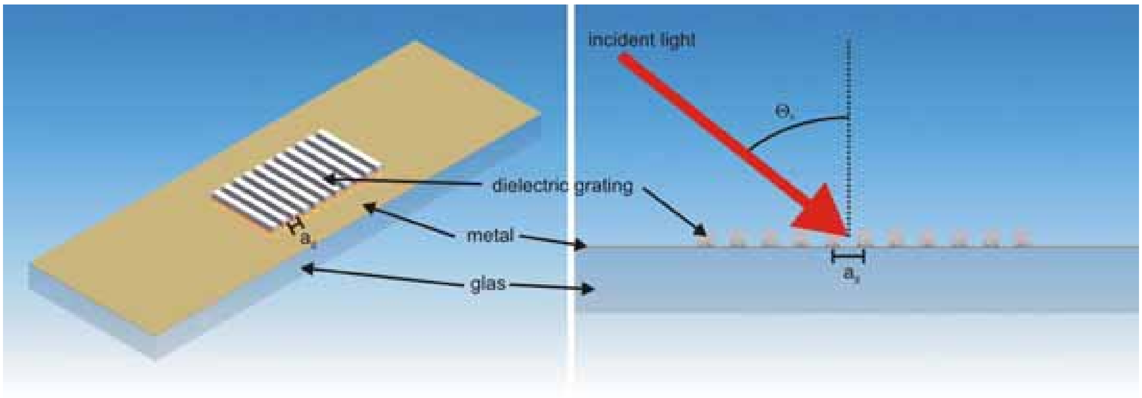

Figure 3.3.: Design of a grating coupler realized by structures on top of the gold layer with periodicity a.

The design of a grating coupler is shown in figure 3.3, where the variables used in the following are illustrated. A grating coupler can be realized using defects introduced into the metal surface, or as illustrated in this figure, by dielectric structures on the top of the metal.

The grating coupler adds to the wavevector of an incident light ($k = \omega/c$) an additional component resulting in

$$k_g = \frac{\omega}{c}\sin(\Theta_0) \pm i\frac{2\pi}{a_g}. \tag{3.8}$$

In this formula, Θ_0 is the incident angle of the light, a_g is the grating constant, and i is an integer. The dispersion relation 3.5 can then be fulfilled by formula 3.9

$$k_g = \frac{\omega}{c}\sin(\Theta_0) \pm i\frac{2\pi}{a_g} = \frac{\omega}{c}\sqrt{\frac{\varepsilon}{\varepsilon+1}} = k_x. \tag{3.9}$$

$\Delta k_x = i\frac{2\pi}{a_g}$ describes an additional wavevector arising from any perturbation of the surface. It can be seen that $\Delta k_x = 0$ does not provide a solution for the dispersion relation.

With a grating coupler, the wave vector matching can be seen as a minimum in the reflected light beam. Also, the generation of light arising from SPPs is possible and takes place at any surface defect. An ATR coupler can be seen in figure 3.4.

The ATR coupler is a dielectric media with an $\varepsilon_0 > 1$, e.g. a quartz half cylinder or prism. The wave vector k becomes $k\sqrt{\varepsilon_0}$ with

$$k_x = \sqrt{\varepsilon_0}\left(\frac{\omega}{c}\right)\sin(\Theta_0) \tag{3.10}$$

as projection to the surface. This expression enables fulfilling the phase matching between the lightline and the SPP dispersion relation taking the prism into account, as it is shown in figure 3.5.

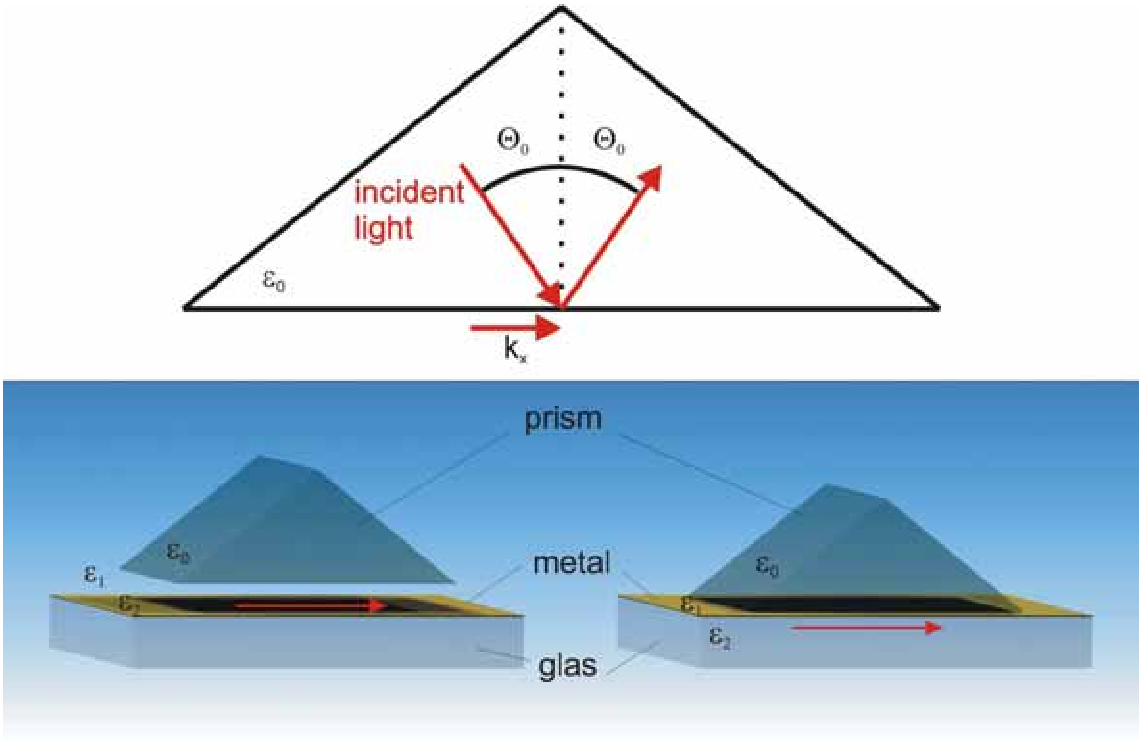

Figure 3.4.: Design for an ATR coupler: Otto-configuration with a slit of air (left) and Kretschmann-configuration (right) realized by a prism above a metal surface on a substrate.

For this excitation principal, two setups known as the Otto and Kretschmann configuration (seen in figure 3.4) are possible. For a detailed description, see [Rae88].

After discussing the possibilities of plasmon excitations, the extension of the plasmon in the metal and the dielectric shall be discussed. The wave vectors k_{z2} and k_{z1} are imaginary for the medium with ε_2 and ε_1 respectively, as seen from the relations $\omega/c = k_x$, $\varepsilon_1' < 0$ and equation 3.4. This leads to an exponential decrease of the amplitude in z-direction as $\exp -|k_{zi}||z|$. The depth at which the field falls to $1/e$ becomes

$$
\begin{aligned}
z_{e2} &= \frac{\lambda}{2\pi}\sqrt{\frac{\varepsilon_1' + \varepsilon_2}{\varepsilon_2^2}} \\
z_{e1} &= \frac{\lambda}{2\pi}\sqrt{\frac{\varepsilon_1' + \varepsilon_2}{\varepsilon_1'^2}}
\end{aligned}
\tag{3.11}
$$

with z_{e2} and z_{e1} the depth in the medium, with ε_2 and ε_1 respectively. ε_1 is given by $\varepsilon_1 = \varepsilon_1' + i\varepsilon_1''$.

For $\lambda = 600\,nm$ at a gold-air interface, this results in $z_{e2} = 280\,nm$ and $z_{e1} = 31\,nm$.

For large k_x, which is given for visible or near infrared wavelengths, the depth z_e can be approximated by $1/k_x$, and the SPP is strongly concentrated at the surface. This strong confinement shows that SPPs can be detected only by near-field imaging optics, e.g. scanning-near-field-optical-microscopy (SNOM) [DPD88] [NVB88]

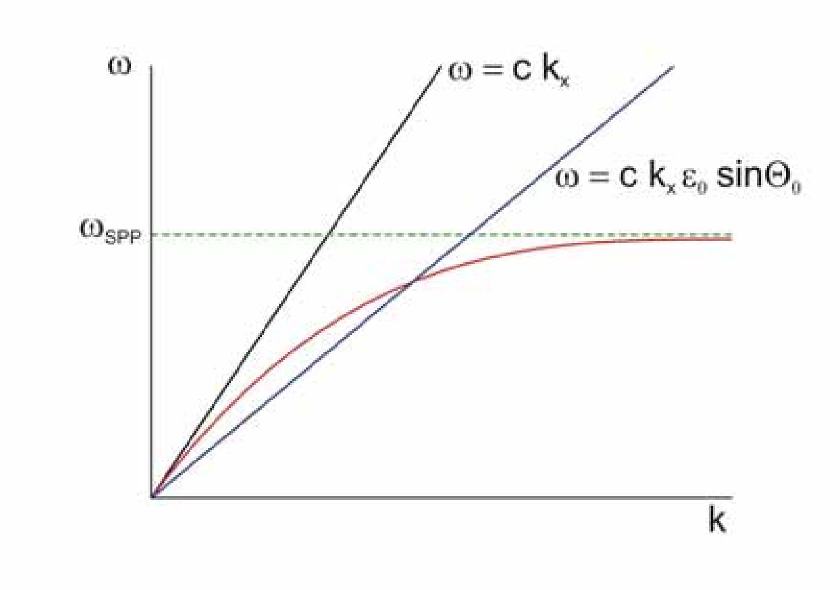

Figure 3.5.: The dispersion relation for a quartz / metal / air system with the light line in air (black line), the light line in a medium with ε_0, e.g. a glass prism, (blue line), and the SPP dispersion (red line).

[AN72], or by leakage-radiation microscopy (see chapter 5.1).

The second important information about SPPs, besides the vertical extension, is the propagation length. The intensity of SPPs propagating along a smooth surface can be expressed by $\exp(-2k_x''x)$ with k_x'' given by equation 3.6. This leads to a propagation length

$$L = \frac{1}{2k_x''} \tag{3.12}$$

for the decrease of the intensity to $1/e$. For a wavelength of $\lambda = 515\,nm$ this propagation length is $21\,\mu m$ at a silver-air interface.

3.2. Guiding SPP devices

As discussed in the previous section, SPPs are very well confined along the z-direction, and propagate along the x-direction with the coordinate system introduced. The confinement in the y-direction has not been discussed up to now. In this direction SPPs are not confined, and show a divergence depending on the excitation conditions. Working with SPPs and the SPP device development, makes a confinement also in the y-direction necessary, and with this requires waveguides for SPPs. There are two possible structural concepts reported in literature. The first one is the structuring of the metallic surface to achieve a guiding of SPPs [FBV99] [Ber99] [BLJ01]. Waveguides structured in the metal surface have been investigated by different groups, and optical components like e.g. mirrors have been realized [MG07]. In these publications efficient components have been demonstrated. The

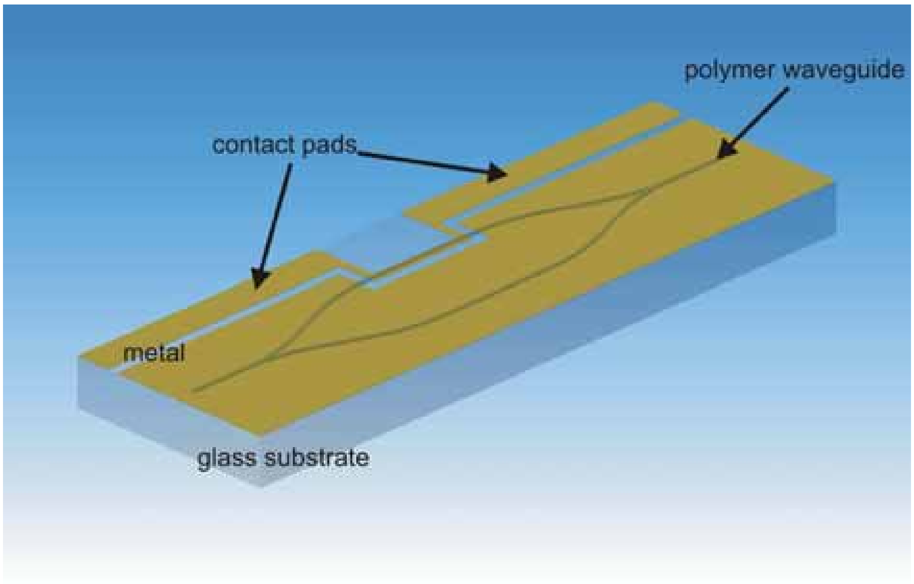

Figure 3.6.: A SPP-Mach-Zehnder-interferometer with electrical contact pads to combine electrical and optical signals, by influencing the material properties of the dielectric with electrical heating.

second structural concept is guiding SPPs using polymer, or in general dielectric structures on a metallic surface. For both concepts, the structuring methods discussed in chapter 2.1 can be applied. The polymer structures on top of the gold are used as mask in an etching process, and with this the structural design is transferred into the metal layer, while for the dielectric waveguides, the structures are directly used as SPP waveguides.

This is one of the advantages of plasmons, that light and electrons can be used for the transportation of information on the same length scale. With polymer structures on metal used as a SPP waveguide, it is still possible to structure the metal itself, and to use it as electrical circuit. This gives the unique possibility to combine an optical circuit realized by SPP optics, and an electrical circuit. Such design allows for an influence of electric current on an optical signal. A simple design can be seen in figure 3.6.

In this figure, a Mach-Zehnder-Interferometer (MZI) made from polymer is shown on a structured metal layer with two contact pads (large enough to make an electrical interconnection to the outside world) allowing the application of an electrical current to one arm of the interferometer [TNB04]. Here, the gap in the metal is made small enough to allow low loss guiding of SPPs, while the electric current is restricted to the contact pads and the metal below the upper arm of the interferometer. By choosing a polymer whose refractive index can be influenced by heat, this design enables the control of the interferometer output, due to the applied electrical voltage controlling the temperature and with this the refractive index in one arm of the interferometer, and the propagation speed of the SPPs in this part of the guide. Also, the direct detection of SPPs using an electrical signal via an integrated plasmon diode device as demonstrated in [HD06] is possible. Because of these advantages polymer structures on metal layers working as SPP waveguides are investigated.

3.3. Materials for SPP structures

Before starting with theoretical investigations and experiments for SPP waveguiding the question of which materials to use has to be addressed. For metals, gold and silver are the most promising materials for a long propagation length of SPPs. The problem with silver is that it sulfides, and becomes covered with a layer of silver sulfide. This change depends on the time silver is exposed to air. With this sulphurization the parameters of the sample change. For this reason gold is chosen, which allows a slightly shorter SPP propagation length than silver, but provides a stable sample which does not change parameters with storage time.

The second material decision for this structure type is the polymer. For 2PP in general, all polymers which are used for lithographic techniques can be used, which gives a wide choice of materials. For 2PP, there are some materials which have already been well tested, like ORMOCER and SU8 (materials used in this work were purchased from *micro resist technology GmbH* unless otherwise noted). Especially ORMOCER is designed as an optical waveguide material, and is well suited for this kind of application. Nevertheless, both materials have the drawback that they can not be spin coated and structured in thin layers of less than a few micrometers. For SPP structures of heights of $600\,nm$ as investigated in this work (see chapters 3.4 and 4), a material which can be reproducibly spin coated to layers of $600\,nm$ thickness would be more favorable. Materials fulfilling this condition and tested during this work are ma-N 1405, mr-NIL 6000 and mr-UVCur 06. For ma-N 1405 it has to be mentioned that structuring is not based on 2PP, but rather on 2-photon induced bond cleavage. After testing these materials, the mr-NIL 6000 turned out to be the best material for SPP waveguide structure fabrication using 2PP.

Besides direct structuring also replication of SPP structures was tested. For this, the master was fabricated using 2PP technique, and then replicated by nano imprint technology first generating a replica and using this replica as new master for the production of the final sample in mr-NIL 6000. In this way, a fast reproduction of the same structures is achieved.

With this fabrication concept, the flexibility and resolution of 2PP as a rapid prototyping technique, and the fabrication speed of stamping as a mass production replication technique are combined.

3.4. SPP modes of dielectric waveguides

For the computational simulations of the fabricated structures two programs are used. These are *FemSim*, a mode solver, and *FullWave*, a Maxwell equation solver, both from *RSoft Design Group Incorporated*. These programs and their theoretical background are briefly described in the two following sections.

3.4.1. SPP mode solving for dielectric waveguides

For mode calculation of structures, the program *FemSIM* is used. The Finite Element Method (FEM) used within *FemSIM* is generally advantageous in complex geometries and/or high index contrast materials compared to the direct solving of Maxwell's equations as used within *FullWave*. It is a full-vector implementation for both propagating and leakage waveguide modes, and for cavity modes. PEC (perfect electrical conductor) or PML (perfectly matched layer) boundary conditions may be selected independently for each direction. It may be used to find all the modes or a small group of modes for a given wavelength.

The starting point to understand the FEM used in *FemSIM* is the electromagnetic boundary value problem. It starts with the source-free, time-harmonic form of the vector wave equation in an arbitrary, anisotropic, lossy media [Jin02] [SK02] shown in equation 3.13,

$$\nabla \times \left[\frac{1}{\overline{s}}\left(\nabla \times \overrightarrow{E}\right)\right] - k_0^2 \overline{\varepsilon_r}\,\overrightarrow{E} \;=\; 0, \tag{3.13}$$

with the vanishing field boundary conditions

$$\widehat{n} \times \overrightarrow{E} \;=\; 0, \tag{3.14}$$

at the domain edges of the simulated volume, with $\widehat{n}$ the unit vector perpendicular to the boundary.

The complex diagonal tensors, $\overline{s}$ and ε, represent coordinate-stretching and the dielectric material, respectively. Throughout the domain, $\overline{s}$ is the identity tensor, but in the boundary layer it has the following form

$$\begin{aligned} \overline{s} \;&=\; \left(\frac{s_y s_z}{s_x}\right)\widehat{x}\widehat{x} + \left(\frac{s_x s_z}{s_y}\right)\widehat{y}\widehat{y} + \left(\frac{s_x s_y}{s_z}\right)\widehat{z}\widehat{z} \\ s_{\alpha=x,y,z} \;&=\; 1 - j\left(\frac{\alpha - L_{PML}}{L_{PML}}\right)^2 \delta_{max} \end{aligned} \tag{3.15}$$

where δ_{max} is the loss tangent, α is the distance from the edge, and L_{PML} is the thickness of the perfectly matched layer (PML). The tensor elements in the PML are matched to those in the rest of the domain according the prescription, to produce arbitrarily small reflections at the PML interface for all frequencies and angles of incidence. The PML is terminated at the domain edge with a PEC boundary condition [DSV98].

The FEM does not solve the boundary value problem 3.13, 3.14 and 3.15 directly, but rather a related one based on a variational expression, or function, constructed from the operator of the differential equation 3.13. This function in two dimensions, over domain A, is given by equation 3.16 [MKH94]

$$F(\overrightarrow{E}) \;=\; \int\!\!\int_A \left[\left(\nabla \times \overrightarrow{E}\right)\frac{1}{\overline{s}}\left(\nabla \times \overrightarrow{E}\right) - k_0^2 \overrightarrow{E}\,\overline{\varepsilon}\,\overrightarrow{E}\right] dA. \tag{3.16}$$

For propagating and leaky modes [TK00], a separable field ansatz, $E(x,y,z) = E(x,y)\exp(-jz)$, where the modal propagation is constant along z, is used.

Instead of finding an expansion basis over the entire domain, which can be difficult in general, the Finite Element Method subdivides the domain into a collection of elements, for which a simple basis can be defined. This basis vanishes outside the element, so that the final solution is only a summation over the solutions of all the elements. For hybrid Node/Edge FEM, the transverse components are expanded in a vector (edge element) basis,

$$\overrightarrow{E}_T(x,y)\exp(-j\beta z) = \sum_{i=1}^{n} \overrightarrow{N_i} E_{Ti} = \sum_{i=1}^{n} (U\hat{x} + V\hat{y})_i \, E_{Ti} \tag{3.17}$$

where the E_{Ti} are the values of the field along each edge. The longitudinal component (perpendicular to the plane of the element) is represented by a scalar (node element) basis,

$$E_z(x,y)\exp(-j\beta z) = \sum_{i=1}^{n_b} N_i E_{zi} \tag{3.18}$$

where the E_{zi} are the values of the field at each node. The basis dimension, n_b, depends on the geometry of the element and the order of the interpolation. Numerous interpolant bases have been described in the literature [YTS97] [KT00] [Pet94], which are mostly based on the edge element proposed by [Nd80].

Lastly, the function is minimized according to equation 3.19

$$\frac{\partial F}{\partial E_i} = 0, \tag{3.19}$$

yielding a matrix eigenvalue equation with β^2 as the eigenvalue, and the field components at the nodes and edges as the eigenvector. With this equations the derivation of the modes in a complex geometrical structure is possible.

3.4.2. FDTD simulations for SPPs in dielectric waveguides

The mode solver *FemSim* can not simulate a propagating mode through a given design, but can only calculate modes and their losses inside a waveguide. For propagation of the electro-magnetic field in polymer structures, the program *FullWave* is used. *FullWave* is based on the finite-difference time-domain (FDTD) technique. The FDTD method is a rigorous solver for Maxwell's equations without any approximations or theoretical restrictions. This method is widely used as a propagation solution technique in integrated optics, because it is much more accurate than other techniques dealing with approximations. Since FDTD provides a direct solution of the Maxwell equations, it therefore includes many more effects than other approximate methods. The FDTD algorithm used within *FullWave* is based on the Maxwell equations in a region of space without flowing currents or isolated charges. In such a region, the Maxwell equations can be written as

$$\frac{\partial H_x}{\partial t} = -\frac{1}{\mu}\left(\frac{\partial E_y}{\partial z} - \frac{\partial E_x}{\partial y}\right)$$

$$\frac{\partial E_y}{\partial t} = -\frac{1}{\epsilon}\left(\frac{\partial H_x}{\partial z} - \frac{\partial H_z}{\partial x}\right) \tag{3.20}$$

with the other four equations as symmetric equivalents to formula 3.20 with cyclically exchanging the x, y, and z subscripts and derivatives. The Maxwell equations describe the temporal change of the $\overrightarrow{E}$ field depending on the spatial variation of the $\overrightarrow{H}$ field and vice versa. The FDTD method is based on solving the Maxwell equations by first discretising the equations via central differences in time and space, and then numerically solving these equations.

Besides the Maxwell equations, some physical and numerical parameters are necessary. The physical parameters are relative permittivity $\varepsilon(\overrightarrow{r},\omega)$ and relative permeability $\mu(\overrightarrow{r},\omega)$ as a function of space and frequency and the excitation of the electromagnetic field. The material properties are specified by the following formula

$$\begin{aligned}\overrightarrow{D} &= \varepsilon_0\overrightarrow{E} + \overrightarrow{P}\\ \overrightarrow{B} &= \mu_0\overrightarrow{H} + \overrightarrow{M}\end{aligned} \tag{3.21}$$

with

$$\begin{aligned}\overrightarrow{P} &= \varepsilon_0\chi\left(\omega\right)\overrightarrow{E} + \varepsilon_0\chi^2\overrightarrow{E}^2 + \chi^3\left(\omega\right)\frac{I}{1+c_{sat}I}\left|\overrightarrow{E}\right|^2\overrightarrow{E}\\ \overrightarrow{M} &= \varepsilon_0\chi_m(\omega)\overrightarrow{H} + \varepsilon_0\chi_m^2\overrightarrow{H}^2 + \chi_m^3(\omega)\frac{I}{1+d_{sat}I}\left|\overrightarrow{H}\right|^2\overrightarrow{H}\end{aligned}$$

and $\overrightarrow{D}$ the electric displacement field, $\overrightarrow{E}$ the electric field, $\overrightarrow{P}$ the polarization, $\overrightarrow{M}$ the magnetization, and χ the first, χ^2 the second and χ^3 the third order nonlinearity of the material.

These formulas for $\overrightarrow{D}$ and $\overrightarrow{B}$ take into account different effects: the first term represents the linear index of the system, and takes material dispersion into account, while the second and third term are non-linear effects corresponding to second- and third-order nonlinearity.

The method used in *FullWave* is based on [Yee66]. In this method, the $\overrightarrow{E}$ and $\overrightarrow{H}$ field components at points on a grid, with grid points spaced Δx, Δy and Δz apart are calculated. The $\overrightarrow{E}$ and $\overrightarrow{H}$ field components are then interlaced in all three spatial dimensions (see Fig.3.7). The $\overrightarrow{H}$ field is computed at points shifted half grid spacing from the $\overrightarrow{E}$ field grid points. Also, the time is discretised into steps of Δt, and the $\overrightarrow{E}$ field components are computed at times $t = n\Delta t$, while the $\overrightarrow{H}$ field components are calculated at $t = (n+1/2)\,\Delta t$, where n is an integer representing the computational steps. In this way, the $\overrightarrow{E}$ field at $t = (n-1)\,\Delta t$ is equal to the $\overrightarrow{E}$ field at $t = n\Delta t$, plus an additional term arising from the spatial variation of the $\overrightarrow{H}$ field at the time t.

This method results in six equations that are used to compute the field at a given mesh point and computation step, resulting from the calculated fields from the prior calculation step. Two of the six formulas are given in equation 3.22 as representatives, with the other four formulas obtained by cyclically exchanging the x, y, and z subscripts and derivatives.

$$H_{x(i,j,k)}^{n+1/2} = H_{x(i,j,k)}^{n-1/2} + \frac{\Delta t}{\mu\Delta z}\left(E_{y(i,j,k)}^{n} - E_{y(i,j,k-1)}^{n}\right) - \ldots$$

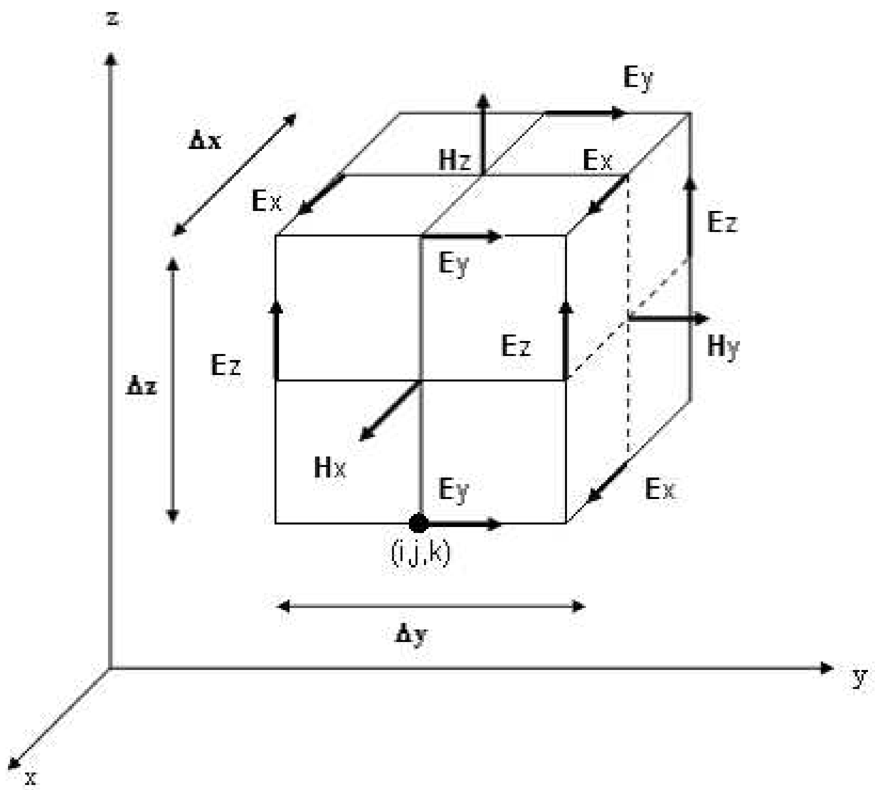

Figure 3.7.: A Yee cell with dimensions Δx, Δy and Δz (from [RDG07b]).

$$\begin{aligned} & ... \quad -\frac{\Delta t}{\mu \Delta y}\left(E^{n}_{z(i,j,k)} - E^{n}_{z(i,j-1,k)}\right) \\ E^{n+1}_{x(i,j,k)} \quad &= \quad E^{n}_{x(i,j,k)} + \frac{\Delta t}{\varepsilon \Delta y}\left(H^{n+1/2}_{z(i,j+1,k)} - H^{n+1/2}_{y(i,j,k)}\right) - ... \\ & ... \quad -\frac{\Delta t}{\varepsilon \Delta z}\left(H^{n+1/2}_{z(i,j,k+1)} - H^{n+1/2}_{y(i,j,k)}\right) \end{aligned} \tag{3.22}$$

These equations are iteratively solved in a leapfrog manner, alternating between the computation of the $\overrightarrow{E}$ and $\overrightarrow{H}$ fields at time intervals of $\Delta t/2$.

The electromagnetic field in the simulations is defined by an initial starting field condition ϕ_L at the starting time $t = 0$, as well as a driving function in time which results in

$$\phi_L\left(\overrightarrow{r}, t\right) \quad = \quad f\left(\overrightarrow{r}_0\right) g\left(t\right) \tag{3.23}$$

where $f\left(\overrightarrow{r}_0\right)$ is the spatial excitation and $g\left(t\right)$ is the temporal excitation.

Besides the physical parameters, some numerical parameters are required for the simulations. These are in detail the computational domain, the boundary conditions and the spatial and temporal grid.
The computational domain is the area which is taken into account for the simulation, and on the one hand has to be large enough that the whole structure fits inside and on the other hand should be as small as possible to reduce computation time.
The boundary conditions for the simulations in this work are chosen as a perfectly

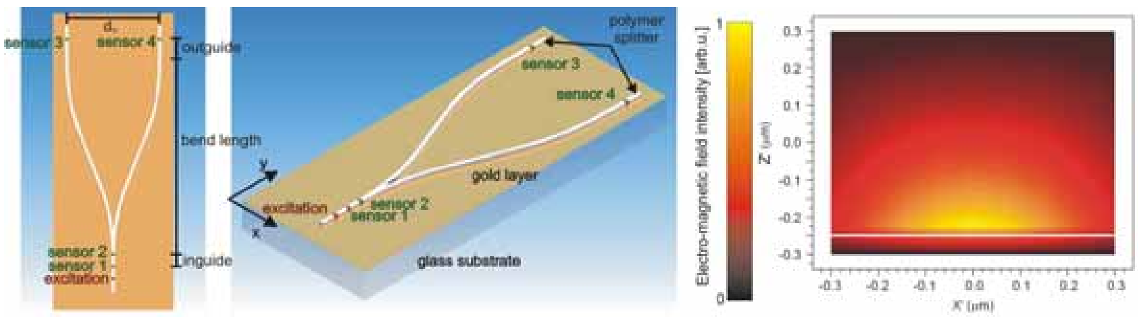

Figure 3.8.: Y-splitter structure for the investigation of the influence of grid size in top view (left), 3-dimensional view (middle) and the cross-section of the electro-magnetic field at the excitation inside the dielectric waveguide (right). The white line in the cross-section represents the top surface of the gold layer.

matched layer (PLM). In the PLM boundary condition, the electric and magnetic fields are damped by implementing electric and magnetic conductivity at the edges of the computational domain, so that the wave impedance remains constant, absorbing the energy without inducing reflections.
In *FullWave*, a uniform or a non-uniform spatial grid can be used. For accurate simulation results, the spatial grid must be small enough to resolve the smallest feature of the simulated field. This size is normally given by the wavelength, but in some designs can be also dictated by the smallest feature of the structure. Typically, the grid spacing must be able to resolve the wavelength in time, and therefore usually be less than $\lambda/10$, where λ is not the free space wavelength, but rather the wavelength in the material(s). This $\lambda/10$ criteria is no safe criteria. For this reason, a convergence study should be performed for a specific problem.
The temporal grid is limited by the stability of the calculation. For a stable simulation, the Courant condition, which relates the spatial and temporal step size by formula 3.24

$$c\Delta t < \frac{1}{\sqrt{\frac{1}{\Delta x^2} + \frac{1}{\Delta y^2} + \frac{1}{\Delta z^2}}} \tag{3.24}$$

is used. In this formula, c is the velocity of light, and the grid sizes are represented by the smallest grid size in the simulation.

To obtain the optimal value of the grid size to use for plasmonic simulations in the *FullWave* program, the structure shown in Fig.3.8 was simulated. In this figure, the polymer structure can be seen in white on the glass substrate covered with the gold layer, while the excitation cross-section of the electromagnetic-field is shown in red, and the sensors in green respectively. The parameters for the structure are a substrate with a refractive index of 1.52, 50 nm thick gold with a refractive index of $n_{Au} = 0.55 - 11.5i$ [Pal84], and a $600\,nm \times 600\,nm$ polymer waveguide structure with a refractive index of n_{Poly}=1.535. This structure was chosen in respect to [HB07]. The excitation of the electro-magnetic field is a Gaussian field distribution and shown in figure 3.8 right for the inner part of the dielectric waveguide..

The grid sizes for homogenous materials (bulk grid) and for areas close to material

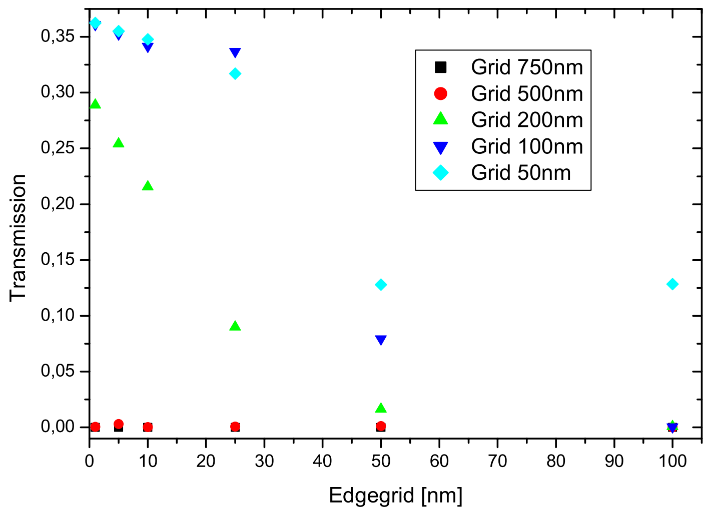

Figure 3.9.: Value of the transmission (Intensity measured in Sensor 2 divided by the intensity measured in Sensor 1) into one arm in Fig.3.8, depending on the bulk and edge grid.

boundaries (edge grid) were set different. For the bulk grid, values of 750 nm, 500 nm, 200 nm, 100 nm, and 50 nm were tested, while for the edge grid, values of 100 nm, 50 nm, 25 nm, 10 nm, 5 nm, and 1 nmwere used. The intensities at the three sensors are taken as reference, and for decreasing grid sizes, an asymptotic behavior of these values is expected. The results from this simulation can be found in Fig. 3.9. Here, the transmission of the y-splitter into one arm is shown. For this, the intensity measured in sensor 2 is divided by the intensity measured in sensor 1.

The results clearly show that with an edge grid smaller than 10 nm, and a bulk grid smaller than 100 nm, the transmission of the structure is very close to an value, to which the transmission is approaching with smaller grid sizes. The results for smaller grid size values differ only a little from the result achieved with a 10 nm and 100 nm grid. Nevertheless, the values obtained with a 1 nm and 50 nm grid would be more exact, so that these would be preferable. Because of limited computer memory and processing capability, the values of 1 nm and 50 nm could not be used for larger structures. Because of this, an edge grid of 5 nm and a bulk grid of 75 nm was chosen for further simulations. The resulting y-component of the electric field for a simulation with an edge grid of 5 nm and a bulk grid of 75 nm is shown in fig.3.10.

3.4.3. Properties of SPP dielectric waveguides

After introducing the programs for the following simulations, now the question of the properties of SPP dielectric waveguides should be addressed. In [JTK97], it has been numerically demonstrated that nanometer-sized metal rods can support confined SPP modes. Similar results were obtained for rods of nanoparticles [MQA98], [SAMR03]. Also, it has been demonstrated that with the decrease in the stripe or channel width in the propagation along metal stripes ([RZB05]) and periodically

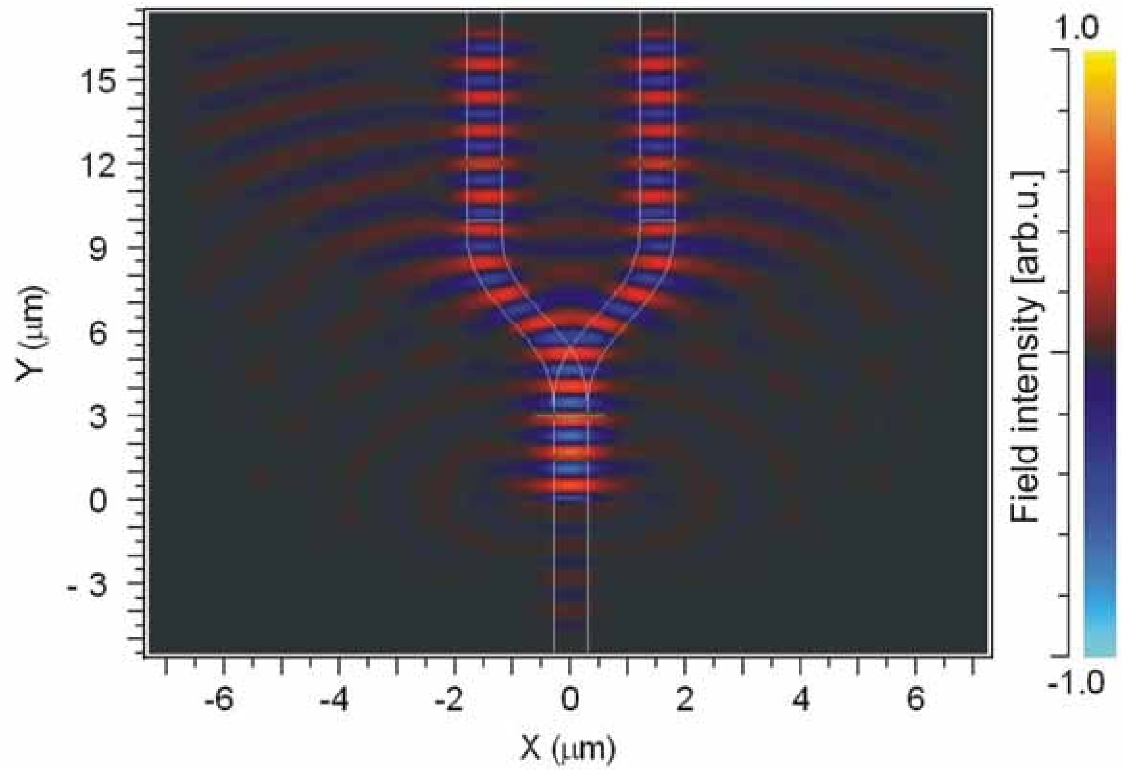

Figure 3.10.: E_y component of the electro-magnetic field 250 nm above the gold surface in a Y-splitter with a 5nm edge grid and 75 nm bulk grid.

corrugated regions ([SIBH01]), the propagation losses increase. Further SPP gap waveguides due to propagation of SPPs between profiled metal surfaces have been suggested [TT03], and various configurations have been modelled [WW04]. Recently, channel plasmon-polaritons (CPPs) [NM02], concentrating the electro-magnetic field at the bottom of V-shaped metal grooves have been predicted [GP04] and shown [SIB05] to realize sub wavelength confinement with low propagation loss. In general, the SPP confinement and with this the guiding is achieved by reducing the spatial extent into the dielectric. This increase in confinement leads to an increase in the absorption in the metal, so that the choice for the best configuration is a trade off between confinement and propagation losses. Conventional integrated optics can reduce waveguide mode size by introducing high-index-contrast waveguides [CMJ99]. This technique has been demonstrated for SPPs [CRB06], [BSK06] recently. The design for this kind of waveguide can be seen in figure 3.15 and it consists of a dielectric substrate with a gold layer and a polymer waveguide on top, and is called dielectric-loaded SPP waveguide (DLSPPW). This configuration was investigated in [HB07], and the single-mode condition was found. The (ridge) width and the thickness t of the waveguide was varied. The most important results for this work can be seen in figures 3.11 and 3.12.

This shows that for a single mode waveguiding for a wavelength of 1550 nm the best sizes are a ridge width of 400 nm to 600 nm, and a waveguide thickness between 400 nm and 600 nm. For all following simulations in this chapter the wavelength of SPP excitation is 1550 nm, if not mentioned otherwise.

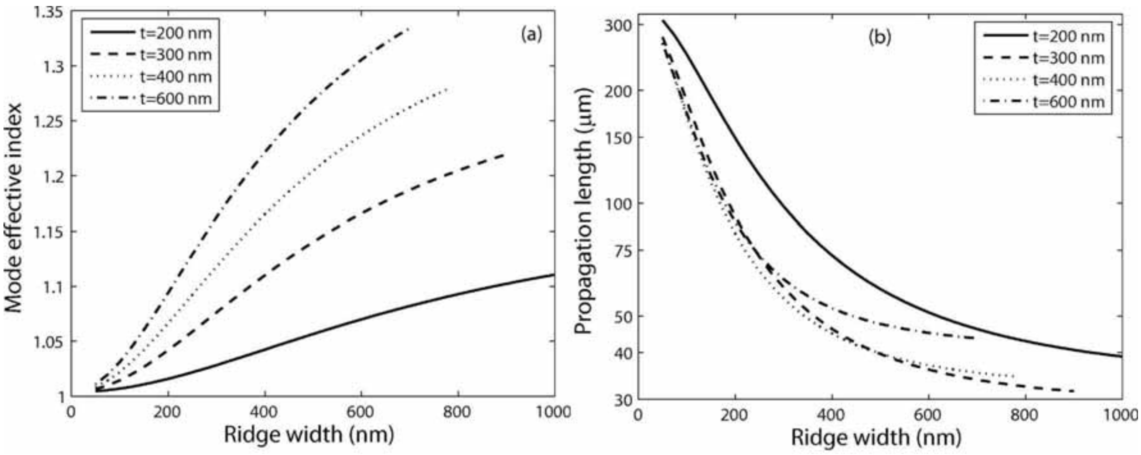

Figure 3.11.: Mode effective index (left) and propagation length for the TM_{00} mode for different waveguide thicknesses t and widths for a wavelength of $1550\,nm$ (by [HB07]).

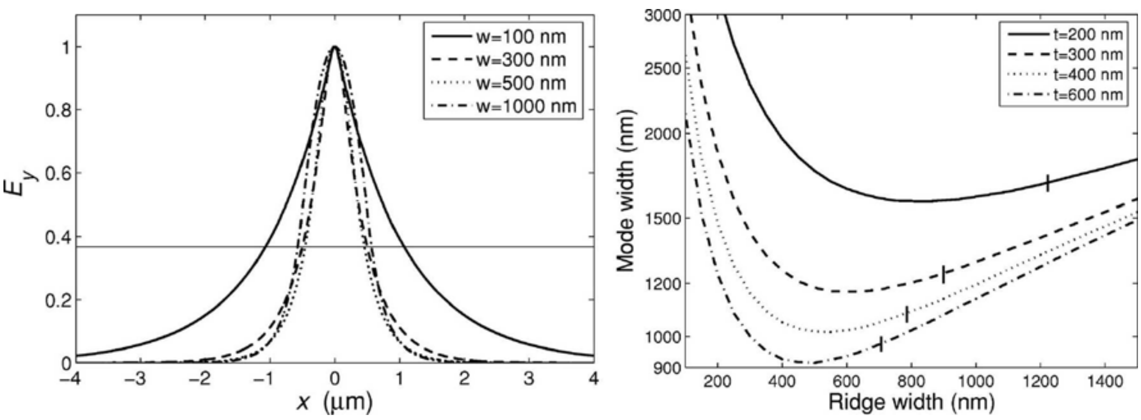

Figure 3.12.: The lateral field distribution and the mode width for different waveguide thicknesses t and widths for a wavelength of $1550\,nm$ (by [HB07]).

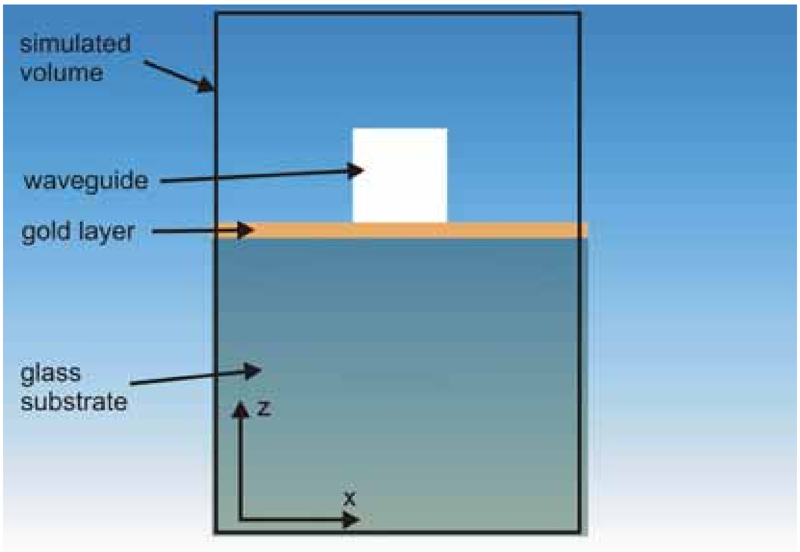

Figure 3.13.: The simulation design used for the *FemSim* simulations with the waveguide on the substrate and gold layer and the simulated volume.

Also, the cut off ridge for the next higher order mode was calculated according to formula 3.25 [KR74]:

$$w = \frac{\pi}{k_0\sqrt{N_{eff}^2 - n_{SPP}^2}} \tag{3.25}$$

with w the width of the waveguide, $k_0 = \frac{2\pi}{\lambda}$, λ the wavelength of the SPP , n_{SPP} the effective index of the SPP supported by the gold-air interface and N_{eff} the effective refractive index of the waveguide. This calculation results in the vertical lines in figure 3.12 right, showing the cutoff width of the TEM_{01} mode inside the waveguide.

For this work, the plasmonic components are fabricated by 2PP as polymer waveguides on a gold surface. Results from [HB07] encourage the decision of a waveguide with a width and height of 400 nm to 600 nm. For easier experimental realization and comparability, the upper edge of this region was chosen, and further calculations in this work are performed with a width and height of the waveguide of 600 nm.

These results are the starting point for the investigations in this chapter. First of all, simulations with the program *FemSim*, as described above, are performed to calculate the propagation length of SPPs inside of these DLSPPWs. The designs for these simulations can be seen in figure 3.13.

The propagation lengths of SPPs depending on the thickness of the gold layer as resulting from these simulations are shown in figure 3.14.

As seen in figure 3.14, the propagation length changes very much for gold thicknesses smaller than 100 nm. These thicknesses below 100 nm are the most interesting ones, because of the experimental observations with a leakage radiation microscope (see chapter 5). In general, the propagation length should be as long as possible, but for a leakage radiation microscope, the loss into light should also be non-zero to achieve a detectable signal. For this reason, a gold layer thickness of 50nm is

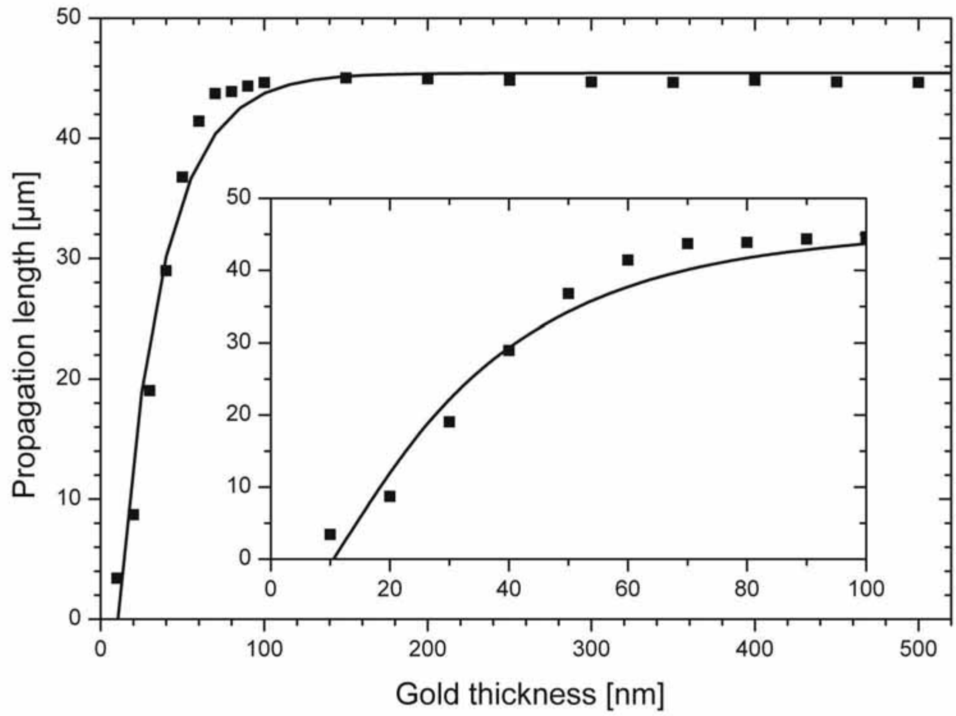

Figure 3.14.: The propagation results of SPPs depending on the gold thickness as simulated with *FemSim*.

typically used. To investigate the propagation length of SPPs not only in straight waveguides but also curved structures a simulation of a design as shown in Fig.3.15 was performed.

A Gaussian mode is excited, and propagates through the structure starting at the excitation. Four sensors are implemented: sensor one (S1) $5\,\mu m$ after the excitation, sensor two (S2) at the beginning of the curved part, sensor three (S3) at the end of the curved part and sensor four (S4) $5\mu m$ after the end of the curved part of the guide. S1 is the reference sensor for the intensity coupled into the waveguide while S2 on the one hand gives, in reference to S1, the loss in a straight waveguide and on the other hand the reference for the incoupling in the curved part of the structure. S3 enables one, in reference to S2, to calculate the loss in the curved part of the structure. The loss rate calculated by S4 in reference to S3 gives again the loss in a straight waveguide and is used as a control for the measured value between S1 and S2.

From that premises, the propagation length of the plasmon results in the formula

$$I_{y_1} = I_{y_0} \exp\left(-\left(y_0 - y_1\right)/L\right)$$

$$L = -\frac{y_0 - y_1}{I_{y_1}/I_{y_0}}. \tag{3.26}$$

In formula 3.26, L is the propagation length of the SPP, the distance after which the intensity of the SPP is decreased to $1/e$ of the initial intensity, I_{y_0} is the initial

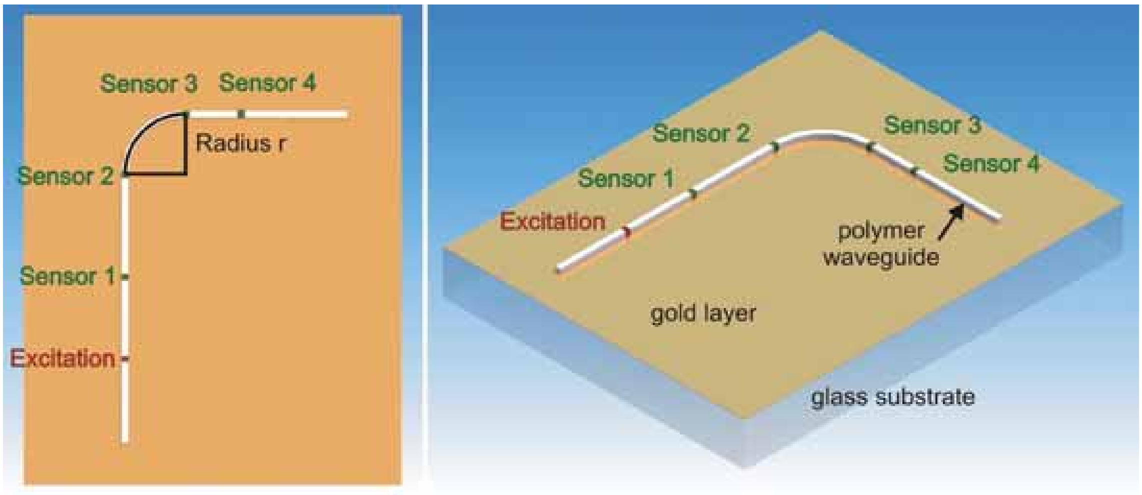

Figure 3.15.: The design of a curved line waveguide for the investigation of the propagation length of SPPs for different curvature radii.

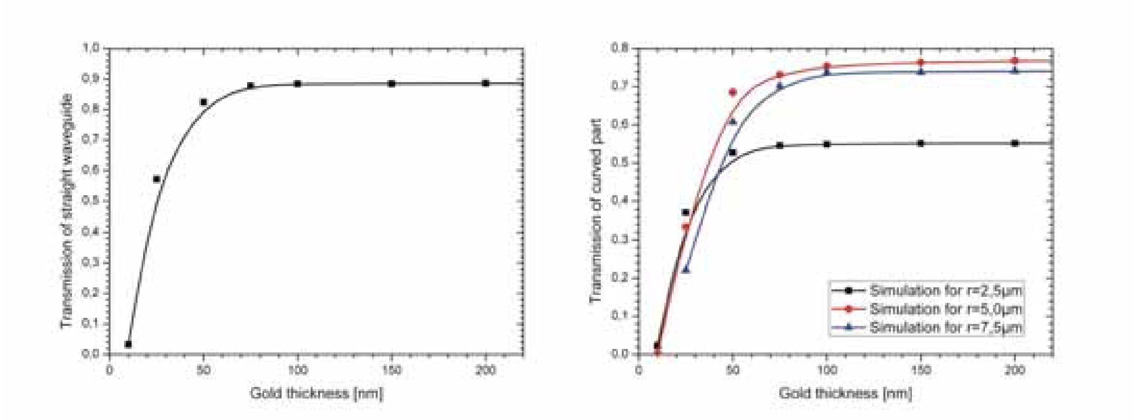

Figure 3.16.: Transmission for a 5 μm long straight waveguide (sensor 1 to 2 in figure 3.15) and a curved waveguide (sensor 2 to 3 in figure 3.15) with different curvature radii depending on the gold thickness.

intensity, I_{y_1} the second measured intensity, y_0 the coordinate of the place the initial intensity was measured, and y_1 the coordinate of the place the second intensity was measured.

The transmission of the single parts of the waveguide is given by

$$T_{ij} = \frac{I_i}{I_j} \tag{3.27}$$

where T is the transmission and I_i is the intensity of the electro-magnetic field measured by sensor i.

The transmissions are obtained directly from the simulation by measuring the intensity at each sensor. The intensities are plotted depending on the gold thickness and curve radius in Fig.3.16 with T_{12} the transmission of the straight waveguide and T_{23} the transmission of the curved part.

From the intensities measured with S1 and S2, first the propagation lengths were calculated for different gold thicknesses in straight waveguides following formula 3.28

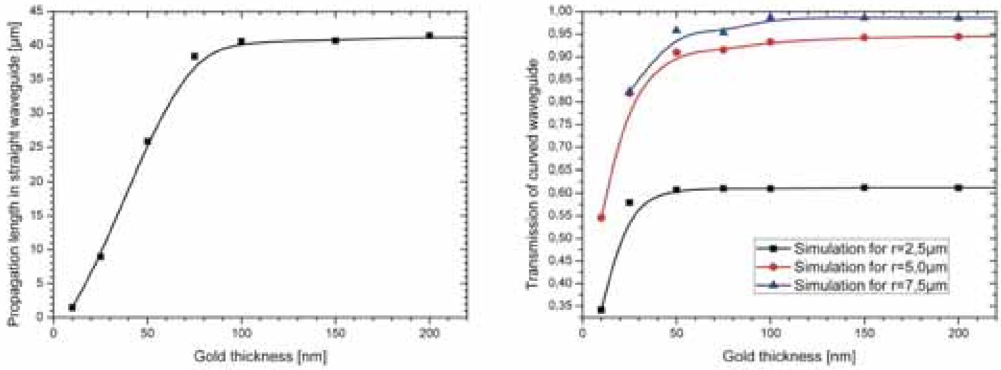

Figure 3.17.: Propagation length of SPPs in a straight waveguide depending on the gold thickness (left) and radiation loss of a curved waveguide depending on the gold thickness and curvature radius (right).

$$I = I_0 \exp\left(-\frac{x}{L}\right). \tag{3.28}$$

In this formula, I is the resulting intensity after a propagation length x, I_0 the entrance intensity of the electro-magnetic wave and L the propagation constant. To calculate L, the intensity values measured by S1 and S2 are used as I and I_0, respectively with x the distance between the sensors. From these calculations figure 3.17 left can be obtained, showing the propagation length in a straight waveguide depending on the gold thickness is shown.

From these results the transmission of the curved part without damping losses is calculated by formula 3.29.

$$T_r = T_{32} - T\left(\frac{\pi}{2}r\right) \tag{3.29}$$

where T_r is the transmission of the curved structure without taking damping losses into account, $T(\frac{\pi}{2}r)$ is the transmission of a straight part of the waveguide of $(\frac{\pi}{2}r)\,\mu m$ length, which corresponds to the length of the curved part of the waveguide with a curve radius r and which is calculated from the propagation lengths, and T_{32} is the transmission measured between S3 and S2. For different gold thicknesses and curve radii, the propagation through this waveguide was calculated.

From this propagation length, the transmission and loss of a straight waveguide of $3.9\,\mu m$, $7.9\,\mu m$ and $11.8\,\mu m$ were calculated, which correspond to the length in a curved waveguide with a radius of $2.5\,\mu m$, $5\,\mu m$ and $7.5\,\mu m$ respectively, which are simulated. These values are subtracted from the losses of the simulated curved part (S2 and S3) and the pure radiation loss of the curved waveguide part calculated depending on curvature radius and gold thickness, as shown in figure 3.17 right.

From these results, it can be seen that the thinnest gold layer giving a good propagation length of $L_0 = 41\,\mu m$ in the straight waveguide and low radiation losses in curved waveguides is $50\,nm$. For this gold thickness the curvature radius is varied one more time to obtain the best radius for a curved waveguide with the

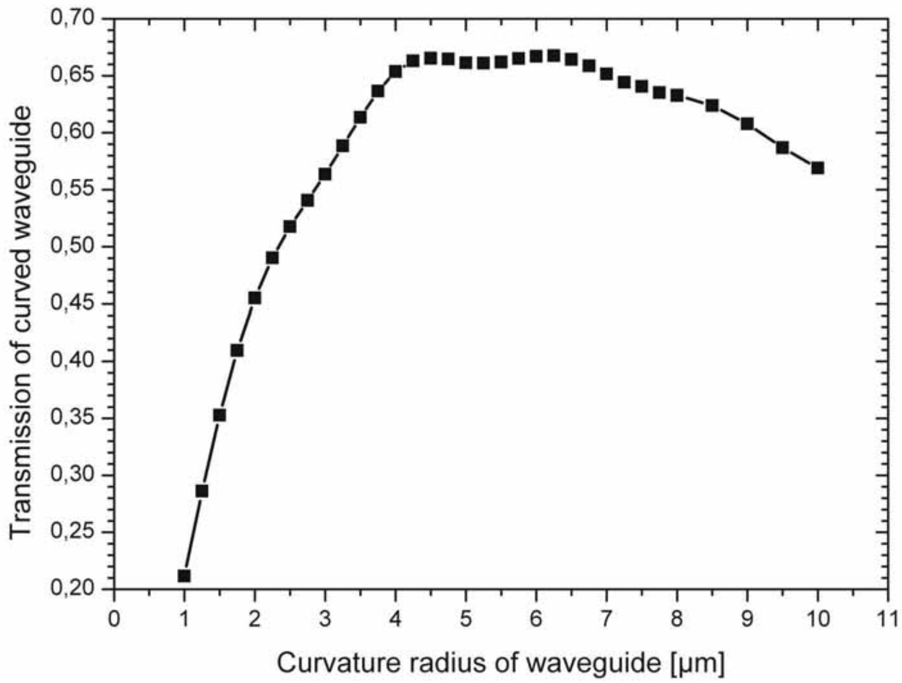

Figure 3.18.: Transmission of a curved SPP waveguide depending on the curvature radius simulated with *FullWave*.

lowest possible losses. The results obtained from these simulations are shown in figure 3.18.

It can be seen that the losses are minimal for a curvature radius in the range from $4.25\,\mu m$ to $6\mu m$ with a transmission of about 66 %.

3.5. Summary

The theoretical description of SPPs has been reviewed in this chapter. The appearance of SPPs and the possibilities to excite them have been described. Also, the materials useful for plasmonic devices have been qualified, and the propagation length of SPPs in dielectric waveguides has been investigated. Besides the investigations on straight waveguides, also simulations for finding the best curvature radius for a 90^o waveguide have been performed.

From the theoretical considerations and simulations carried out in this chapter, the parameters for further simulations have been fixed. These parameters are shown in table 3.1, and are used in all other simulations, if not mentioned otherwise.

Variable	**Value**
Edge-Gridsize	$5\,nm$
Bulk-Gridsize	$75\,nm$
Timestep	$0.05/0.1 \cdot (Edge - Gridsize)$
Wavelength	$1550\,nm$
Width of waveguide	$600\,nm$
Height of waveguide	$600\,nm$
Gold thickness	$50\,nm$
Refractive index of polymer	1.545
Refractive index of gold	0.55
K value of gold	11.5
Best curvature radius	$5\,\mu m$
Obtainable propagation length L_0	$41\,\mu m$

Table 3.1.: Parameters for the theoretical simulations of SPPs in chapter 3 and 4.

4. Theoretical analysis of SPP Y-splitters

After the discussion of general parameters for SPP-structures in chapter 3, the simulation and theoretical optimization of a basic SPP-structure will be discussed in this chapter. For investigations, a Y-splitter was chosen as simplest and most important basic structure for optical components. The simulation of the Y-splitter design suggested in [KZ07] is revised. From this, the simulations are extended to a more realistic model where defects arising during fabrication and their contribution to losses are investigated. After that, a new, more efficient design for a Y-splitter is introduced and simulated. Also, possible defects in this design are investigated and, besides the higher efficiency, also a higher defect tolerance for the new Y-splitter design is demonstrated.

For the simulations performed in this chapter, the software *FullWave* described in chapter 3 with parameters given there is used.

4.1. Review of known Y-splitter designs

In integrated optics, Y-splitters, or more generally multiplexers and de-multiplexers are well known. Much effort has been made to improve the efficiency of splitters for integrated optics. Different designs for high-index-contrast material systems were investigated by [REO01]. [VM04] investigated similar structures of straight and curved waveguides on the silicon-on-insulator material system basis in theory and experiment. This material basis was also analysed by [WBB06], and even more complex structures like arrayed waveguide-gratings and Mach-Zehnder lattice filters and ring resonators were examined. Another system investigated by [CSR07] was deeply etched photonic wires made of GaAs. A further approach for highly efficient integrated optical components are two-dimensional photonic crystals. Low loss Y-splitter designs and other components for optical devices on this material system base were studied by [SLJ02] [LFB04] and [PBB04]. In all these publications, very low losses of less than $2\,dB$ for the devices could be achieved.

[SBE06] showed that the designs known from integrated optics could be transferred to channel plasmon polaritons and compared experimental results of bends, Y-splitters, interferometers and ring resonators, with theoretical calculations. Also, [VF05] simulated guiding for a metal-air-metal structure, and showed theoretically that high transmissions for curved waveguides and splitters could be achieved. Another possibility is the structuring of the metal surface and the propagation of SPPs in these metal waveguides, as published in [JWG01] and [BLJ01]. [JWD05] demonstrated right angle bend structures realized by Bragg mirrors inscribed in the metal

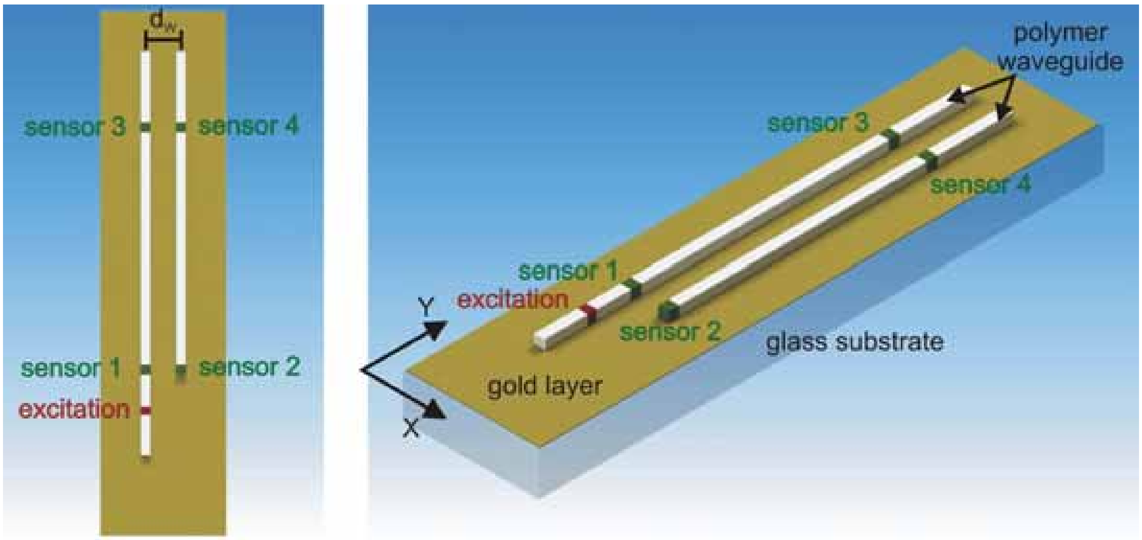

Figure 4.1.: Design of double line waveguides for the analysis of the cross talk of two SPP wave guides in top view (left) and 3-dimensional view (right). The distance between the center of the waveguides (d_W) is shown in the top view.

surface. [BL06] calculated guiding and propagating properties for a thin metal film embedded in a homogeneous dielectric. In a material system similar to the one investigated in this work and consisting of a substrate, a metal layer and a dielectric waveguide [BSK06] and [BSK07] showed guiding of SPPs, and the design of bends and directional couplers. For the special case of dielectric single mode waveguides on a gold layer as calculated in chapter 3, [KZ07] performed first simulations of directional couplers, curved waveguides and Y-splitter designs. As a starting point to improve the efficiency of SPP Y-splitter, the simulations presented in [KZ07] are reproduced with the program *FullWave*.

Before starting with the simulation of Y-splitter, first the crosstalk of two parallel waveguides depending on their distance is investigated. This is done to determine which distance between the two exit arms in a Y-splitter is necessary to achieve a negligible crosstalk. The design which is shown in figure 4.1 in top view (left) and 3-dimensional view (right) is used.

At the position of excitation the TEM_{00} mode of the waveguide is launched as a continuous wave. Sensor 1 at position $y = 0$ serves as a reference sensor for the incoming power into the parallel waveguide section, while sensor 2 is applied for controlling that none or only a negligible electro-magnetic field enters the second waveguide from the front. Sensor 3 and 4 at position $y = 20\,\mu m$ are for the measurement of the power of the electro-magnetic field in the left and the right arm after $20\,\mu m$ propagation inside the waveguides. Also, the electro-magnetic field, and with this the power distribution in the complete structure, is recorded after achieving a steady state. This simulation is performed for different distances between the centers of the $600\,nm$ wide waveguides. A distance of $600\,nm$ means that there is no gap between the waveguides. The distance between the line centers is varied from $600\,nm$ up to $5\,\mu m$. The distances simulated are shown in table 4.1, where the

Distance between center of lines d_W $[\mu m]$	**Coupling length** L_c $[\mu m]$
0.6	3.4
0.7	4.7
0.8	6.1
0.9	7.8
1.0	10.5
1.2	18.5
1.4	33.0
1.6	59.0
1.8	106.0
2.0	190.0
2.5	822.4
3.0	3564.6
3.5	15453.7
4.0	67004.4
4.5	290519.3
5.0	1259641.8

Table 4.1.: Coupling length between two polymer waveguides depending on the center to center distance of the waveguides.

coupling length L_c resulting from these is also specified. The coupling length L_c is the distance in which the electro-magnetic field performs a complete oscillation from the first (left) waveguide into the second (right) waveguide and back. Damping of the intensity inside the left waveguide, where the excitation takes place, is fitted by the following equation:

$$I(y) \; = \; A + I_0 \left\{1 - \cos\left(\pi \left[y - y_0\right] / L_c\right)\right\} \exp\left(- \left[y - y_0\right] / L_0\right). \tag{4.1}$$

In this formula, $I(y)$ is the intensity of the field inside the left waveguide at position z, I_0 the start intensity at position y_0, z the distance which the field propagates in the waveguide, L_0 the propagation length due to Ohmic losses as calculated in chapter 3.4, A and y_0 fitting parameters shifting the curve, depending on the coordinate system used, and L_c the coupling length. From these fittings the coupling lengths in table 4.1 are obtained.

These results are also shown in figure 4.2 on the left with the coupling length plotted in a logarithmic scale over the distance between the center of the lines.

The calculated coupling lengths in figure 4.2 on the left are fitted by an exponential function, which yields

$$L_c(d_w) \; = \; 0.379 + 0.538 \exp d_w / 340.92, \tag{4.2}$$

where d_w is the distance between the center of the waveguides.

On the right of figure 4.2, the intensity in the second (right) waveguide divided by the intensity of the first (left) waveguide after the propagation length $L_0 \; = \; 41\,\mu m$ as

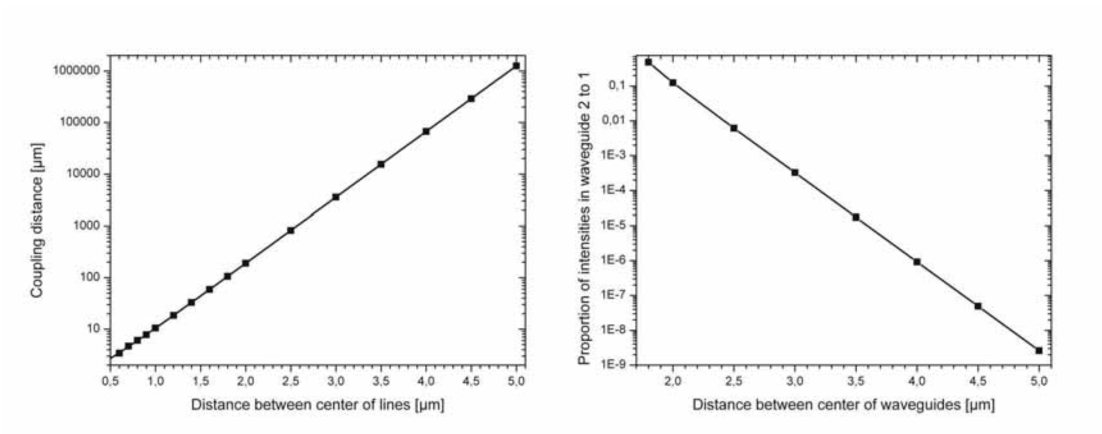

Figure 4.2.: Results from the simulation of double lines: the coupling-length (L_c) (left) and the intensity in the second (right) waveguide divided by the intensity of the first (left) waveguide after the propagation length (L_0) of the SPP depending on the distance between the centers of the two waveguides.

calculated in chapter 3.4.3 is shown, depending on the distance between the center of the waveguides. The intensities are calculated according to equation 4.1, with L_0 inserted for the length $[y - y_0]$. Distances between the center of the waveguides shorter than $1.8\,\mu m$ are not shown because the crosstalk length is shorter than the propagation length.

From these results the distance between two waveguides should be between $2\,\mu m$ and $3\,\mu m$, to achieve on the one hand a negligible crosstalk for the propagation length of the SPPs, and on the other hand a packaging of components as small as possible. For further simulations, a distance of $3\,\mu m$ between two waveguides, especially between the exit arms of a Y-splitter, is used to minimize the crosstalk, while keeping the SPP devices as small as possible.

After determining the distance necessary for two waveguides to achieve a negligible crosstalk, simulations of the Y-splitter can be performed. The first design of a Y-splitter for dielectric waveguides for SPPs is transferred from integrated optics by [KZ07], and is shown in figure 4.3 in top-view (left) and 3-dimensional view (right).

In this design, the excitation where the TEM_{00} mode of the waveguide is launched, and the position of sensors 1 to 4 are shown. The sensors are measurement points for the power flux inside the waveguide. Also, the names of different parts of the Y-splitter as used in this work are introduced. The splitter consists of a straight waveguide part before the splitting, the inguide, of $2\,\mu m$, the bend part and a straight waveguide part after the bending, the outguide, of $2\,\mu m$. The in- and outguide are used to have a short distance where the mode of the electro-magnetic field can be observed before and after the bend part. Sensor 1 is used to monitor the mode profile of the excitation, while sensors 2, 3 and 4 are the power measurement sensors to obtain the transmission of the splitter.

Besides the distance of the Y-splitter arms (splitter distance d_Y), the parameters mostly influencing the efficiency of the splitter are the curvature and the length of the bend part. The function describing the bend used in this work is

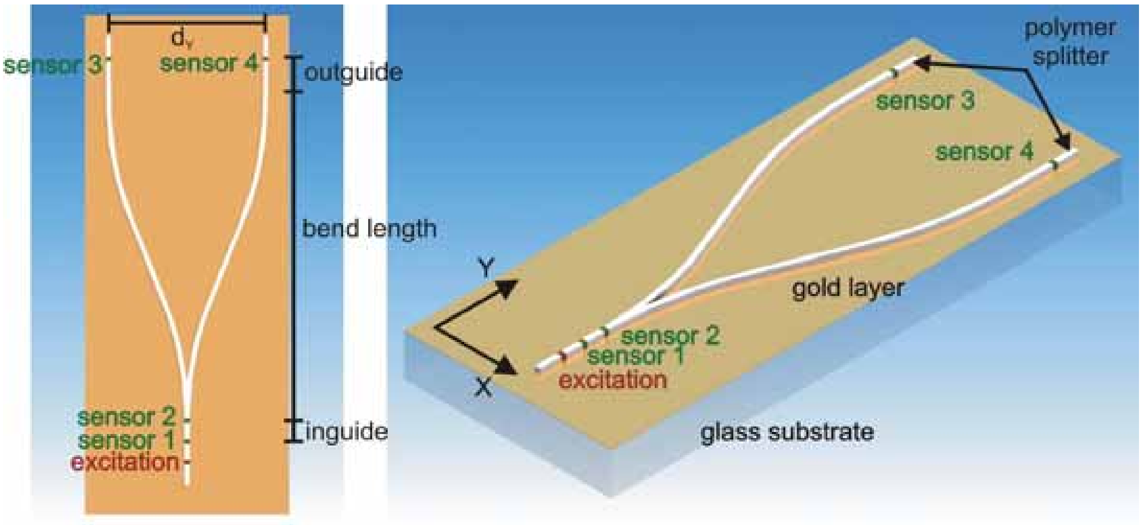

Figure 4.3.: Design of the Y-splitter for SPPs suggested by [KZ07] in top-view (left) and 3-dimensional view (right).

$$x(y) = d_B \left(\frac{y}{L_B} - \frac{\sin\left(2\pi \frac{y}{L_B}\right)}{2\pi} \right). \tag{4.3}$$

In this L_B is the length of the bend and d_B is the side shift in the bend of the waveguide. This equation describes the x-position of the bend $x(y)$ in the positive x-direction depending on the y-position, and represents the right arm of the splitter. For the bend in the negative x-direction the prefix of the position is changed to minus. It is taken from [KA98], and is well known from optical simulations to be one of the best solutions for efficient guiding of electro-magnetic fields. Also, [KZ07] showed that this is one of the best designs for the bend part of SPP splitters. Because of this, this bend function is chosen for the simulations.

Nevertheless, the question of the best parameters in formula 4.3 for SPP guiding has to be answered. Because of this, the following simulations are performed to find the most efficient length of the bend (L_B). Therefor the design as shown in figure 4.3 is simulated, and L_B is varied from $1\,\mu m$ up to $20\,\mu m$. The power at the sensor positions after reaching a steady state of the electro-magnetic field is measured and shown in figure 4.4, left.

The power measured at sensor 2 for a bend length of $1\,\mu m$ is slightly lower than for other bend lengths. This is due to the very sharp bending of the waveguide for this bend length, what causes reflections back into the entrance waveguide. The reflected power is also measured and subtracted from the total amount of power because the measurement is direction sensitive.

From the measured power P of sensors 2, 3 and 4, the transmission of the Y-splitter is calculated by

$$T = \frac{P_{sensor3} + P_{sensor4}}{P_{sensor2}}, \tag{4.4}$$

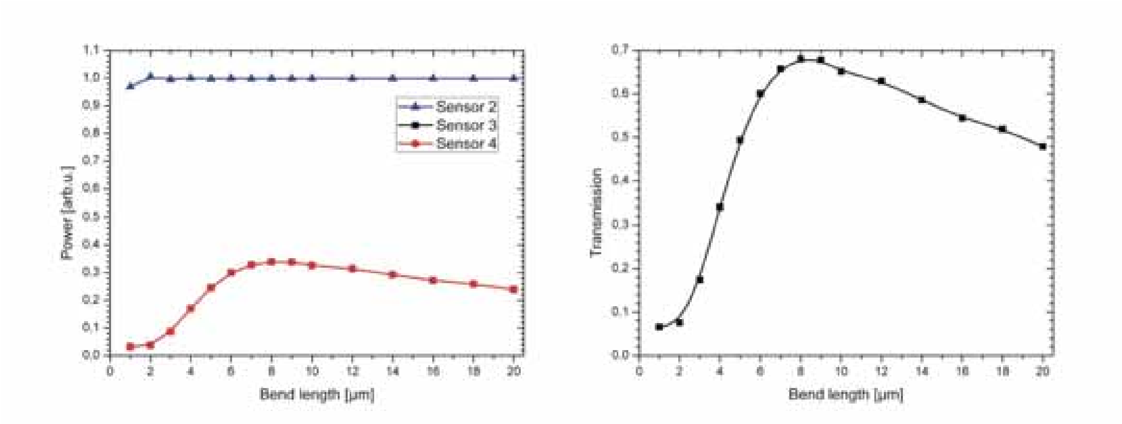

Figure 4.4.: Simulation results of the Y-splitter design showing the power measured in sensors 2, 3 and 4 (left), and from these sensor values calculated transmission of the Y-splitter (right). Sensors 3 and 4 show the same value, as it is expected for an ideal Y-splitter, and their curves overlap completely.

and shown in figure 4.4, right. The transmission reaches a maximum of about 68 % at $7\,\mu m$ to $8\,\mu m$ bend length. Besides the efficiency of the splitter, also the conservation of the mode profile is very important.To investigate this, the power distribution inside the waveguide (cut perpendicularly to the propagation of the field) at the sensors 1 (corresponding to the excitation), 2 (the entrance of the Y-splitter) and 3 (the left arm) is plotted in figure 4.5. For all simulations, the field distribution at the excitation and at the beginning of the splitter are the same, showing that a straight waveguide does not change this excited mode. The field distribution at sensor 3 changes drastically depending on the bend length and arm distance.

As can be seen in figure 4.5 the power distribution at the exit of the splitter (represented by sensor 3) varies for different bend lengths. For a length of $3\,\mu m$ (figure 4.5 middle left), the field maximum shifts to the left, while for a bend length of $5\,\mu m$ (middle right), the shift is slightly to the right side of the waveguide at the position of sensor 3. These simulations show that the excited mode profile is conserved, but for small bend lengths, reflected at the sidewalls of the polymer guide in the bend, leading to a fluctuating position of the field maximum from one sidewall to the other. This is not preferable compared to mode profile with the field maximum in the middle of the waveguide, and leads to additional losses. For a bend length of $7\,\mu m$ and $20\,\mu m$, this shift is not observed, and as can be seen in figure 4.5 bottom left and right, the mode profile is conserved, and the maximum remains centered in the middle of the waveguide.

From these results, a bend length of about $7\,\mu m$ seems the most appropriate length for a Y-splitter.

A further question for this design is the contribution of the Ohmic and the guiding losses. The transmission as shown in figure 4.4 on the right first increases with a maximum at about $7\,\mu m$ to $8\,\mu m$ bend length, and then again decreases. To understand the contribution of the Ohmic losses, the propagation length from sensor

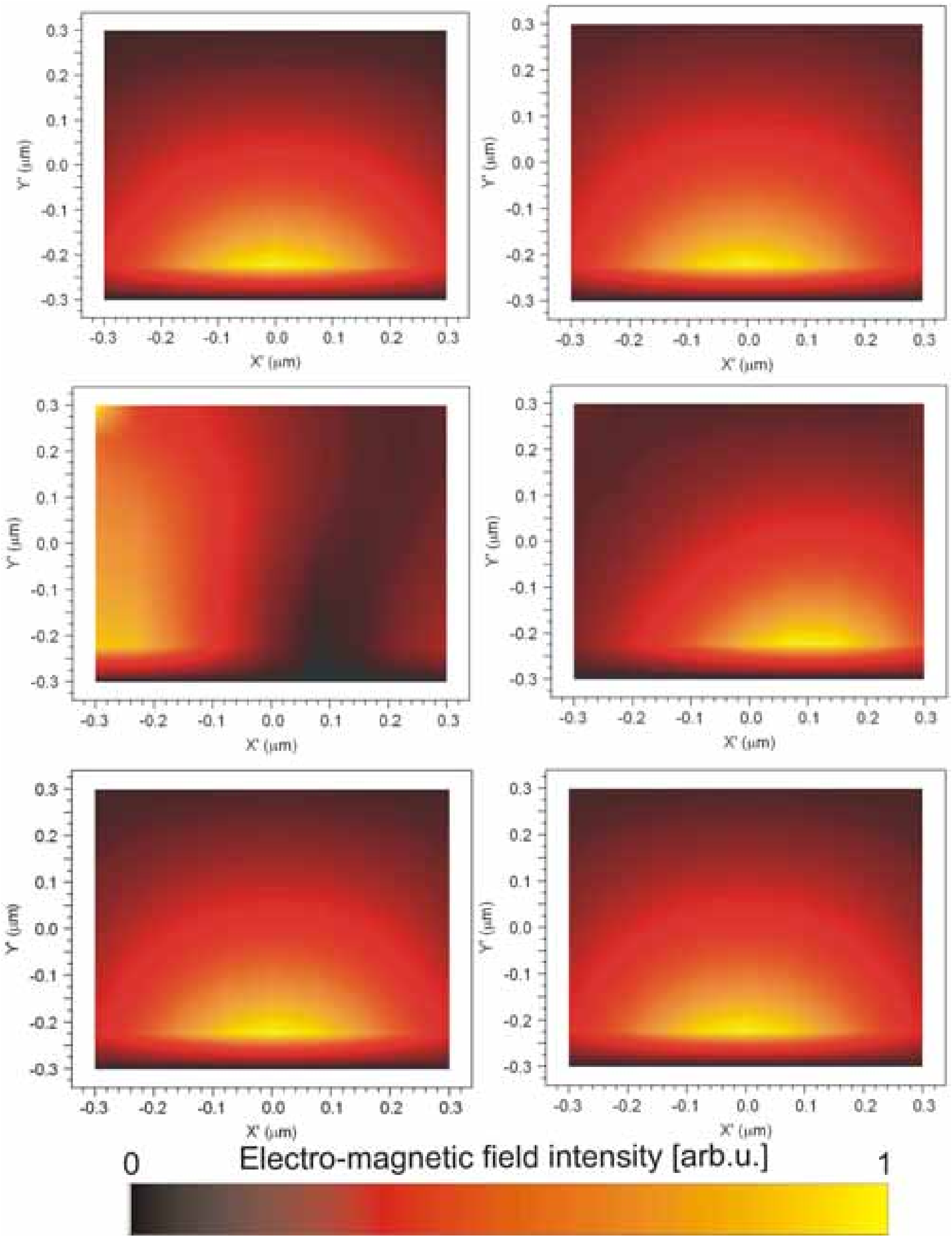

Figure 4.5.: Power distribution of modes observed inside the Y-splitter for different bend lengths: excitation mode (top left), mode at sensor 2 (top right) and at sensor 3 for a bend length of $3\,\mu m$ (middle left), $5\,\mu m$ (middle right), $7\,\mu m$ (bottom left), and $20\,\mu m$ (bottom right)

2 to sensors 3 and 4 must be calculated. This propagation length consists of the propagation inside the bend, and the straight part following the bend. The length in the straight part is $2\,\mu m$ while the propagation length in the bend part has to be calculated. In general, the path length of a function is obtained by

$$L_{f(x)} = \int_a^b \sqrt{1 + (f'(x))^2}dx, \tag{4.5}$$

providing the design of the bend. This formula gives the length of a function path L_f for the function $f(x)$ from point a to point b. This is applied to equation 4.3 giving

$$\begin{aligned} L_{f(y)} &= \int_0^{L_B} \sqrt{1 + (f'(y))^2}dy \\ &= \int_0^{L_B} \sqrt{1 + \left(\frac{d_Y}{2L_B} - \cos\left(2\pi\frac{y}{L_B}\right)\right)^2}dz, \end{aligned} \tag{4.6}$$

which is numerically solved for the necessary bend lengths and arm distances using the program *Maple*. The propagation lengths obtained from this are inserted into equation 4.7

$$T(L_B) = \exp\left[-\left(L_B + 2\right)/41.6\right] \tag{4.7}$$

and the Ohmic losses for SPPs in the bend are calculated. The Ohmic losses inside the waveguide are defined as the losses in the straight waveguide and are calculated as $[1 - T(L_B)]$ with $T(L_B)$ the transmission defined in equation 4.7.

In this equation, T is the transmission in and L_B is the length of the bend. The additional $2\,\mu m$ in the exponential part of the transmission arise from the propagation in the straight part of the waveguide following the bend structure before the sensor.

In figure 4.6 left, these Ohmic losses are plotted together with the total simulated transmission of the Y-splitter. From the Ohmic losses (the transmission with only ohmic losses (T_{ohmic})) and the total simulated transmission T_{total}, the splitter loss (the transmission of the splitter without taking Ohmic losses into account (T_{split})) is calculated using

$$T_{total} = T_{ohmic} \cdot T_{split} \tag{4.8}$$

for the different bend lengths.

This gives the third curve in figure 4.6 left, showing the splitter transmission without taking Ohmic losses into account.

The splitter losses can be investigated in more detail. They consist of the losses due to bending the waveguide (the bend losses with the bend transmission T_{bend}) and the diffraction at the edge in the middle of the Y-splitter (the diffraction losses with

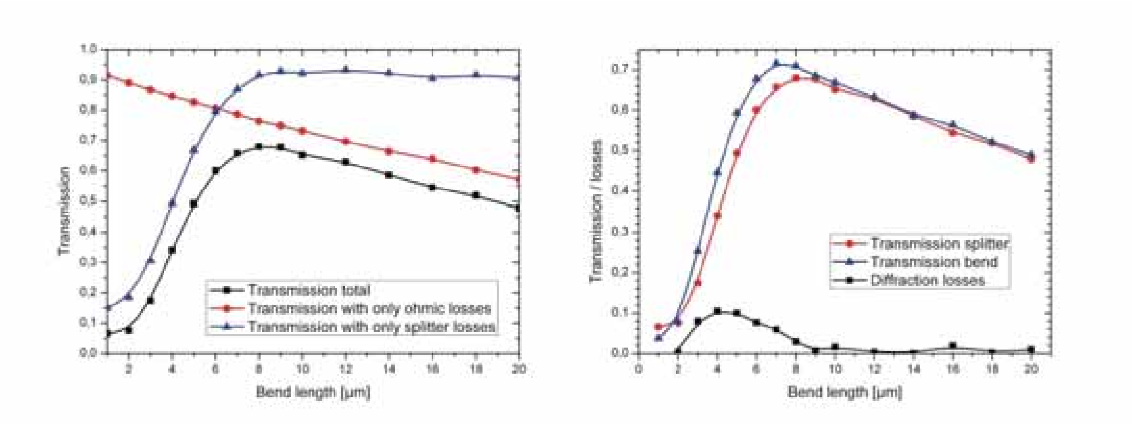

Figure 4.6.: Transmission of the Y-splitter with separation into Ohmic losses and splitter losses (left), and the transmission of a Y-splitter compared to a bend structure of the same parameters and extraction of diffraction losses (right).

the diffraction transmission T_{diff}). To divide the splitter losses into these two parts, a S-bend structure with the same bend lengths L_B as the Y-splitter is simulated. This bend structure is a Y-splitter with only one arm, and for this reason without an edge and diffraction losses. The simulation results of a S-bend with different bend lengths give the bend losses (bend transmission), and allow the determination of the losses in more detail by dividing the splitter transmission into bend transmission and diffraction transmission, following equation 4.9

$$T_{split} = T_{bend} \cdot T_{diff}. \tag{4.9}$$

On the right of figure 4.6, the transmission of a S-bend is shown in comparison to the transmission of a Y-splitter and the calculated diffraction losses.

The results given in figure 4.6 show that the Ohmic losses dominate the total transmission losses for bend lengths larger than $7\,\mu m$. For shorter lengths, the splitter losses dominate, while the maximum contribution from the diffraction losses arise at a bend length of $4\,\mu m$. The splitter losses consist of the losses out of and refraction at the curved part of the bend (bend losses), and the losses induced by the edge in the middle of the splitter (diffraction losses). These effects can be seen in figure 4.7, where the E_z-component of the electro-magnetic field $300\,nm$ above the gold surface for different bend lengths is plotted. On the one hand, for a bend length of $3\,\mu m$, the electro-magnetic field is distorted at the middle edge of the splitter (as seen in figure 4.7 left), while for a bend length of $7\,\mu m$, this distortion is reduced (middle), and for a bend length of $20\,\mu m$, this distortion is nearly negligible.

On the other hand, a longer bend length results in a longer propagation length with increased Ohmic losses. The combination of Ohmic, bend and diffraction losses results in the total losses and with this in the transmission of the Y-splitter with a maximum at about $7\,\mu m$ to $8\,\mu m$ bend length.

With these investigations, the losses in such a Y-splitter design can be divided into Ohmic, bending and diffraction losses. The results of these investigations are shown

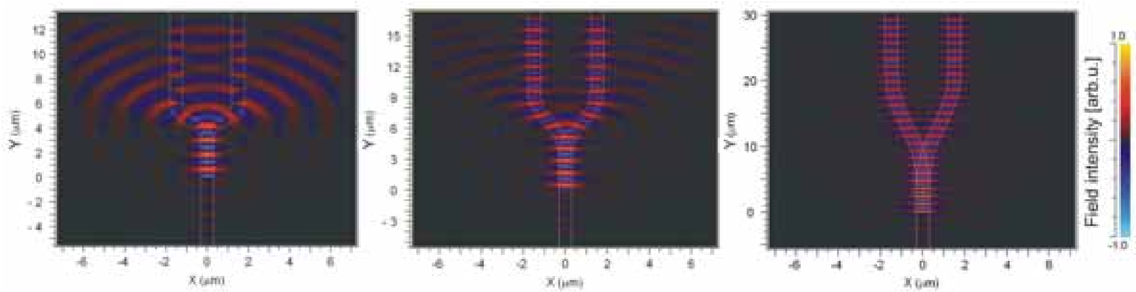

Figure 4.7.: Distribution of the E_z-component of the electromagnetic field 300 nm above the gold surface, for a bend length of 3 μm (left), 7 μm (middle) and 20 μm (right).

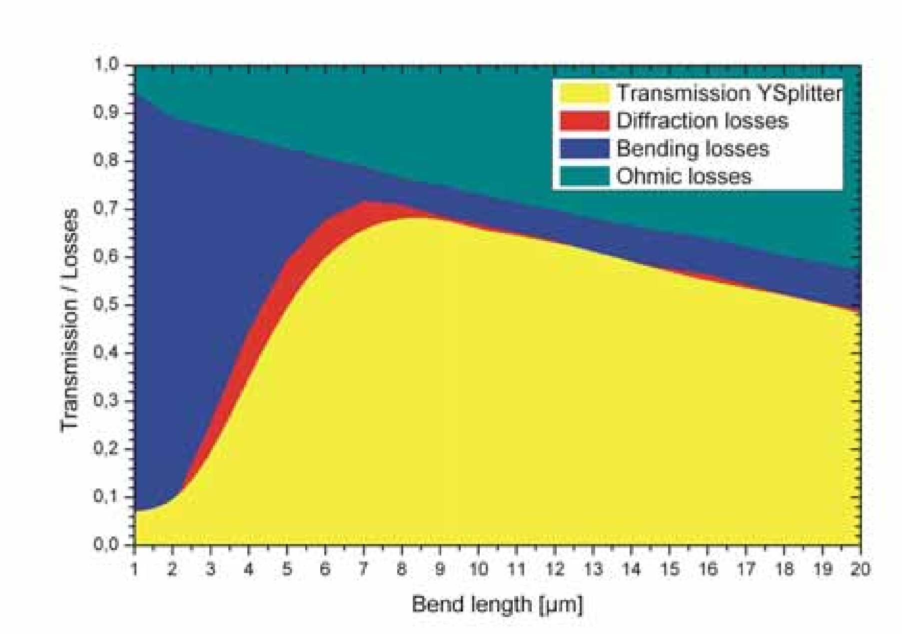

Figure 4.8.: Losses in a Y-splitter divided into Ohmic, diffraction, and bending losses and the transmission of the simulated Y-splitter.

in figure 4.8, with the total transmission and all losses of the Y-splitter design.

This figure shows that the most promising bend length for a splitter is in the range of 7 μm to 9 μm. For further simulations, the bend length is chosen as 7 μm, if not mentioned otherwise.

It must be pointed out that the simulations are performed with an ideal splitter design. To achieve a prediction of the efficiency of a fabricated splitter defects which could arise during the fabrication or due to the fabrication process have to be taken into account.

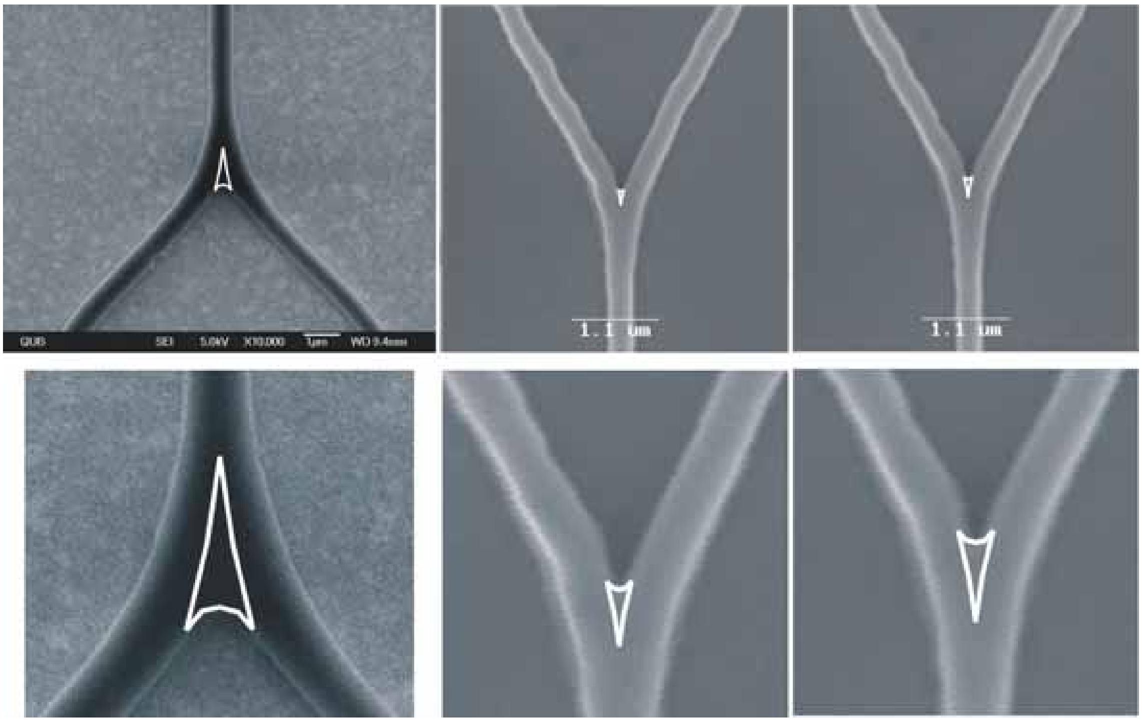

Figure 4.9.: SEM image of a Y-splitter fabricated using UV-lithography (left) (by the 'Laboratory for Nanosciences: Submicron Optics & Nanosensors' at the 'Universit de Bourgogne' in Dijon, France) and by 2PP (middle and right) with a magnification of the middle of the splitter (lower pictures) and the white marked defect region shown.

4.2. Real Y-splitter model

To get a prediction of the transmission of the Y-splitter, which was discussed in the last chapter, closer to experimental results, a more realistic model has to be simulated. For this reason Y-splitter fabricated using UV-lithography and 2PP are investigated by SEM. Figure 4.9 shows real Y-splitters obtained by UV-lithography (left) and two by 2PP (middle and right). Fabrication of such structures would also be possible by e-beam or ion-beam lithography. Nevertheless, only UV-lithography and 2PP are compared here. The reason taking UV-lithography into account is the ability for the mass production of dielectric structures. 2PP as a rapid prototyping technology is used for the flexible fabrication of DLSPPWs. Compared to e-beam and ion-beam lithography 2PP provides a better fabrication time and lower costs. Also the handling of samples and the structuring is easier using 2PP, because the structuring is done in normal atmosphere and with online observation.

The figure shows a magnification of the splitting region with the defect illustrated in white. It can clearly be seen that there is not an infinitely sharp separation into the two arms resulting in a non-perfect splitting. This effect is due to the limited resolution of fabrication techniques. The resolution of different UV-lithography techniques has been well investigated. For G- or I-line lithography illumination systems, a resolution of $1\,\mu m$ is commercially available, while for deep-UV lithography systems, a resolution of $250\,nm$ is achievable. The UV-structures shown in figure

L_B [μm]	d_Y [μm]	L_{defect} [nm] for a resolution of		
		500 nm	250 nm	100 nm
7	2	1872	727	372
7.5	2	2004	777	398
8	2	2137	829	424
7	2.5	1466	757	321
7.5	2.5	1572	828	343
8	2.5	1676	867	367
7	3	1261	671	288
7.5	3	1353	720	307
8	3	1441	767	329

Table 4.2.: Defect length for different fabrication process resolutions.

4.9 were fabricated using a MJB4 manual mask aligner from *SÜSS MicroTec* at the 'Laboratory for Nanosciences: Submicron Optics & Nanosensors' at the 'Universit de Bourgogne' in Dijon, France. This system provides a resolution of 500 nm at a wavelength of 250 nm. Using deep UV-technology, a resolution of 250 nm would be possible, while for the research in this work only a resolution of 500 nm was possible. It must be noted that this resolution is not the defect length as used in this work. To calculate the defect length from the process resolution, the formula for the bend structure (equation 4.3) has to be taken into account. Also, the bend length and the distance between the splitter arms influence the defect length for a specific resolution. For the bend function used, this problem can not be analytically solved. Because of this, the defect length for a Y-splitter fabricated with a resolution of 500 nm and 250 nm is calculated, using equation 4.3, computing the distance between the two arms of the splitter numerically. Calculating the defect length it has to be taken into account that the arms of a perfect Y-splitter do not split at $y = 0$ because they have a width of 600 nm. The results from these calculations are used to obtain the defect length for the 500 nm and 250 nm resolution techniques, which is shown in table 4.2, depending on the bend length and arm distance.

As seen from this table, the achievable resolution is very critical, especially for a small Y-splitter design. Even with techniques providing a resolution of 250 nm, the defect still remains around 700 nm and larger. This effect is also visible in the SEM pictures for the UV fabricated waveguide in figure 4.9. In this Y-splitter a defect length of 1000 nm for an arm distance and a bend length of 10 μm is observed, corresponding to a resolution of 845 nm, which is achievable with the UV-lithography system used. It must be pointed out that the Y-splitter shown in figure 4.9 has an arm distance and a bend length of 10 μm, which is much larger than the ideal arm distance of 2 μm to 3 μm and bend length of 7 $\mu m$to 8 μm.

Using this calculations starting from the SEM images, the resolution of the 2PP process can be estimated. The Y-splitters in figure 4.9, which were fabricated using 2PP, have an arm distance of 5 μm, a bend length of 7 μm and a defect length of 200 nm to 350 nm. This shows that the 2PP process has a resolution between 90 nm and 165 nm. Some publications show a resolution for 2PP around 30 nm [SPL06] [FQG07]. This would reduce the defect length to about 100 nm, but these results

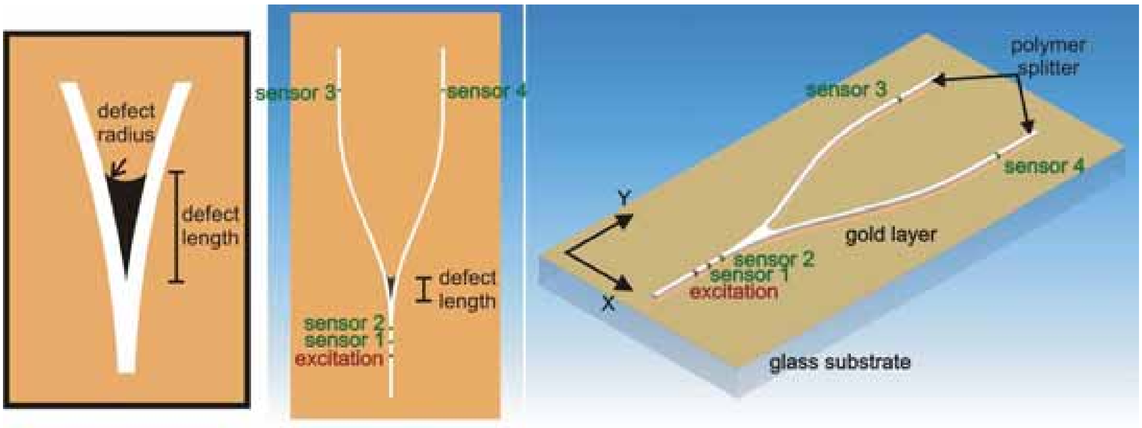

Figure 4.10.: Model of a Y-splitter with a defect taken from fabricated structures, in top-view (middle) and 3-dimensional view (right). On the left the magnification of the defect region with the defect length and the defect radius are shown.

were obtained in different polymers, and this is probably not directly transferable to the polymer used in this work (mr-NIL 6000 from *micro resist technology GmbH*). Even though the resolution of the 2PP processes could be taken from these publications, it is measured from 2PP fabricated Y-splitter as the ones shown in figure 4.9. The resolution obtained for this specific structure is $100\,nm$. The simulated model can be seen in figure 4.10.

The parameter of interest is the total transmission of the Y-splitter, depending on the length of the defect structure. The defect structure itself is approximated by an inverted circular filling between the two arms of the splitter. From the SEM pictures of the splitters, this seems to be the best approximation of the defect region. This defect approximation is defined by the defect radius and the defect length. In different structures it is observed, that the defect radius changes only very less and is similar for UV-lithography and 2PP. For this reason the radius is kept constant during all simulations. The length of the defect structure L_{defect} is defined as the distance parallel to the y-direction, from the position where the arms of an ideal splitter without a defect start separating, to the end of the defect structure, as shown in figure 4.10. For the UV-fabricated splitter, the defect has a length of about $1000\,nm$, while for the 2PP fabricated structure, the distortion is $200\,nm$ to $350\,nm$. To investigate the influence of the defect length, simulations with varying L_{defect} from $0\,\mu m$ to $2\,\mu m$ are performed. The results from these simulations are shown in figure 4.11, where the transmission of the Y-splitter is plotted over the defect length for $L_{defect} = 0..2\,\mu m$ (left) and $L_{defect} = 0..1\,\mu m$ (right).

The transmission decreases with increasing defect length. The right plot shows a magnification for defect lengths below $1000\,nm$. This is the most interesting region, due to the fact that the defect length obtained by 2PP is smaller than this value. Nevertheless, the defect causes a significant transmission reduction. The Y-splitter without a defect has an efficiency of 69 %, which decreases to 47 % for the UV-fabricated splitter and to about 66 % for the 2PP fabricated splitter. This clearly shows that not only perfect designs must be simulated, but also imperfections arising

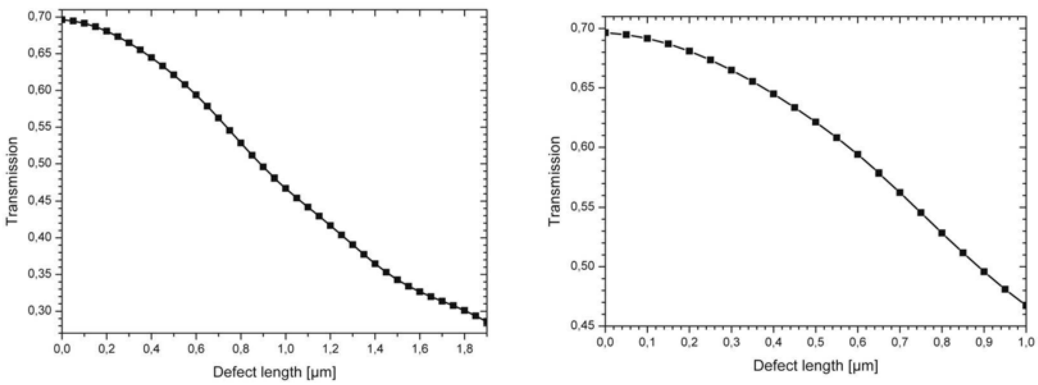

Figure 4.11.: Transmission of the Y-splitter, depending on the length of the defect introduced, shown for a defect length for $L_{defect} = 0..2\,\mu m$ (left) and $L_{defect} = 0..1\,\mu m$ (right).

from the fabrication process. Beside the losses due to defects, it was demonstrated that the simulated Y-splitter design has a maximum efficiency of 69 %, which is slightly lower than the efficiency of a bend structure of the same size, which is 71 %.

The question arising now is if a further improvement of this Y-splitter design is possible. Because the losses observed in this splitter have different reasons, they can be treated and improved separately. The Ohmic losses are induced by the metal, the polymer and the waveguide size chosen. The parameters for the metal (gold) and the polymer are taken in respect to experimental conditions for the real fabrication of these structures, and can not be changed. Also, the waveguide size is chosen in respect to [HB07] and the computational simulations shown in chapter 3, and should also not be changed. For these reasons, the Ohmic losses can not be further reduced in this design. The bend losses are mainly influenced by the first and second derivation of the function describing the bend (equation 4.3). This deviation should be, on the one hand, as small and as smooth as possible, but on the other hand the bend length should be as small as possible to minimize Ohmic losses. Optimization of the function describing such a bend has already been done in integrated optics resulting in the equation 4.3. There are some other functions proposed which are good for low loss bend structures [KA98] [WMA82]. Nevertheless, all the reported functions give a very similar transmission for optical components. For this reason, changing the function describing the bend does not increase the transmission significantly. The last losses are the diffraction losses, which would allow a small increase of efficiency. Unfortunately, the simulations were already performed with an ideal sharp edge in the middle of the waveguide, which could not be improved. An improvement on this design to achieve a higher efficiency for the given distance between the splitter exit arms does not seem to be possible.

This leads to the idea of optimizing transmission by introducing a new splitter design which gives a higher transmission for an ideal splitter, and also a lower sensitivity to defects introduced by the fabrication process, like the non ideal splitting.

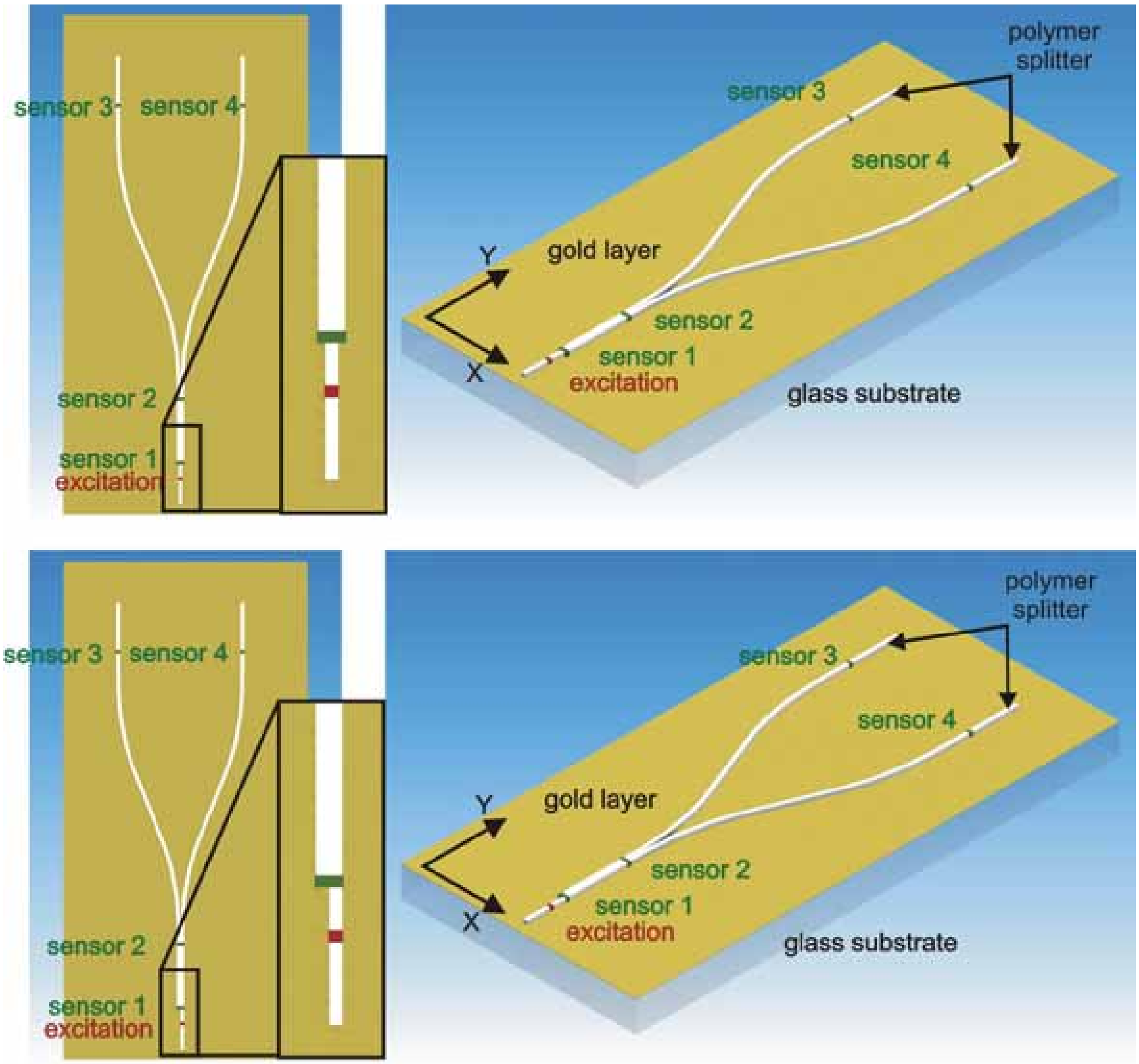

Figure 4.12.: Designs for a Y-splitter with a multi-mode waveguide section with a central incoupler (top) and a shifted incoupler (bottom) seen from the top (left) and 3-dimensionally (right).

4.3. Alternative Y-splitter designs

4.3.1. Multi-mode-splitter

A design which is very well known from integrated optics is the splitter with a multi-mode-section (multi-mode-splitter) [JXS07] [LL96] [GY90]. This design is shown in figure 4.12.

At the top of the figure, the multi-mode-splitter with a central single mode waveguide is shown. The multi-mode-splitter is the Y-splitter introduced in the previous section combined with a multi-mode-section of double the width of the waveguide, corresponding to a waveguide with $1200\,nm$ width. The sensors shown in figure 4.12 measure the transmission of the multi-mode-section (between sensors 1 and 2) and the transmission of the Y-splitter (between sensors 2, 3 and 4). The idea of this multi-mode-splitter is that the TEM_{00} mode propagating inside a multi mode

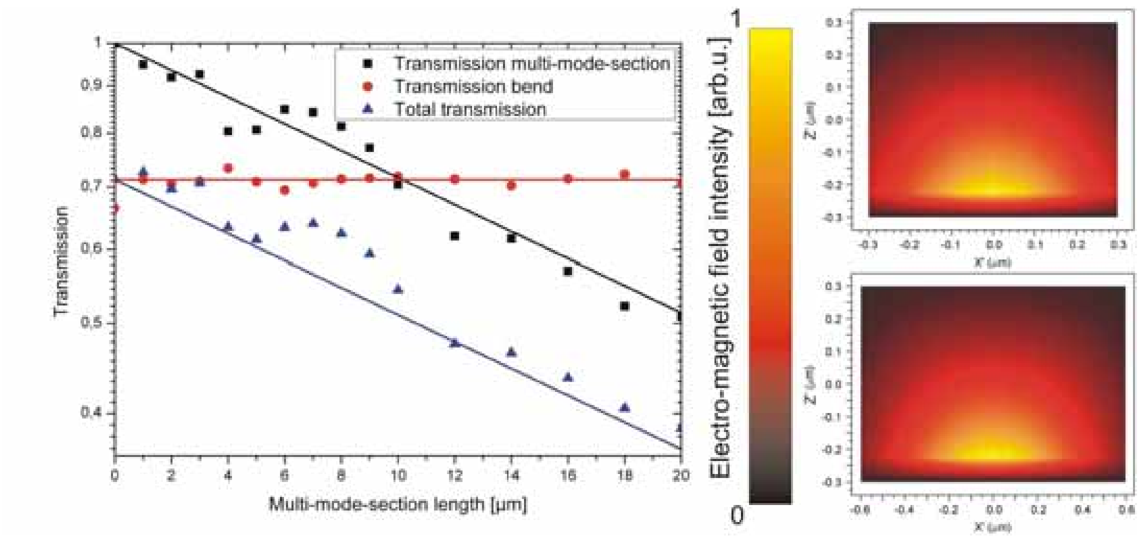

Figure 4.13.: The transmission of a Y-splitter with a multi-mode waveguide section and a central incoupler divided into losses due to the Y-splitter and due to the additional multi-mode-section (left), and mode profile at the beginning of the multi-mode-section(right top) and after 20 μm propagation in this section (corresponding to about half the propagation length of the SPPs ($L_0/2$)) (bottom right).

waveguide transforms into higher order modes, which have an intensity minimum in the middle of the multi-mode-section. This would lead to an intensity minimum at the edge in the middle of the splitter, and a reduction of the diffraction losses. It is also very important, that the losses introduced by a non-ideal edge in the center of the splitter should be reduced, and the splitter design should be less sensitive for this kind of defects.

The easiest possibility to realize this, as known from integrated optics, is the design shown in figure 4.12 top. The single mode waveguide with a width of 600 nm is attached in the center of the multi-mode section of 1200 nm width. This design is simulated with different lengths of the multi-mode-section (L_{mms}) from 0 μm to 20 μm. The results of these simulations are shown in figure 4.13.

The figure shows, besides the total transmission of the multi-mode-splitter, the transmission of the splitter part and the multi-mode-section. It can be seen that the total transmission of the multi-mode splitter is lower than the transmission of a splitter without a multi-mode-section ($L_{mms} = 0$). This can be easily understood by viewing the transmission of the splitter part, which is constant, and the transmission of the multi-mode-section, which is decreasing. The decrease of the multi-mode-section transmission is based on the increasing propagation length with a longer multi-mode-section and the increasing Ohmic losses. It seems that the positive effect of transforming the TEM_{00} mode to higher order modes observed in integrated optics does not increase efficiency in this kind of SPP waveguide. This can be easily understood by viewing the intensity profiles of the electro-magnetic wave inside the waveguide at the entrance of the multi-mode-section shown in figure 4.13 right top, and the intensity profile after 20 μm propagation length inside the multi-mode-

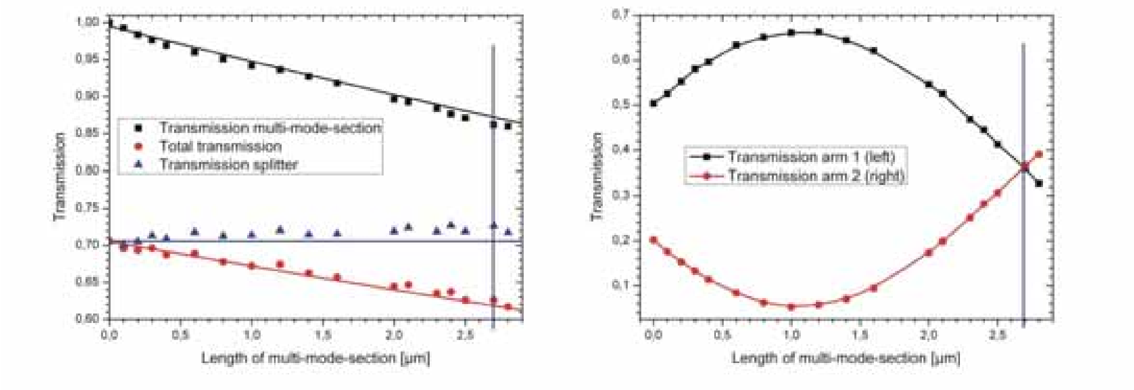

Figure 4.14.: Transmission of a shifted-multi-mode-splitter (left) and the intensity in each arm of the splitter (right) depending on the length of the multi-mode-section.

section (right bottom). Both profiles show a TEM_{00} mode. Thus, no transformation to higher order modes is observed during a propagation length of $20\,\mu m$, which corresponds to about half of the propagation length of SPPs as calculated in 3.4.3 to $L_0 = 41\,\mu m$. This implies that an additional multi-mode-section does not lead to a higher efficiency than the first Y-splitter design, because the propagation length of SPPs is too small, so that transformation from the ground mode to higher order modes does not take place on this length scale. This is analogous to integrated optics, where the multi-mode-sections for such a design are normally a few hundred micrometers, which is not achievable for this kind of SPP waveguide.

Now the question arises if the transformation of the TEM_{00} mode to higher order modes can be accelerated. A faster transformation should increase the efficiency of the splitter due to the intensity minimum at the edge of the splitter where the diffraction losses arise. For this reason, the design shown in figure 4.12 bottom is simulated. It is the same multi-mode-splitter investigated before, with the only difference that the single mode waveguide is not attached at the center of the multi-mode-section, but shifted $300\,nm$ to the side, corresponding to half of the width of the waveguide (shifted-multi-mode-splitter). This induces the effect which could already be observed in chapter 4.1 with the double line waveguides. The electromagnetic field oscillates from one side of the multi-mode-section to the other, and back. During these oscillations, there are specific positions which have half the intensity on the left, and the other half on the ride side of the waveguide, with an intensity minimum in the middle. At these positions, the efficiency of the splitter should increase, due to decreasing diffraction losses, as long as the additional Ohmic losses do not compensate the efficiency gain. To investigate this behavior, the shifted multi-mode-splitter is simulated for different lengths of the multi-mode-section. The results of these simulations are shown in figure 4.14.

In the left part of figure 4.14, the transmission of the splitter is plotted over the length of the multi-mode-section. Again, the transmission is split into the additional Ohmic losses induced by the multi-mode-section, and the transmission of the Y-splitter. The right part of the figure shows the contribution to the transmission

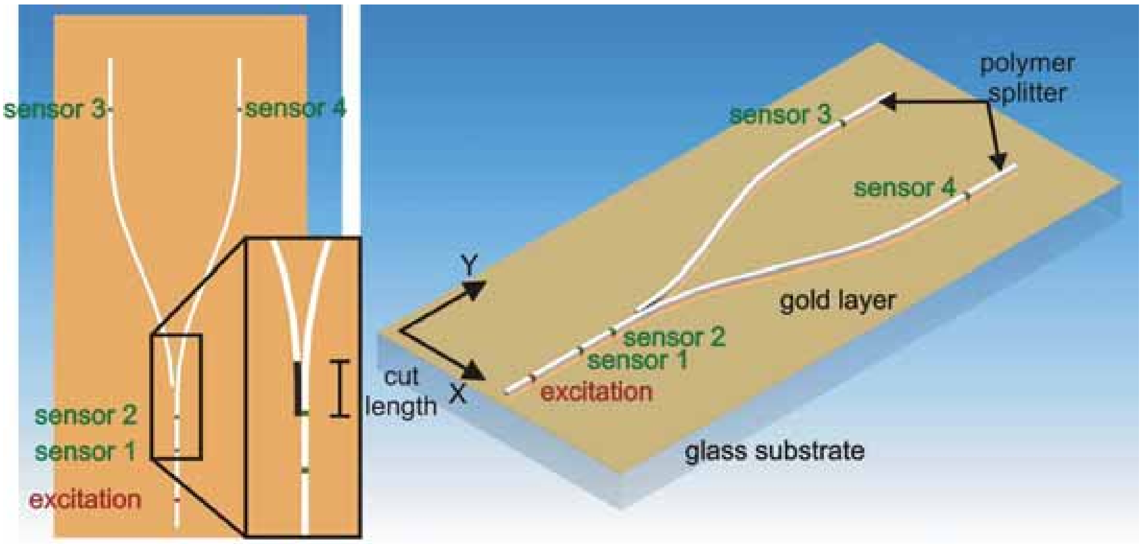

Figure 4.15.: Designs for a cut-splitter with a part of the left arm cut away (shown as dark area in the magnification) and shifted incoupler.

of the left and the right exit arm of the splitter. It can be seen that the splitting ratio is only 50 % for a specific length of the multi-mode-section. This length is 2.69 μm, and marked as a blue vertical line in both graphs. For lengths between 0 μm and 2.69 μm, the intensity in the left arm is higher than the intensity in the right arm, while for longer multi-mode-sections the intensity in the right arm is higher. As seen in figure 4.14 left, the transmission for a 50 % Y-splitter is 63 %. This is slightly smaller than the transmission for a perfect Y-splitter, as discussed in chapter 4.1. Nevertheless, this multi-mode-splitter shows the possibility of further efficiency increase. When the length of the multi-mode-section becomes smaller, the efficiency of the splitter increases up to about 71 %. However the fact that the splitting ratio of this design changes with varying multi-mode-section length makes it impossible to use this high efficiency for equal splitting. The advantage of this design is that not only symmetric splitters can be realized, but also other splitting ratios. Anyhow, the reason to simulate this design is to increase the overall efficiency of a 50 % Y-splitter. To increase the efficiency further, the shifted multi-mode-section design seems to be a good starting point.

4.3.2. A high efficient Y-splitter design

The idea is to extend the multi-mode-section into the negative direction. For this no multi-mode-section is added to the splitter but a part of the left arm is cut away. This cut-splitter design is shown in figure 4.15.

This design is the extension of the shifted multi-mode-splitter, to increase the transmission not by adding a longer path which induces higher Ohmic losses. For the following simulations, the cut length is varied. The cut length is measured from the point where the straight waveguide changes to the bend part of the splitter. This zero position is also taken as point for sensor 2 measuring the input power of the splitter. The results of these simulations are shown in figure 4.16, where in the left

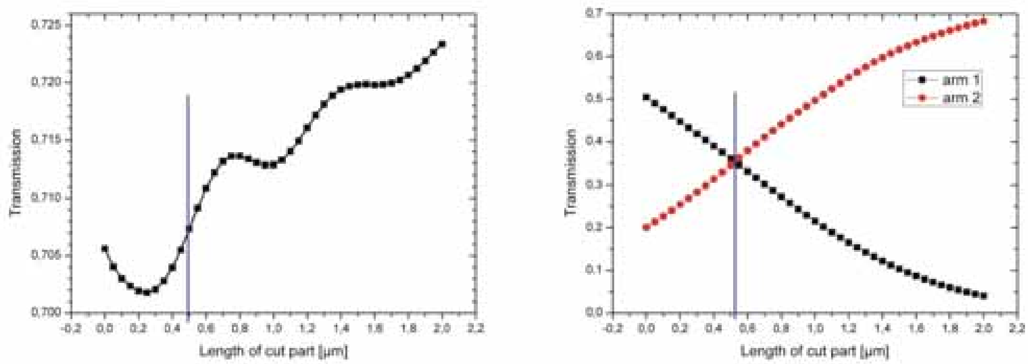

Figure 4.16.: Transmission of a cut-splitter (left) and the intensity in each arm of the splitter (right), depending on the length of the cut part.

part the total transmission of the splitter, and in the right part the transmission into both arms are plotted with the splitting ratio of 1 to 1 at a cut length of $520\,nm$, marked by a blue vertical line.

The transmission for this design is nearly 71 %, which is an increase of 3 % compared to the initial design of the Y-splitter. It is also an increase of 8 % compared to the 50 % multi-mode-splitter. Furthermore, the cut-splitter has the same advantage as the multi-mode-splitter and can be tuned from a 50 % splitter to other splitting ratios with no significant loss of transmission. Thus, this splitter gives the highest efficiency of the compared designs, and at the same time the possibility to tune the splitting ratio very easily from the complete transmission into the right arm to nearly the complete transmission of the intensity into the left arm. Taking the multi-mode-splitter together with the cut-splitter design into account, the splitting can be adjusted to any ratio with a total transmission larger than 68 %.

To judge the total efficiency of the cut-splitter design, one must compare it either to a bend structure or to a straight waveguide of the same length. The bend part of the simulated splitter is $7\,\mu m$, the distance between the exit arms is $3\,\mu m$ and the path length is calculated using equation 4.6. This gives a path length of $8\,\mu m$, where further $2\,\mu m$ have to be added for the straight waveguide after the bend part. With this, the total propagation length inside the cut-splitter between the sensors is $10\,\mu m$. A bend with the same parameters has a transmission of about 71 %, which was already obtained and shown in figure 4.6. The Ohmic losses for a propagation length of this distance in a straight waveguide are calculated in regards to equation 3.28, with the previously obtained propagation length of $L_c = 41\,\mu m$ (chapter 3.4.3). This results in a transmission of 82.4 % for a straight waveguide of this length. The cut-splitter design has a transmission of about 71 % for a 1 to 1 splitting ratio (and also for other splitting ratios), which is very close to this value. The transmission is about the same as for a bend structure .

As a next step modelling of a real cut-splitter with a defect as it can be expected in a fabricated structure is simulated. The model used for this simulation is analogous to the simulation of the real-Y-splitter performed in chapter 4.1, and is shown in figure 4.17.

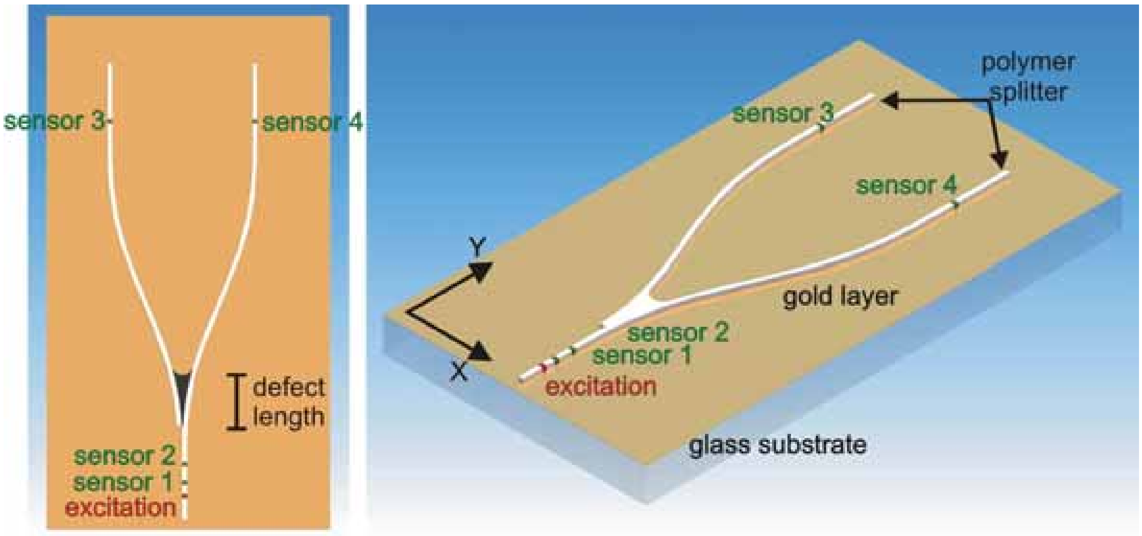

Figure 4.17.: Model for a cut-splitter with a defect inside the splitter in top view (left) and 3-dimensional (right). In the top view the defect is shown as dark area.

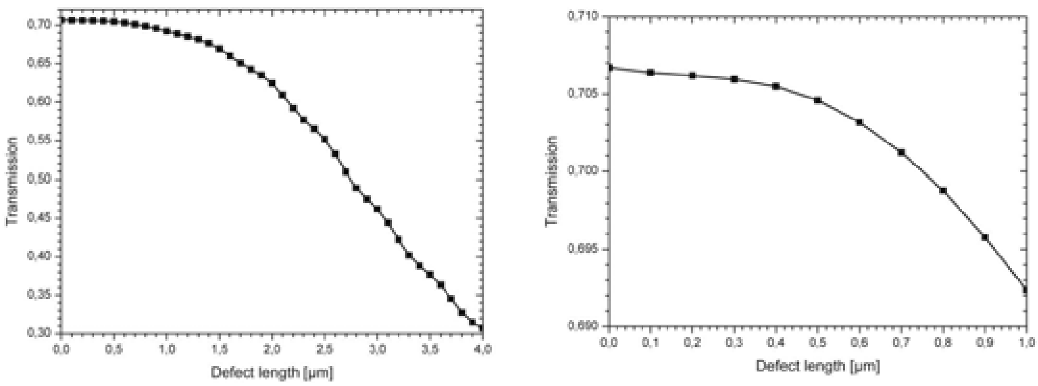

Figure 4.18.: Transmission of a cut-splitter depending on the defect length.

The cut length is set to 520 nm, which corresponds to a 1 to 1 splitter without defect, while the defect length is varied from 0 μm to 4 μm. The defect length is measured in z-direction from the position where a perfect splitter divides into two parts to the end of the defect. The results of these simulations are shown in figure 4.18.

The transmission of the splitter remains over 70 % for a defect length up to 700 nm. For the defect length observed in UV-lithography fabricated splitters, which would be about 1300 nm for the simulated parameters, the transmission still remains about 68 %, while for the defect in 2PP fabricated structures the transmission is about 70.6 %. Thus, the cut-splitter has a very good failure tolerance for defects arising due to the fabrication process.

Beside the total transmission although the splitting ratio has to be observed for an introduced defect. The transmission separated into the right and left arm of the splitter is shown in figure 4.19 for the defect length from 0 μm to 4 μm (left), and

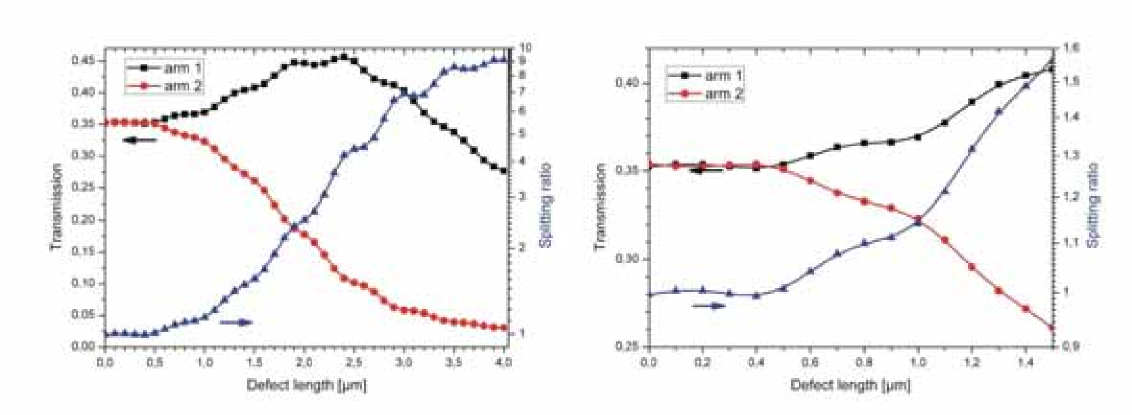

Figure 4.19.: Transmission of a cut-splitter depending on the defect length. The defect lengths from $0\,\mu m$ to $4\,\mu m$ (left) and the magnification of the defect length from $0\,\mu m$ to $1\,\mu m$ (right) are shown. Transmission separated into left and right arm (black squares and red circles) and the ratio of these transmissions (blue triangles) are plotted.

zoomed in to the defect length from $0\,\mu m$ to $1.5\,\mu m$ (right).

This figure shows that for a defect length below $500\,nm$, the splitting ratio into the exit arms is 1 to 1 while for a larger defect length, the splitting ratio becomes more and more shifted to the left arm. From these results, splitters fabricated using UV-lithography are not a 1 to 1 splitter, but would have a splitting ratio of 1 to 1.4. For 2PP fabricated structures, the defect is smaller than $500\,nm$, giving a splitting ratio of 1 to 1 with an efficiency of above 70 %.

With these simulations, a splitter design is obtained giving an efficiency of about 71 %. Moreover, a model for real fabricated splitters is simulated, showing that with the achievable resolution of 2PP, a splitter with a good transmission can be fabricated. The splitter produced using UV-lithography shows a larger defect, which leads to decreasing efficiency, but nevertheless still has a very high efficiency for the cut-splitter design. Also, the cut splitter allows to compensate the limited resolution of fabrication techniques. By simulating the cut-splitter for a technique with known resolution the expected defect length can be taken into account and the cut length can be adjusted to the desired splitting ratio. With this it is possible to achieve a high efficient splitter, equal or non equal, for both UV-lithography and 2PP.

4.4. Summary

In this chapter, the design for the single mode SPP Y-splitter by [KZ07] has been reviewed. This design of an ideal splitter has been extended to a more realistic model taking the limited resolution of fabrication techniques into account. The total transmission of this splitter model has been simulated depending on the resolution of fabrication technique and is has been shown that the effectiveness strongly decreases with worse resolution. From this two other Y-splitter designs with a multi-mode splitting, which are well known from integrated optics, have been transferred to SPPs. It was demonstrated that these designs do not provide an increase in efficiency, but the possibility to realize both equal and arbitrary splitting ratios. From this a novel design, the cut splitter, has been developed providing a higher efficiency and a better tolerance on the limited resolution of fabrication techniques. Also, it has been shown that this cut splitter allows to design a high efficient splitter with arbitrary splitting ratio taking the limited resolution of fabrication techniques into account.

5. Experimental investigations on Surface Plasmon Polaritons

After the presentation of the 2-Photon-Polymerization technology in chapter 2 and the theoretical considerations of surface plasmon polariton waveguides in chapter 3 and 4, in this chapter the experimental realization of SPP waveguides and their investigations are presented. For this DLSPPWs are fabricated on gold layers by 2PP. These waveguides are investigated in a leakage radiation (LR) setup and the experimental results are compared with computational simulations of these structures.

5.1. Experimental realization

5.1.1. Fabrication of DLSPPWs

The fabrication of DLSPPWs is done by 2PP technology. Because for SPPs an interface between a dielectric and a metal is needed the dielectric structures generated by 2PP could not be directly build on glass substrates as it was done in the application examples presented in chapter 2. Thus, the glass substrates are covered by a 50nm layer of gold. As metal gold and silver would have been possible because they are promising the longest propagation length for SPPs. Although silver will provide a longer propagation length than gold, it sulfides (see chapter 3.3) and in this way the material does not provide stable material constants over some time. For this reason silver is not used as supporting metal. The gold is deposited on the glass substrate by sputtering with a 'E5000M S.E.M. Coater' from *Bio-Rad Polaron Division*. Other techniques for the deposition of gold have been tested, such as thermal evaporation, and have given better quality of gold layers. Nevertheless, for the investigations presented in this work the quality of sputtered gold layers is sufficient and for availability reasons the sputter coater is used for the preparation of the gold layers.

The process steps for the preparation and development of the sample are well known for the materials used. After covering the glass sample with gold, the dielectric structures are fabricated by adding a droplet of ORMOCER from *micro resist technology GmbH* onto the top. A second glass is assembled with a $150\,\mu m$ thick spacer on the gold surface, resulting in a $150\,\mu m$ high volume between the gold surface and the second glass filled with ORMOCER. This sample is structured as described in chapter 2.3. The difficulty in the process chain is the structuring by 2PP. Before this work no report about the structuring of polymer by 2PP on metallic or in general reflecting surfaces has been published. There is a big difference between 2PP structuring on transparent materials like glass and on reflecting

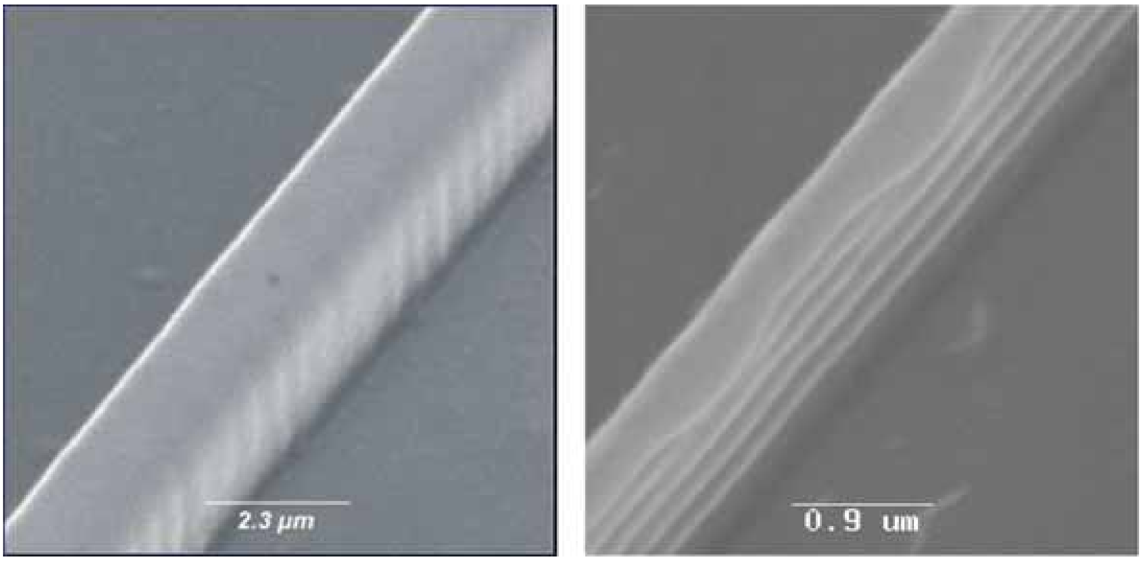

Figure 5.1.: A line of ORMOCER fabricated by 2PP on a glass substrate (left) and on a 50 nm gold layer (right).

materials like gold [CRB06]. The difference between the structuring of photopolymer on a glass substrate and metal is demonstrated by structuring ORMOCER on both surfaces with the 780 nm Tsunami laser (see chapter 2.4). Structuring of ORMOCER onto transparent dielectric substrates by 2PP has been reported in several publications [Ser04] [SMK97]. Laser-induced polymerization on the reflecting metal surface is more problematic owing to interference effects and poor polymer adhesion to metals. On a gold layer the fabrication of 2PP structures is possible for a smaller range of laser powers than on glass. Simultaneously, the required threshold power for 2PP decreases. The first effect could be related to adhesion problems and laser heating of the gold layer. The reduction of the 2PP threshold can be explained by the interference of the incoming and reflected laser beams in the vicinity of the gold surface. In the interference maxima the polymerization threshold is reduced owing to higher laser intensity.

In figure 5.1, scanning electron microscope (SEM) images of waveguide structures fabricated on glass and gold surfaces are shown. Modulations of the waveguide sidewalls along the direction perpendicular to the gold surface are evident in the structure fabricated on the gold, whereas they are not observed on the transparent glass substrate. This modulation appears to be due to the interference effects. The measured period of the interference pattern is $(251 \pm 4)\ nm$. This value is in good agreement with interference period $d = \frac{\lambda}{2n_{uc}} \sim 254\,nm$ determined by the half of the laser wavelength in the uncured ORMOCER. The slight transversal modulation of the sidewalls observed on the glass substrate can be attributed to small mechanical vibrations in the system.

To compare resolution limits of the 2PP technique on transparent (glass) and reflecting (gold) substrates, single polymerized voxels in ORMOCER on several surfaces are fabricated, using the same experimental setup. The diameters of the voxels fabricated on the glass and gold surfaces are measured as a function of the applied laser power. The measured voxel diameter are fitted by equation 2.6 with the pa-

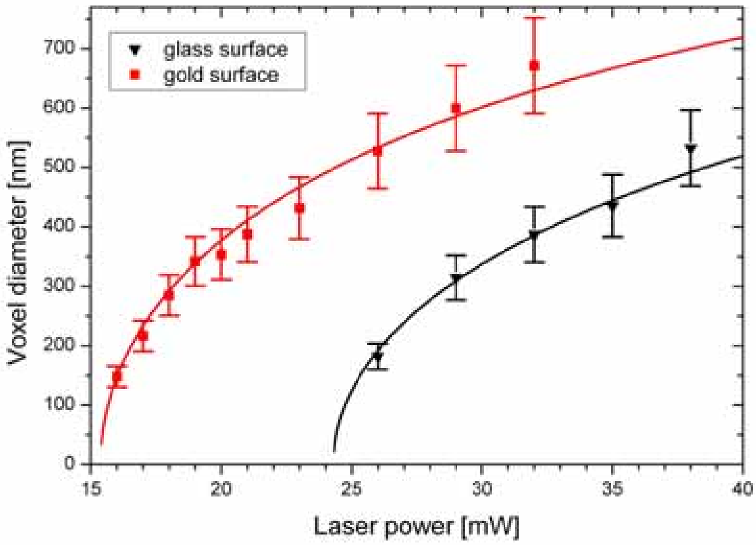

Figure 5.2.: Dependencies of the voxels diameter on average laser power for the structures fabricated on the gold and glass surfaces by 2PP at a fixed illumination time of $200\,ms$. The curves provide theoretical fits of the experimental data.

rameters of the Tsunami laser. The applied illumination time is $t = 200\,ms$. The experimental measurements of the voxel diameter and the fit are shown in figure 5.2.

In calculations of the voxel diameter on the glass surface, the beam radius $r_0 = 520\,nm$ is used as a single fit parameter. To reproduce the experimental data for the voxel diameter on the gold surface, the influence of the reflected beam must be taken into account and the photon flux in equation 2.6, N_0 must be replaced by $N_0 \times \eta_R$, with $\eta_R = 1.6$ the reflection factor. This value is below the maximum possible flux enhancement in the interference maxima. The reason for this is that, in our experiments, tightly focused laser pulses with a focus position slightly above the surface are used. Therefore the reflected beam is divergent and has lower intensity. The interference enhancement factor of 1.6 corresponds to the expected value.

The visibility of the interference pattern can be reduced when a structure is written several times with gradually increasing laser power. With this procedure, also the possibility of structural defects decreases. In this case the field enhancement effects at pointlike inhomogeneities are reduced because a thin layer of polymerized material is created on top of these inhomogeneities during the first, lower-power scan. To fabricate SPP structures such as waveguides, bends, and beam splitters with a smooth surface quality, the initial laser power is set to $6mW$ and gradually increased to $14\,mW$ in $1\,mW$ steps. For every laser power the structure is scanned twice. The structures still show a weak interference pattern close to the metal surface but have much better surface quality. A SEM image of a Y splitter fabricated by this procedure is shown in figure 5.3.

Dielectric structures could be fabricated on metal from ORMOCER this material

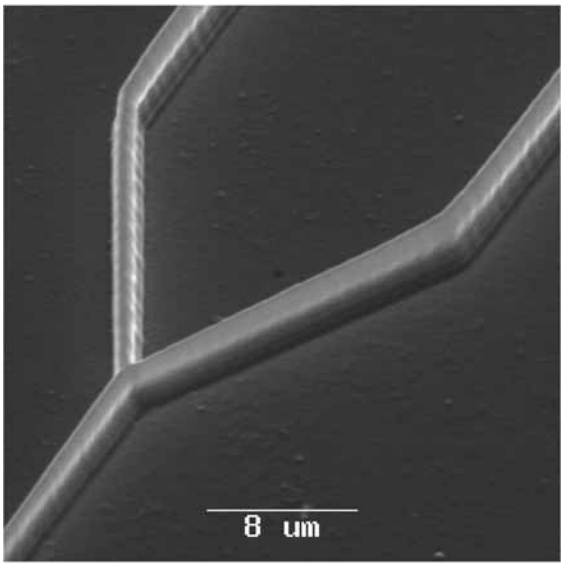

Figure 5.3.: SEM image of a Y splitter waveguide fabricated with gradually increasing laser power from $6\,mW$ to $14\,mW$ in ORMOCER.

is not suitable for further investigation of the targeted DLSPPWs with a waveguide width and height of $500\,nm$. The reflection from the gold layer lead to an enlargement of the focus perpendicular to the gold surface and with this makes it impossible, with the available structuring system, to reduce the structure height down to the targeted $500\,nm$. One possibility to overcome this limitation would be the reduction of the ORMOCER thickness to the targeted $500\,nm$ by spin coating. However, structuring of thin ORMOCER layer is not possible under normal atmosphere because the polymerization of ORMOCER is a radical polymerization. This polymerization is suppressed in the presence of oxygen, which is working as scavenger. For this reason the polymer mr-UVL 6000.5 is used for all further investigations, because it can be spin coated to $500\,nm$ layer thickness and structured. With this material it is possible to achieve a structure height of $500\,nm$ given by the layer thickness. A typical DLSPPW fabricated in this way is shown in figure 5.4.

The sample preparation changes for the polymer mr-UVL 600.5 compared to ORMOCER. The complete process chain for the sample preparation, the structuring and the development is shown in table 5.1. First the glass substrates are rinsed with acetone. After that a 50nm layer of gold is sputtered onto the glass. After the deposition of the gold the sample is covered with the dielectric. As dielectric the photosensitive polymer mr-UVL 6000.5 from *micro resist technology GmbH* is used. It is spin coated in a two-step coating process. First $3000\,rpm$ are applied for $30\,s$ resulting in a polymer layer of $500\,nm$ thickness. In the second step the revolutions per minute are increased to $6000\,rpm$ for $5\,s$ to throw excessive polymer of the sample. This procedure results in a homogenous $500\,nm$ thick layer over the whole glass substrate. The next processing step is the prebake for $3\,min$ at $110^o\,C$ on a hot plate to get rid of remaining solvent in the polymer. After the prebake the sample is structured by 2PP and then postbaked for $5\,min$ at $110^o\,C$ on a hot plate to solidify the structures. The last steps are then the development of the sample in SU-8 Developer (1-Methoxy-2-propyl acetate) and the cleaning of the sample in

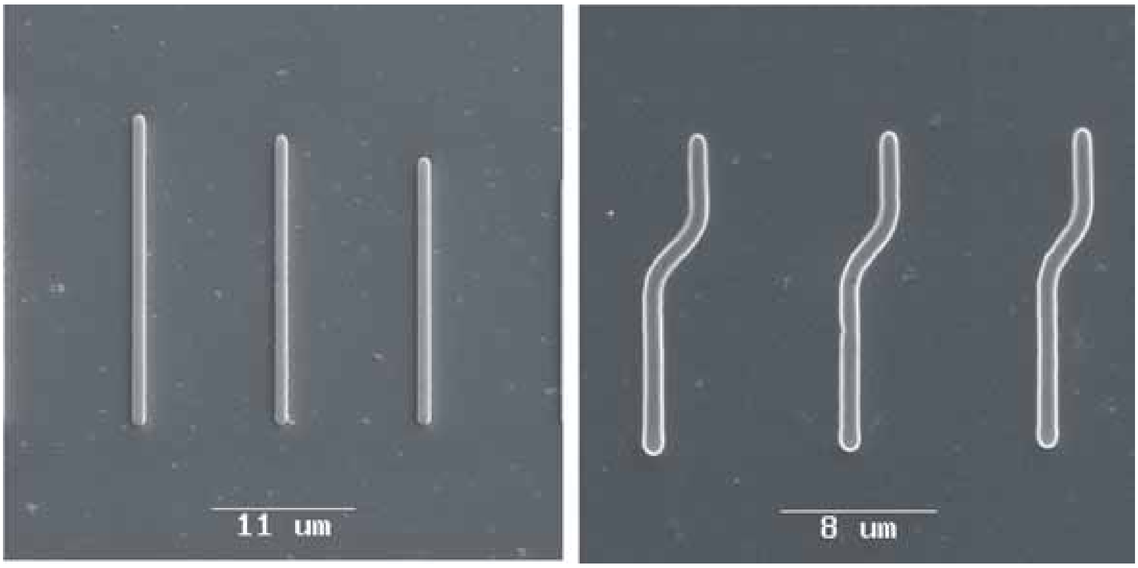

Figure 5.4.: SEM image of DLSPPW fabricated from mr-UVL 6000.5 on gold by 2PP. Three straight waveguides (left) with different lengths and three bends (right) with slightly different deviation between the incoming and the outgoing waveguide part.

Process step	**Parameter**
cleaning of glass substrate	by hand with acetone
gold deposition	50nm by a 'E5000M S.E.M. Coater'
spin coating	mr-UVL 6000.5 with
for 500 nm layer height	1) 3000 rpm for 30 s
	2) 6000 rpm for 5 s
alternative spin coating	mr-UVL 6000.3 with
for 300 nm layer height	1) 3000 rpm for 30 s
	2) 6000 rpm for 5 s
prebake (hot plate)	for 3 min at 110^o C
structuring	by 2PP with typical 5 mW and 20 m/s
postbake (hot plate)	for 5 min at 110^o C
development	for 60 s in SU-8 Developer
	(1-Methoxy-2-propyl acetate)
rinse	distilled water

Table 5.1.: Process chain for the sample preparation and structuring of first DLSPPWs.

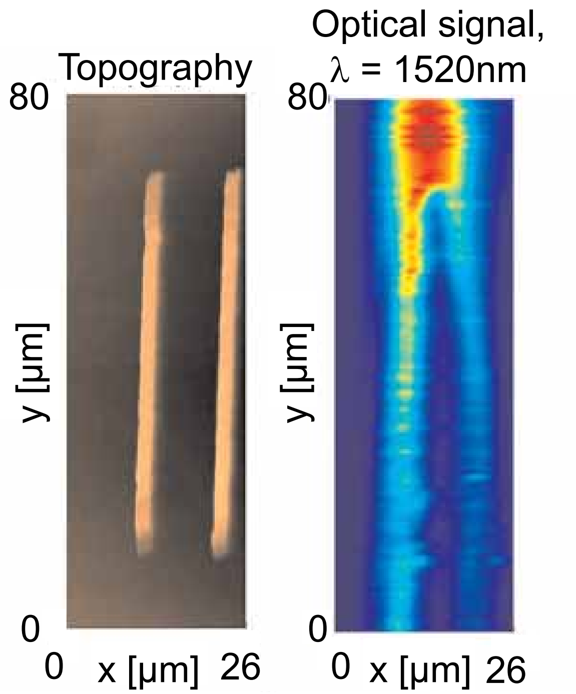

Figure 5.5.: A SNOM image of 2PP fabricated dielectric structures on gold. The topography of the structures (left) and the optical signal of SPPs (right). In the optical signal it can be seen, that plasmons are propagating inside the left dielectric line, but are also reflected by the right dielectric line.

distilled water.

All structures reported and shown in the following sections are made from mr-UVL 6000 on 50 nm gold by 2PP following these preparation steps if not otherwise mentioned.

5.1.2. Scanning-near-field-optical-microscopy and leakage radiation microscopy

After fabrication of DLSPPWs these structures have to be characterized. The most exact possibility of analysis would be a Scanning-Near-Field-Optical-Microscope (SNOM) [HP94]. A SNOM image of straight dielectric structures and their influence on SPPs is shown in figure 5.5.

The topography shows two dielectric lines of about 1 μm width and 60 μm length. On the right image the optical signal detected by the SNOM is shown. On the top the excitation of plasmons shows up as bright red spot. The plasmons are propagating inside the left dielectric line. Also a second plasmon beam propagates to the lower right and is reflected by the right dielectric line. This clearly shows the possibility of SPPs propagating inside 2PP generated structures. The wavelength used for the excitation of SPPs in this image is 1520 nm. The waveguide structures have been fabricated at the Laser Zentrum Hannover e.V. by 2PP structuring of ORMOCER on gold covered glass substrates. The image has been grabbed at the 'Institute of

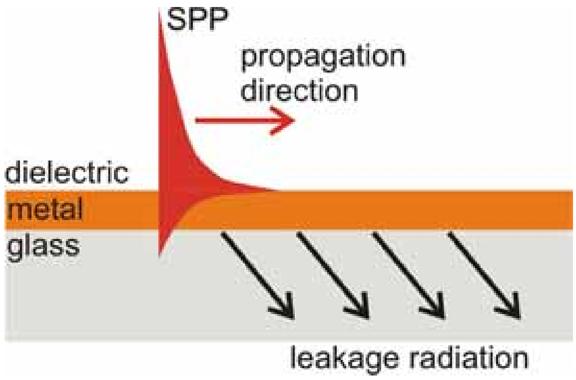

Figure 5.6.: The principal of a leakage radiation microscope. SPPs propagating at the interface metal-dielectric emit light into the glass substrate. The angle of emission is around 44^o.

Physics', 'Aalborg University' in Denmark, because no SNOM was available at the Laser Zentrum Hannover.

Unfortunately a SNOM uses a scanning technique for image acquisition and is, because of this scanning, a very slow technique. Furthermore, it is a very expensive technology. For these reasons it has been decided not to build up a SNOM during this work, but a leakage radiation (LR) microscope. The principal of this is shown in figure 5.6.

SPPs are excited at a dielectric structure on top of the gold and propagate on the surface. They emit light, the leakage radiation (LR), under a very specific angle of about 44^o into the glass substrate [Mai06]. This emission angle is too large to be detected with a normal microscope objective. For this reason an immersion oil objective with a high numerical aperture is necessary. Behind the immersion oil objective a 4f-setup is realized as it is shown in figure 5.7 to allow the Fourier filtering of different components of the image.

In this figure the laser is shown on the left. The beam is focussed by a microscope objective onto the sample. The dielectric structures are on the side of the focussing objective. On the back side of the sample a high numerical immersion oil objective is mounted to image the sample and the leakage radiation. Behind this objective a so called 4f-setup is arranged. The lenses L_1, L_2 and L_3 with the focal lengths of $f_1 = 200\,mm$, $f_2 = 300\,mm$ and $f_3 = 250\,mm$ are placed, as seen in figure 5.7, in a distance of $40\,mm$, $93\,mm$ and $114\,cm$ behind the back side of the immersion oil objective. This configuration allows a fourier filtering of the beam at L_2. With this filtering it is possible to block the light from the exciting laser beam by an inverse pinhole. This can be done because the leakage radiation is emitted under a larger angle than the light of the exciting laser beam [ADK06]. The third lens L_3 works as an imaging lens. This allows, depending on the position of the imaging camera, the observation of the image plane or the fourier plane. With this it is not only possible to observe the propagation of light and plasmons (in the image plane) but also the fourier transformed image.

After the introduction of the principle of the leakage radiation microscope the design of the real setup is shown in figure 5.8.

The SPPs can be excited by two different lasers, a HeNe-laser or a TiSa-laser

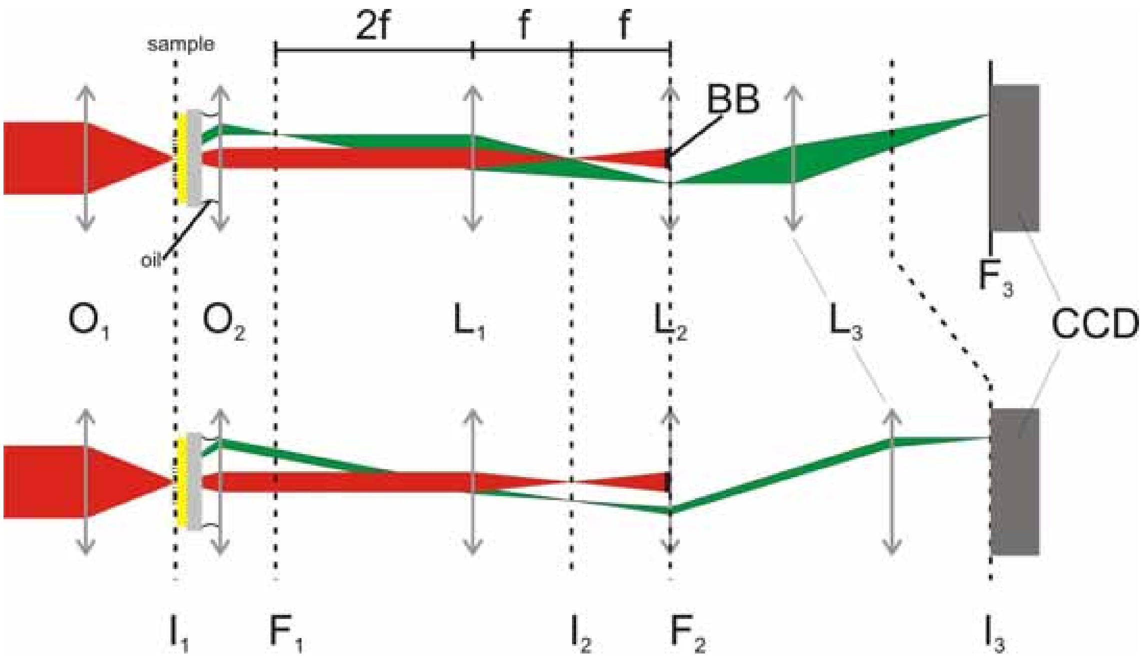

Figure 5.7.: The principal of the 4f-setup. This configuration allows the filtering of components in the Fourier plane depending on their emission angle and direction. The SPPs are excited by the laser beam (red) coming in from the left and focussed by the microscopy objective O_1 on the dielectric structure. The dielectric structure is situated on a gold layer and a glass substrate. The LR (green) is emitted from the gold-glass interface I_1 and collected from the immersion oil objective O_2. Lenses L_1 and L_2 form a telescope. Depending on the position of the third lens L_3 the Fourier plane F_3 (top image) or the image plane I_3 (bottom image) can be imaged to the CCD. With an inverse diaphragm (beam block - BB) in the Fourier plane F_2 the exciting laser beam can be filtered out.

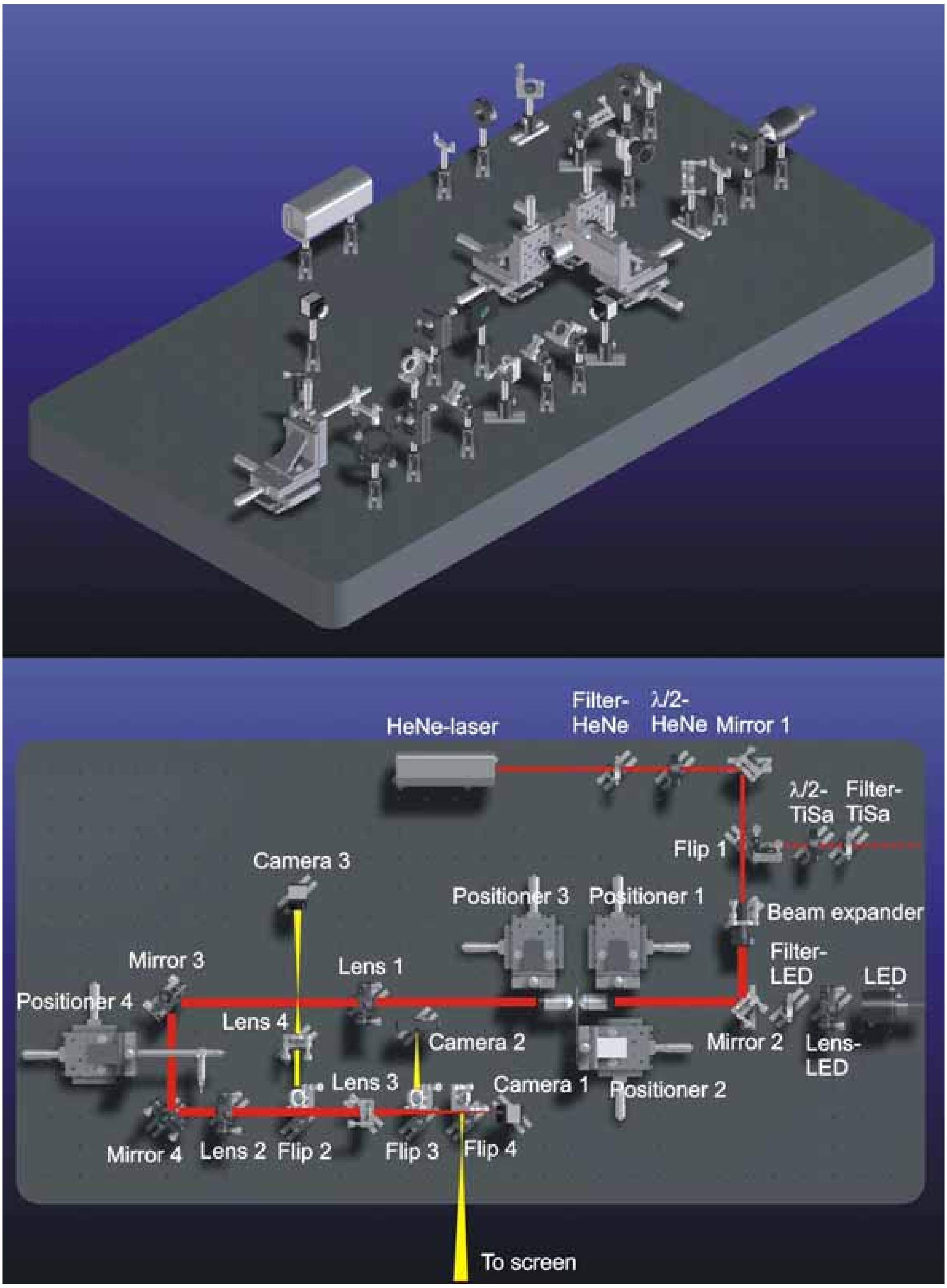

Figure 5.8.: Design of the leakage radiation microscope with two possible laser systems and four imaging alternatives seen in isometric view (top) and from the top (bottom).

system. The HeNe-laser beam is adjusted through a changeable filter (Filter-HeNe) to regulate the beam power and a $\lambda/2$-waveplate ($\lambda/2$-HeNe) for polarization turning onto 'mirror 1'. From this it is reflected through the beam expander onto 'mirror 2' and into the focussing microscope objective, a '40× Plan' from *Carl Zeiss AG*. The beam expander is needed for expanding the laser beam to a size filling the complete entrance aperture of the focussing objective to achieve focussing to a small size. The second laser which can be used is the TiSa-system. This can be coupled into the setup by the mirror on the flip mount 'flip 1' after passing through a filter ('filter-TiSa') and a $\lambda/2$-waveplate ('$\lambda/2$-TiSa') and is then propagating the same path as the HeNe-laser beam. Behind 'mirror 2' a LED is mounted shining through this dielectric mirror, transparent for wavelength smaller than $600\,nm$. The LED is focussed by the lens-LED onto the entrance of the focussing objective and can be dimmed by the changeable filter allowing an ideal illumination of the sample surface. The objective on 'positioner 1' is focussing the laser beam onto the sample mounted on 'positioner 2'. The high numerical aperture oil objective 'Plan-Apochromat 63× 1.4 Oil DIC' from *Carl Zeiss AG* is mounted on 'positioner 3'. The objectives are aligned along the laser beam axis in a confocal configuration with the sample in the focal position. With this the parallel laser beam is focussed onto the sample and the light emerging from it is again parallelized by the oil objective. The alignment of the two objectives and the sample is very sensitive. First the objectives are aligned along the beam axis in confocal configuration without the sample and after that the sample is attached into the focal position. 'Lens 1', placed two times its focal distance away from the back plane of the oil objective on the beam axis, focusses the laser beam. Due to the long focal length of $200\,mm$ for lens 1 and $300\,mm$ for 'lens 2' the beam is folded by 'mirror 3' and 'mirror 4'. 'Lens 2' is situated $530\,mm$ behind 'lens 1'. In this distance the image of the sample is Fourier transformed allowing the separation of the excitation laser and the scattered light, and the leakage radiation of the plasmons. This is possible due to an inverse diaphragm mounted on 'positioner 4' because the LR is emitted under an other angle than the excitation laser light or the scattered light. 'Lens 2' parallelizes the beam again, while 'lens 3' focusses the laser beam on 'camera 1'. In this way the image of the sample is displayed on camera with the possibility of filtering out the excitation laser and scattered light. 'Camera 1' is a 'NC-305 webcam' from *Conrad Electronic SE*, which allows imaging the sample with a rate of 25 frames per second. The drawback of this camera is that it is not intensity calibrated and with this no quantitative analysis is possible. For this reason 'camera 2', a 'WinCamD-UCD 12' from *Data Ray Inc.* with a rate of 10 frames per second, is implemented and the beam can be redirected to this camera by the 'flip 3' (yellow color in figure 5.8). This camera is intensity calibrated and is used for quantitative measurements. The lower frame rate makes a sample adjustment using this camera difficult. For this reason 'camera 1' is used for the adjustment of the sample and the imaging of the sample itself, while 'camera 2' is used for the observation of the leakage radiation and the quantitative analysis. With these two cameras the observation and analysis of the sample is possible, while for the imaging of the Fourier plane 'camera 3', a 'NC-305 webcam' from *Conrad Electronic SE* is used. With 'flip 2' the beam can be reflected through 'lens 4' onto 'camera 3' which is positioned in the Fourier plane. Besides the three cameras also the observation

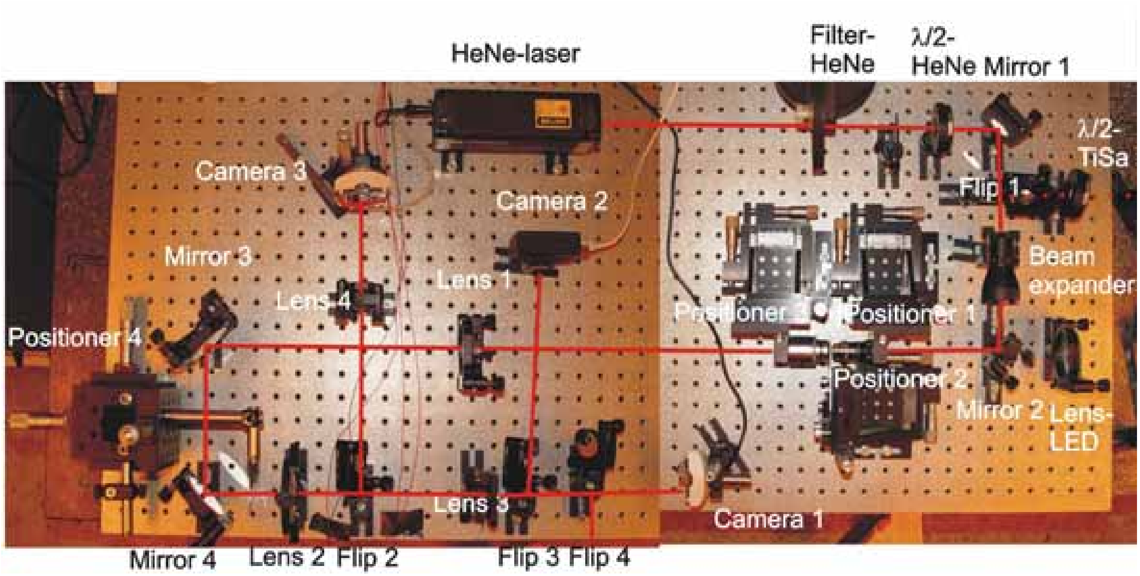

Figure 5.9.: The leakage radiation microscope set up during this work with the components named and the beampath for the HeNe- and the TiSa-laser.

on a screen is possible. The beam is redirected by 'flip 4' onto the screen positioned to observe the Fourier plane. This allows a very fast control of the Fourier plane during adjustment and with this the decision whether the imaged light in 'camera 1' and 'camera 2' is a plasmon or not as discussed later. A photograph of the real LR setup can be seen in figure 5.9.

After the adjustment of the LR setup it is tested if really the LR of SPPs can be seen. For the following investigations the HeNe-laser is used until mentioned otherwise. The first test performed is the polarization dependence of the detected light. The polarization of the laser beam is adjusted by the $\lambda/2$ plate (see figure 5.8). The polarization direction of the laser beam is identified by putting a glass plate into the beam under the Brewster angle, detecting the reflection minimum from the glass plate. A single polymer voxel on the gold surface (which is shown in figure 5.10 on the top left image) is adjusted below the focus of the laser beam. The direction vertical in all following pictures is defined as 0^o (figure 5.10 middle left), while the horizontal polarization is 90^o (figure 5.10 bottom left).

In these images the polarization direction and the points for the intensity measurement are marked. In the middle left image the measurement area for the vertical intensity is illustrated, while the bottom left one shows the horizontal measurement area. For polarization directions from 0^o to 180^o in 10^o steps the intensity of the light is measured at the points shown on the left middle and bottom. The measured intensities are plotted over the polarization angle resulting in figure 5.10 on the right. It can be seen that the measured intensity is depending on the polarization of the laser beam and that the maximum is detected in the direction of polarization. This indicates that the LR of SPPs is measured. Nevertheless, this is no proof for the presence of SPPs, because their could be also scattered light showing such a polarization dependence. To decide whether a SPP or scattered light is present the Fourier plane is imaged. In figure 5.11 the Fourier planes for 0^o and 90^o polarization

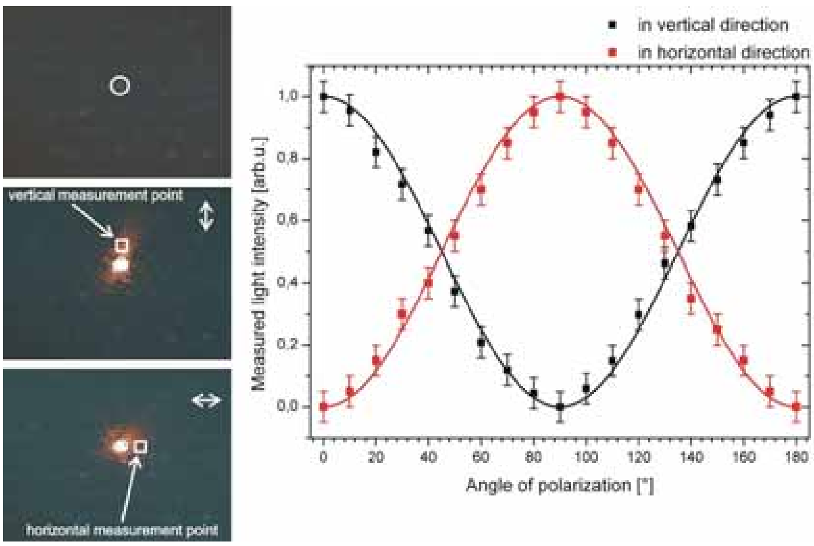

Figure 5.10.: The polarization dependency of the light excitation at a single polymer voxel. The single polymer voxel without the laser is shown in the top left inside the white circle. The emitted light is detected depending on the polarization direction as seen for 0^o (vertical) polarization (middle left) and 90^o (horizontal) polarization, respectively. The polarization direction is indicated as white arrow. The measured intensity shows a clear maximum along the polarization direction (right).

are shown.

As can be seen from this figure the exciting laser beam shows up as a bright spot in the middle of the non Fourier filtered images (this spot can be and is in most of the following images removed by Fourier filtering), while also half-moon like sickles are appearing in the direction of polarization. These sharp half-moons are representing the SPPs in the Fourier plane. The sharp contours of the half-moons are a clear evidence for SPPs, while scattered light would give a more washed out ring around the exiting laser spot. To distinguish between SPPs and scattered light the Fourier plane is examined in all following investigations even if this is not explicitly mentioned. With the polarization dependency and the half-moon appearance in the Fourier plane it is certain that SPPs are imaged.

After the excitation of SPPs on a single polymer voxel, the same is demonstrated on a straight line. For this the polarization is chosen perpendicular to the line and the focal position P_i is changed perpendicular to the metal surface. The parameter i gives the distance of the focus from the metal surface in μm with positive above and negative algebraic sign below the surface. The structure and different focussing can be seen in figure 5.12. The reason for the different excitation is explained in figure 5.13.

With the focussing above the surface the wavefront of the exciting laser beam is concave and the beam divergent at the structure. This results in divergent SPPs as seen in figure 5.12 for positive distances. For P_{20} it seems that a plane wave is excited. This is based on the fact that the wavefront is nearly parallel over the whole image area for this focussing. For P_0 the focus is on the metal surface, resulting in a

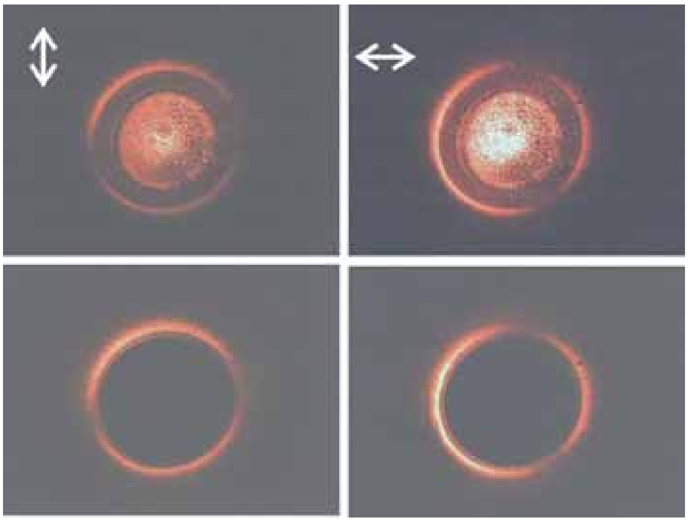

Figure 5.11.: The Fourier plane of the excitation at a single polymer voxel for 0^o (left) and 90^o (right) polarization angles without (top) and with Fourier filtering (bottom). SPPs are only excited along the polarization direction. The images show the corresponding Fourier planes to the images for 0^o and 90^o polarization direction in figure 5.10. The polarization direcetion is indicated as white arrow.

divergent SPP beam. By focussing below the metal surface the wavefront is curved convex and the excited SPPs are focussed. The focussing depends on the distance between the focus of the exciting laser and the metal surface. To sum it up the wavefront curvature of the exciting laser beam is transferred to the SPP beam.

After the demonstration of excitation and detection of SPPs on a polymer surface defect SPPs are investigated inside dielectric waveguides. For this a straight dielectric line on a gold layer is investigated. As seen in figure 5.14 different modes are possible inside a dielectric line.

In this figure the left column shows the image plane without Fourier filtering and with back light illumination, while in the middle one the same images are shown with a previous Fourier filtering. The right column represents the corresponding Fourier plane. In each row the polarization direction is marked by a white arrow. The two top rows show the excitation of scattered light, while the two bottom rows show this for SPPs. The difference can be seen already in the image plane. For the excitation point used in the two upper images the light detected inside the waveguides is more intense with the polarization direction perpendicular to the propagation direction. This indicates the presence of optical modes. The excitation point used in the two lower images shows another polarization dependence. The light detected inside the waveguide is more intense with the polarization parallel to the the propagation direction than perpendicular to this. This points to the presence of SPPs, but is again no proof for SPPs because also light can show this polarization dependency. Nevertheless, for both excitation points light from the waveguide can be detected for both polarization directions. Depending on the shape of the end of the waveguide the excitation efficiency for optical and plasmon modes varies. For most cases the excitation of plasmons can be optimized by varying the laser

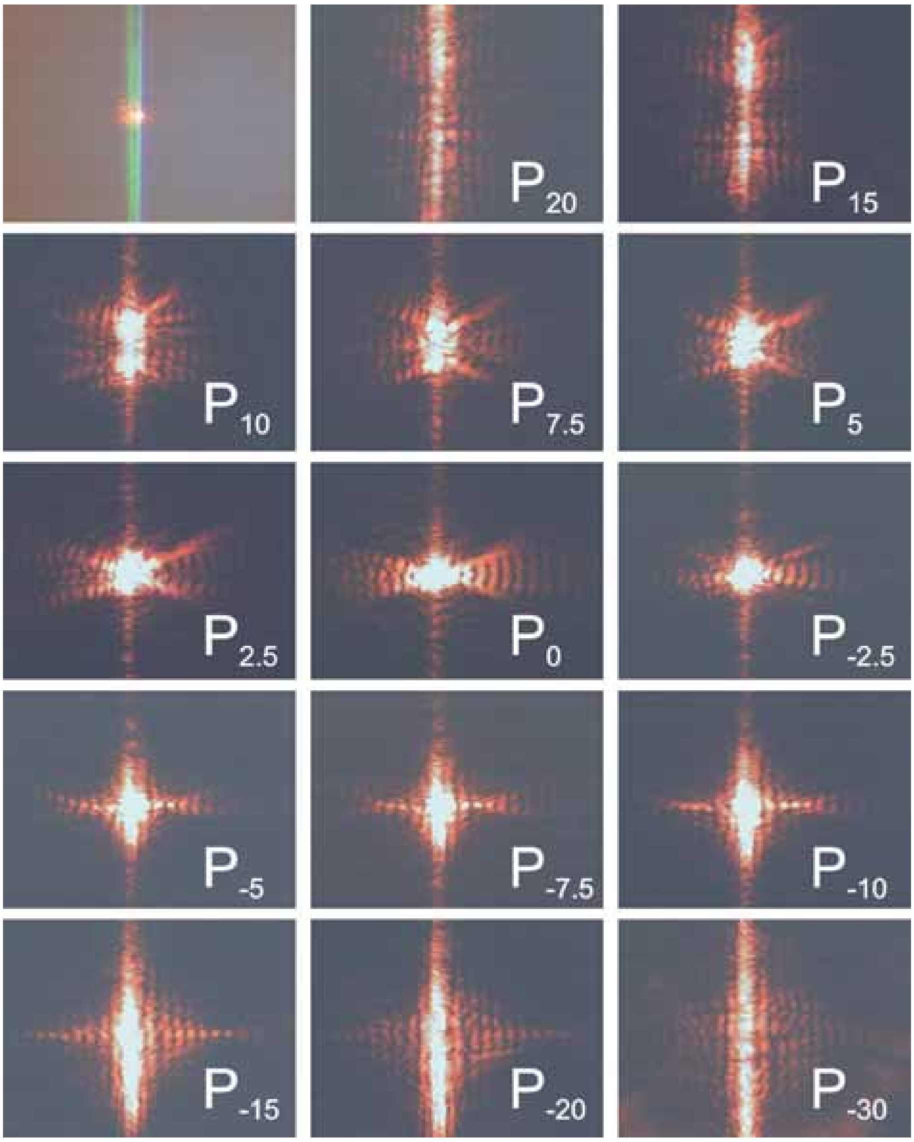

Figure 5.12.: The excitation of SPPs on a line defect. The structure with the exciting laser spot for P_0 is shown on the top left, while the other images present different focus heights above or below the gold surface as shown with the parameter P_i. The polarization is perpendicular to the line (horizontal in the images).

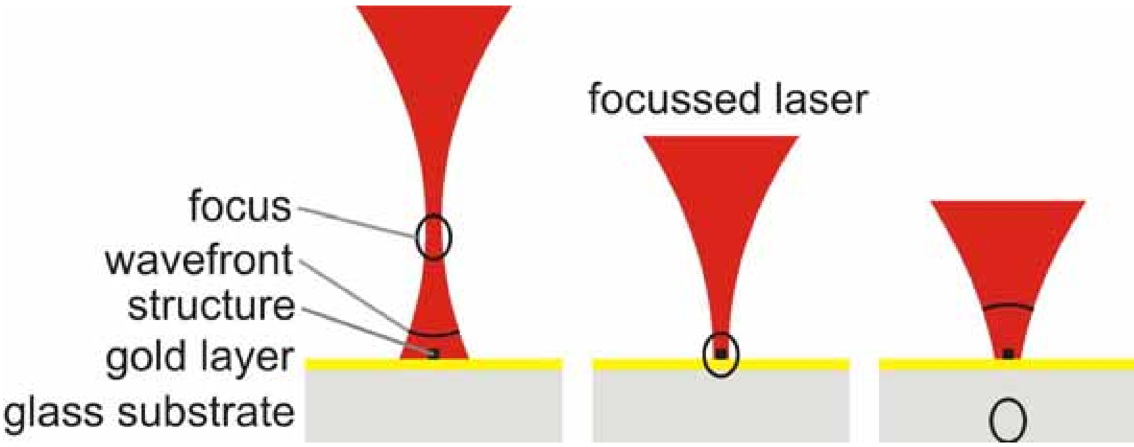

Figure 5.13.: The principal of exciting SPPs with different focussing on a dielectric line, with the focal position and the wavefront of the exciting beam. The focussing above (left), at (middle) and below (right) the metal surface.

beam focussing and the excitation position, while the scattered light is minimized. Although the minimization of scattered light is possible, it is not possible to suppress its excitation completely. This can be seen in the image plane by the fact that for both polarization direction, along and perpendicular to the waveguide, light can be detected from the waveguide. In the Fourier plane the presence of SPP and optical modes is even more obvious. Especially in the second top row of figure 5.14 the SPPs propagating along the polarization direction outside the waveguide can be seen as two clear half moon like rings. These rings appear also in both images with the polarization direction parallel to the waveguide and verify SPPs propagating inside the waveguide. Nevertheless, the washed out regions in the Fourier plane are generated by optical modes. This proofs that in all images optical modes are present. To investigate the electro-magnetic field inside the waveguide and the possibility of the complete suppression of optical modes further simulations of this configuration are performed.

5.1.3. Simulations of DLSPPWs for different wavelengths

As seen in the previous section SPP and optical modes can be excited in DLSPPWs. As shown in chapter 3 a $600 \times 600\,nm$ DLSPPW is working as a single mode waveguide and not supporting any optical modes for a wavelength of $1.55\,\mu m$. For $632\,nm$ one can expect a waveguide of this size working as multi mode. This is confirmed by the results presented in figure 5.15.

A straight waveguide of $600 \times 600\,nm$ is simulated with the program *FullWave* for a wavelength of $632\,nm$. The design for these simulations seen from the top is shown in figure 5.15 on the left. The first SPP mode is excited and the power distribution inside the waveguide is observed at different positions as shown in the middle and right image after a propagation distance of $0\,\mu m$, and $3\,\mu m$. As seen from these cross sections the intensity maximum is at the metal-dielectric interface for excitation and shifts to the upper edge of the dielectric after some micrometer propagation distance.

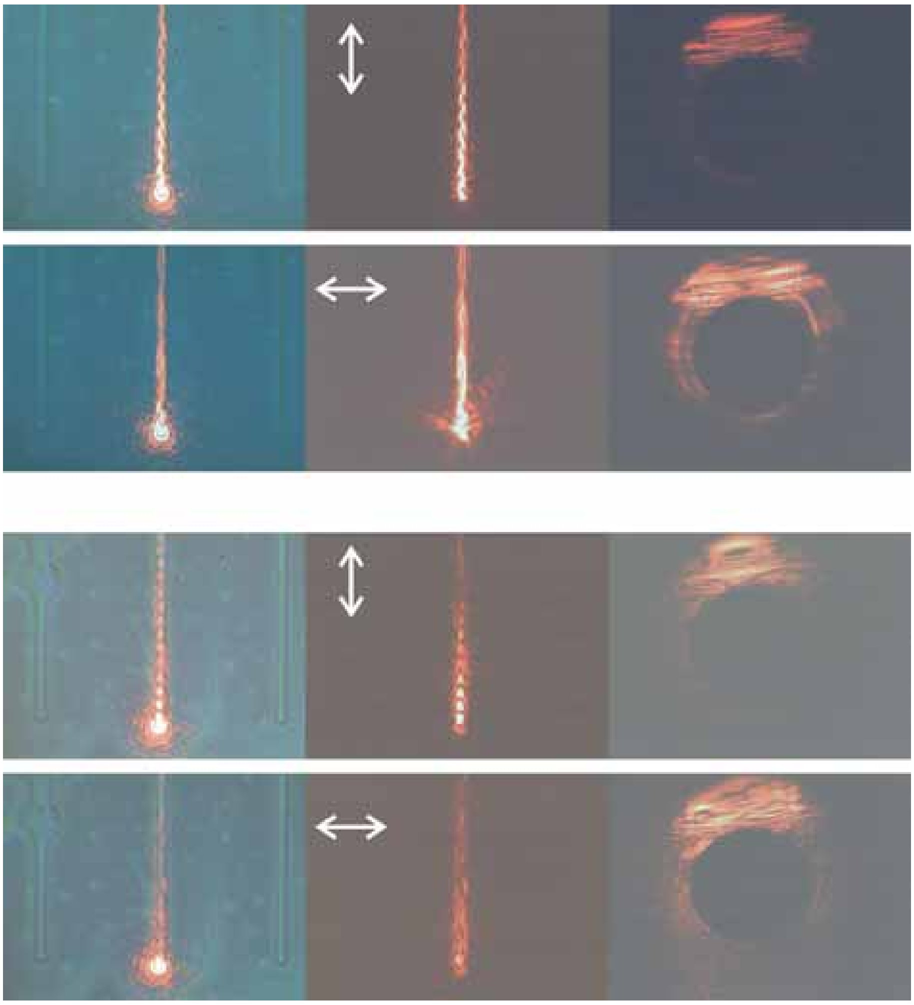

Figure 5.14.: The dependency of the exited modes in a dielectric line on gold depending on the excitation position and on the polarization of the laser beam. The left column shows the image plane with the exciting laser beam, while in the middle column the Fourier filtering is applied and the right one represents the Fourier plane of the images above. In each row the polarization direction is represented by a white arrow.

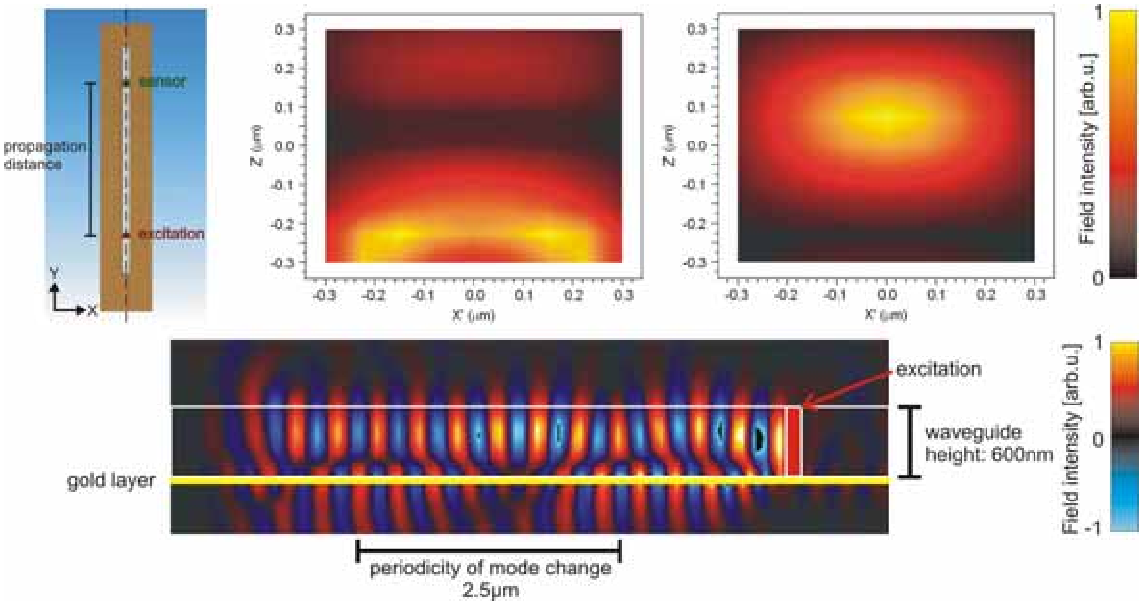

Figure 5.15.: A straight waveguide of $600 \times 600\,nm$ simulated for $632\,nm$ excitation wavelength. The design seen in top view (left), the power distribution at the excitation (middle) and after $3\,\mu m$ propagation distance in the waveguide (right). The bottom image shows the view from left onto the cut, seen as dashed line in the design, and illustrates the intensity of the electro-magnetic z-component inside the waveguide.

The electro-magnetic field inside the waveguide shows a beating between optical and plasmonic modes. This is also observed in the cross section of the waveguide shown in figure 5.15 bottom. This cross section shows the z-component of the electrical field along a cut through the middle of the dielectric line perpendicular to the metal (dashed line in the design in figure 5.15 top left). As seen from this the intensity maximum of the field changes its z-position from the metal-dielectric interface to the top of the waveguide and back. This indicates the energy transfer from the SPP modes with the intensity maximum at the metal-dielectric interface to optical modes with the intensity maximum inside or at the top of the waveguide. The periodicity of the change from the SPP mode to the optical mode and back is $2.5\,\mu m$. To suppress this transformation between SPP and optical modes the height of the waveguide can be reduced. As seen in the calculations in chapter 3 the higher order modes can be inhibited by reducing the width and height of the waveguide below a critical dimension.

First of all the optical modes should be suppressed. For this reason the propagation of the electro-magnetic field in the waveguide is simulated for different waveguide heights and the power distribution inside the waveguide is observed.

In figure 5.16 a change in the height of the intensity maximum from the metal-dielectric interface to the upper part of the waveguide and back for waveguide heights of $600\,nm$ (top images), $300\,nm$ (second row images) and $200\,nm$ (third row images) is observed. This is reduced with less high waveguides and for $150\,nm$ (bottom images) height this change is not observed any more. The power distribution in figure 5.16 is shown inside the waveguide. The gold layer is at the lower end of

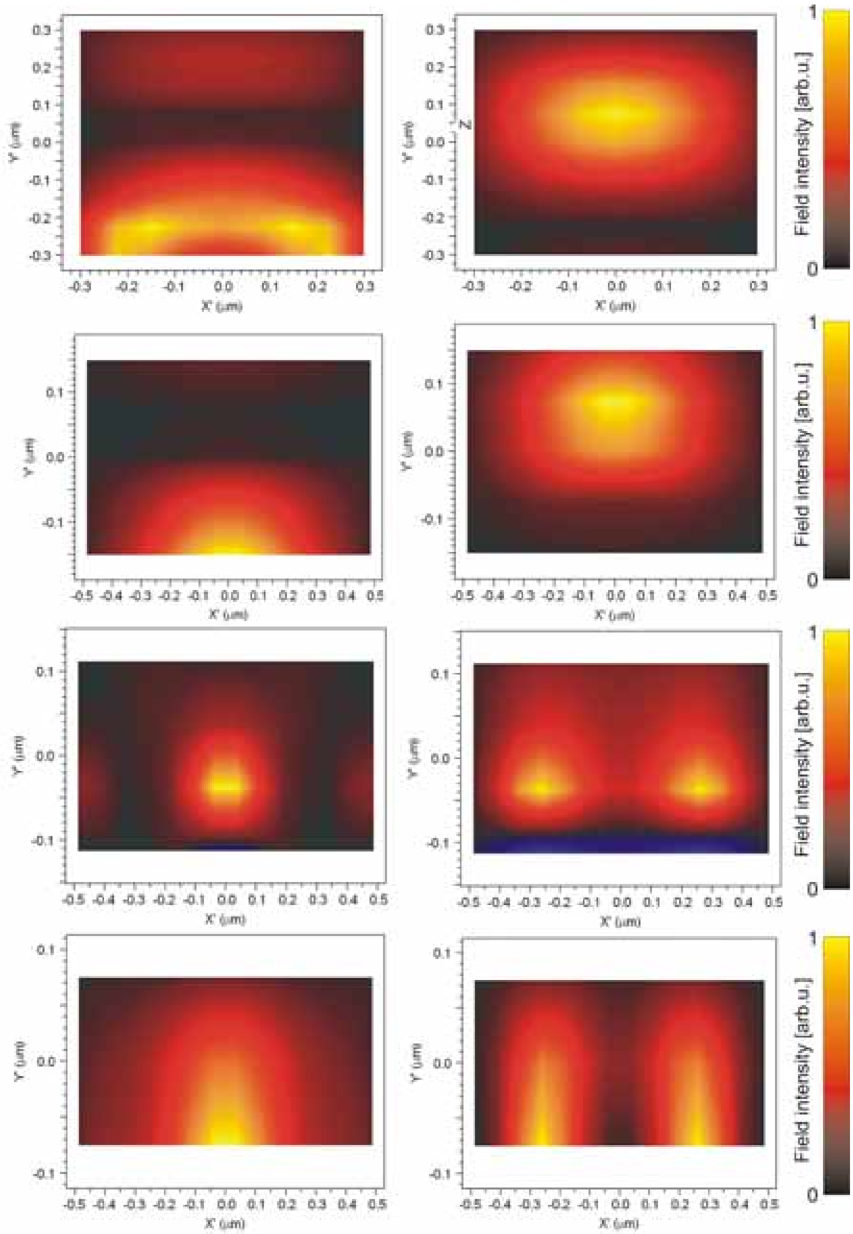

Figure 5.16.: The power distribution at different positions inside dielectric waveguides of different heights for a waveguide height of 600 nm (top), 300 nm (second row), 200 nm (third row), and 150 nm (bottom row). All waveguides have a width of 600 nm.

Wavelength $[nm]$	**Height** $[nm]$	**Width** $[nm]$	**Propagation length** L_0 $[\mu m]$
632	150	300	1
800	300	400	4
900	325	500	6
1000	400	600	8
1550	600	600	41

Table 5.2.: The critical dimensions for the maximum height and width of single mode DLSPPWs and the propagation length inside these waveguides.

the images shown. Power distributions with the intensity maximum at the lower edge of the images are judged as plasmonic while the intensity maximum in the upper part of the waveguide are optical modes. Simulations in between $150\,nm$ and $200\,nm$ height have also been performed, but are not presented here with images. It is observed that the optical modes become lossier with less waveguide height and for $150\,nm$ height no optical mode can be excited anymore. So for $150\,nm \times 600\,nm$ DLSPPWs no optical modes are observed, but the power distribution changes during the propagation. This is seen in figure 5.16 in the bottom images, where the power distribution inside the $150\,nm \times 600\,nm$ waveguide is shown. The left image at excitation shows a power distribution corresponding to the first order SPP mode. On the right image, after $1.5\,\mu m$ a power distribution corresponding to higher order SPP modes can be seen. After a further propagation of some micrometers this higher order mode power distribution transfers back to the first order SPP mode. To suppress also the higher order SPP modes the width of the waveguide is varied. From this variation the upper limit for a single mode waveguide width is calculated as $250\,nm$. These results show that for $632\,nm$ wavelength a single mode waveguide has to be smaller than $150\,nm \times 250\,nm$. With this wavelength and this small waveguide the propagation length of SPPs is calculated as described in chapter 3.4.3 from these simulations to $L_0 = 1\,\mu m$. Besides the drawback of very small propagation length such small waveguides are very difficult to fabricate. For this reason the simulations are redone for $800\,nm$, $900\,nm$ and $1000\,nm$ wavelength. From these the critical dimensions for an only SPP supporting single mode waveguide are calculated. The results of these calculations are summarized in table 5.2.

These simulations show, that the critical dimensions of single mode DLSPPWs and the propagation length inside these waveguides become smaller with the wavelength. For this reason the longest wavelength available for experiments is used for all following investigations to achieve a propagation length as long as possible. For this reason the *Tsunami* laser (as introduced in chapter 2) is adjusted to the leakage radiation microscope as seen in figure 5.8. It is a tunable laser system with a wavelength ranging from $750\,nm$ to $830\,nm$ and capable of working as fs- or cw-laser. The wavelength used for all following simulations and experiments is $800\,nm$ from the *Tsunami* in cw-operation mode. The polymer waveguide height is $300\,nm$ if not mentioned otherwise. To achieve a single mode DLSPPW the structural width has to be smaller than $400\,nm$. The problem is, that the resolution of 2PP on metallic surfaces is limited to about $800\,nm$ due to the reflections arising from the surface.

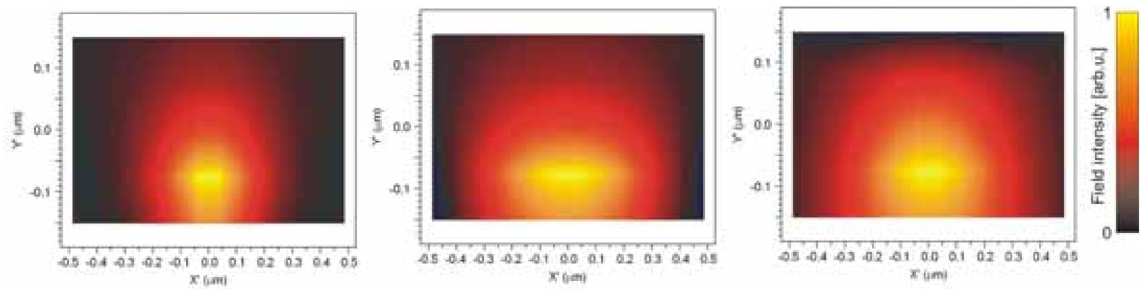

Figure 5.17.: The power distribution inside a $300\,nm \times 1\,\mu m$ DLSPPW at excitation (left), and after $5\,\mu m$ (middle) and $10\,\mu m$ (right) propagation inside the waveguide.

Variable	**Value**
Edge-Gridsize	$5\,nm$
Bulk-Gridsize	$75\,nm$
Timestep	$0.05/0.1 \cdot (Edge - Gridsize)$
Wavelength	$800\,nm$
Width of waveguide	depending on fabricated structure
Height of waveguide	$300\,nm$
Gold thickness	$50\,nm$
Refractive index of polymer	1.58
Refractive index of substrate	1.52
Refractive index of gold	0.1814
K value of gold	5.1267

Table 5.3.: Parameters for all following experiments and simulations of DLSPPWs if not mentioned otherwise.

Because of this experiments and simulations are made for multi mode SPP waveguides with a width of about $1\,\mu m$. The properties of a $300\,nm \times 1\,\mu m$ waveguide are simulated and the different SPP modes are reflected in the intensity distributions shown in figure 5.17.

This figure shows the power distribution inside the waveguide at the excitation (left), and after $5\,\mu m$ (middle) and $10\,\mu m$ (right) propagation distance. An intensity transfer from one mode to the other and back can be seen. For such a waveguide the propagation length is with $L_0 = 11\,\mu m$ larger than in a $300\,nm \times 400\,nm$ single mode waveguide. For the following simulations performed in this chapter the parameters shown in table 5.3 are used if not mentioned otherwise.

During these simulations it has been recognized that SPPs guided inside the DLSPPWs are cross-talking with SPPs propagating on the back side of the gold surface. This effect is negligible for single mode DLSPPWs, while it becomes important for multi-mode DLSPPWs. The effect on a multi-mode DLSPPW can be seen in figure 5.18.

The E_y component of electro-magnetic field illustrates the change from the SPP on the top of the gold to the one at the bottom and back (top image). The bottom image shows the E_y component of electro-magnetic field $1.2\,\mu m$ below the gold layer. The power, corresponding to the square of the E_y component of electro-magnetic

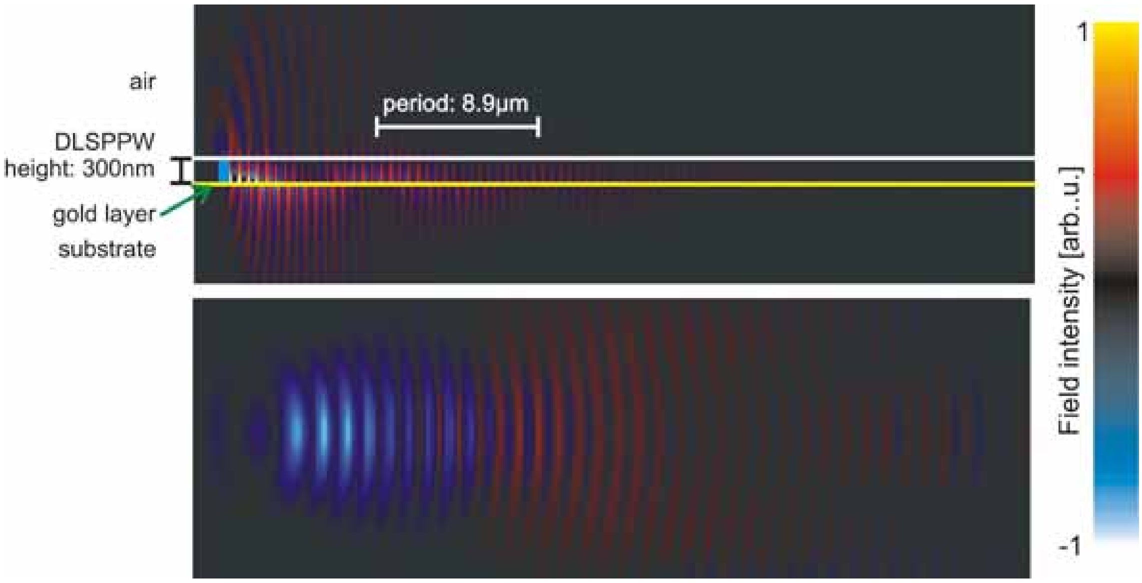

Figure 5.18.: The E_y component of electro-magnetic field seen along a cross-section through the middle of a straight DLSPPW (top). The intensity maximum is clearly seen shifting from the top side of the gold layer to the bottom side and back, pointing out the cross-talk of the SPPs on top and bottom side of the gold layer. The bottom image shows the E_y component of electro-magnetic field measured $1.2\,\mu m$ below the gold layer.

field, will give no pronounced intensity fluctuations corresponding to the cross-talk. Due to this the differentiation between the different SPPs is difficult in experiment and can be neglected. For the simulations this cross-talk plays an important role, because the intensity of SPPs is measured only inside the waveguide. This gave correct results for single mode, but not for multi-mode waveguides. For multi-mode waveguides the intensity has also to be measured on the bottom side to obtain the complete intensity of SPPs.

5.1.4. Excitation of SPP and optical modes in DLSPPWs

After the investigations on polymer voxels, straight dielectric lines, and the modes supported by different DLSPPWs for different wavelengths the polarization dependence inside a dielectric structure is examined. For this the structure in figure 5.19 top left is fabricated and the laser spot is placed on the lower end of the line as shown in the top right.

The images below this show the Fourier filtered image plane (on the left) and the corresponding Fourier plane (on the right). From top to bottom the polarization is rotated from 0^o to 80^o in 20^o steps as indicated by the arrow representing the polarization direction. In the last row also the images for 90^o polarization are shown. As seen in this figure the polarization parallel to the waveguide excites a beam inside the guide showing a smooth divergence after entering the funnel part. Besides this behavior it can be seen that also for a polarization vertical to the waveguide

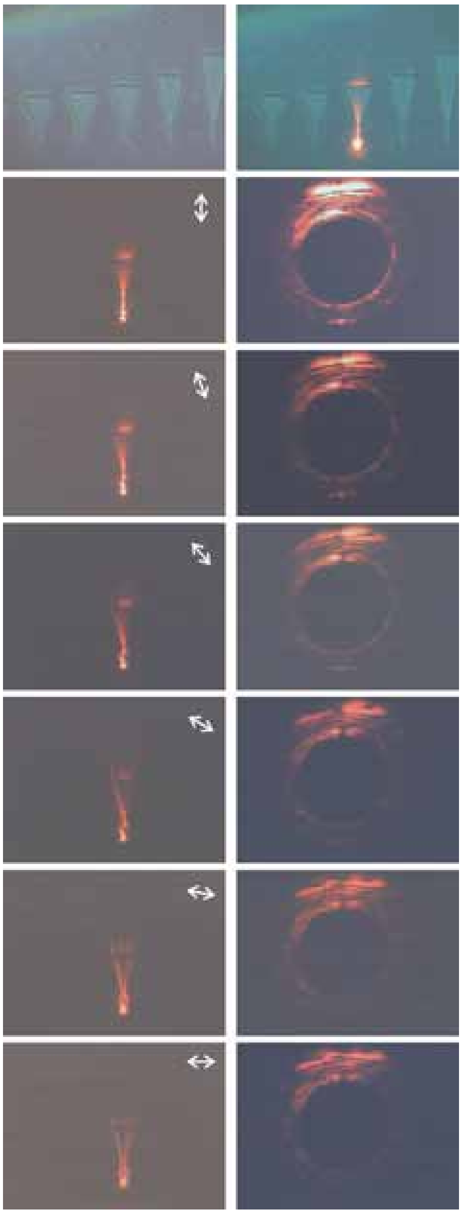

Figure 5.19.: The polarization dependence of SPP excitation inside a dielectric waveguide. On the top left the structure fabricated for these investigations is shown, while on the top right the same image with the exciting laser beam can be seen. Below this the Fourier filtered images for different polarization angles are shown on the left, while on the right the corresponding Fourier plane is imaged. The polarization direction in each row is indicated by the white arrow. SPP excitation is made with the HeNe-laser at 632 nm wavelength in a 500 nm high waveguide.

light is propagating inside the waveguide, which can be identified as SPP in the Fourier plane. This SPPs are excited along the polarization direction and reflected inside the waveguide. When the waveguide opens up to the funnel structure the propagation direction of SPPs is given by the excitation direction and reflections inside the dielectric line resulting in a non smooth divergence, but two main beams propagating inside the funnel. This behavior clearly shows the ability of dielectric lines to work as waveguide for SPPs and the possibility to excite them at the end of such line. Even though SPPs are identified in the Fourier plane as sharp ring, also optical modes arise as larger illuminated area. SPPs and optical modes in the waveguide can be distinguished in the Fourier plane. Optical modes can only arise inside the waveguide. Because of this they are only present in one direction from the exciting point. In comparison to this SPPs can propagate in all directions from the excitation. Because of this the complete ring in the Fourier plane can be identified as SPPs, while the bright area seen in the upper part of the Fourier plane images are optical modes, which provide no complete ring in the Fourier plane. This corresponds very well to the simulations performed in the last section, which have shown that for such waveguide dimensions the SPP and optical modes are cross-talking.

Also when exciting propagating modes at the base of the funnel some interesting investigations can be performed. It can be seen in figure 5.20 that the intensity profile of the LR is modulated (images are made with the HeNe-laser and $500\,nm$ high polymer layer). This modulation could be due to two reasons. First the SPPs could be reflected at the end of the waveguide and interfere with themselves. This can be excluded here, because the modulation also arises for very long funnels and the intensity of modulation remains constant for the whole observation length, what would not be expected for interference with reflected SPPs. The second possibility is the presence of different modes inside the funnel. To proof the theory of different modes one funnel is investigated in more detail. SPPs are excited at the base of the funnel as seen in figure 5.20 top.

In the other images of this figure the image plane (left) and the corresponding Fourier plane (right) are shown. The excitation of modes inside the dielectric is the same for all images, while the Fourier filtering changes. The top images show the mode propagation without Fourier filtering. In the images in the third row from the top the outer ring is blocked in the Fourier plane, while in the bottom row the inner ring is filtered out. From these images the different modes can be divided in the modes with larger (outer) and a smaller (inner) angle of reflected beam. The inner modes are imaged in the third row from the top in figure 5.20. In the middle of the image plane a beam is propagating vertical without any interference pattern. The interferences arising in the lower part of this image on the left and right of this beam are due to the reflection at the walls of the funnel. These reflected beam interferes with the non-reflected, which comes directly from the excitation point. In the bottom row of this figure the outer modes are mapped. These do not show an interference pattern anymore, but three fringes of beams propagating into slightly different directions. With this it is possible to distinguish between different modes propagating inside a DLSPPW. Now the question arises if these modes are SPP or optical modes. As discussed in the previous section waveguides with these dimensions support both kind of modes for $632\,nm$. For this reason the investigations

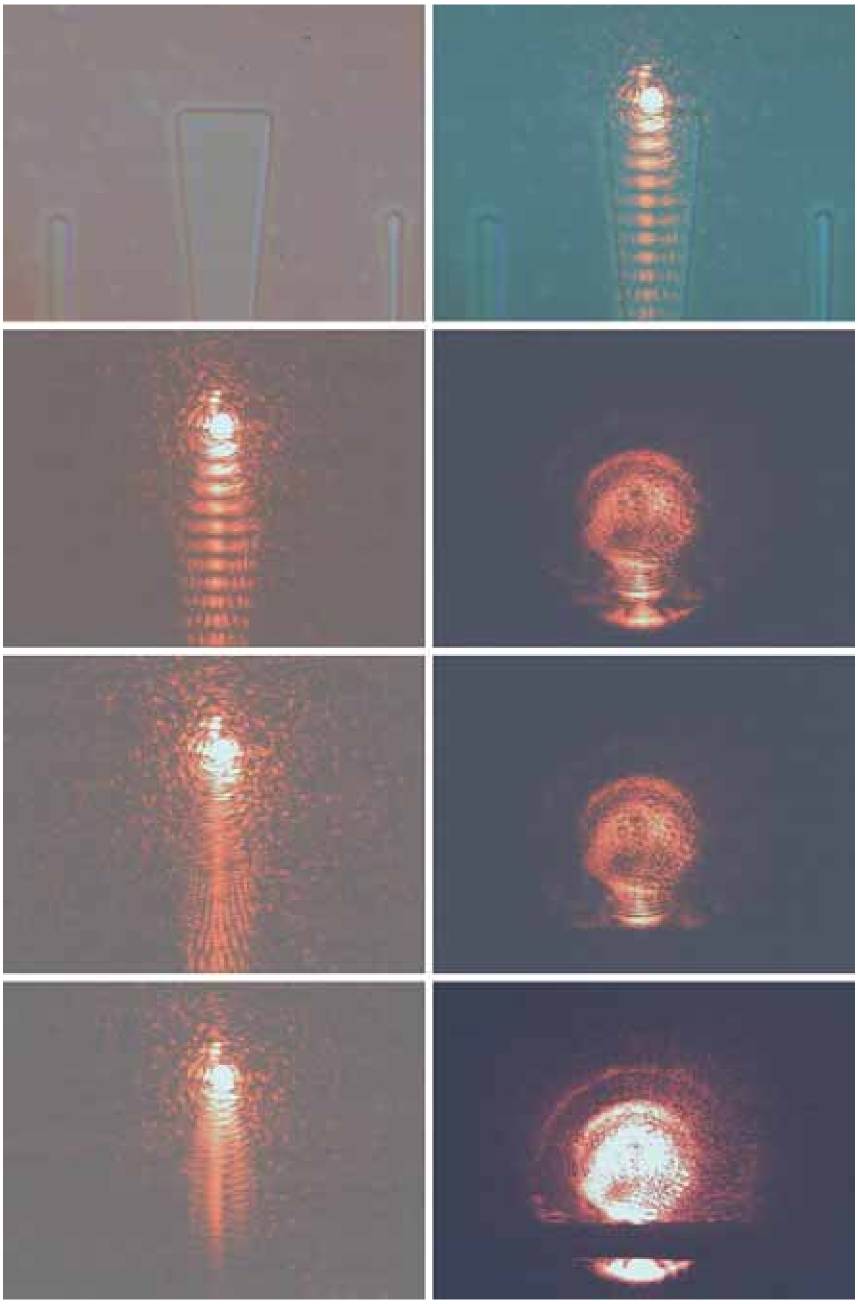

Figure 5.20.: The interference of different modes inside a funnel. The structure (top left) and the excitation of modes at the base of the funnel (top right). The rows below show the image plane on the left and the corresponding Fourier plane on the right. Without Fourier filtering (second top row) the image shows an intensity modulation perpendicular to the propagation direction. With Fourier filtering the outer or the inner ring seen in the Fourier plane the interference vanishes and different propagation patterns are observed. The images have been obtained using the HeNe-laser at 632 nm and a 500 nm high polymer layer.

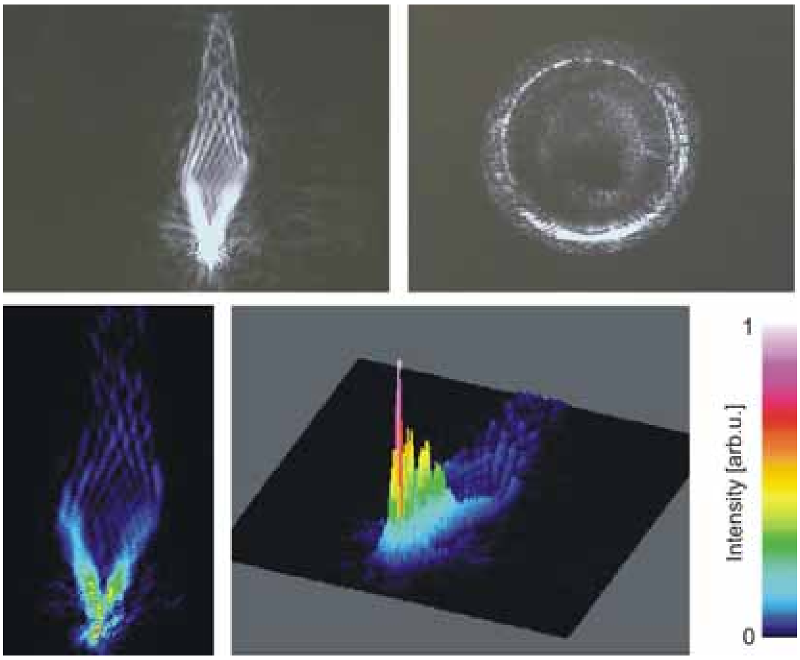

Figure 5.21.: The image plane (top left) and Fourier plane (top right) of a funnel with $10\,\mu m$ base width and 80^o angle imaged with the 'NC-305 webcams'. The lower images show the same funnel grabbed with the 'WinCamD-UCD 12': the intensity profile (bottom left) and the 3-dimensional illustration (bottom right) showing the intensity as height modulation.

are redone with $800\,nm$ wavelength and $300\,nm$ polymer height supporting only SPP modes. The results of these investigations are shown in figure 5.21. The structure and excitation used are the same as in figure 5.20, but with the funnel base at the bottom of the image and the SPPs propagating to the top.

The difference between the results obtained with the HeNe-laser at $632\,nm$ and the TiSa-laser at $800\,nm$ is the absence of the interference pattern perpendicular to the propagation direction in the second measurements. This is explained by the suppression of optical modes in the $300\,nm$ height structures for $800\,nm$ excitation wavelength as simulated in the previous section. This shows that the outer modes seen with the $632\,nm$ excitation are optical modes, while the inner modes are SPPs. In this way the interference between optical and SPP modes is observed and proofed for the $632\,nm$ laser.

After demonstrating the ability to differ between optical and SPP modes, the question arises if the excitation efficiency of SPPs inside dielectric waveguides can be increased. For this the funnel is used to guide SPPs, which are excited at the wall of the funnel perpendicular to the waveguide, into the straight waveguides. The structure can be seen in figure 5.22 showing the base width w_B and the funnel angle α_F.

The base width is varied from $1\,\mu m$ over $3\,\mu m$ and $5\,\mu m$ to $10\,\mu m$, while the angle is changed in 5^o steps ranging from 30^o to 85^o. Some examples images of these measurements are shown in figure 5.23 with the base width and funnel angle.

From these investigations one can see that on the one hand funnels with large

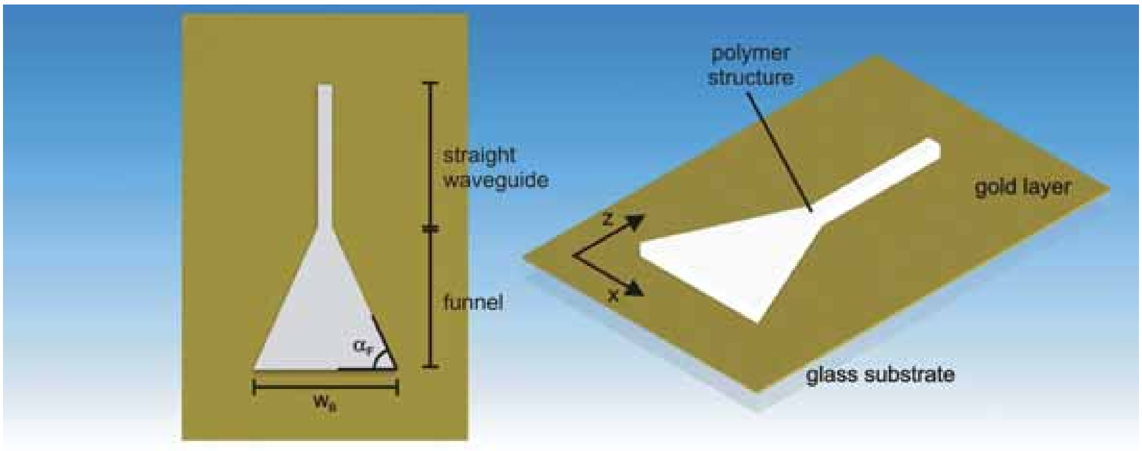

Figure 5.22.: The design of the funnel structure with a short waveguide attached. The base width w_B and the funnel angle α_F are shown in the top view (left), while the coordinate system used can be seen in the isometric view (right).

angles are guiding the SPPs very well, while small angle funnels show a lot of scattering out of the funnels and especially at the change to the waveguide. On the other hand funnels with large angles are longer than with small angles and with this lead to a longer propagation length and higher Ohmic losses. Also one has to take into account the limited image size of the LR microscope of about 60 μm to 110 μm. Because of this the funnels should be not longer than 30 μm to be left with enough space for DLSPPW structures for investigation. Also the comparison of excitation with a funnel and in a waveguide without a funnel shows about the same excitation efficiency. Furthermore, the funnel increases, depending on the size, the fabrication time drastically. Due to this the following structures are again build without funnels.

Besides the fact, that the funnels do not provide an increase of excitation efficiency it could be observed during these investigations that the excitation efficiency is very sensitive to the parameters like focussing of the laser beam, the beam position and the structure used for excitation. For the structure the most important condition for the good generation of SPPs is a sharp etch. During the experiments it pointed out that the sidewall or defect should be a 90^o step like structure for the most efficient SPP excitation. On structures showing not a sharp etch due to fabrication defects the excitation has been less efficient or even impossible. The focussing plays a similar important role for excitation. On a straight line the excitation perpendicular to this line is most efficient for a very good focussing as seen in figure 5.16. The best excitation with sharp focussing is also observed for the excitation at the end of a DLSPPW targeting the propagation inside the waveguide. One could also think of other structures used for SPP generation. One possibility would be to adjust the structure for the beam profile of the laser. For this reason curved lines with different curvature radius ranging from 1 μm to 10 μm in 1 μm steps have been fabricated. SPPs are excited on these structures and the focussing of the laser beam is adjusted in respect to the best possible excitation for any curvature radius. The best possible excitation conditions for some example curvatures can be seen in figure 5.24.

These investigations show that the highest efficiency for the excitation at a curved

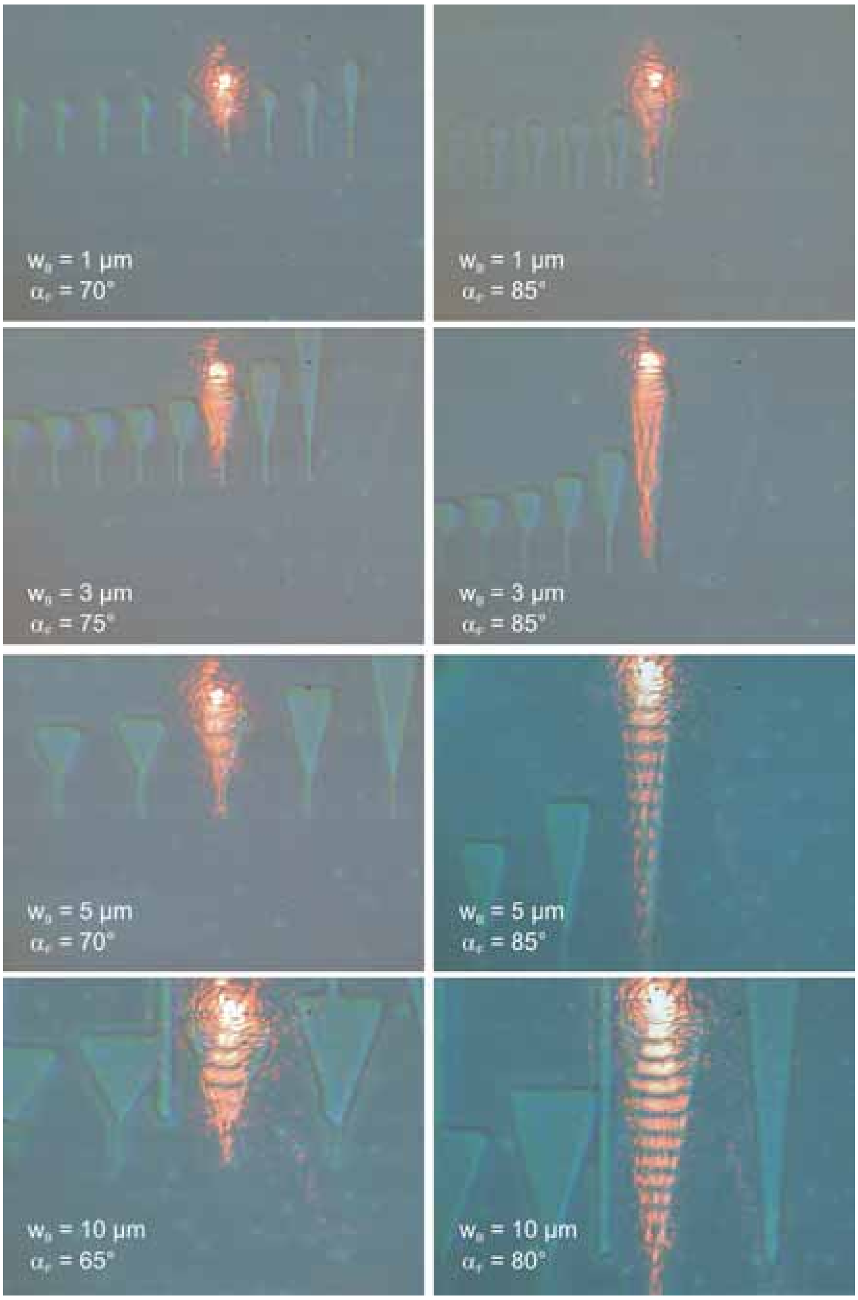

Figure 5.23.: Some funnels with different parameters for the base width w_B and the funnel angle α_F with SPPs excited at the base of the funnel and propagating into a $5\,\mu m$ long waveguide. Excitation wavelength is $632\,nm$.

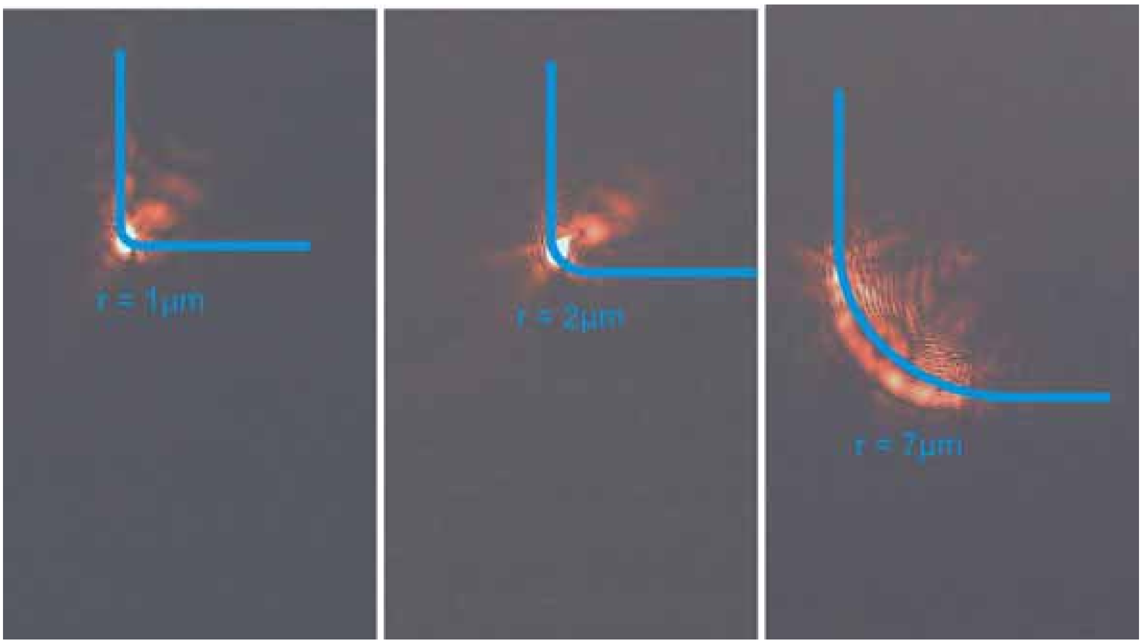

Figure 5.24.: The excitation of SPPs at curved structures with different curvature radius. For any curvature the focussing of the laser beam was adjusted for the highest excitation efficiency. The structures have a curvature radius of $1\,\mu m$ (left), $2\,\mu m$ (middle), and $7\,\mu m$ (right).

structure is achieved with the smallest curvature radius of $1\mu m$ and the best focussing of the exciting laser. This can be understood by the examination of the laser power distribution. For all excitations the same laser power is applied, but the diameter of the laser beam must be adjusted to the curvature of the structure to achieve the highest possible power in the focus of the structure. This results in larger beam diameter for larger curvature radii. By expanding the beam the power is distributed over a larger area and with this the power applied directly to the structure is reduced resulting in less intense SPPs. Because of these investigations it becomes clear that a small curvature at the entrance of a DLSPPW is the easiest and effective excitation scheme. Due to the round shape of the focussed beam applied for 2PP all waveguides have a round shaped end with the diameter the same as the width of the waveguide. For this reason all waveguides provide a very good excitation of SPPs propagating inside the waveguide and this excitation scheme is used in the following investigations if not mentioned otherwise.

5.1.5. The effective refractive index of DLSPPWs

For the guiding of SPPs it is interesting to know the effective refractive index n_{eff} of the DLSPPWs. The effective refractive index is defined as the difference between the refractive index for SPPs propagating on the interface between a metal surface and air (n_{met}), and for SPPs on the interface between a metal surface and a dielectric waveguide on the top (n_{die}). It can be calculated by

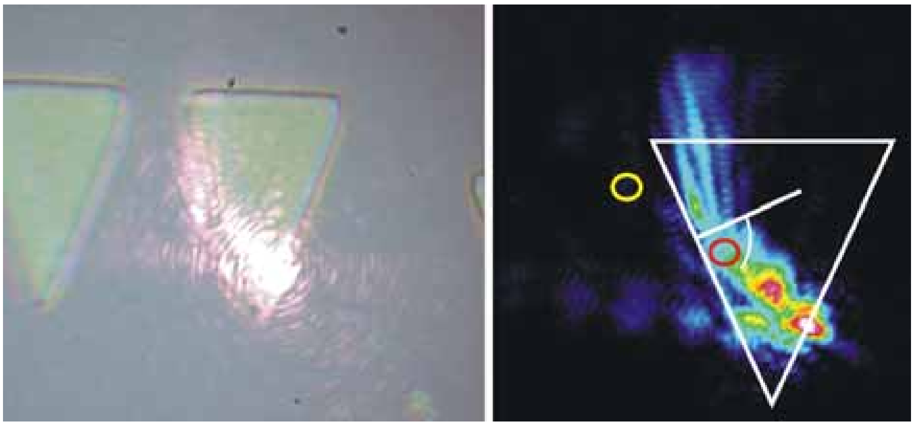

Figure 5.25.: The reflection of SPPs at the sidewall of a funnel. The excitation of SPPs at the funnel structure (left) and the Fourier filtered image (right) for the measurement of transmission for an angle of 60^o. The funnel is outlined white in the right image with the normal on the sidewall of the funnel corresponding to 0^o. The two measurement points are shown as red (intensity in the funnel) and yellow circle (intensity outside of the funnel).

$$n_{eff} = \frac{n_{die}}{n_{met}}. \tag{5.1}$$

The effective refractive index is determined by the refractive index of the polymer and the geometrical characteristics of the waveguide. The effective refractive index is determined here in three different ways: first by the reflection angle of SPPs propagating from inside of a dielectric structure to the outside, second by the interference of reflected SPPs inside a DLSPPW, and last from the comparison of the Fourier plane of free propagating and guided SPPs.

To investigate the effective refractive index by reflection and transmission at the interface between a dielectric waveguide and an uncovered metal surface, figure 5.25 shows the excitation of SPPs at the side of a funnel (left). The plasmons propagating to the upper right are partially reflected, while the ones to the lower right are transmitted by the sidewall of the funnel (right image).

Funnels with different base widths and angles are build and the reflection and transmission for different angles between the SPP beam and the wall are measured. The resulting graph of reflection is shown in figure 5.26.

The measurements are fitted with the Fresnel Formula (from [GV93])

$$R = I_1 + I_0 \left(\frac{n_{eff}^{-2} \cos(\alpha) - \sqrt{n_{eff}^{-2} - \sin(\alpha)^2}}{n_{eff}^{-2} \cos(\alpha) + \sqrt{n_{eff}^{-2} - \sin(\alpha)^2}} \right)^2, \tag{5.2}$$

for the reflection of the SPP. Here α_T is the angle of incident, I_0 is the incoming power, I_1 is an offset and n_{eff} is the effective refractive index. The fitting parameters are calculated to be $I_0 = 0.285 \pm 0.3$, $I_1 = 0.229 \pm 0.022$ and $n_{eff} = 1.062 \pm 0.015$.

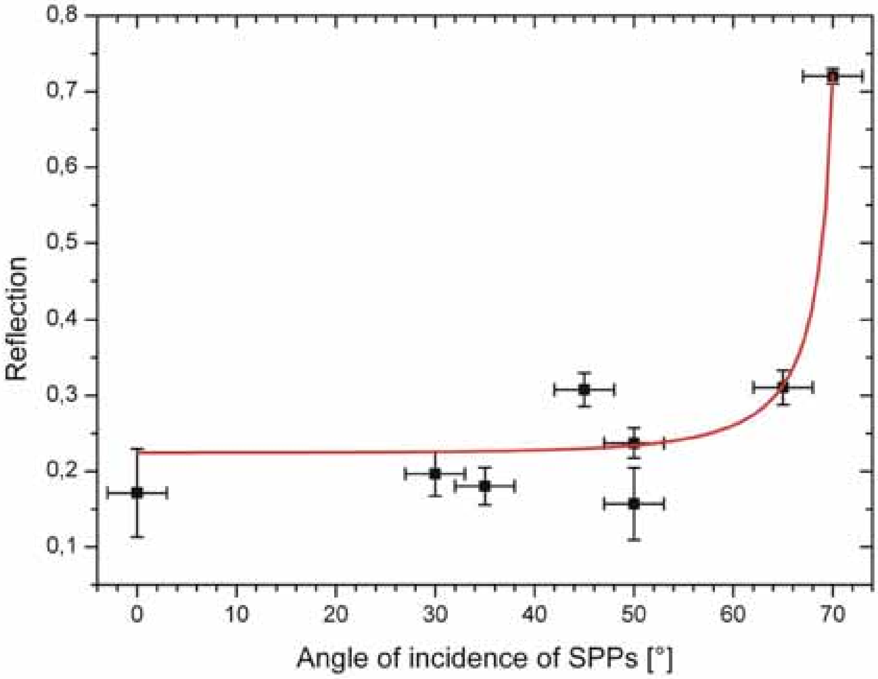

Figure 5.26.: The reflection at the side wall of a dielectric structure depending on the angle between the normal of the wall and the incident beam. The total reflection is reached for an angle of about 72^o.

The failure of this method is relatively high, because the transmission can change by choosing other positions for the measurement, due to the complicate structure of the LR. Also the angle of incident can only be measured with an accuracy of about $\pm 5^o$, because of the bright and divergent SPP beam. Because of this the effective refractive index calculated here should be handled with care.

The second method used to determine n_{eff} is the interference arising at the end of a DLSPPW due to the reflected SPPs. The resulting interference pattern of such reflection can be seen in figure 5.27.

The field of view for the immersion oil microscopy objective used which is imaged to the camera is about $138\,\mu m$ by $138\,\mu m$. The camera has a pixel number of 1024 horizontal and 1024 vertical. This gives the best possible resolution in this configuration to $135\,nm$ theoretical achievable with the camera.

Because of this in the LR intensity profile shown in figure 5.27 right appear steps, which are corresponding to the camera resolution. Nevertheless, the interference periodicity can be fitted by

$$I(y) \;=\; I_0 + I_1 \sin\left(\pi(y - y_c)/w\right) + I_2 \exp\left(-y/L_0\right), \tag{5.3}$$

with I the measured LR intensity, I_0 the excitation intensity, I_1 and I_2 intensity factors for the periodic and exponential function, y_c a phase shift, w the periodicity and y the coordinate. This equation consists of a periodic part, given by the sinus function and representing the interference, and an exponential decay arising from the losses of the guided SPP. In principal also the reflected SPP from the end of the waveguide has to be taken into account as wave propagating in the opposite direction. This can be neglected due to the very low reflection and with this the very low intensity of this wave. The fit in figure 5.27 with equation 5.3 gives a propagation length $L_0 \;=\; 11\,\mu m \pm 0.4\,\mu m$ and a periodicity of $w \;=\; 419\,nm \pm 5\,nm$. From this periodicity the effective refractive index n_{eff} seen by the SPPs can be calculated by [GV93]

$$a_I \;=\; n_{eff}\lambda_L/2, \tag{5.4}$$

with a_I the interference periodicity and λ_L the wavelength of the laser beam. With this the effective refractive index is calculated to $n_{eff} \;=\; 1.048 \pm 0.012$.

The Fourier plane provides the third possibility of retrieving the effective refractive index. The left part of figure 5.28 shows the propagation of SPPs on a pure metal surface excited on a point surface defect, while the right one is dedicated to guided SPPs inside a straight waveguide. The top images present the propagation of the SPPs, the middle ones the corresponding Fourier plane with the exciting laser beam and the bottom ones with Fourier filtering applied. For the propagation on a pure metal surface the SPPs are divergent and for this reason they appear as a half moon

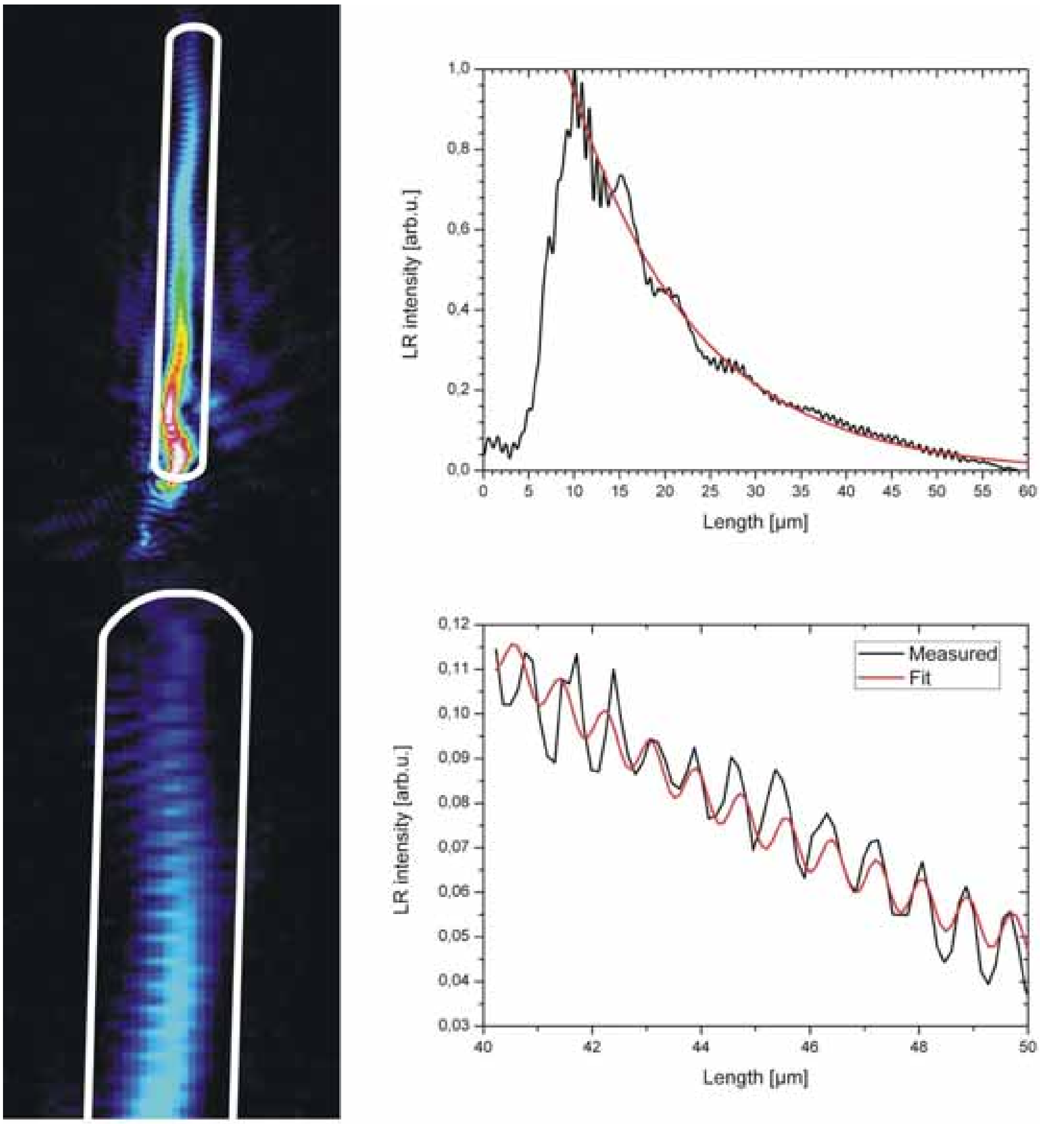

Figure 5.27.: The reflection at the end of a straight waveguide. The contour of the waveguide structure is outlined as white line in the left images. SPPs are excited at the bottom end of and propagate inside the waveguide (top left image). They are partially reflected at the waveguide end (magnification bottom left).The intensity of LR decreases exponentially resulting in a propagation length of $L_0 = 11\,\mu m$ as seen in the intensity cross-section along the middle of the waveguide (top right image). The interference has a periodicity of $425\,nm$ as seen in the magnification of of the LR intensity cross-section with the sinus fit in the bottom right.

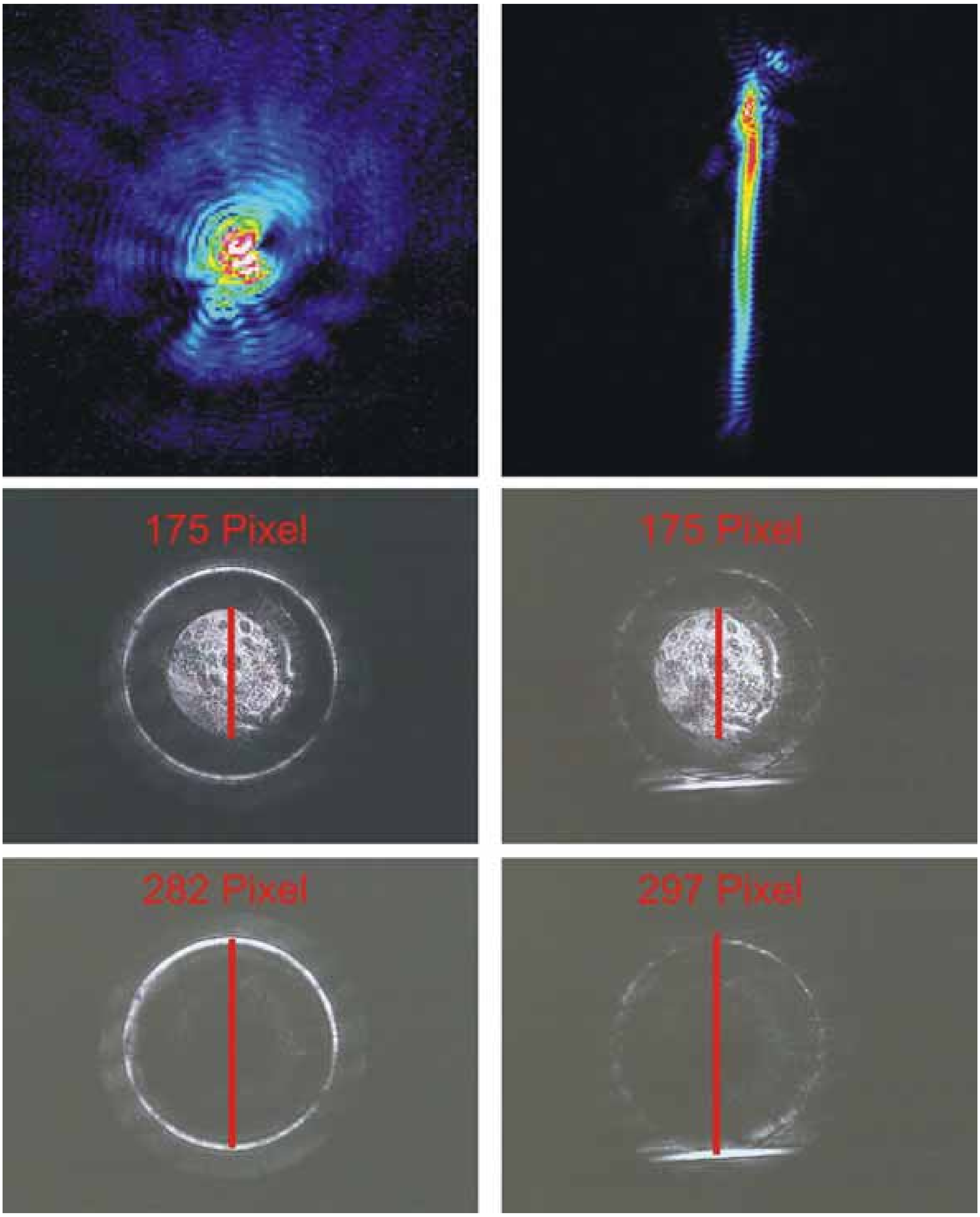

Figure 5.28.: Propagating SPPs on a pure metal surface (left) and guided SPPs (right). The top images show the propagation of SPPs, while the middle images present the Fourier plane with the exciting laser and the bottom ones with Fourier filtering. In both Fourier planes the diameter of the exciting laser and the SPPs are shown. The polarization is in the vertical direction.

in the Fourier image. The guided SPPs are confined into one direction and show up as a straight line in the Fourier plane. Besides this they differ also in the angle of light emission, because the propagating SPPs do not have a polymer on top of the gold, while the guided SPPs are influenced by the refractive index of the DLSPPW. From the difference of the opening angle of the LR of SPPs propagating on a pure metal surface and guided SPPs the effective refractive index of the waveguide can be calculated.

As seen in figure 5.28 the opening diameter of the SPPs propagating on a pure metal surface is $d_{met\,SPPs} = 282 \pm 2\,Pixel$, while the one for guided SPPs is $d_{guided\,SPPs} = 297 \pm 2\,Pixel$. From the ratio of these two values the effective refractive index is determined as $n_{eff} = 1.053 \pm 0.015$.

With this technique also the opening angle of the light emitted by SPPs can be calculated. The numerical aperture of an objective is defined by

$$NA = n \sin(\Theta), \tag{5.5}$$

with n the refractive index and Θ the half opening angle of the cone of light, which can be transmitted by such a numerical aperture. With the known $NA = 0.63$ of the focussing objective the angle of propagating SPPs on a metal surface can be calculated by

$$\frac{d_{Obj}}{d_{SPP}} = \frac{NA_{Obj}}{NA_{SPP}} = \frac{NA_{Obj}}{n \sin(\Theta_{SPP})}, \tag{5.6}$$

with d_{Obj} and d_{SPP} the diameter measured in figure 5.28 for the exciting laser and the SPPs, NA_{Obj} and NA_{SPP} the numerical aperture of the focussing objective and the emitted SPPs, n the refractive index and Θ_{SPP} the half opening angle of the LR emitted by the SPPs. For the calculations of the opening angle the refractive index of the glass substrate has to be taken into account. It gives no contribution for the exciting laser beam , because the laser is focussed on the metal surface, resulting, in good approximation, in a plane wave at the interface air-gold and at the interface air-glass, whose propagation direction is not changed by the refractive index change. For the plasmons the refractive index of the glass has to be taken into account, because the LR is emitted non perpendicular to the surface. With the refractive index of the glass substrate taken into account, the measured diameter of the exciting laser $d_{Obj} = 174 \pm 2\,Pixel$ and the diameter of the propagating SPPs on a pure metal surface $d_{met\,SPPs} = 282 \pm 2\,Pixel$ this results in $\Theta_{met\,SPPs} = 42.81^o \pm 2^o$. The problem of this technique are the uncertainness arising from the numerical aperture of the objective. This numerical aperture is given only for a perfectly focused beam, requiring an illumination of the objective entrance aperture as assumed for the design of the objective. Also the focal position in respect to the metal surface adds an additional uncertainty. With the focal position not on the metal surface the approximation of a plane wave does not hold anymore and the refractive index of the metal and substrate influence the propagation of the exiting laser beam. The difference between the really achieved focussing and a perfect focused beam can not be measured easily and because of this an error occurs, which can not be determined

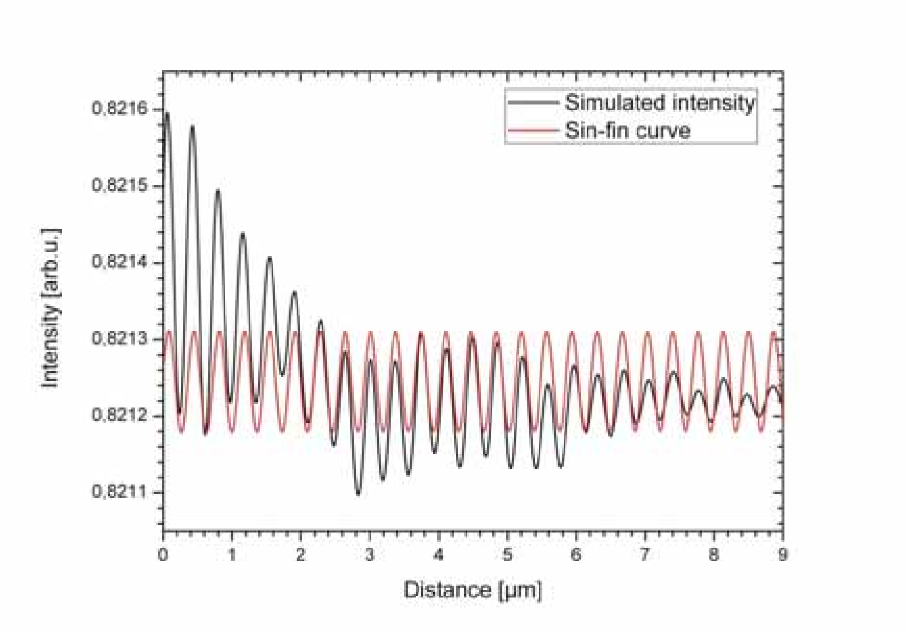

Figure 5.29.: The intensity of SPPs simulated inside a $300\,nm \times 1\,\mu m$ waveguide for $800\,nm$ wavelength. The graph shows the power distribution of the last $9\mu m$ of the DLSPPW before the end of the waveguide where the reflection takes place in a cross-section along the middle of the waveguide. The intensity scale is magnified very much compared to other images shown in this chapter to make the interference structure visible.

exactly. For this reason the value of $\Theta_{met\,SPPs} = 42.81^o \pm 2^o$ has to be handled with care.

The effective refractive index has been determined in three different ways to 1.062 ± 0.015, 1.048 ± 0.012 and 1.053 ± 0.015, respectively. Within the measurement tolerance these values are in good agreement with each other. Besides the different experimental methods of measuring n_{eff} it can also be obtained by simulating the propagation inside and reflection of SPPs at the end of a DLSPPW. The result of the simulation of a $300\,nm$ high and $1\,\mu m$ wide waveguide for $800\,nm$ wavelength, as outlined in figure 5.27, is shown in figure 5.29.

The intensity profile of the last $9\,\mu m$ of the waveguide, at the end where the reflection takes place, is shown and fitted with a sin-curve. Due to the style of measurement used for the simulation no exponential decay of the wave has to be taken into account. Because of this the fit is performed with equation 5.3 with $I_2 = 0$. The fit has a periodicity of $w = 423\,nm \pm 4\,nm$ fitting very well to the experimental obtained interference pattern and resulting in a effective refractive index of 1.058 ± 0.01 applying equation 5.4.

The second simulation method to determine the effective refractive index is the use of the mode solver *FemSim* as described in chapter 3.4. From these calculations the value is $n_{eff} = 1.07$.

Determination method	Effective refractive index	Error
Reflection	1.052	0.015
Interference	1.048	0.012
Fourier plane	1.053	0.015
Interference simulation	1.058	0.03
Mode solver	1.07	—

Table 5.4.: The values for the effective refractive index determined with different methods as described in this section.

The effective refractive index has been found out in five different ways. An overview of the values obtained for n_{eff} by the different methods is shown in table 5.4.

The independently achieved values are in very good agrement with each other, proofing the correctness of the simulations and the experiments.

5.2. Leakage radiation measurements on DLSPPWs

After the basic investigations performed in the last section the following paragraphs deal with the analysis of different structures fabricated by 2PP. First investigations concentrate on the cross-talk of two parallel waveguides and the transmission efficiency of bend structures. After that more complex structures like different designs for Y-splitters and Mach-Zehnder interferometers (MZIs) are analysed. At the end 3-dimensional structures for an increased and easier excitation of SPPs are suggested. For all investigations in this chapter first the LR microscopy is applied. After that the samples are imaged by SEM and the appearance of the structures is used as basis for theoretical simulations.

5.2.1. Straight lines and bend structures

As described already in chapter 3 the first important thing for complex DLSPPW structures is the propagation length of SPPs and the cross-talk of two waveguides. For this reason two parallel waveguides are fabricated with different distances between the center of waveguides. The design for these structures has already been introduced in chapter 3.4.3, where this kind of structure has been simulated for $1550\,nm$ excitation wavelength. Analogue to this, the parallel waveguides are investigated and simulated for $800\,nm$ wavelength. The images obtained by LR microscopy are shown in figure 5.30.

Unfortunately the cross-talk could not be measured, because the intensity detected by LR microscopy has been too week. For the simulations a similar problem arose. The weakness of the cross-talk yields to an error quiet high compared to the calculated intensities that a much larger simulation area would be needed. This would lead to computation times not maintainable for these calculations. For these reasons no cross-talk distance is measured or theoretical derived.

The weakness of cross-talk compared to the results in chapter 4.1 is based on the single- and multi-mode design of the waveguides. In chapter 4.1 the DLSPPW

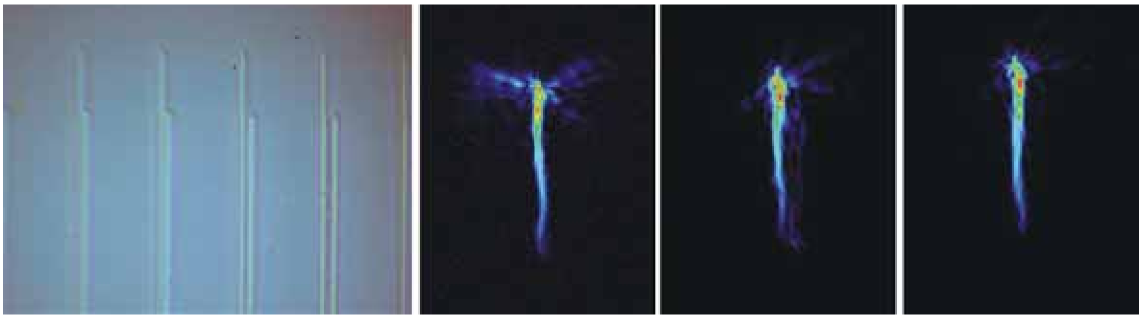

Figure 5.30.: Double lines for the investigation of the cross-talk between DLSPPWs. The image of the double lines (left) and Fourier filtered images of the LR in double lines with different distances $d_W = 0$, $d_W = 1\,\mu m$, and $d_W = 2\,\mu m$ (from left to right).

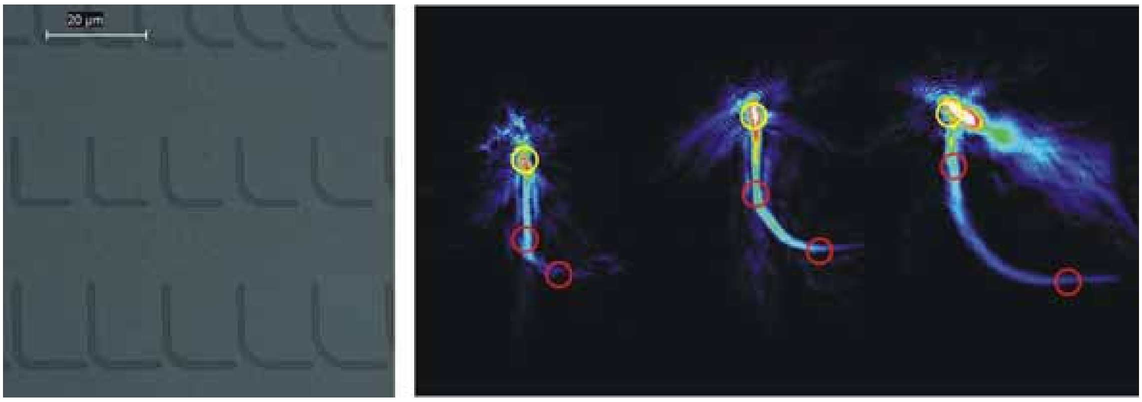

Figure 5.31.: Some curved waveguides with a curvature radius of $1\,\mu m$, $2\,\mu m$, $3\,\mu m$, $4\,\mu m$, and $5\,\mu m$ (middle of the left image from left to right) and the LR images after Fourier filtering for $3\,\mu m$, $6\,\mu m$, and $9\,\mu m$ curvature radius (from left to right). The excitation of SPPs is shown as yellow circle, while the points for the transition measurement are shown as red circles.

is a single-mode waveguide. For this a not negligible part of the electro-magnetic field is outside of the waveguide, while for a multi-mode waveguide, as used in this chapter, the electro-magnetic field can be assumed as completely confined inside the waveguide. Because of this the influence of an other waveguide next to a multi-mode waveguide on the electro-magnetic field is very small.

After the investigations on the cross talk, the next experimentally investigated and simulated design is a curved waveguide as presented in figure 3.15 and shown as fabricated structures in figure 5.31 left.

The LR images presented in figure 5.31 show obtained results for a curvature of $3\,\mu m$, $6\,\mu m$, and $9\,\mu m$ (from left to right). From the LR images the transmission of the curved structure is calculated by

$$T_{curve} = \frac{I_{out}}{I_{in}}, \tag{5.7}$$

with I_{in} the intensity at the entrance and I_{out} the intensity at the exit of the curved part, and compared with simulations of such a structure. The intensity of LR is measured in images taken with the 'WinCam' with the program *ImageJ*. One possible error for this kind of measurements is founded in the SPP excitation. Slight alignment differences for the excitation point or the focussing of the laser beam can influence the SPPs propagating inside the DLSPPW. Another possible error arises from the intensity measurements, because the position of measurement in the image has to be set by hand and the structure itself can only be identified by the LR detected, resulting in an inaccuracy of measurement position. To estimate an error for these measurements one structure is measured several times and an average value with a standard deviation is calculated. From this an error of 250 intensity levels is determined for the measurements, while the range of intensity levels available for the images is about 32000. This measurement procedure with an error of 250 intensity levels is applied for all following experiments. As seen in figure 5.32 for $6\,\mu m$ curvature radius simulated and measured value do not fit perfectly within the measurement uncertainty. In the curved structure investigated for this radius a small defect is observed, giving the reason for this intensity loss.

The simulations are performed in analogy to the one presented in chapter 3.4.3, and the results of experimental measurements and simulations are shown in figure 5.32. The theoretical predictions show a good agreement with the measured transmissions within the measuring tolerance. As seen from these results the most efficient curvature radius for $800\,nm$ wavelength is with about $3.5\,\mu m$ the half of the best radius for $1550\,nm$ wavelength.

After this first comparison of experimentally realized and simulated structure, the bend, as the first structure to optimize, is investigated. The formula describing the bend is defined by equation 4.3 as discussed in chapter 4.1. To maximize the transmission of the bend its length L_B and the deviation of the waveguide d_B are changed. This is done in experiment by fabricating several bends with different L_B and d_B and the measurement of transmission as shown in figure 5.33.

In the LR images the points, where the intensity is measured are shown. The points are situated directly at the beginning and the ending of the bend part of the waveguide. From these measurements the transmission is calculated by

$$T_{bend} = \frac{I_{out}}{I_{in}}. \tag{5.8}$$

The experimentally obtained transmission is plotted together with the transmission achieved by simulations over the bend length and the deviation of the waveguide in figure 5.34.

The experimental and simulated results show a good agreement over the whole investigated set of parameters. For a bend deviation of $1\,\mu m$ and $3\,\mu m$ the obtained

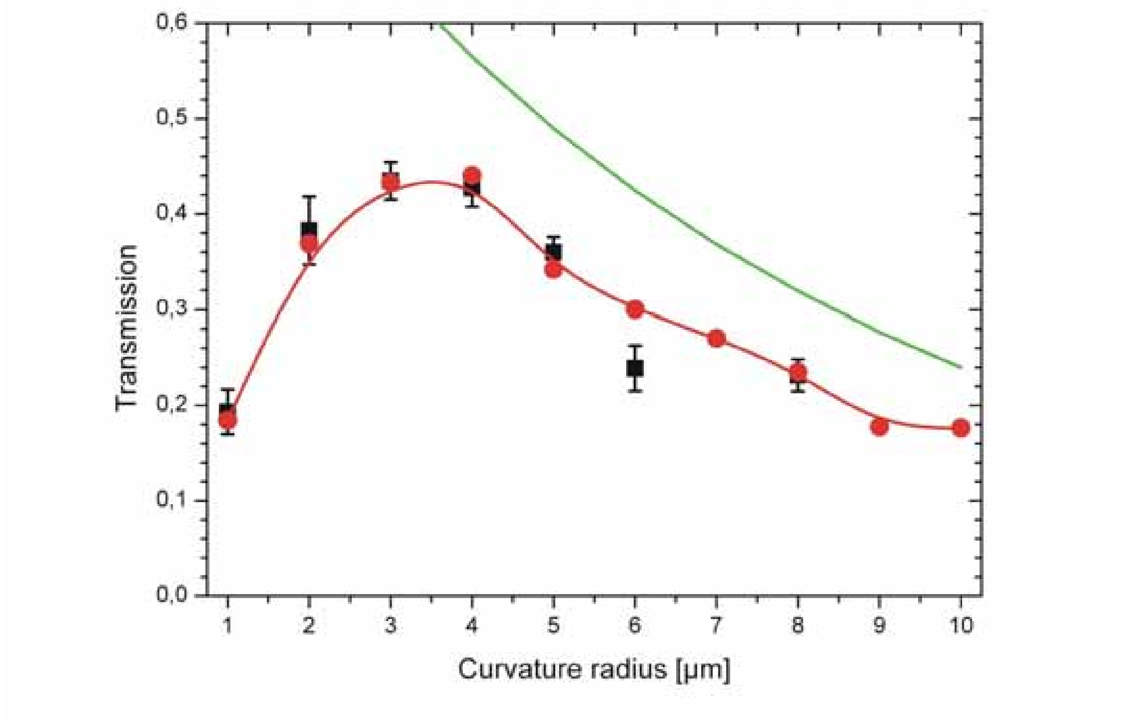

Figure 5.32.: The transmission of curved DLSPPWs depending on the curvature radius as found out experimentally (black squares) and by simulations (red circles and line). The green line represents the transmission for a straight waveguide with the same length as the curved waveguide with the given curvature radius.

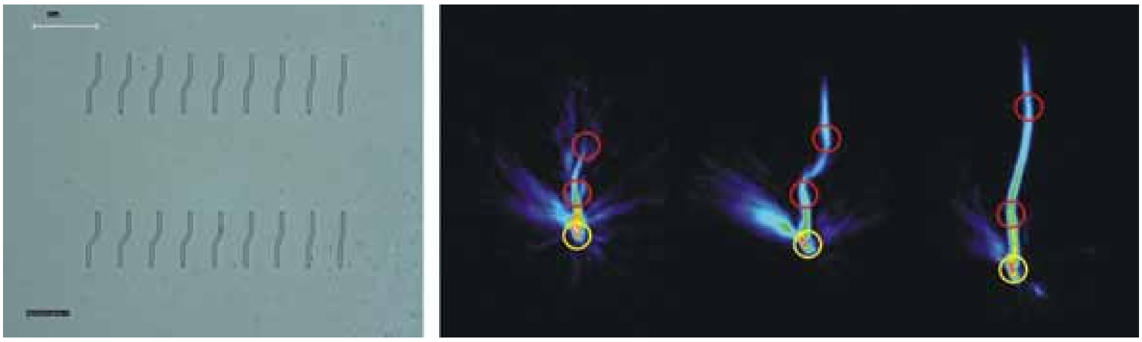

Figure 5.33.: Some bends fabricated with different L_B and d_B (left) and the measurement points (red circles) in different LR images obtained for $L_B = 1\,\mu m$ and $d_B = 2\,\mu m$ (middle left), $L_B = 7\,\mu m$ and $d_B = 1.5\,\mu m$ (middle right), and $L_B = 13\,\mu m$ and $d_B = 2\,\mu m$ (right).

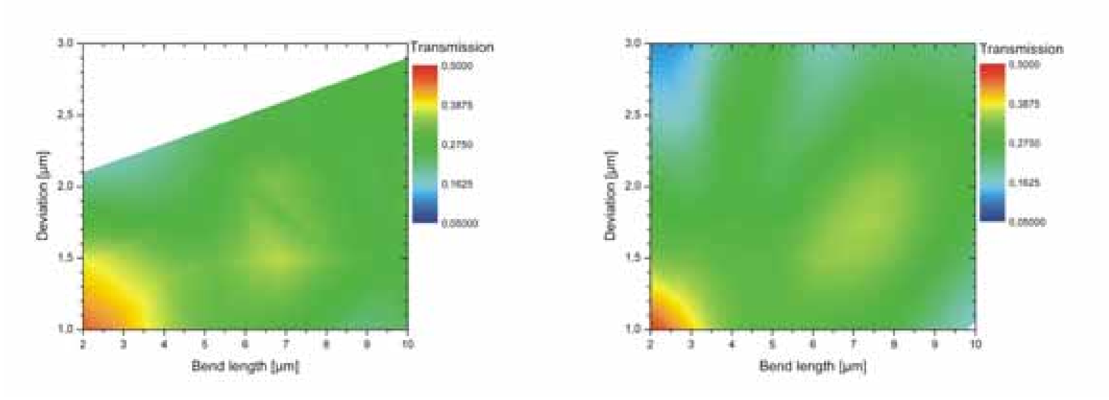

Figure 5.34.: The transmission of bend structures with different bend length and deviation of the waveguide as experimentally measured (left) and simulated (right).

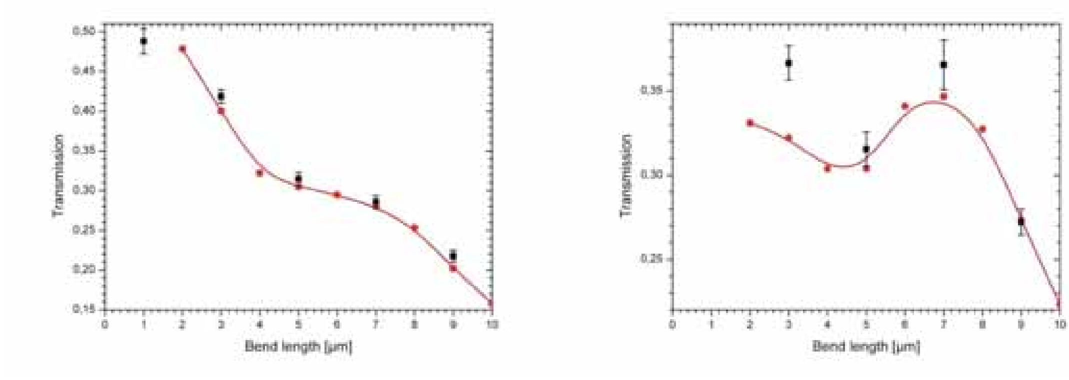

Figure 5.35.: The transmission of bend structures with different bend lengths for a deviation of the waveguide of $1\,\mu m$ (left) and $3\,\mu m$ as simulated (red circles) and measured (black squares).

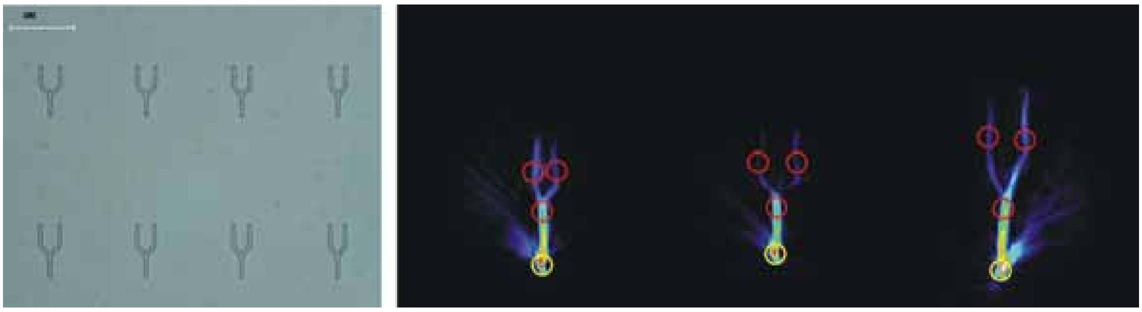

Figure 5.36.: Some Y-splitters fabricated with different L_B and d_B (left) and the measurement points in different LR images obtained for $L_B = 1\,\mu m$ and $d_B = 2\,\mu m$ (middle left), $L_B = 5\,\mu m$ and $d_B = 2\,\mu m$ (middle right), and $L_B = 9\,\mu m$ and $d_B = 2\,\mu m$ (right).

results are shown in figure 5.35. The experimental values for $1\,\mu m$ deviation are conform to the simulated ones taking the measurement failure into account. For $3\,\mu m$ deviation the experimental values differ slightly from the theoretical prediction. The slightly smaller transmission experimentally obtained can be explained by defects in the fabricated structure resulting in additional losses.

The results presented in this section give the proof for the correctness of the simulations performed in this work. These results encourage that the cut-splitter design as introduced in chapter 4.3 gives a more efficient splitter than the conventional Y-splitter. This will be investigated in the next section.

5.2.2. Different designs for Y-splitter structures

As already demonstrated for the bend structure in the last section, Y-splitters and cut-splitters have been fabricated. Some Y-splitters and LR images are shown in figure 5.36.

For the Y-splitters the distance between the arms (corresponding to twice the deviation as introduced in the last section for bend structures) and the length of the bend are varied and the transmission of the splitters depending on these parameters is plotted in figure 5.37.

Figure 5.38 shows the comparison between measurements and simulation. The left image displays the magnification of the measurements presented in figure 5.37 for the bend length in the range of $4\,\mu m$ to $10\,\mu m$ and an arm distance from $2\,\mu m$ to $4\,\mu m$. This is the most interesting range of parameters, because it provided the best transmission measured. For the same range the Y-splitter design is simulated for $300\,nm \times 1000\,nm$ waveguides. The transmission obtained from these simulations is shown in figure 5.38 right.

The achievable agreement between experimental and simulated results is limited by the measurement errors. Within this uncertainty experiment and simulations show good agreement. To demonstrate this figure 5.39 shows the results obtained by simulation and experiments with the measurement errors for an arm distance of $2\,\mu m$ (top left) and $3\,\mu m$ (top right) and for a bend length of $5\,\mu m$ (bottom left) and $7\,\mu m$ (bottom right). From the results obtained by simulation and experiment

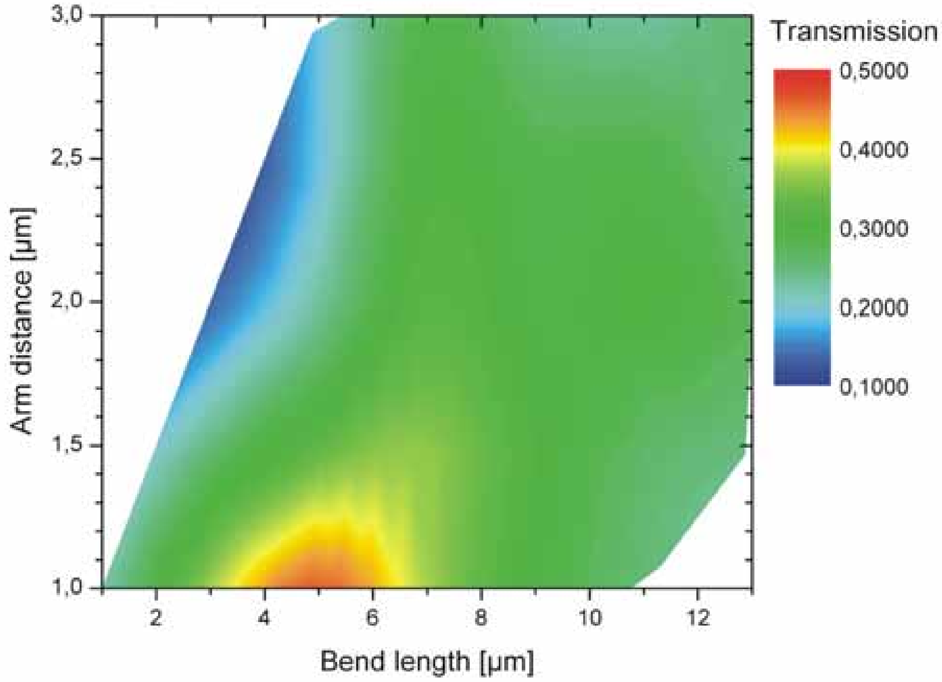

Figure 5.37.: The transmission of Y-splitter structures as measured with the LR microscopy for different bend lengths and arm distances.

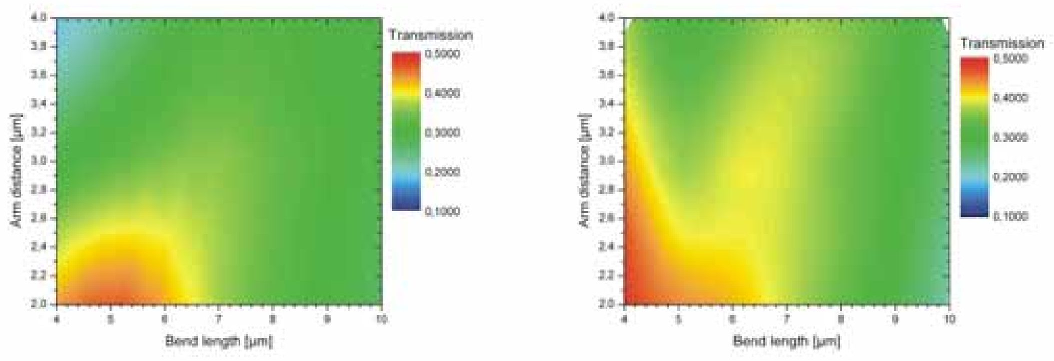

Figure 5.38.: The transmission of Y-splitter structures as measured (left) and simulated (right) for different bend lengths and distances between the arms.

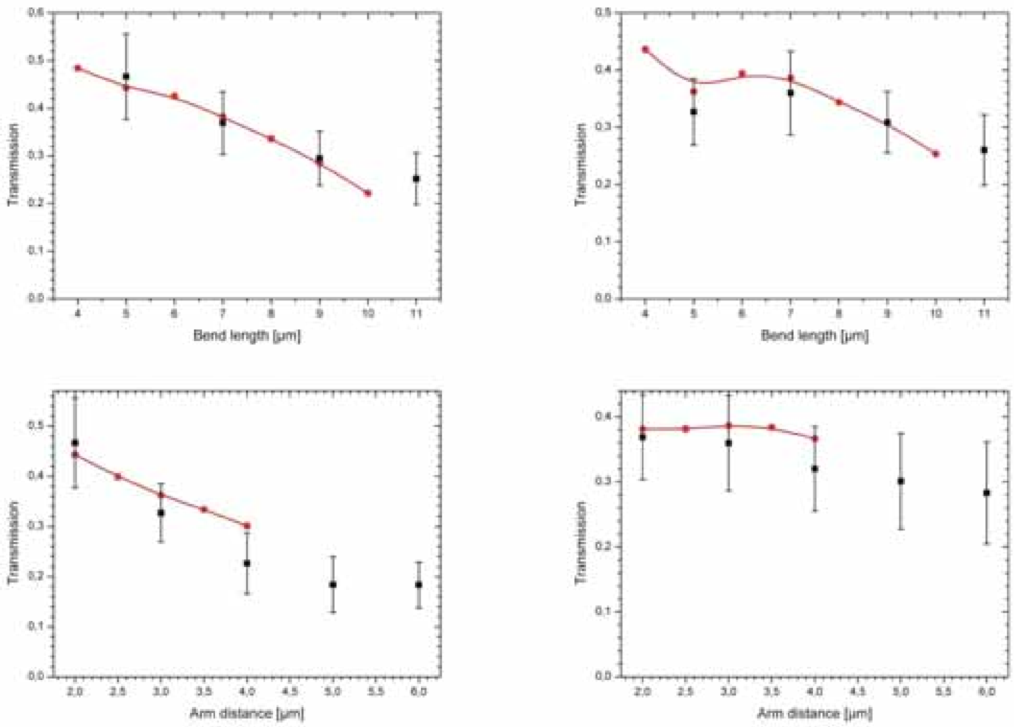

Figure 5.39.: The transmission of Y-splitter structures as measured (black squares) with error bars and simulated (red circles) for different an arm distance of $2\,\mu m$ (top left) and $3\,\mu m$ (top right) and bend lengths of $5\,\mu m$ (bottom left) and $7\,\mu m$ (bottom right).

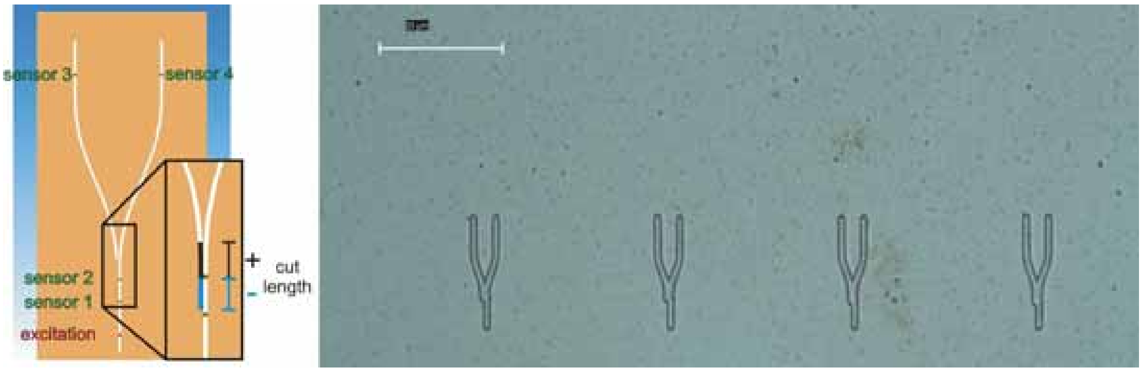

Figure 5.40.: The design for the cut-splitter (left) with the positive and negative cut-length and some cut-splitters fabricated by 2PP (right) with different cut-lengths.

bend lengths of 5 μm with an arm distance of 2 μm are the most efficient Y-splitters. Nevertheless, these structures are very small and because of this difficult to measure in the LR microscope. For an arm distance of 3μm and bend lengths from 6 μm to 10 μm the transmission is only slightly less. Because of this reason Y-splitters in this range of parameters are more preferable for experimental investigation and are used for the analysis of the cut-splitter in this section and the Mach-Zehnder-interferometer (MZI) in the next section.

As next step the novel cut-splitter design suggested in chapter 4.3 is tested and compared to simulations. For this a cut-splitter as shown in figure 4.15 is fabricated by 2PP. The DLSPPW is 300 nm × 1000 nm and the width of the wider part of the waveguide is about 1800 nm. The bend length and arm distance used for these investigations are 8 μm and 3 μm, respectively. The transmission is calculated analogue to the investigations on the Y-splitter. Unfortunately the cross-talk of 800 nm excited SPPs is small as seen at the beginning of this section, due to the multi-mode design of the waveguides. Because of this no 50% splitter can be realized in the cut-splitter configuration. Nevertheless the cut-splitter can be extended with the shifted-multi-mode-splitter as described in chapter 4.3. The design used for the experiments and simulations is shown in figure 5.40 together with some fabricated splitters.

The positive cut-length corresponds to the suggested cut-splitter design, while a negative cut-length represents a shifted-multi-mode-splitter design. As demonstrated in chapter 4.3 both designs complement one another. The cut-length is varied from $-5\,\mu m$ to $+2\,\mu m$ for the following experiments and simulations. The transmission obtained from these is shown in figure 5.41.

A cut length of 0 μm is given for a conventional Y-splitter design, with the difference, that the left bend part and left arm are shifted 600 nm to the left side. As seen from figure 5.41 the experimental results reproduce the simulated values very well. The total transmission of the cut-splitter remains nearly constant for all investigated cut-lengths. The total transmission is slightly lower than for a conventional Y-splitter design. The explanation for this can be found again in the multi-mode design of the waveguide. For a single-mode waveguide the field is very strong confined in the middle of the waveguide resulting in high losses for a conventional Y-splitter

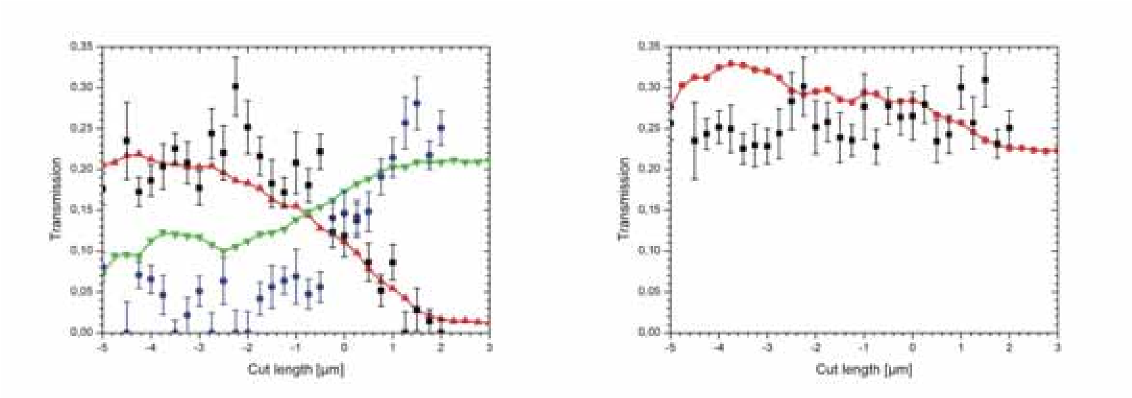

Figure 5.41.: The transmission into each arm of the cut splitter (left) and the total achieved transmission (right). On the left image the transmission into the left arm (simulated red triangles and line, measured black squares) and the right arm (simulated green triangles and line, measured blue circles) are shown. The right image illustrates the total achieved transmission as simulated (red circles and line) and measured (black squares).

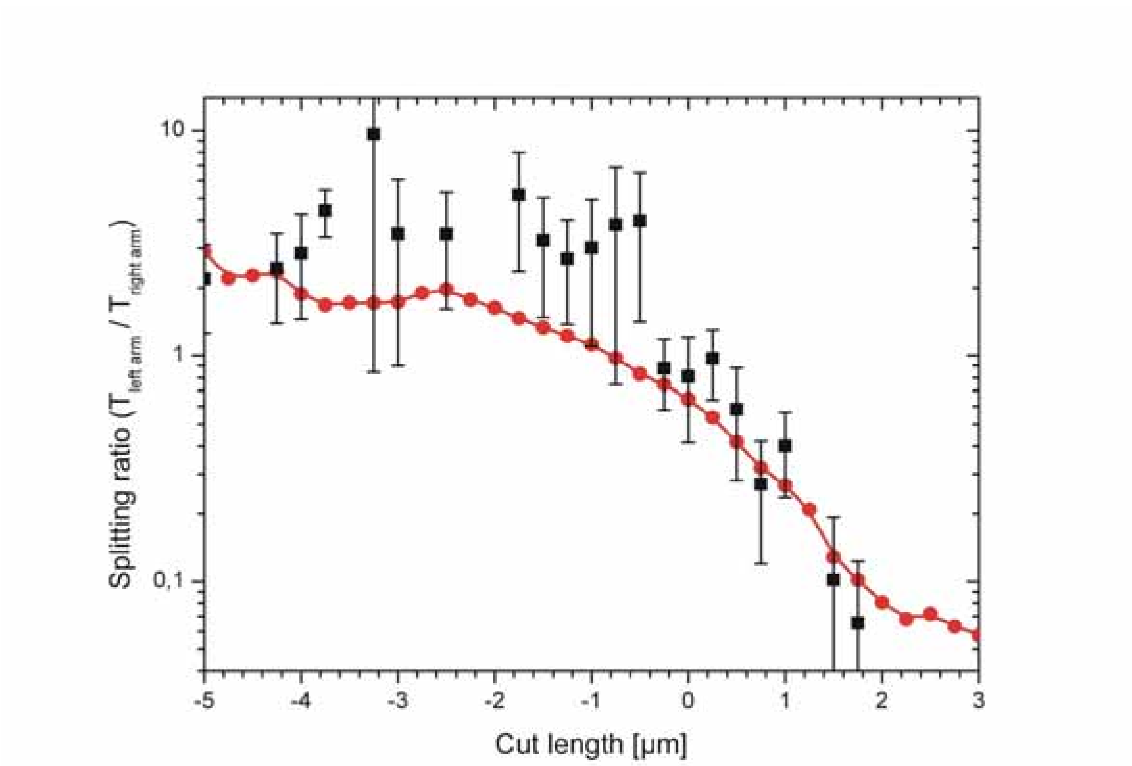

Figure 5.42.: The splitting ratio given by the transmission into the left arm divided by the transmission into the right arm as achieved by simulation (red circles and line) and experiment (black squares).

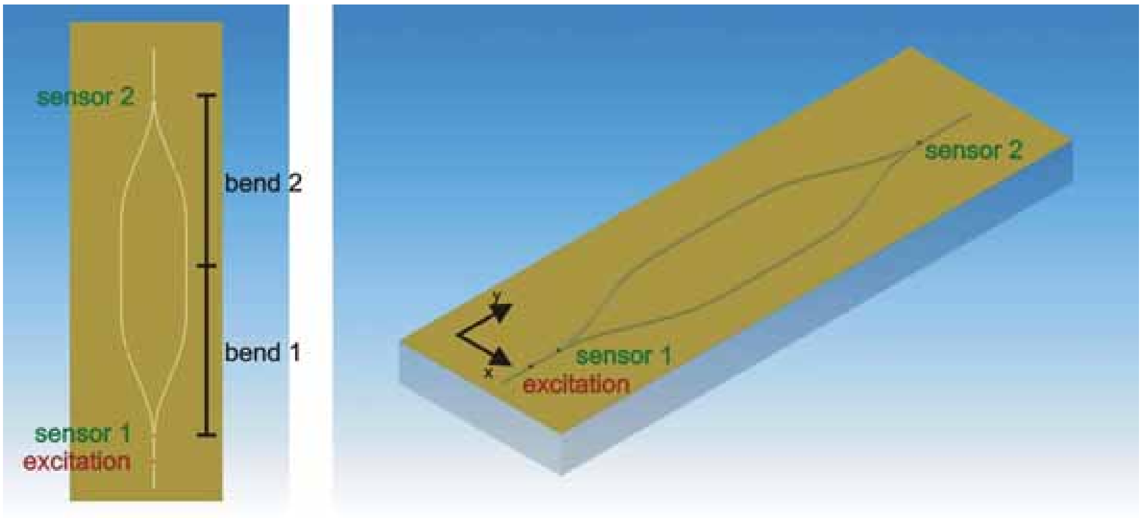

Figure 5.43.: The design of a Mach-Zehnder-interferometer.

design at the splitting of the two arms. For a multi-mode waveguide this splitting loss is already reduced compared to a single-mode waveguide, because the power inside the waveguide is not so much concentrated to the middle of the waveguide. Due to this the splitting losses are less important. At the same time the widening of the waveguide in the cut-splitter design induces losses, e.g. by the distortion of the straight propagation induced by the corner of the double width waveguide, resulting in a slight less efficient transmission. For this reason the cut-splitter does not provide an improved efficiency for a multi-mode waveguide, but about the same as for a conventional Y-splitter.

The advantage of the cut-splitter, which can be demonstrated for a multi-mode waveguide is the adjustable splitting ratio. The splitting ratio, which is the intensity transmitted into the left arm divided by the intensity transmitted into the right arm, is plotted over the cut-length in figure 5.42. Again the prediction of the simulations and the experimental values are in good agreement.

5.2.3. Mach-Zehnder interferometer

After the investigations on basic DLSPPWs and the comparison of simulation and experimental results a wavelength depending structure is analysed. The design of a Mach-Zehnder-interferometer (MZI) is shown in figure 5.43 with the excitation, and the measurement points represented by 'sensor 1' (as entrance intensity) and by 'sensor 2' (as exit intensity).

In general the intensity transmitted by a MZI can be calculated by [KS99]

$$I_T = I_1 + I_2 + 2\sqrt{I_1 I_2}\cos(2\pi\frac{\Delta s}{\lambda}), \tag{5.9}$$

with I_T the transmitted intensity, I_1 and I_2 the intensities at the end of the left and right interferometer arm, respectively, Δs the path length difference of both arms, and λ the wavelength. The path length difference can be introduced by different

Path length difference [μm]	**Splitting ratio**	**Intensity at the end of the left arm**	**Intensity at the end of the right arm**
0	1 : 1	0.175	0.175
3	2.7 : 1	0.26	0.083
5	4.9 : 1	0.29	0.047
7	10.2 : 1	0.32	0.022
9	1 : 0	0.35	0

Table 5.5.: The splitting ratio of the intensity in the left arm divided by the one in the right arm of the MZI and the intensities estimated for the end of the arms taking only the splitting ratio and Ohmic losses into account.

deviations for the left and the right arm. With the *Tsunami* laser system introduced in chapter 2 and used in cw operation mode, a tunable system, with a wave length range from 730 nm to 830 nm, is available. Before starting with experimental investigations on different MZIs, the expected behavior in the wavelength range of the *Tsunami* is analysed. MZIs with path length differences of 0 μm, 3 μm, 5 μm, 7μm, and 9μm are fabricated and investigated. These path length differences are realized for MZIs with 11 μm bend length and a fixed deviation of 1.5 μm for the left arm, while the deviation of the right arm is adjusted to 1.5 μm, 6 μm, 10 μm, 15 μm, and 20 μm, respectively. For the MZIs with different path lengths the propagation losses of SPPs have to be taken into account. These can be calculated by equation 3.28. Furthermore the asymmetric deviations of the interferometer arms result in a non equal splitting of the incoming SPP intensity. This splitting can not be calculated analytical. For this reason it is measured for these MZIs. In table 5.5 the measured splitting ratio is given in the second column as ratio of the intensity entering the left arm to the one entering the right arm of the MZI. The third and fourth column show the intensity at the end of the left and right arm, respectively. In these intensities the splitting ratio and the propagation losses in the arms are taken into account. They are given in respect to an intensity of 1 at the entrance of the MZI (at 'sensor 1'). In these estimations the losses of the bend structure are neglected.

For the path length differences of $\Delta s = 0\,\mu m$, $\Delta s = 3\,\mu m$, $\Delta s = 5\,\mu m$ and $\Delta s = 7\,\mu m$ equation 5.9 is plotted over the wavelength in figure 5.44. As seen from these calculations the appearance of the intensity function is different for changing path length differences.

The transmission for the MZIs is measured with the LR microscope as described for the Y-splitters before. The intensities are measured at 'sensor 1' and 'senor 4' as shown in figure 5.43. The transmission of the MZIs is measured for the whole wavelength range available. The results of these measurements are shown in figure 5.45.

For the experimental realization only MZIs with a pathlength difference of $\Delta s = 0\,\mu m$, $\Delta s = 3\,\mu m$, and $\Delta s = 5\,\mu m$ could be analysed. This is due to the reduced transmission for larger deviations. For deviations larger than 10 μm the transmission of the arm is to low to be measured. Also the contrast at the output port for such an interferometer is reduced with non-uniform splitting into the arms. For the MZI with $\Delta s = 0\,\mu m$ as shown in figure 5.45 top no fluctuation of the output

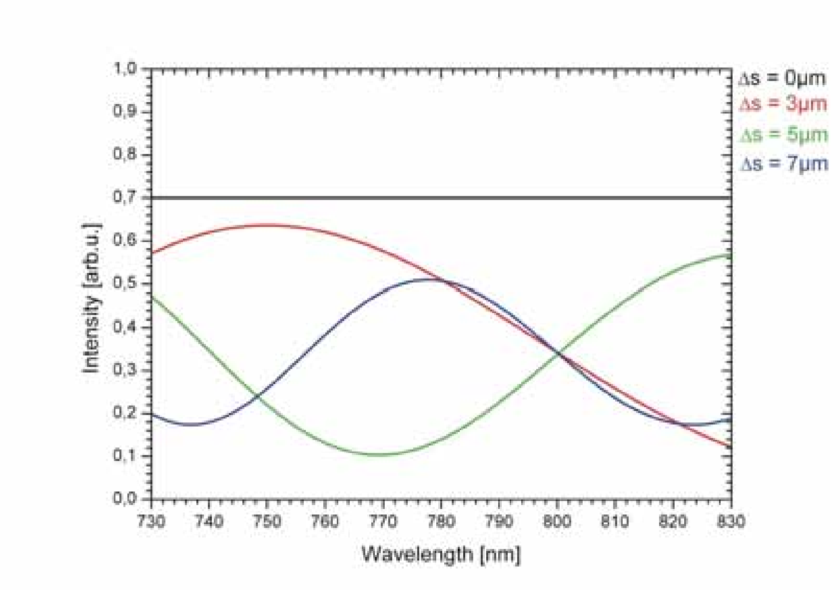

Figure 5.44.: The transmitted intensity of a Mach-Zehnder-interferometer in the wavelength range from $730\,nm$ to $830\,nm$ for some path length differences of $0\,\mu m$, $3\,\mu m$, $5\mu m$, and $7\mu m$.

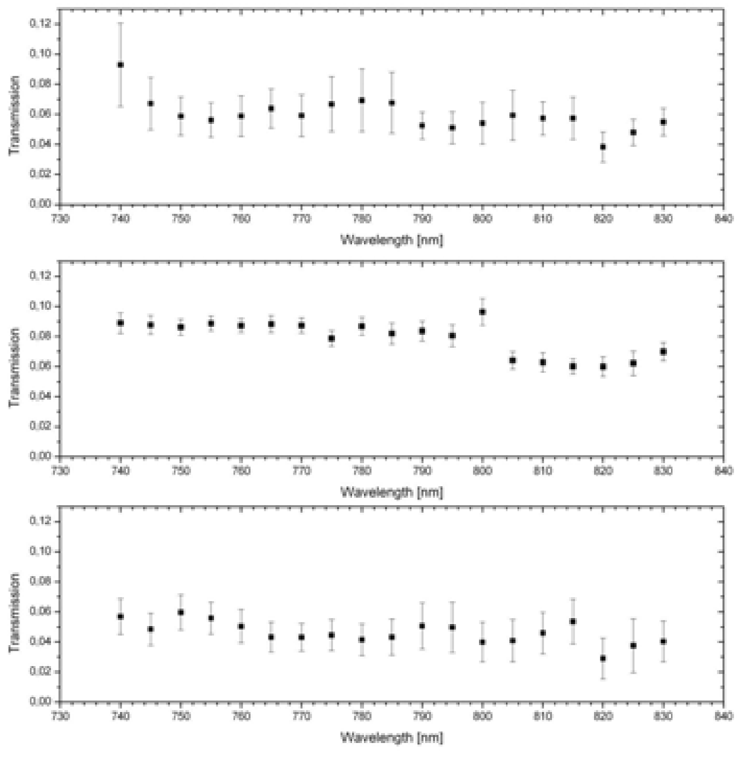

Figure 5.45.: The transmitted intensity of a Mach-Zehnder-interferometer for different $\Delta s = 0\,\mu m$ (top), $\Delta s = 3\,\mu m$ (middle), and $\Delta s = 5\,\mu m$ (bottom).

intensity with the wavelength is observed. Comparing the calculation of a MZI with $\Delta s = 0\,\mu m$ showing a transmission of 70% to the measured transmission of about 7% points to very high losses due to the bending of the waveguide or structure failures. For $\Delta s = 3\,\mu m$ (figure 5.45 middle) a slight decrease of the output intensity could be interpreted to this graph. Unfortunately the difference between the highest transmission with about 9% and the lowest transmission of 6% is very small. Because of this it could point to a working MZI, but not proof a functioning wavelength selective component. One reason of the small intensity change over the wavelength range is based on the bending losses increasing with larger deviation (longer path length). For the MZI with $\Delta s = 5\,\mu m$ no periodical behavior of the output intensity is observable.

The problems with the experimental realization are founded in the very high phase sensitivity of the MZIs fabricated. The experiments are performed with a multi-mode DLSPPW. The problem in the multi-mode configuration is, that the transition between the different modes has many influences. It is starting with the splitting of the incoming waveguide, where different modes could be excited in the arms. Also the transformation from one mode into another can be completely different for the arms, resulting in different propagation velocities, due to different refractive indices for different modes. Furthermore, the excitation point, which has to be readjusted for every wavelength because the laser beam is slightly shifting while changing the wavelength, and the wavelength of SPPs influence the splitting behavior and with this the transformation between the modes. Besides the different modes, also fabrication defects influence the behavior of the MZI. A defect in one arm influences the propagation and can also be wavelength dependent. All these reasons reduce the contrast achievable in the output arm, make a trustful measurement very difficult and nearly impossible for the multi-mode MZIs. For single mode MZIs, e.g. by applying the waveguide dimensions calculated in chapter 3 for a wavelength of $1550\,nm$, these measurements would be easier, but still very difficult. Again the shift of the excitation position and fabrication defects would influence the output intensity, but are expected to give a lower reduction of the output contrast as for a multi-mode MZI.

5.3. Further SPP structures

In this chapter the ability of 2PP fabricated 2-dimensional SPP structures has been demonstrated. However, one big advantage of 2PP compared to other micro- and nano-structuring techniques is the aspect of real 3-dimensional structuring. This enables one to fabricate real 3-dimensional structures with a resolution down to $100\,nm$ opening up new possibilities for SPP structures.

Figure 5.46 shows a first 3-dimensional surface modelled by 2PP. The simple structure demonstrates the possibility to bring SPPs onto modelled surfaces. This is a preliminary investigation for the structure shown in figure 5.47. The twisted structure is designed for the SPP excitation by a laser focussed into the taper structure. The angle between taper and sidewall is chosen suitable for the excitation of SPPs, resulting in SPPs propagating along the sidewall and down the twisted part onto the

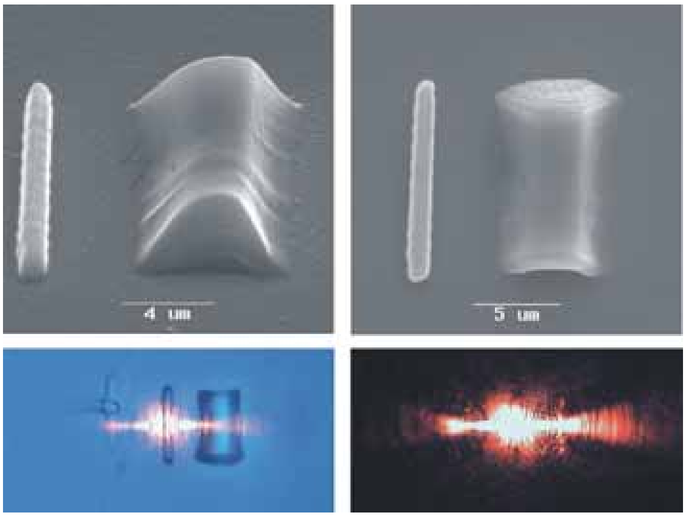

Figure 5.46.: A simple 3-dimensional surface fabricated by 2PP. The top images show an excitation line and surface structuring made from ORMOCER by 2PP on a glass substrate. The structure is covered with 50 nm gold afterwards. The bottom left image shows the excitation of SPPs at the line and their propagation over the tailored surface imaged in the LR microscope with back light illumination. The bottom right image shows only the SPP propagation without back light illumination.

substrate. The taper can be optimized for the best angle of SPP excitation. With this a highly efficient excitation of SPPs should become possible.

5.4. Summary

For the first time DLSPPWs have been fabricated by 2PP. These waveguides have been investigated in experiment and simulation in this chapter. The SNOM and LR microscope have been introduced. For different wavelength the waveguide size for single mode SPP waveguiding has been calculated and models of experimentally realized structures have been simulated. The excitation of SPPs on surface defects and in DLSPPWs has been shown and the excitation efficiency for different structures compared. A method to distinguish between SPP and optical modes inside waveguides has been demonstrated and the effective refractive index for SPP waveguides has been figured out by 5 different methods. Different DLSPPWs have been investigated by LR microscopy and compared with simulation results. The enhanced transmission of the cut-splitter suggested in chapter 4 compared to a normal Y-splitter design has been demonstrated and a Mach-Zehnder-interferometer as first wavelength selective component has been realized. At the end novel ideas 3-dimensional SPP structures have been presented as suggestion for a high efficient SPP excitation.

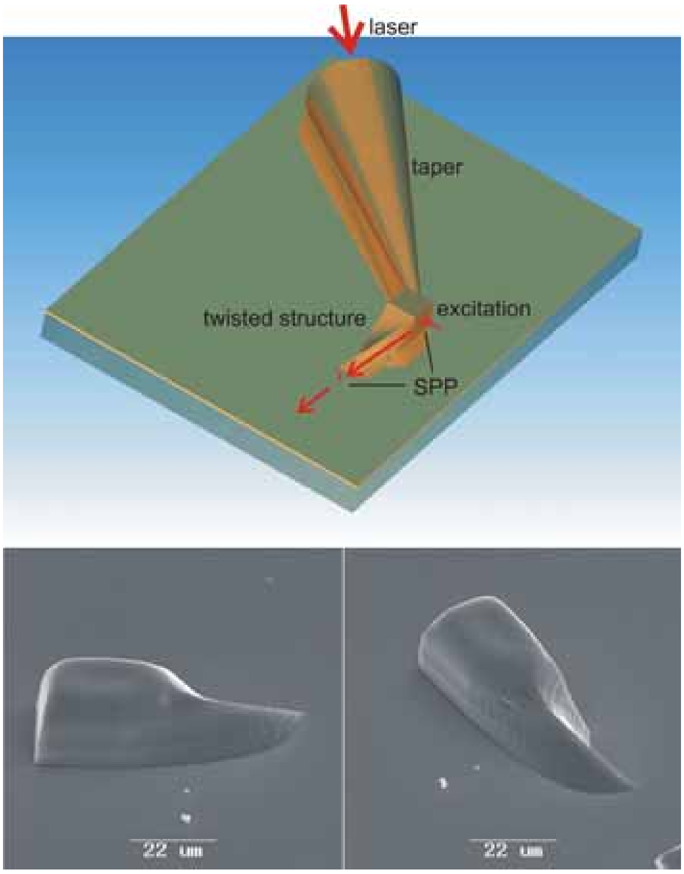

Figure 5.47.: A twisted structure as idea for the high efficient excitation of SPPs. The design of the twisted structure with a taper is shown on the top, while a 2PP fabricated structure without taper is imaged on the bottom. The exciting laser beam is focussed into the taper and guided onto the sidewall of the twisted structure. The angle between taper and sidewall is chosen suitable for the excitation of SPPs, resulting in SPPs propagating along the sidewall and down the twisted part onto the substrate.

6. Summary and outlook

In this thesis dielectric loaded surface plasmon polariton waveguides (DLSPPWs) have been fabricated and analysed. A highly flexible rapid prototyping technology has been chosen for the fabrication, the 2-Photon-Polymerization (2PP). To support the decision for 2PP as the fabrication technology, different technologies of micro- and nanostructuring, e.g. UV-lithography, e-beam lithography, micro-stereolithography, nano-imprint technology, and 2-Photon-Polymerization, were compared. The state-of-the-art for 2-Photon Polymerization has been reviewed, and a commercially available system for 2PP developed during this work, was introduced. The theoretical description of 2PP has been summarized and explained. On the experimental side, different laser systems, providing different wavelengths, pulse durations and repetition rates, have been tested to improve the processing stability and speed. The 2-Photon-Absorption-Cross-Section and efficiencies of structuring for these laser systems have been investigated, and the structuring speed of 2PP has been increased from $100\,\mu m/s$ to about $30\,mm/s$. Example applications of 2PP in micro-optics, micro-fluidics, micro-mechanics, and biomedicine have been demonstrated. 3-dimensional structures in the millimeter range with resolutions better than $300\,nm$ have been fabricated for the first time using 2-Photon Polymerization, opening the possibility of large area structuring and the step from pure research to industrial applications.

As a starting point for the investigations of SPPs, the theoretical description and some possibilities to excite them, especially the attenuated-total-reflection (ATR) setup have been reviewed. Also, the materials useful for plasmonic devices have been qualified by theoretical considerations, and the propagation length of SPPs in dielectric waveguides has been computed. Besides the computational investigations on straight waveguides, also simulations for finding the best radius for a 90^o curve realized by a waveguide have been performed. The design for a single mode SPP Y-splitter by [KZ07], as a simple DLSPPW, has been reviewed and simulated. This ideal design of a defect free Y-splitter has been extended to a more realistic model, taking into account the limited resolution of nano-fabrication techniques. The total transmission of this splitter model has been simulated depending on the resolution of the fabrication technique, and it has been shown that the effectiveness strongly decreases with worse fabrication resolution. To improve the efficiency of SPP Y-splitters, a multi-mode Y-splitter design, well known from integrated optics, has been transferred to SPPs and extended to a more efficient multi-mode splitting. It has been demonstrated that this design does not provide any increase in efficiency, but the possibility to realize both equal and arbitrary splitting ratios. After that a novel design, the cut-splitter, has been developed, providing a higher efficiency and a better tolerance on the limited resolution of fabrication techniques. Also, it has been shown that this cut-splitter allows the design of a highly efficient, equal or non-equal splitter, taking the limited resolution of fabrication techniques into account.

After the computational investigations, DLSPPWs have been fabricated using 2PP for the first time. These waveguides have been investigated in experiments and compared to simulation results. The scanning-near-field-optical-microscope (SNOM) and leakage radiation (LR) microscope have been introduced, the background for LR measurement has been reviewed, and the experimental realization of an LR microscope is described in detail. For different wavelengths of $1550\,nm$, $1000\,nm$, $900\,nm$, $800\,nm$, and $632\,nm$, the waveguide dimensions for single mode SPP waveguiding has been calculated. For $800\,nm$ and $632\,nm$ wavelength models of experimentally realized structures have been simulated and the achieved results have been compared with simulated results. The excitation of SPPs on surface defects and in DLSPPWs has been shown, and the excitation efficiency for different structures has been compared. A method to distinguish between SPP and optical modes inside waveguides has been demonstrated, and the effective refractive index for SPP waveguides has been figured out using five different methods, and showing very good agreement. Different DLSPPWs, in detail straight waveguides, curved waveguides, bend structures, Y-splitters, and cut-splitters, have been investigated using LR microscopy, and compared with simulation results. The enhanced transmission and fabrication defect tolerance of the cut-splitter developed in this work, has been compared to a conventional Y-splitter design. Furthermore a Mach-Zehnder-interferometer as a first wavelength selective component fabricated using 2PP has been realized and analysed. Also, novel ideas for 3-dimensional SPP structures have been presented as a highly efficient SPP excitation method.

This work shows the capabilities of 2PP for flexible rapid prototyping of 2- and 3-dimensional structures. Furthermore, the operation of DLSPPWs fabricated using 2PP has been shown for the first time, and flexible structuring has been used for the development of a more efficient SPP splitter structure.

Unfortunately, the achieved resolution of 2PP on metal surfaces is worse than on glass substrates. No single mode DLSPPWs could be realized by direct writing on gold. To overcome this, 2PP could be combined with nano-imprint technology. This would allow the fabrication of single mode DLSPPWs on glass using 2PP, and copying these structures on metal layers by nano-imprint technique.

Furthermore, for this work only a leakage radiation microscope with excitation wavelengths from $632\,nm$ to $800\,nm$ was available. This could be extended to telecommunication wavelength at $1550\,nm$ giving a longer propagation length of SPPs and more efficient devices.

With these extensions 2PP can become a highly flexible rapid prototyping tool for the investigations of not only multi-mode, but also single mode SPPs, giving a new degree of freedom for the design of structures.

List of Figures

List of Tables

Bibliography

[ADK06] A. Stepanov H. Ditlbacher B. Steinberger N. Galler F. Aussenegg A. Leitner A. Drezet, A. Hohenau and J. Krenn. How to erase surface plasmon fringes. *Applied Physics Letters*, 89(091117), 2006.

[AKK04] M. J. Lederer A. Killi, U. Morgner and D. Kopf. Diode-pumped femtosecond laser oscillator with cavity dumping. *Optics Letters*, 29(11), 2004.

[AKK05] U. Morgner M. Lederer J. Frei A. Killi, J. Dörring and D. Kopf. High speed electro-optical cavity dumping of mode-locked laser oscillators. *Optics Express*, 13(6), 2005.

[AN72] E. Ash and G. Nicholls. Super-resolution aperture scanning microscope. *Nature*, 237(510), 1972.

[BBC06] S. O'Brien B. Bhuian, R. Winfield and G. Crean. Investigations of the two-photon polymerisation of a zr-based inorganic-organic hybrid material system. *Applied Surface Science*, 252(4845), 2006.

[Ber99] P. Berini. Plasmon-polariton modes guided by a metal film of finite width. *Optics Letters*, 24(15), 1999.

[BH02] C. M. Blanca and S. Hell. *Optics Express*, 10(893), 2002.

[BL06] P. Berini and J. Lu. Curved long-range surface plasmon-polariton waveguides. *Optics Express*, 14(6), 2006.

[BLJ01] G. Schider H. Ditlbacher M. Salerno N. Felidj A. Leitner F. Aussenegg B. Lamprecht, J. Krenn and J.Weeber. Surface plasmon propagation in microscale metal stripes. *Applied Physics Letters*, 79(1), 2001.

[BLL83] C. Nylander B. Liedberg and I. Lundstrom. Surface plasmon resonance for gas detection and biosensing. *Sensors Actuators*, 4(299), 1983.

[Bra98] M. Braguglia. Biosensors: An outline of general principles and application. *Chem. Biochem. Eng. Q.*, 12(183), 1998.

[BSK06] D. Ditlbacher A. I. Stepanov A. Drezet F. R. Aussenegg A. Leitner B. Steinberger, A. Hohenau and J. R. Krenn. Dielectric stribes on gold as surface plasmon waveguides. *Appl. Phys. Lett.*, 88(094104), 2006.

[BSK07] D. Ditlbacher F. R. Aussenegg A. Leitner B. Steinberger, A. Hohenau and J. R. Krenn. Dielectric stribes on gold as surface plasmon waveguides: Bends and directional couplers. *Appl. Phys. Lett.*, 91(081111), 2007.

[CC03] F. Chien and S. Chen. A sensitivity comparison of optical biosensors based on four different surface plasmon resonance modes. *Biosensors Bioelectron.*, 20(633), 2003.

[Cho06] S. Chou. Subwavelength optical elements and nanoimprint technology for optical mems/nmes. *Optical MEMS and Their Applications Conference, 2006*, (3), 2006.

[CMJ99] S. Fan P. R. Villeneuve H. A. Haus C. Manolatou, S. G. Johnson and J. D. Joannopoulos. *J. Lightwave Technol.*, 17(1682), 1999.

[CRB06] B. N. Chichkov C. Marquardt I. P. Radko C. Reinhardt, S. Passinger and S. I. Bozhevolnyi. *Opt. Lett.*, 31(1307), 2006.

[CS80] Y. Chabal and A. Sievers. High-resolution infrared study of hydrogen (1×1) on tungsten (100). *Phys. Rev. Lett.*, 44(944), 1980.

[CSR07] A. Forchel C. Etrich T. Pertsch R. Iliew F. Lederer C. Schuller, S. Hfling and J. Reithmaier. Highly efficient and compact photonic wire splitters on gaas. *Appl. Phys. Let.*, 91(221102), 2007.

[dJK95] P. de Jager and P. Kruit. Applicability of focused ion beams for nanotechnology. *Microelectronic Engineering*, 27(327), 1995.

[DPD88] U. Fischer D. Pohl and U. Durig. Scanning near-field optocal microscopy (snom). *Journal of microscopy - Oxford*, 152(853), 1988.

[DSV98] M. Bludszuweit D. Schulz, C. Glingener and E. Voges. Mixed finite element beam propagation method. *IEEE JLT*, 16, 1998.

[DSY05] B. Feng D. Schaadt and E. Yub. Enhanced semiconductor optical absorption via surface plasmon excitation in metal nanoparticles. *Applied Physics Letters*, 86(063106), 2005.

[Ell89] D. J. Elliott. *Integrated Circuit Fabrication Technology.* McGraw-Hill Book Co., Inc., New York, 1989.

[EP75] P. Echenique and J. Pendry. Absorption profile at surfaces. *J. Phys. C: Solid State Phys.*, 8(2936), 1975.

[EPMJ81] Barberan N Echenique P M, Ritchie R H and Inkson J. Semiclassical image potential at a solid surface. *Phys. Rev. B*, 23(6486), 1981.

[EPN03] N. Halas E. Prodan, C. Radloff and P. Nordlander. A hybridization model for the plasmon response of complex nanostructures. *Science*, 302(419), 2003.

[FBV99] D. Van Labeke F. Baida and J. Vigoureux. Near-field surface plasmon microscopy: A numerical study of plasmon excitation, propagation, and edge interaction using a three-dimensional gaussian beam. *Physical Review B*, 60(11), 1999.

[Fei71] P. Feibelman. Inclusion of dynamics in the ion-metal surface interaction. *Surf. Sci.*, 27(438), 1971.

[Fer58] R. Ferell. Predicted radiation of plasma oscillations in metal films. *Phys. Rev.*, 111(1214), 1958.

[FQG07] D. Tan H. Yang F. Qi, Y. Li and Q. Gong. Polymerized nanotips via two-photon photopolymerization. *Opt. Express*, 15(3), 2007.

[GE80] J. Gordon and S. Ernst. Surface plasmons as a probe of the electrochemical interface. *Surf. Sci.*, 101(499), 1980.

[GFE95] B. Pettinger K. Doblhofer H. Junkes G. Flätgen, K. Krischer and G. Ertl. Two-dimensional imaging of potential waves in electrochemical systems by surface plasmon microscopy. *Science*, 269(668), 1995.

[GM31] M. Gppert-Mayer. *Ann. Physik*, 9(273), 1931.

[GM80] J. Gadzuk and H. Metiu. Theory of electron-hole pair excitations in unimolecular processes at metal surfaces. *Phys. Rev. B*, 22(2603), 1980.

[GP04] D. K. Gramotnev and D. F. P. Pile. *Appl. Phys. Lett.*, 85(6323), 2004.

[GV93] C. Gerthsen and H. Vogel. *Physik*. Springer-Verlag, 1993.

[GY90] N. Goto and G. Yip. Y-branch wavelength multi / demultiplexer for $\lambda = 1.30$ and $1.55\mu m$. *Eletronics Letters*, 26(2), 1990.

[Han06] A. Hand. High-index lenses push immersion beyond $32\,nm$. *Semiconductor International*, 1, 2006.

[HB07] Tobias Holmgaard and Sergey I. Bozhevolnyi. Theoretical analysis of dielectric-loaded surface plasmon-polariton waveguides. *Physical Review B*, 75(245405), 2007.

[HD06] J. Krenn B. Lamprecht G. Jakopic G. Leising H. Ditlbacher, F. Aussenegg. Organic diodes as monolithically integrated surface plasmon polariton detectors. *Applied Physics Letters*, 89(16), 2006.

[HDA02] G. Schider A. Leitner H. Ditlbacher, J. Krenn and F. Aussenegg. Two-dimensional optics with surface plasmon polaritons. *Applied Physics Letters*, 81(1762), 2002.

[HHT95] M. Ogura M. Komuro H. Nakazawa Y. Nakagawa K. Ohi H. Hiroshima, S. Okayama and K. Tanaka. Electron beam writing and direct processing system for nanolithography. *Nuclear Instruments and Methods in Physics Research A*, 363(73), 1995.

[HLE02] E. Devaux R. Linke L. Martin-Moreno F. Garcia-Vidal H. Lezec, A. Degiron and T. Ebbesen. Beaming light from a subwavelength aperture. *Science*, 297(820), 2002.

[HP94] H. Heinzelmann and D. Pohl. Scanning near-field optical microscopy. *Applied Physics A*, 59(89), 1994.

[Hul84] C. Hull. No. 4575 330. *US Patent*, 1984.

[IPAR03] G. de Valcarcel I. Perez-Arjona and E. Roldan. *Revista Mexicana De Fisica*, 49(91), 2003.

[ISD05] A. Zayats I. Smolyaninov, J. Elliott and C. Davis. Far-field optical microscopy with a nanometer-scale resolution based on the in-plane image magnification by surface plasmon polaritons. *Physical Review Letters*, 94(057401), 2005.

[IW75] J. Inglesfield and E. Wikborg. The van der waals interaction between metals. *J. Phys. F: Metal Phys.*, 5(1475), 1975.

[JAD04] R. Paige J. Amanda, W. Haes and P. Van Duyne. A localized surface plasmon resonance biosensor: First steps toward an assay for alzheimers disease. *Nano Letters*, 4(1029), 2004.

[JAdAK98] F. Morier-Genoud-M. Moser J. Aus der Au, F. H. Loesel and U. Keller. Femtosecond diode-pumped nd:glass laser with more than 1 w of average output power. *Optics Letters*, 23(4), 1998.

[JAdW84] A. Le Methaute J. Andre and O. de Wittee. 8411241. *French Patent*, 1984.

[JdKH07] R. Droste L. Levasier-L. Jorritsma E. van Setten H. Kattouw J. Jacobs J. de Klerk, C. Wagner and T. Heil. Performance of a 1.35na arf immersion lithography system for 40-nm applications. *Proc. SPIE*, 6520(65201), 2007.

[JHG99] S. Yee J. Homola and G. Gauglitz. Surface plasmon resonance sensors: review. *Sensors Actuators B*, 54(3), 1999.

[Jin02] J. Jin. *The Finite Element Method In Electromagnetics*. John Wiley & Sons, New York, 2002.

[JK00] E. Jger and M. I. Kaganow. *Grundlagen der Festkrperphysik*. Harri Deutsch, 2000.

[JTK97] H. Taki A. Morimoto J. Takahara, S. Yamagishi and T. Kobayashi. *Opt. Lett.*, 22(475), 1997.

[JWD05] A. Baudrion J. Weeber, M. Gonzalez and A. Dereux. Surface plasmon routing along right angle bent metal strips. *Appl. Phys. Let.*, 87(221101), 2005.

[JWG01] A. Dereux B. Lamprecht Y. Lacroute J. Weeber, J. Krenn and J. Goudonnet. Near-field observation of surface plasmon polariton propagation on thin metal sripes. *Phys. Rev. B*, 64(045411), 2001.

[JXS07] X. Liu J. Xiao and X. Sun. Design of an ultracompact mmi wavelength demultiplexer in slot waveguide structures. *Optics Express*, 15(13), 2007.

[KA98] A. Kumar and S. Aditya. Performance of s-bends for integrated-optic waveguides. *Microwave Opt. Technol. Lett.*, 19(289), 1998.

[KG61] W. Kaiser and C. Garret. *Phys. Rev. Lett.*, 7(229), 1961.

[Kno98] W. Knoll. Interfaces and thin films as seen by bound electromagnetic waves. *Annu. Rev. Phys. Chem.*, 49(569), 1998.

[Kod81] H. Kodama. Automatic method for fabricating a three-dimensional plastic model with photo-hardening polymer. *Rev. Sci. Instrum.*, 52(1770), 1981.

[KR68] E. Kretschmann and H. Raether. Radiative decay of non-radiative surface plasmons excited by light. *Z. Naturforsch.*, 23, 1968.

[KR74] H. Kogelnik and V. Ramaswamy. *Appl. Opt.*, 13(1857), 1974.

[KS99] F. Kneubühl and M. Sigrist. *Laser.* Teubner Studienbücher Physik, 1999.

[KT00] M. Koshiba and Y. Tsuji. Curvilinear hybrid edge/nodal elements with triangular shape for guided-wave problems. *IEEE JLT*, 18, 2000.

[KZ07] A. V. Krasavin and A. V. Zayats. Passive photonic elements based on dielectric-loaded surface plasmon polariton waveguides. *Applied Physics Letters*, 90(211101), 2007.

[Las07] Laser Zentrum Hannover e.V., Nanotechnology Department. *User manual for the Micro-3-Dimensional Structuring System.* 2007.

[LFB04] Y. Zhuang A. Harpoth M. Thorhauge M. Kristensen W. Bogaerts P. Dummon R. Baets V. Wiaux J. Wouters L. Frandsen, P. Borel and S. Beckx. Ultralow-loss 3-db photonic crystal waveguide splitter. *Opt. Letters*, 29(14), 2004.

[LFTB83] C. G. Willson L. F. Thompson and M. J. Bowden. *Introduction to Microlithography.* American Chemical Society, 1983.

[LL96] K. Lin and W. Lee. Guided-wave $1.3/1.55\mu m$ wavelength division multiplexer based on multimode interference. *Electronic Letters*, 32(14), 1996.

[LLD01] A. Wong M. Lavin W. Leipold L. Liebmann, S. Mansfield and T. Dunham. Tcad development for lithography resolution enhancement. *Advanced Semiconductor Lithography*, 45(5), 2001.

[LP77] D. Langreth and J. Perdew. Exchange-correlation energy of a metallic surface: Wave-vector analysis. *Phys. Rev. B*, 15(2884), 1977.

[Mai06] S. Maier. *Plasmonics - Fundamentals and Applications*. Springer-Verlag, 2006.

[Mal93] M. Malmqvist. Biospecific interaction analysis using biosensor technology. *Nature*, 261(186), 1993.

[Man98] S. Mantl. Strukturierungsverfahren. *Physik der Nanostrukturen*, 29, 1998.

[MBK02] I. Maximov E.-L. Sarwe T.G.I. Ling L. Montelius M. Beck, M. Graczyk and M. Keil. Improving stamps for 10 nm level wafer scale nanoimprint lithography. *Microelectronic Engineering*, 61, 2002.

[MG07] J. Weeber A. Hohenau A. Dereux R. Quidant J. Krenn M. Gonzalez, A. Stepanov. Analysis of the angular acceptance of surface plasmon bragg mirrors. *Optics Letters*, 32(18), 2007.

[MKH94] S. Maruyama M. Koshiba and K. Hirayama. A vector finite element method with the high-order mixed-interpolation-type triangular elements for optical waveguiding problems. *IEEE JLT*, 12, 1994.

[Mor88] W. M. Moreau. *Semiconductor Lithography*. Plenum Publishing Co., New York, 1988.

[MQA98] J. R. Krenn M. Quinten, A. Leitner and F. R. Aussenegg. *Opt. Lett*, 23(1331), 1998.

[MSL72] G. Toulouse M. Sunjic and A. Lucas. Dynamical corrections to the image potential. *Solid State Commun.*, 11(1629), 1972.

[MSMSB03] E. Tapley D.-J. Kang M. E.Welland M. S. M. Saifullah, K. R. V. Subramanian and M. Butler. *Nano Lett.*, 3(1587), 2003.

[MSMSK04] K. R. V. Subramanian-M. E. Welland K. Yamazaki M. S. M. Saifullah, D-J. Kang and K. Kurihara. *J. Sol-Gel Sci. Technol.*, 29(5), 2004.

[MTK07] A. Ghnermeier M. Totzeck, W. Ulrich and W. Kaiser. Pushing deep ultraviolet lithography to its limits. *Nature Photonics*, 1(629), 2007.

[Nd80] J. C. Ndlec. Mixed finite elements in r3. *Numerische Mathematik*, 35(315), 1980.

[NM02] I. V. Novikov and A. A. Maradudin. *Phys. Rev. B.*, 66(35403), 2002.

[NTM94a] K. Shinmou N. Tohge and T. Minami. *J. Sol-Gel Sci. Technol.*, 2(581), 1994.

[NTM94b] K. Shinmou N. Tohge and T. Minami. *Proc. SPIE-Int. Soc. Opt. Eng.*, 2288(589), 1994.

[NVB88] N. Deboer N. Vanhulst and B. Bolger. An evanescent-field optical microscope. *Journal of microscopy - Oxford*, 163(117), 1988.

[Ott68] A. Otto. Excitation of nonradiative surface plasma waves in silver by the method of frustrated total reflection. *Z. Phys.*, 216(398), 1968.

[Ozb06] E. Ozbay. Plasmonics: Merging photonics and electronics at nanoscale dimensions. *Science*, 311(189), 2006.

[Pal84] E. Palik. *Handbook of Optical Constants of Solids*. Academic New York, 1984.

[PBB04] A. Harpoth J. Leon H. Liu M. Kristensen W. Bogaerts P. Dumon R. Baets V. Wiaux J. Wouters P. Borel, L. Frandsen and S. Beckx. Bandwidth engineering of photonic crystal waveguide bends. *Electronic Letters*, 40(20), 2004.

[Pen99] J. Pendry. Playing tricks with light. *Science*, 285(1687), 1999.

[Pet94] A.F. Peterson. Vector finite element formulation for scattering from two-dimensional heterogeneous bodies. *IEEE Trans. On Antennas and Propagation*, 43, 1994.

[PR85] B. Persson and R. Ryberg. Vibrational phase relaxation at surfaces: Co on ni(111). *Phys. Rev. Lett.*, 54(2119), 1985.

[PS57] C. Powell and J. Swan. Effect of oxidation on the characteristic loss spectra of aluminum and magnesium. *Phys. Rev.*, 118(640), 1957.

[Rae88] Heinz Raether. *Surface Plasmons*. Springer Verlag, 1988.

[RBJ91] J. Gimzewski R. Berndt and P. Johansson. Inelastic tunneling excitation of tip-induced plasmon modes on noble-metal surfaces. *Phys. Rev. Lett.*, 67(3796), 1991.

[RDG07a] Inc. RSoft Design Group. Femsim 3.0 user guide. *RSoft Design Group, Inc.*, 2007.

[RDG07b] Inc. RSoft Design Group. Fullwave 6.0 user guide. *RSoft Design Group, Inc.*, 2007.

[REO01] F. Pizzuto M. Steel R. Espinola, R. Ahmad and R. Osgood. A study of high-index-contrast 90 waveguide bend structure. *Opt. Express*, 8(517), 2001.

[Rez02] N. Rezai. *BioTeach Journal*, 1(75), 2002.

[RGT00] K. Shakesheff M. Davies C. Roberts R. Green, R. Frazier and S. Tendler. Surface plasmon resonance analysis of dynamic biological interactions with biomaterials. *Biomaterials*, 21(1823), 2000.

[Rit57] R. H. Ritchie. *Phys. Rev.*, 106(874), 1957.

[Rit72] R. Ritchie. Surface plasmons and the image force in metals. *Phys. Lett. A*, 38(189), 1972.

[RJM03] E. Hao G. Metraux G. Schatz R. Jin, C. Cao and C. Mirkin. Controlling anisotropic nanoparticle growth through plasmon excitation. *Nature*, 425(487), 2003.

[RJZ01] C. Mirkin K. Kelly G. Schatz R. Jin, Y. Cao and J. Zheng. Photoinduced conversion of silver nanospheres to nanoprisms. *Science*, 294(1901), 2001.

[RK88] B. Rothenhäusler and W. Knoll. Surfaceplasmon microscopy. *Nature*, 332(615), 1988.

[RM72] R. Ray and G. Mahan. Dynamical image charge theorystar, open. *Phys. Lett. A*, 42(301), 1972.

[RNC05] A. Doraiswamy I. Mihailescu M. Jelinek A. Ovsianikov B. Chichkov R. Narayan, C. Jin and D. Chrisey. Laser processing of advanced bioceramics. *Advanced Engineering Materials*, 7(12), 2005.

[RR99] Mendelsohn A R and Brend R. Protein biochemestry: Protein interaction methods-toward an endgame. *Science*, 284(1948), 1999.

[RZB05] M. D. Selker R. Zia and M. L. Brongersma. *Phys. Rev. B*, 71(165431), 2005.

[SAMR03] H. A. Atwater S. Meltzer E. Harel B. E. Koel S. A. Maier, P. G. Kik and A. A. G. Requicha. *Nat. Mater.*, 2(229), 2003.

[SBE06] E. Devaux J. Laluet S. Bozhevolnyi, V. Volkov and T. Ebbesen. Channel plasmon subwavelength waveguide components including interferometers and ring resonators. *Nature Letters*, 440(508), 2006.

[SC93] M. Shea and R. Compton. Surface-plasmon ejection of ag^+ ions from laser irradiation of a roughened silver surface. *Phys. Rev. B*, 47(9967), 1993.

[SC96] P. Renstrom S. Chou, P. Krauss. Imprint lithography with 25-nanometer resolution. *Science*, 5(5258), 1996.

[Sch97] P. Schuck. Reliable determination of binding affinity and kinetics using surface plasmon resonance biosensors. *Curr. Opin. Biotechnol.*, 8(498), 1997.

[Sch03] A. Schultz. Plasmon resonant particles for biological detection. *Current Opinion in Biotechnology*, 14(13), 2003.

[Ser04] Jesper Serbin. *Fabrication of Photonic Structures by Two-Photon Polymerization.* 2004.

[Ser05] B. Sernelius. Effects of spatial dispersion on electromagnetic surface modes and on modes associated with a gap between two half spaces. *Phys. Rev. B*, 71(235114), 2005.

[SHP97] H. Gau R. Conradt D. Reinelt H. Ulmer P. Leiderer S. Herminghaus, J. Vorberg and M. Przyrembel. Hydrogen and helium films as model systems of wetting. *Ann. Phys. Lpz.*, 6(425), 1997.

[SIB05] E. Devaux adn T. W. Ebbesen S. I. Bozhevolnyi, V. S. Volkov. *Phys. Rev. Lett.*, 95(46802), 2005.

[SIBH01] K. Leosson P. M. W. Skovgaard S. I. Bozhevolnyi, J. Erland and J. M. Hvan. *Phys. Rev. Lett.*, 86(3008), 2001.

[SK02] K. Saitoh and M. Koshiba. Full-vectorial imaginary-distance beam propagation method based on a finite element scheme: Application to photonic crystal fibers. *IEEE JQE*, 38, 2002.

[SL72] J. Schmit and A. Lucas. Plasmon theory of the surface energy of metals. *Solid State Commun.*, 11(415), 1972.

[SLJ02] J. Bur S. Johnson S. Lin, E. Chow and J. Joannopoulos. Low-loss, wide-angle y-splitter at $\sim 1.6\mu m$ wavelength built with a two-dimensional photonic crystal. *Opt. Letters*, 27(16), 2002.

[SLS98] D. Hetherington B. Smith R. Biswas K. Ho S. Lin, J. Fleming and M. Sigalas. *Nature*, 394(251), 1998.

[SMK97] O. Nakamura S. Maruo and S. Kawata. Three-dimensional microfabrication with two-photon-absorbed photopolymerization. *Opt. Lett.*, 22(2), 1997.

[Som09] A. Sommerfeld. Über die ausbreitung der wellen in der drahtlosen telegraphie. *Ann. d. Physik*, 28(665), 1909.

[SPL06] D. Yanga N. Cho S. Park, T. Lim and K. Lee. Fabrication of a bunch of sub-30-nm nanofibers inside microchannels using photopolymerization via a long exposure technique. *Appl. Phys. Lett.*, 89(173133), 2006.

[SPW07] C. Reinhardt K. Subramanian B. Chichkov S. Passinger, M. Saifullah and M. Welland. Direct 3d patterning of tio_2 using femtosecond laser pulses. *Advanced Materials*, 19(1218), 2007.

[SSCI93] Alex L A Bourret R B Schuster S C, Swanson R V and Simon M I. Assembly and function of a quaternary signal transduction complex monitored by surface plasmon resonance. *Nature*, 365(343), 1993.

[TEW98] H. Ghaemi T. Thio T. Ebbesen, H. Lezec and P. Wolff. Extraordinary optical transmission through subwavelength. *Nature*, 391(667), 1998.

[TK00] Y. Tsuji and M. Koshiba. Guided-mode and leaky-mode analysis by imaginary distance beam propagation method based on finite element scheme. *IEEE JLT*, 18, 2000.

[TNB04] K. Leosson T. Nikolajsen and S. Bozhevolnyia. Surface plasmon polariton based modulators and switches operating at telecom wavelengths. *Applied Physics Letters*, 85(24), 2004.

[TRGB93] H. C. Pfeiffer D. Puisto T. R. Groves, J. G. Hartley and D. K. Bailey. Electron beam lithography tool for manufacture of x-ray masks. *BM J. Res. Develop.*, 37(3), 1993.

[TT03] K. Tanaka and M. Tanaka. *Appl. Phys. Lett*, 82(1158), 2003.

[Ueb92] H. Ueba. Theory of core-hole-decay dynamics of adsorbates on metal surfaces: Role of the $2\pi^*$ level of a chemisorbed co molecule. *Phys. Rev. B*, 45(3755), 1992.

[VF05] G. Veronis and S. Fan. Bends and splitters in metal-dielectric-metal subwavelength plasmonic waveguides. *Appl. Phys. Lett.*, 87(131102), 2005.

[VKVV01] Xiaoning Jiang Vijay K. Varadan and Vasundara V. Varadan. *Microstereolithography and other Fabrication Techniques for 3D MEMS*. John Wiley & Son Ltd, 2001.

[VM04] Y. Vlasov and S. McNab. Losses in single-mode silicon-on-insulator strip waveguides and bends. *Opt. Express*, 12(1622), 2004.

[WBB06] D. Van Thourhout D. Taillaert P. Jaenen J. Wouters S. Beckx V. Wiaux W. Bogaerts, P. Dumon and R. Bacts. Compact wavelength-selective functions in silicon-on-insulator photonic wires. *IEEE J. of selected topics in quantum electronics*, 12(6), 2006.

[WBE03] A. Dereux W. Barnes and T. Ebbesen. Surface plasmon subwavelength optics. *Nature*, 424(824), 2003.

[WI77] E. Wikborg and J. Inglesfield. Collective modes and ground state energy of the semi-infinite electron gas. *Phys. Scr.*, 15(37), 1977.

[WMA82] S. Korotky W. Minford and R. Alferness. Low-loss ti:linbo_3 waveguide bends at $\lambda = 1.3\mu m$. *IEEE Journal of Quantum Electronics*, 18(10), 1982.

[WW04] B. Wang and G. P. Wang. *Appl. Phys. Lett*, 85(3599), 2004.

[XL07] R. Austin S. Chou X. Liang, K. Morton. Single sub-20 nm wide, centimeter-long nanofluidic channel fabricated by novel nanoimprint mold fabrication and direct imprinting. *Nano Letters*, 7(12), 2007.

[Yee66] K. S. Yee. Numerical solution of initial boundary value problems involving maxwell's equations in isotropic media. *IEEE Trans. Antennas Propagat.*, (302), 1966.

[YTS97] M. Koshiba Y. Tsuji and T. Shiraishi. Finite element beam propagation method for three-dimensional optical waveguide structures. *IEEE JLT*, 15, 1997.

[YVMW03] A. Blanco G. von Freymann K. Busch W. Koch C. Enkrich M. Deubel Y. V. Miklyaev, D. C. Meisel and M. Wegener. Three-dimensional face-centered-cubic photonic crystal templates by laser holography: fabrication, optical characterization, and band-structure calculations. *Appl. Phys. Lett.*, 82(1284), 2003.

[Zen07] J. Zenneck. Über die fortpflanzung ebener elektromagnetischer wellen längs einer ebenen leiterfläche und ihre beziehung zur drahtlosen telegraphie. *Ann. d. Physik*, 23(846), 1907.

[ZK76] E. Zaremba and W. Kohn. Van der waals interaction between an atom and a solid surface. *Phys. Rev. B*, 13(2270), 1976.

[ZK04] S. Zhijun and K. Hong Koo. Refractive transmission of light and beam shaping with metallic nano-optic lenses. *Applied Physics Letters*, 85(642), 2004.

A. List of own publications

A.1. List of own publications

- S. Passinger, C. Ohrt, A. Seidel, W. Cheng, R. Kiyan, C. Reinhardt, and B. Chichkov,
Large scale high speed Two-Photon-Polymerization with 100 *nm resolution,*
in preparation.

- S. Passinger, A. Seidel, C. Ohrt, C. Reinhardt, A. Stepanov, R. Kiyan, and B. Chichkov,
Novel splitter design for surface plasmon polariton applications,
Optics Express **submitted**.

- A. B. Evlyukin, S. I. Bozhovolnyi, A. L. Stepanov, C. Reinhardt, S. Passinger R. Kiyan, B. N. Chichkov,
Focussing and directing of surface plasmon polaritons by curved chains of nanoparticles,
Optics Express **16667**, Vol. 15, No. 25, (2007).

- Sven Passinger, Mohammad S. M. Saifullah, Carsten Reinhardt, Kavasseri R. V. Subramanian, Boris N. Chichkov, and Mark E. Welland,
Direct 3D patterning of TiO_2 using femtosecond laser pulses,
Advanced Materials **19**, pp. 1218 - 1221 (2007).

- Roman Kiyan, Carsten Reinhardt, Sven Passinger, Andrei L. Stepanov, Andreas Hohenau, Joachim R. Krenn, and Boris N. Chichkov,
Rapid prototyping of optical components for surface plasmon polaritons,
Optics Express **4205**, Vol. 15, No. 7, (2007).

- C. Reinhardt, S. Passinger, V. Zorba, B.N. Chichkov, C. Fotakis,
Replica molding of picosecond laser fabricated Si microstructures,
Applied Physics A **87**, 673 - 677 (2007).

- R. Houbertz, P. Declerck, S. Passinger, A. Ovsianikov, J. Serbin, and B. N. Chichkov
Investigations on the generation of photonic crystals using two-photon polymerization (2PP) of inorganic-organic hybrid polymers with ultra-short laser pulses,
phys. stat. sol. (a) **204**, No. 11, 3662 - 3675 (2007)

- A. Ovsianikov, S. Passinger, R. Houbertz, B. N. Chichkov,
Three dimensional material processing with femtosecond lasers

C. R. Phipps - Laser Ablation and its applications, New York : Springer, S. 121-157 (2007)

- S. Passinger, A. L. Stepanov, A. Evlyukhin, C. Reinhardt, R. Kiyan, B. N. Chichkov,
  Two-Photon Polymerization and Applications in Plasmonics,
  Metamaterials II, SPIE Vol. **6581**. S. 65810U-1 ff (2007)

- C. Reinhardt, R. Kiyan, S. Passinger,A. L. Stepanov, A. Ostendorf, B. N. Chichkov,
  Rapid laser prototyping of plasmonic components,.
  Applied Physics A **89** 2, S. 321-325 (2007)

- P. Declerck, R. Houbertz, G. Jakopic, S. Passinger, and B.N. Chichkov *High refractive index inorganic-organic hybrid materials for photonic applications,*
  Organic/Inorganic Hybrid Materials2007 MRS Proceedings Volume 1007-S01-02 (2007)

- Carsten Reinhardt, Roman Kiyan, Andreas Seidel, Sven Passinger, Andrey L. Stepanov, Andrey B. Evlyukhin, and Boris N. Chichkov
  Focusing and manipulation of surface plasmons by laser fabricated dielectric structures
  Proc. SPIE **6642** 664205 (2007)

- Sven Passinger, Roman Kiyan, Alexandr Ovsianikov, Carsten Reinhardt and Boris Chichkov
  Two-photon polymerization and applications in plasmonics
  Proc. SPIE **6581** 658104 (2007)

- Sven Passinger, Roman Kiyan, Aleksandr Ovsianikov, Carsten Reinhardt and Boris Chichkov
  3D nanomanufacturing with femtosecond lasers and applications
  Proc SPIE **6591** 659104 (2007)

- C. Reinhardt, S. Passinger, B. N. Chichkov, W. Dickson, G. A. Wurtz, P. Evans, R. Pollard, and A. V. Zayats,
  Restructuring and modification of metallic nanorod arrays using femtosecond laser direct writing,
  Applied Physics Letters **89**, 231117 (2006)

- B. Chichkov, J. Koch, A. Ovsianikov, S. Passinger, C. Reinhardt, J. Serbin,
  Direct-write micro- and nanostructuring with femtosecond lasers.
  Ultrafast Lasers for Materials Science, MRS Symposium Proc. Vol. **850**. S. 179 - 186

- Carsten Reinhardt, Sven Passinger, Boris N. Chichkov, Carsten Marquart, Ilya P. Radko, and Sergey I. Bozhevolnyi
  Laser-fabricated dielectric optical components for surface plasmon polaritons,
  Optics Letters Vol. **31**, No. 9, (2006)

- S. Passinger, C. Reinhardt, B.N. Chichkov,
  2D and 3D photonic and plasmonic structures fabricated by two-photon polymerization,
  Nanophotonics, SPIE Vol. 6195. S. 61950U.1-61950U.9 (2006)

- B.N. Chichkov, E. Fadeeva, J. Koch, A. Ostendorf, A. Ovsianikov, S. Passinger, C. Reinhardt,
  Femtosecond laser lithography and applications.
  Photon processing in microelectronics and photonics V, SPIE Vol. **6106**. S. 610612 (2006)

- C. Reinhardt, S. Passinger, B. N. Chichkov, W. Dickson, G. A. Wurtz, P. Evans, R. Pollard, A. V. Zayats,
  Restructuring and modification of metallic nanorod arrays using femtosecond laser direct writing,
  Applied Physics Letters **89** S. 231117 (2006)

- S. Passinger, J. Koch, R. Kiyan, C. Reinhardt, B. N. Chichkov,
  Multiphoton laser lithography for the fabrication of plasmonic components,
  Plasmonics: nanoimaging, nanofabrication, and their applications II, SPIE Vol. **6324**. S. 63240O (2006)

- C. Reinhardt, S. Passinger, R. Kiyan, A. L. Stepanov, B. N. Chichkov,
  Laser based rapid prototyping of plasmonic components,
  Plasmonics: Metallic Nanostructures and their Optical Properties IV, SPIE Vol. **6323**, S. 63230P (2006)

- Carsten Reinhardt, Roman Kiyan, Sven Passinger, and Boris N. Chichkov
  Dielectric and metallic plasmonic components fabricated with femtosecond lasers
  Proc. SPIE **6462** 646215 (2007)

- Carsten Reinhardt, A. Ovsianikov, Sven Passinger, and Boris N. Chichkov
  Fabrication of mecromechanical and microoptical systems by two-photon polymerization
  Proc. SPIE **6466** 64660 (2007)

- Boris N. Chichkov, Jürgen Koch, Jie Li, Alexandr Ovsianikov, Sven Passinger, and Carsten Reinhardt
  High-resolution photofabrication with fs lasers, materials, and applications
  ACS Div. of Polymeric Materials: Science and Engineering (2005)

- A. Ovsianikov, S. Passinger, C. Reinhardt, B. N. Chichkov,
  Micro- and nanostructuring by two-photon illumination of photosensitive materials, Laser in Manufacturing
  Third International WLT-Conference, S. 867 (2005)

A.2. List of won prizes

- Beste wissenschaftliche Veröffentlichung 2007
  des Laser Zentrum Hannover e.V.
  Dipl. Phys. Sven Passinger, Dr. Carsten Reinhardt, Prof. Boris N. Chichkov
  für: *Direct 3D patterning of* TiO_2 *using femtosecond laser pulses,*
  Advanced Materials **19**, pp. 1218 - 1221 (2007).

- Preisträger Hochschul-Impuls 2006
  Gündungswettbewerb der Wirtschaftsentwicklungsgesellschaft
  der Region Hannover
  Dipl. Phys. Sven Passinger and Prof. Boris N. Chickov
  Laser Zentrum Hannover e.V., Abteilung Nanotechnologie
  'M3D – Verfahren und Maschine zur 3D-Mikrostrukturierung'

A.3. Curriculum vitae

Name	Sven Passinger
Date and place of birth	19. March 1979, Hildesheim, Germany
Nationality	German
Martial status	single
Parents	Edith Passinger (nee Stolz) Robert Passinger
Education	
1985 - 1989	Elementary School Schulenburg, Germany
1989 - 1991	Middle School (Orientierungsstufe Pattensen) Pattensen, Germany
1991 - 1996	High School (Gymnasium Sarstedt), Sarstedt Germany
1996 - 1998	High School (Gymnasium Himmelsthür), Hildesheim, Germany
1998 - 1999	Military service
1999 - 2004	Academic studies of Physics (Leibniz University Hannover), Hannover Germany
2003 - 2004	Diploma thesis at the Leibniz University Hannover Topic: "Optimierung von Plasmaparametern für XUV Rekombinationslaser - Aufbau eines "GRENOUILLE"-Autokorrelators zur Charakterisierung kurzer Pulse "
June 2004	Diploma in physics at the "Institute of Quantum Optics" (Leibniz University Hannover, Hannover, Germany)
2004 - 2006	Scholarship of the "European Graduate College Interference and Quantum Applications" at the Leibniz University Hannover, Hannover, Germany
2004 - 2008	PhD at the "Laser Zentrum Hannover e.V.", Hannover, Germany Topic: " Two-Photon Polymerization and application to Surface Plasmon Polaritons "
2006 - today	Scientific co-worker at the "Laser Zentrum Hannover e.V.", Hannover, Germany

B. Acknowledgments

In the last four years, many people have contributed, either directly or indirectly, to the work resulting in this thesis. I would like to thank all my colleagues, friends and relatives for their invaluable contributions and support. Without this help, it would have been impossible to finish the dissertation.

First, I would like to thank my supervisor Prof. Boris N. Chichkov for providing me with an interesting work position in the Nanotechnology Department of the Laser Zentrum Hannover, for the excellent supervision during the last four years and for many suggestions and ideas which have contributed significantly to the success of my work.

I would also like to express my gratitude to Dr. Carsten Reinhardt and Dr. Roman Kiyan for supporting the research in the laboratory, and for many fruitful discussions and the correction of this work.

Also the contributions of my colleagues Christoph Ohrt and Andreas Seidel should be mentioned here. Without their help in the laboratory and discussions concerning the work, this thesis would not have been possible in this manner.

I am also very grateful to the diploma students, trainees and student assistants in our group who supported me during these four years, especially Wei Cheng, Alexander Gold, Matthias Nguyen Ba, Rebecca Cotton and Yasemin Acar.

Furthermore, I would like to express my gratitude to the members of the Nanotechnology Division for the good working atmosphere and for their support, especially Dr. Ulf Hinze, with whom I shared an office and who was always willing to help with advice.

Also, I am indebted to Michael Botts, not only for many interesting and well organized industrial fairs, but especially for the language correction of this thesis.

Furthermore, I would like to thank all colleagues at the LZH for a very good working atmosphere. Especially Reiner Gebauer should be thanked for the many SEM images, which are an important part of this paper. Also, many thanks to the staff of the mechanical- and electronic-workshop, without their contributions, many experiments could have not been realized.

Last but not least, I am extremely grateful to my family, especially my parents, who made my studies and this work possible, and to my girlfriend Christina, who accompanied and supported me since the beginning of my academic studies.